Intra-Operative Shape Acquisition of Tibio-Femoral Joints Using 3D Laser Scanning for Computer Assisted Orthopaedic Surgery: A Proof of Concept

by

Shailesh Vasant Joshi

This thesis is submitted in partial fulfilment of the requirements for the degree of

Doctor of Philosophy

Department of Biomedical Engineering

University of Strathclyde

Glasgow, United Kingdom

May 2015

COPYRIGHT STATEMENT

Signed:

Date:

DEDICATION

I dedicate this thesis to my late father (Mr. Vasant Shrinivas Joshi) who believed in me and guided me towards excellence throughout his life. I miss him every day.

His inspiration and motivation will always linger on.

ACKNOWLEDGEMENTS

I offer my sincerest gratitude to my supervisor Professor Philip Rowe who has supported and has provided an extraordinary guidance throughout the duration of my doctoral studies. His depth of the knowledge with the envisagement of the application has played a very important role in the completion of this thesis. I attribute the level of my Ph.D. thesis to his motivation, enthusiasm and patience without which this thesis would not have been written or completed.

I take this opportunity to appreciate all the faculty members of the Department of Biomedical Engineering for their support and cooperation. I am really grateful to my co-supervisor Dr. Philip Riches who arranged the samples and the lab space as well as provided assistance in acquiring the ethical approvals for the experiments. I would like to thank Dr. Heba Lakany for her exceptional guidance in the statistical data analysis. In addition, I am thankful to Dr. Gareth Pierce (Dept. of CUE, EEE) for introducing me to his team of world class researchers and allowing me to perform pilot studies using their departmental laser scanner. I would also like to thank the technician staff Mr. John MacLean, Mr. Stephen Murray and a friend Hariprashanth for their valuable advices and assistance in building the system used for the study. Many thanks to the research radiology team of the Western Infirmary, Glasgow for the clinical scanning of the samples and also to Mr. John Wilson for driving us to and fro the infirmary.

I am indebted to all my friends who have helped me throughout this duration. I did not know that some of the many entertaining talks we had would turn out to be useful for the studies. Thank you very much Shiny for proof reading the thesis and bearing the long, endless questions and discussions before the Viva Voce. I am also thankful to my colleagues Georgia, Matthew, Andre, Socrates, Cheryl and Gwen for assessing my presentation, asking me tricky questions and providing valuable tips.

Finally, I express my love and my gratitude to my beloved mother (Mrs. Smita Joshi) and my charming sister (Mrs. Ashwini Purohit) for their understanding and boundless love, throughout the duration of my studies. Without their

encouragement and patience this doctoral study was merely fictitious. Special thanks to my lovely nephews Atharva and Akshaj and my brother in law Mr. Prashant Purohit for bringing joy in my life.

Over and above all, I thank God who has abled me to be who I am.

PUBLICATION DETAILS

Joshi SV, Rowe PJ, Pierce G, Ahmed KE, MacLeod C, Whitters CJ (2013). Automated Laser Registration and Quantitative Assessment of Articular Cartilage for Computer Assisted Orthopaedic Surgery. Bone Joint Journal. 95(B): 28

Joshi SV, Rowe PJ (2014). Intra-Operative 3D Laser Scanning and Best-Fit Alignment for Computer Assisted Orthopaedic Surgery. Bone Joint Journal. 96(B): 16.30

Joshi SV, Rowe PJ (2014). Automated laser registration for Computer Assisted Orthopaedic Surgeries at 14th Annual Meeting of International Society for Computer Assisted Orthopaedic Surgery, Milan, June18-21

Liu X, Wang L, Ji J, Yao W, Wei W, Fan J, **Joshi S**, Li D, Fan Y (2014). A Mechanical Model of the Cornea Considering the Crimping Morphology of Collagen Fibrils. Invest Ophthalmol Vis Sci. 55(4):2739-2746

ABSTRACT

Image registration is an important aspect in all computer assisted surgeries including Neurosurgery, Cranio-maxillofacial surgery and Orthopaedics. It is a process of developing a spatial relationship between pre-operative data, such as Computed Tomography (CT) scans or Magnetic Resonance Imaging (MRI) scans and the physical patient in the operating theatre. Current image registration techniques for Computer Assisted Orthopaedic Surgery (CAOS) in minimally invasive Unicompartmental Knee Arthroplasty (UKA) surgery are invasive, time consuming and often take 14-20 minutes and are therefore costly. The rationale for this study was to develop a new operating theatre compliant, quick, cost effective, contactless, automated technique for image registration during CAOS based on an accurate rigid body model of the ends of the exposed knee joint, produced using 3D laser scans taken intra-operatively by a Laser Displacement Sensor.

Bespoke automated 3D laser scanning techniques based on the DAVID Laserscanner method were developed and were used to scan surface geometry of the knee joints in cadaveric legs. The laser scanned knee joint models were registered with the pre-operative (MRI/CT) models and the deviations were evaluated. Furthermore, trends in the deviations were studied along with a supportive validity study. Results indicated that the laser scanner can repeatedly produce accurate 3D models of the human tibio-femoral joint in the operating theatre.

This study has provided a proof of concept for a new in situ automated shape acquisition and registration technique for CAOS with the potential for providing a

quantitative assessment of the articular cartilage integrity during lower limb arthroplasty.

CONTENTS

LIST OF FIGURES

LIST OF TABLES

LIST OF ABBREVIATIONS

AAE	Average Absolute Error
AAPE	Average Absolute Percentage Error
ACL	Anterior Cruciate Ligament
ACROBOT	Active Constraint Robot
AIB	Apparent Integrated Backscatter
ASCII	American Standard Code for Information Interchange
AVI	Audio Video Interleave
BMP	Bitmap
BRIGIT	Bone Resection Instrument Guidance by Intelligent Telemanipulator
CAD/CAM	Computer Aided Design/Computer Assisted Manufacturing
CAOS	Computer Assisted Orthopaedic Surgery
CAS	Computer Assisted Surgery
CASC	Clinical Anatomy Skills Centre
CASPAR	Computer Assisted Surgical Planning and Robotics
CE-FFE	Contrast-Enhanced Fast Field Echo
CIS	Computer Integrated Surgery
CMM	Coordinate Measuring Machine
CMOS	Complementary Metal Oxide Semiconductor
CNR	Contrast to Noise Ratio
CRIGOS	Compact Robot for Image-Guided Orthopaedic Surgery
CSF	Cerebrospinal Fluid System
NIRS	Near-Infrared Spectroscopy
CT	Computed Tomography
CTA	Computed Tomography Angiography
DAQ	Data Acquisition
dGEMERIC	Delayed Gadolinium-Enhanced MRI of Cartilage
DICOM	Digital Imaging and Communications in Medicine
DIP	Dual-In-Line-Package
d_{max}	Maximum Deviation
DXF	Drawing Interchange Format
ENT	Ear, Nose and Throat

ECG	Electro-Cardiography
EMG	Electro-Myography
pMRI	Perfusion Magnetic Resonance Imaging
f-MRI	Functional Magnetic Resonance Imaging
f-PAM	Functional Photo-acoustic Microscopy
MPI	Magnetic Particle Imaging
MEG	Magnetic-Encephalography
fCT	Functional Computed Tomography
EIT	Electrical Impedance Tomography
MRE	Magnetic Resonance Elastography
FDA	Food and Drug Administration
FEA	Finite Element Analysis
FLASH	Fast Low Angle Shot
FOV	Field of View
FSE	Fast Spin Echo
GAG	Glycosaminoglycan
HPA	Health Protection Agency
IBM	International Business Machine
ICP	Iterative Closest Point
ISS	Integrated Surgical Systems Limited
IGS	Image Guided Surgery
IR	Image Registration
IRC	Integrated Reflection Coefficient
JPEG	Joint Photographic Experts Group
JSN	Joint Space Narrowing
JSW	Joint Space Width
KSS	Knee Society Clinical Rating System
LIDAR	Light Detection and Ranging
LRS	Laser Range Scanner
MAPE	Mean Absolute Percent Error
MARS	MiniAture Robot for Surgery
MBARS	Mini Bone-Attached Robotic System for Joint Arthroplasty

MIS	Minimally Invasive Surgery
MRA	Magnetic Resonance Angiography
MRI	Magnetic Resonance Imaging
NEX	Number of Excitations
NIST	National Institute of Standards and Technology
NMR	Nuclear Magnetic Resonance
NS	Not Significant
OA	Osteoarthritis
PCL	Posterior Cruciate Ligament
PFA	Patella-Femoral Arthroplasty
PFS	Precision Freehand Sculptor
PKR	Partial Knee Replacement/Resurfacing
PTB	Physikalisch-Technische Bundesanstalt Institute
RANSAC	Random Sample Consensus
RF	Radio Frequency
RIO	Robotic Interactive Orthopaedic
ROM	Range of Motion
SCARA	Selective Compliance Assembly Robot Arm
SD_{AE}	Standard Deviation of Absolute Error
SNR	Signal to Noise Ratio
SPECT	Single Photon Emission Computed Tomography
PET	Positron Emission Tomography
EEG	Electro-Encephalography
SPGR	Spoiled Potential Gradient Recoil
SSN	Surgical Segment Navigator
STL	Stereolithography
TE	Time of Echo
THA	Total Hip Arthroplasty
THR	Total Hip Replacement
TKA	Total Knee Arthroplasty
TKR	Total Knee Replacement/Resurfacing
TOF	Time of Flight

TR	Time of Repetition
TURP	Transurethral Resection Prostate Surgery
UBM	Ultrasound Biomicroscopy
UKA	Unicompartmental Knee Arthroplasty
UKR	Unicompartmental Knee Replacement/Resurfacing
URI	Ultrasound Roughness Index
WAM	Whole-Arm Manipulation
WOMAC	Western Ontario and McMaster University Osteoarthritis Index

CHAPTER 1. INTRODUCTION

1.1 FIELD OF RESEARCH

Osteoarthritis (OA) is one of the most common musculoskeletal diseases affecting around 8.75 million of the population in the UK (Arthritis Research UK, 2013). It is a chronic joint disorder characterised by degeneration of the articular cartilage which results in severe pain while performing daily voluntary musculoskeletal activities. The knee joint is the most common site to get affected by OA and nearly 4.7 million people in the UK (as of 2010) have OA of knee with an estimated rise up to 5.4 million by 2020 (Arthritis Research UK, 2013).

After non-surgical treatments have been exhausted, patients suffering from OA of knee are usually advised to undergo a knee replacement surgery where the articulating surfaces of the tibio-femoral joint are resected and are replaced with the prosthetic implants. Recently, the knee replacement surgery is increasingly supported by the use of the computers (Computer Assisted Orthopaedic Surgery (CAOS)) along with advanced robotic systems. CAOS systems such as MAKO RIO® usually comprise of three main phases i.e. 1) Pre-operative planning; 2) Intra-operative execution; and 3) Implant placement. The pre-operative planning consists of acquiring high resolution scans (usually CT scans) of the patient's knee joint and segmenting them to generate a patient specific knee model which is then used to plan the surgery. Based on this plan, the surgery is performed intra-operatively with the help of computers and robotic consoles and finally the implant prosthesis is precisely placed.

1.2 RESEARCH PROBLEM

In most CAOS applications for knee surgery, pre-operative CT scans are acquired on the patient's leg and are segmented to create a patient specific 3D knee model. Image registration is one of the important intra-operative phases of CAOS which is a process of developing a spatial relationship between the pre-operative data and the physical patient present in the operating theatre.

Registration in most CAOS knee surgery applications is achieved manually and laboriously with the help of a hand-held navigated probe where digitised points on the articulating surfaces (tibial plateaux and femoral condyles) of the knee joint are acquired and fitted to the pre-operative scan data using a best fit type minimisation. However, this manual digitisation approach is invasive, time consuming and hence costly. In this study, an automated shape acquisition technique using a laser sensor has been developed which was used in situ to produce 3D models of the articulating surfaces of the tibio-femoral joint to be registered with the pre-operative scans.

1.3 STRUCTURE OF THE THESIS

The organisation of the thesis is as follows:

Chapter 2 Literate Review: This chapter is dedicated to an extensive review of the existing literature starting from the anatomy and morphology of the knee joint, OA of the knee, its diagnosis and treatment options focussing on the knee replacement surgeries. The second part of this chapter covers computers and robotics in medicine which includes computer assisted surgery (CAS) and CAOS. In the succeeding part

of the chapter, medical image registration, its classification and its application in CAOS are explained emphasizing on the surface based registration technology. The concluding section of this chapter comprises use of lasers in medicine and laser based medical image registration approaches with a description of 3D laser scanners and their principles.

Chapter 3 Study design: Chapter 3 of the thesis describes the rationale of the study, aim and objectives of the investigation. It also clarifies the stages of the investigation and the research questions.

Chapter 4 Pilot studies: A set of pilot experiments explained in this chapter were used to select optimum parameters for the laser sensor. 3D laser scanning of bovine and porcine knee joints was performed followed by mono-modal and multi-modal imaging comparison to obtain the proof of concept as well as to establish the initial validity of the technique.

Chapter 5 Building the Equipment: This chapter enlightens the process of designing of the scanner and components used with their specifications. In addition, it also illustrates the procedure that was followed to acquire a 3D scan using the chosen setup.

Chapter 6 Methodology: Chapter 6 gives a description of the demography of the cadaveric samples utilised in the validation study and methods for the pre-operative and the intra-operative data acquisition. The data analysis and the statistical analysis approaches used are stated including the research hypotheses. In the last part of the chapter, the design of a second validity experiment is described.

Chapter 7 Results: This chapter is divided into two sections. The key findings of the concurrent validity study (1) are reported in the first section where the alignment statistics between pre-operative and intra-operative cadaver data is presented. Also, the effects of the independent variables on the deviation between the data are reported along with the summary of the investigation. The results of the second validity experiment are illustrated in the latter section of the chapter.

Chapter 8 Discussion: This chapter concentrates on interpreting the outcomes reported in the Chapter 7 (Results). The inferences of the results and the hypotheses testing for the studies are discussed. The chapter also includes a description of the limitations of the study and the recommendations for the future research.

Chapter 9 Conclusion: The final chapter of the thesis provides a summary of the work done pointing out the implications of the findings with respect to the research questions and the research objectives.

CHAPTER 2. LITERATURE REVIEW

2.1 KNEE JOINT

The knee is a synovial pivotal hinge type of joint and one of the most complex and largest skeletal structures of the human anatomy (figure 2.1). It facilitates numerous daily activities such as walking, bending, running, sitting, squatting, climbing, etc. by allowing flexion up to 120°-160° depending upon the position of the hip (Brugioni and Falkel, 2004), extension of 0°-15° and slight medial/internal and lateral/external rotation (Tortora, 2005).

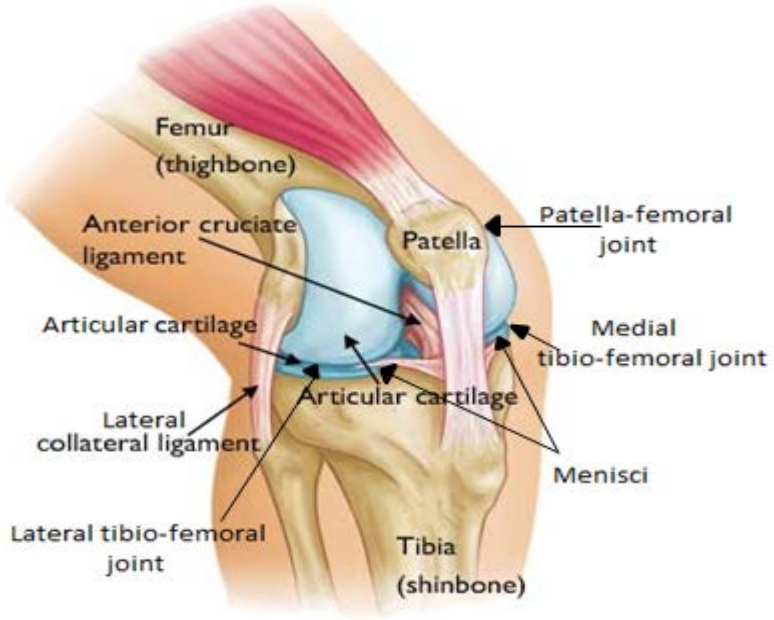

Figure 2.1 Anatomy of the knee joint
(Adapted from American Academy of Orthopaedic Surgeons, 2014)

The knee joint is a single joint cavity comprising of three incongruent bones, distal femur, proximal tibia and patella contributing to three articulating joints: (Tortora, 2005).

(i) Lateral tibio-femoral joint: A modified hinge joint between lateral condyle of distal femur, lateral condyle of proximal tibia and lateral meniscus.

(ii) Medial tibio-femoral joint: A modified hinge joint between medial condyle of distal femur, medial condyle of proximal tibia and medial meniscus.

(iii) Patella-femoral joint: An Intermediate planar joint between patella and lower end of distal femur (Tortora, 2005).

2.1.1 Distal Femoral Condyles

Distal femoral condyles are convex, asymmetric and slightly cuboid in shape (figure 2.2). The lateral and medial condyles have a characterised distinct shape corresponding to their respective articulating tibial plateau. This shape plays an important role in the articulation of the tibio-femoral joint (Blackburn and Craig, 2015). Prominent landmarks of lateral and medial femoral condyles such as epicondyles are important in finding proper rotational alignment during knee arthroplasty surgeries (Griffin *et al.*, 2000).

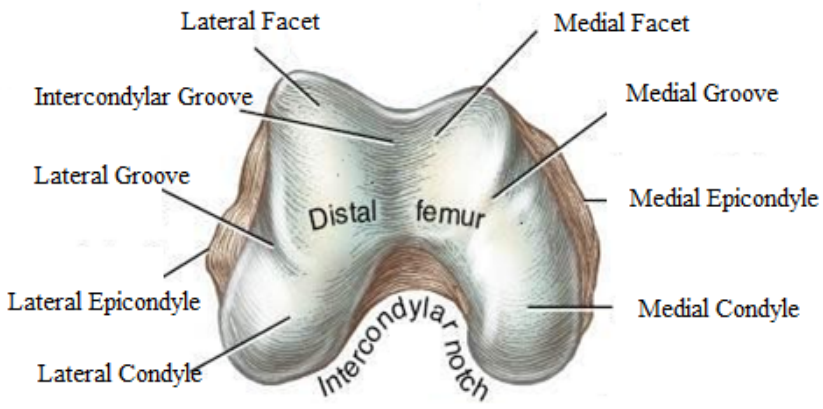

Figure 2.2 Anatomy of the distal femur
(Adapted from Alphonso B, 2013)

Lateral and medial epicondyles also serve as attachment sites for extra capsular fibular and tibial collateral ligaments respectively which strengthen and support the knee joint (Yoshioka *et al.*, 1987; Margo *et al.*, 2010). The trochlea, a counterpart of the patella-femoral joint consists of medial and lateral facets of the femoral sulcus which articulate with the patellar groove to facilitate articulation of the patella-femoral joint (Tecklenburg *et al.*, 2006).

2.1.2 Tibial Plateaux

Articulating surface of the tibia comprises of lateral and medial tibial plateaux which articulate with the respective femoral condyles (figure 2.3). The lateral side of the tibia is convex and nearly circular in shape whereas medial side is slightly larger than lateral and is flat and oval (Margo *et al.*, 2010).

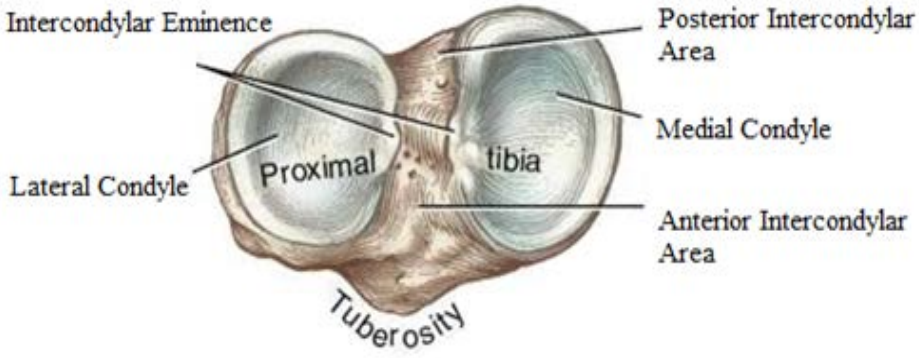

Figure 2.3 Anatomy of the proximal tibial plateaux
(Adapted from Alphonso B, 2013)

Both tibial plateaux are raised on their respective medial end where they border inter-condylar eminences (Margo *et al.*, 2010). Anterior and posterior intercondylar areas of tibial plateau serve as attachment sites for two intra-capsular ligaments viz anterior cruciate ligament (ACL) and posterior cruciate ligament (PCL)

respectively. The ACL averts hyperextension of the knee and prevents sliding of the anterior region of tibia on the femur whereas PCL prevents posterior sliding of tibia on femur, which is very vital when the knee is flexed (Tortora, 2005).

2.1.3 Patella

Patella is an ovoid sesamoid bone also known as the knee cap (figure 2.4). It consists of medial and lateral facets (later being broader and deeper) which articulate with the trochlea of the distal femur (Margo *et al.*, 2010).

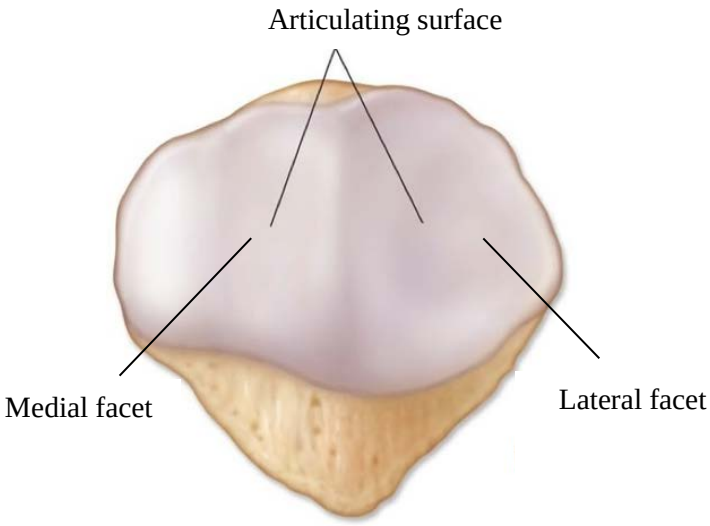

Figure 2.4 Anatomy of the patella
(Adapted from LaBarbera, 2015)

2.1.4 Meniscus

The menisci are two crescent shaped fibrocartilage discs present between the articulating surfaces of lateral and medial tibio-femoral joint (figure 2.5) (Tortora, 2005; Margo *et al.*, 2010). Largely they are composed of collagen (75%) and non-collagenous proteins (8%-13%) (Margo *et al.*, 2010).

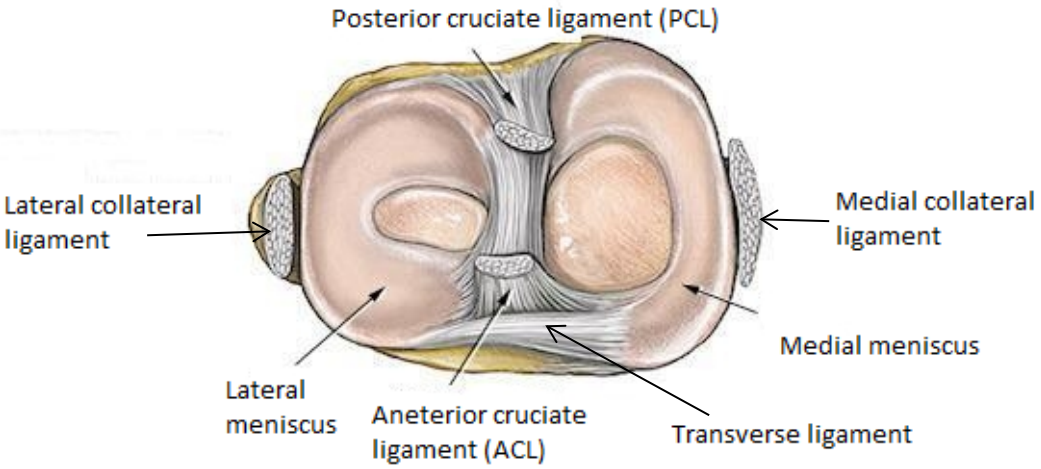

Figure 2.5 Anatomy of the meniscus and surrounding ligaments in the knee joint (Adapted from Artro, 2008)

The medial meniscus is C-shaped and is larger than the lateral meniscus. Anteriorly it is attached to the anterior intercondylar fossa of the tibia, just in front of ACL and posteriorly it attaches to the posterior intercondylar fossa between lateral meniscus and PCL (Tortora, 2005). The lateral meniscus is almost circular in shape and covers a larger surface area than the medial meniscus. Its anterior end is attached to the anterior and lateral side of the intercondylar eminence. Posteriorly, it is attached at the posterior end of the intercondylar eminence and in front of posterior end of medial meniscus (Tortora, 2005; Margo *et al.*, 2010). Key functions of the menisci are facilitating load transmission by providing larger contact surface area,

distribution and circulation of the synovial fluid and enhancement of articular conformity (Tortora, 2005; Scott and Scuderi, 2006).

2.1.5 Articular Cartilage

Articulating surfaces of the knee joint are covered with smooth, white connective tissue called hyaline cartilage (figure 2.6) which transmits and distributes load uniformly across the joint (Plancher and Lipnick, 2010). It can also be said that the functional capacity of synovial joints highly depends on the state of the articular cartilage (Buckwalter *et al.*, 1988). Researchers consider articular cartilage as the most important biomarker for degenerative and traumatic joint diseases (Koo *et al.*, 2009; Link *et al.*, 2007; Link, 2011). [In general, a biomarker is a biochemical material which not only assists in the disease diagnosis but also enables the classification of the disease severity, its onset and progression and assessment of efficacy of the treatment (Baucer *et al.*, 2006)].

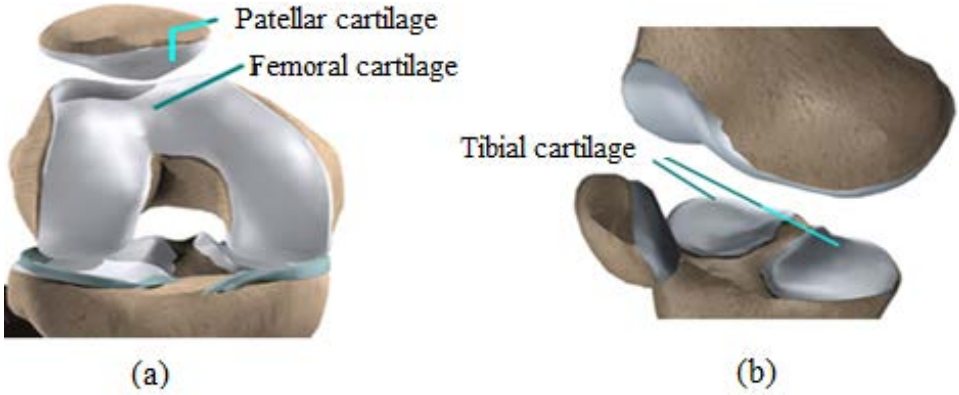

Figure 2.6 Articular cartilage of the knee joint
(a): Distal femoral and posterior patellar cartilage. (Adapted from Medical Multimedia Group, MMG, 2008) (b): Proximal tibial cartilage. (Adapted from Medical Multimedia Group, MMG, 2000)

Articular cartilage varies in its mechanical properties such as volume, thickness, strength, cell density and matrix composition in the same joint, among joints and among species; however, its general structure, composition and functions is similar in all the synovial joints (Athanasiou *et al.*, 1991). Chief components of articular cartilage are: 65% - 80% of water, 10% - 20% of collagen (90% - 95% of Type II collagen), 10% - 20% proteoglycan proteins and 1% - 5% of chondrocytes (Bhosale and Richardson, 2008). Unlike other connective tissues, blood vessels and nerves are absent in the cartilage and it receives its nutrition only from diffusion which also makes its healing capacity limited (Maroudas *et al.*, 1968; Buckwalter *et al.*, 2005; Plancher and Lipnick, 2010). On the ultra-structural level, articular cartilage consists of four levels: Superficial zone, Transitional zone, Middle zone and Calcified zone (Bhosale and Richardson, 2008).

Functions of articular cartilage:

- It acts as a shock absorber and possesses extraordinary durability and stiffness to compression and resilience (Buckwalter *et al.*, 2005; Bhosale and Richardson, 2008).
- It has an excellent capacity to distribute loads uniformly throughout the joint to reduce peak stresses acting on the subchondral bone which facilitates pain free and composed joint movements (Mandelbaum *et al.*, 1998; Mow and Rosenwasser, 1988; Bhosale and Richardson, 2008; Plancher and Lipnick, 2010).
- It provides smooth gliding surface for articulation of the joint with a low co-efficient of friction (Bhosale and Richardson, 2008; Plancher and Lipnick, 2010).

2.2 OSTEOARTHRITIS OF THE KNEE

Osteoarthritis (OA) is a chronic joint disorder characterized by progressive softening and disintegration of articular cartilage. Primarily, it results from inequality between the stresses applied at the articular cartilage and subchondral bone and their ability to withstand them (Solomon *et al.*, 2005). The knee joint is the most prone structure to be affected by OA which creates a debilitating condition (Arthritis Research UK, 2013). There are several factors that increase the risk of this condition such as joint injuries, ageing, obesity as well as lack of nutrition and physical exercise (Manninen *et al.* 2001; Tortora 2005; Mezhov *et al.*, 2014). In addition, there is a strong evidence of genetic factors associated with the onset and progression of OA (Spector and MacGregor, 2004; Bian *et al.*, 2012).

Scuderi (2010) reported that about 25% - 39% of people aged between 45 - 64 show some symptoms associated with the OA of knee and 85% of individuals above the age of 65 have radio-graphically detectable OA. In a cohort study of 29 women, Weidow *et al.* (2005) stated that patients with lateral and medial knee OA had a wider pelvis and a longer distance between centres of the femoral head to proximal femoral shaft respectively.

In a healthy knee joint, there is a continuous dynamic process of breaking down and formation of healthy cartilaginous matrix. It is believed that this action is carried out with the help of Metalloproteinases enzymes which break down the damaged articular cartilage especially its collagen matrix. When affected by OA, there is a higher rate of destruction of articular cartilage than replacement which is associated with the over secretion of these enzymes and eventually degradation of the proteoglycans and the collagen network (Woessner and Gunja-Smith, 1991;

Lohmander *et al.*, 1993; Tortora, 2005; Marieb and Hoehn 2007; Roach and Tilley, 2008).

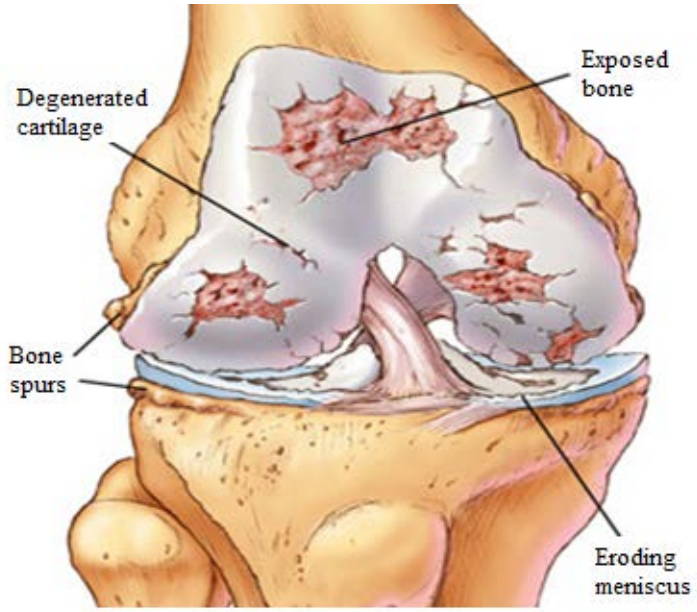

Figure 2.7 Osteoarthritis of knee
(Adapted from Chiropractic Books, 2008)

Affected cartilage then slowly degenerates and bone ends become exposed (figure 2.7). Smooth and easily gliding surfaces dry out and sub-articular bone forms cysts where there is maximum load distribution (Solomon *et al.*, 2005). Ligaments and menisci tear which becomes highly painful. The consequence is nocturnal or permanent pain, localised swelling, and stiffness where voluntary movements are highly restricted (Tortora, 2005, Joern *et al.*, 2010).

2.2.1 Diagnosis of OA

Knee OA is classified as either primary (idiopathic) or secondary depending on the predisposing pathology, the former being the most common (Altman, 1995; Roach and Tilley, 2008). An effective diagnosis is required to evaluate the presence of OA which then enables effective treatment. After examining the patient's history

and related symptoms, a physical inspection is carried out. Special functional tests such as gait analysis, ligament stability, meniscus tests, etc. are performed to assess the patient's range of motion (ROM) (Joern *et al.*, 2010).

However, imaging modalities are the most decisive diagnostic techniques for inspecting knee OA as they can not only confirm its presence but can also indicate affected joint compartments with progression and stage of the disease (Carrillon, 2008). Conventional radiography techniques (X-ray) are still used as reference methods and are preferred over other modalities as they are relatively cost-effective, quick and readily available (Carrillon, 2008, Joern *et al.*, 2010). Techniques such as CT are utilised with or without contrast injections in order to acquire three dimensional information about the patient's joint to assess the joint degradation. High-resolution CT imaging can be used to visualize trabecular bone and osteophyte formation (Blackburn *et al.*, 1996).

A common drawback of radiography and conventional CT modalities is that they fail to visualise articular cartilage directly in the images. However radiography can provide indication of the progression of the disease indirectly through narrowing of the joint space width (JSW), subchondral sclerosis and osteophyte formation as shown in figure 2.8 (a) (Carrillon, 2008; Hayashi *et al.*, 2011; Roemer *et al.* 2011; Stacy and Basu, 2013).

(a) (b)

Figure 2.8 Imaging osteoarthritis

(a): Radiograph of osteoarthritic knee showing joint space narrowing (JSN) and osteophyte formation, (b): Arthro-CT scan of the patella-femoral joint depicting cartilage loss in the lateral facet of the patella (Adapted from Carrillon *et al.*, 2012)

Newer CT techniques such as Arthro-CT scanner when used with contrast injection allow good visualisation of intra-articular structures including articular cartilage, especially patella-femoral cartilage (figure 2.8 (b)) and can be substituted for conventional radiography and CT scanning (Carrillon, 2008; Saggin *et al.*, 2010; Carrillon, 2012).

One of the most recent techniques for diagnosing OA is Magnetic Resonance Imaging (MRI). A standard and satisfactorily acquired MRI can depict thin and high resolution slices of the rigid structures such as bones as well as soft tissues surrounding it and most importantly articular cartilage. Choosing an accurate protocol is a crucial step when performing MR imaging. The selection of type of sequence (T1, T2 weighted fast spin echo (FSE), proton density weighted, etc.) and pre-setting parameters such as time of echo (TE), time of repetition (TR), slice

thickness, gap between the slices, number of slices, field of view (FOV), flip angle, etc. have a critical impact on the final quality of the images (Carrillon, 2008).

Apart from standard MRI sequences such as T1 or T2-weighted 2D FSE (figure 2.9(a)), newer techniques like Fast Low Angle Shot, 3D FLASH (also known as Spoiled potential gradient recoil, SPGR) are becoming more popular in quantitatively assessing articular cartilage (figure 2.9 (b)) as they provide excellent contrast between cartilage and the surrounding structures with better signal to noise ratio (SNR), contrast to noise ratio (CNR) and spatial resolution (Haase *et al.*, 1986; Kornaat *et al.*, 2005; Eckstein *et al.* 2006; Rogers *et al.*, 2013).

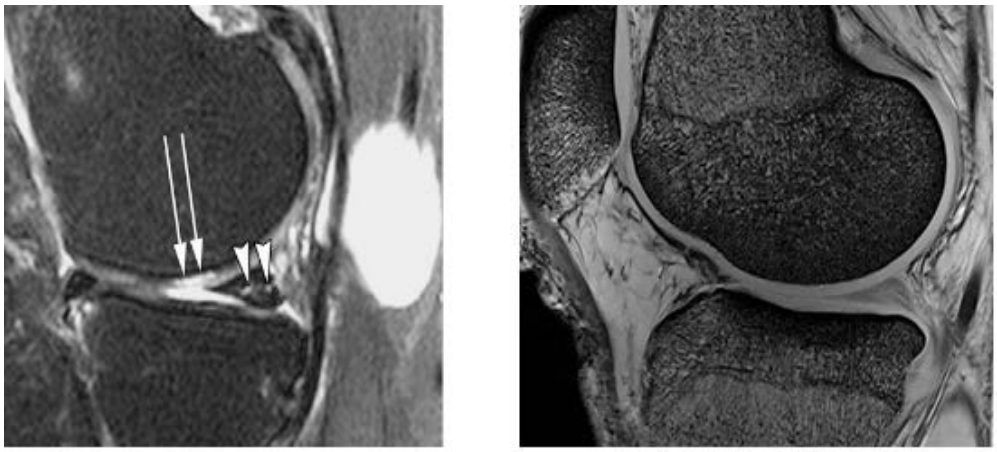

(a) (b)

Figure 2.9 MRI imaging in the diagnosis of OA

(a): Sagittal 2D T2-weighted fat supressed FSE image showing focal full thickness cartilage defect at weight bearing of medial femoral condyle. (b): High field strength (7 T) MRI imaging using 3D FLASH protocol which shows excellent differentiation of articular cartilage, subchondral bone, and intra-articular joint fluid (Reprinted with permission, Roemer *et al.*, 2011).

Further developments in quantitative MRI techniques, for instance Delayed Gadolinium-Enhanced MRI of Cartilage (dGEMRIC) and sodium MRI have a potential of identifying glycosaminoglycan (GAG) content in vivo in early stages of OA which in turn elucidates gross morphologic abnormality of the cartilage (Bashir *et al.*, 1999; Tiderius *et al.*, 2003).

Researchers have illuminated the fact that the pathophysiology of OA depends upon the biomechanical stresses affecting the articular cartilage as well as the subchondral bone i.e. a whole organ disorder leading to the joint failure (Beuf *et al.* 2002, Sowers *et al.* 2003, Felson and Neogi 2004, Mrosek *et al.* 2006, Roemer *et al.* 2011). However, onset and progression of OA is associated with the articular cartilage degeneration and there is plenty of research carried out showing changes in its thickness and volume when affected by OA as assessed by MRI (Cohen *et al.*, 1999; Felson *et al.* 2000, Cicuttini *et al.*, 2001; Link *et al.* 2003, Ecsktein *et al.*, 2006; Koo *et al.*, 2009; Eckstein *et al.*, 2011). Other imaging methods such as commercial 3D laser scanners have been used to estimate cartilage volume and thickness, either in vitro or on synthetic models (Koo *et al.*, 2005; Trinh *et al.*, 2006; Koo *et al.*, 2009). This has also steered attention towards quantitative assessment of articular cartilage using various techniques such as high-frequency (12-55 MHz) ultrasound and indentation methods to understand the integrity of the articular cartilage based on its mechanical properties e.g. Young's modulus, thickness, volume as well as its acoustic properties such as apparent integrated backscatter (AIB), ultrasound roughness index (URI) and integrated reflection coefficient (IRC) (Toyras *et al.*, 1999; Saarakkala *et al.*, 2003; Saarakkala *et al.*, 2004; Laasanen *et al.*, 2006; Aula *et al.*, 2010).

2.2.2 Treatment Options for OA

At present OA is one of the few non-curable diseases and all the treatment options are applied to alleviate the symptoms (most importantly pain and restricted movement) and attempt to slow down its progression (Joern *et al.*, 2010). The first line of treatment is actually preventing OA by patient education, exercise, evading obesity, etc. Intra-articular corticosteroids may be injected to reduce the inflammation. Creamer and Hochberg (1997) described a treatment pyramid for OA of the knee as shown in figure 2.10.

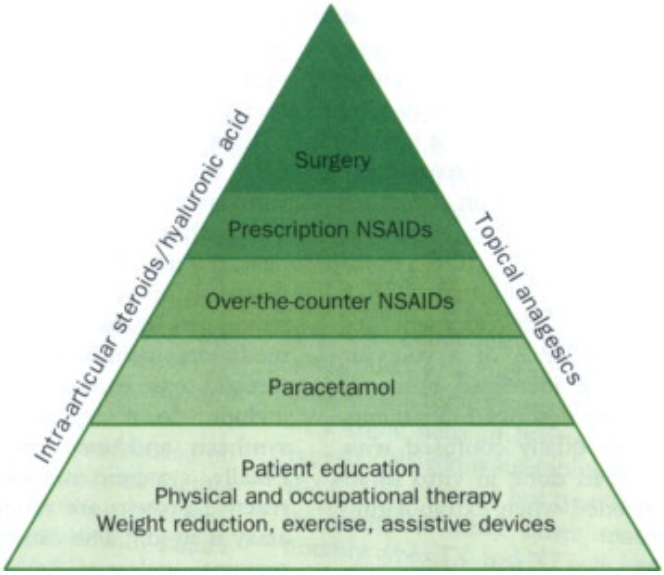

Figure 2.10 Treatment pyramid for osteoarthritis of knee
(Reprinted with permission, Creamer and Hochberg, 1997)

After failed conservative treatments, patients with persisting symptoms of knee OA are advised to undergo one of the major types of surgeries such as arthroscopic debridement, realignment osteotomy or knee replacement (Lutzner *et al.*, 2009). Badly aligned joints are more prone to OA of knee (Marieb and Hoehn, 2007); hence osteotomy realignment surgeries are performed to shift joint forces in the varus/valgus knee from the osteoarthritic part of the joint to the relatively

healthier compartment. Arthroscopy refers to inserting an endoscopic instrument called an arthroscope consisting of a tube through which a camera and surgical instruments can be passed to diagnose and treat the early stages of OA of the knee. Bone marrow stimulating techniques like microfracture surgeries have gained popularity due to their minimally invasive nature and shorter recovery period but their significance in treating OA is still not well researched (Lutzner *et al.*, 2009). Other options such as ligamentous reconstruction are also available but are not used often (Hanssen *et al.*, 2000). However, all these options are anyways only directed towards relieving pain and perhaps slowing down the progression of OA and they cannot be used as a routine treatment (Lutzner *et al.*, 2009).

2.2.3 Knee Replacement Surgeries

Fundamentally, the key motive behind all orthopaedic treatments is to restore the natural pain-free movement and ROM of the affected musculoskeletal system. Dye (2005) coined a term ‘Envelope of Function’ for the capacity of knee and other joints to sustain the load, angular displacement and frequency distribution while maintaining homeostasis of the surrounding tissues. Thus, the purpose of knee replacement surgery or knee arthroplasty is to restore and/or maximise the envelope of function of the arthritic knee as safely and precisely as possible.

The two major types of knee replacement surgeries are Total Knee Replacement/Resurfacing/Arthroplasty (TKR/TKA) and Partial/Unicompartmental/ Unicondylar Knee Replacement/Resurfacing/Arthroplasty (PKR/PKA/UKR/UKA). TKA is a more conventional and reliable technique and is applied when all other options in treating knee OA have been rejected. Its primary goal is to re-establish the normal mechanical axis of the knee with a stable prosthesis implant (Scuderi, 2002).

In TKA, the entire articulating surfaces of the femoral condyles and tibial plateau are resurfaced and the implant prosthesis is placed to facilitate smooth movement as shown in figure 2.11. UKA on the other hand is also aimed at re-establishing knee joint function and pain relief but with much less bone resection. UKA is a less invasive approach and is applied when only one compartment of the knee joint is damaged (figure 2.12).

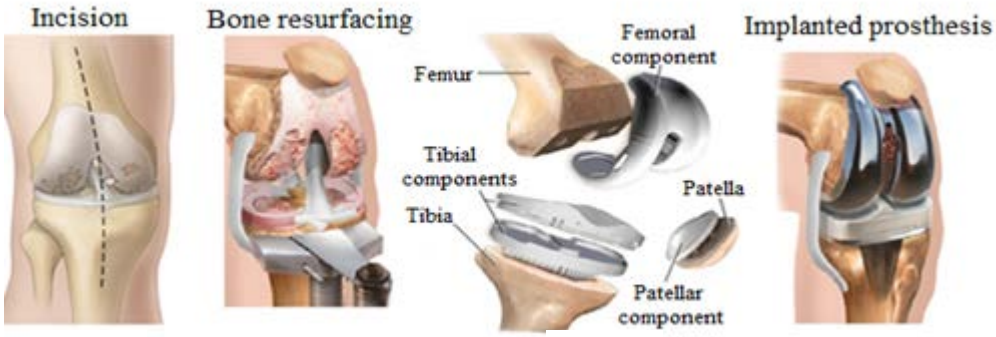

Figure 2.11 Total knee arthroplasty stages

(a): Incision of 6-9 inches (150-225 mm) is made between two compartments. (b): Patella is moved out of the way and arthritic tibio-femoral joint is exposed and shaved to remove degraded area. (c): Polyethylene and metal implants are fixed on resurfaced tibial and femoral condyles usually using cement. (d): Implants are adhered in place for smoother articulation of the knee joint (Adapted from Teitel AD, 2013)

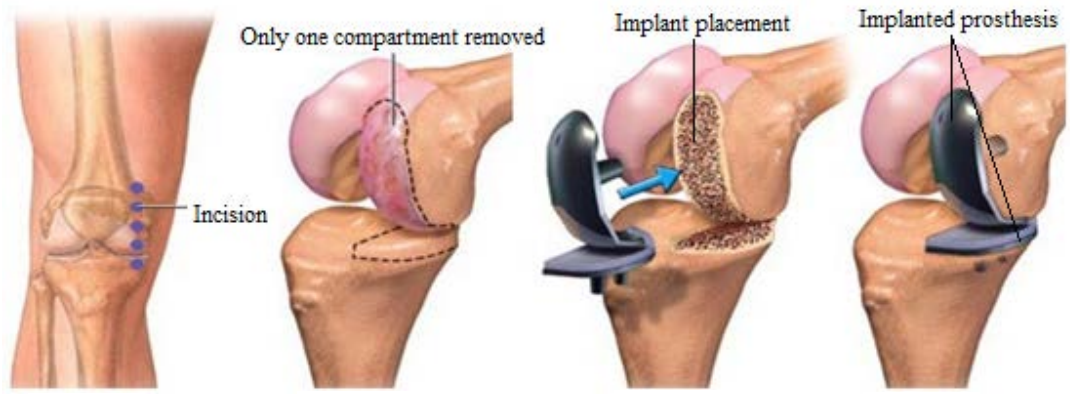

Figure 2.12 Unicompartmental knee arthroplasty stages
(a): Incision of 3-4 inches (80-100 mm) is made on the affected knee compartment. (b): Degraded articular cartilage and subchondral bone are removed. (c): Polyethylene and metal implants are fixed on the tibial plateau and femoral condyles respectively, usually using cement. (d): Implants are adhered in place for smoother articulation of the knee joint (Adapted from Benjamin CMa, 2011)

In both surgeries, the arthritic tibial plateau is usually replaced with a polyethylene component often backed by metal and the femoral condyle is replaced with a metal component. TKA has demonstrated predictability, durability and some effectiveness in restoring the envelope of function and relieving pain (Colizza *et al.*, 1995; Diduch *et al.*, 1997; Aglietti *et al.*, 1999). UKA is a more surgically conservative technique in restoration of maximum ROM and knee kinematics (Price *et al.*, 2001; Hollinghurst *et al.*, 2006; Akizuki *et al.*, 2009, Lyons *et al.*, 2012) but is less frequently performed.

Table 2.1 Comparison between Total Knee Replacement and Unicompartmental Knee Replacement

Criteria	Total knee arthroplasty (TKA)	Unicompartmental knee arthroplasty (UKA)
Patient Selection	Gold standard technique for treating severe knee OA and still accepted by majority of the experienced surgeons. Ultimate option when knee joint is severely damaged in both lateral and medial compartments and is beyond repair.	Advised to patients with localised area of damage (one compartment) to the knee joint. Still not widely accepted. Cannot be applied to severely damaged knee joints.
Cumulative revision rate	Lower Survival of implants up to 98.9 % and for 19 years (Keating *et al.*, 2002; Abdeen *et al.*, 2010; Goodfellow *et al.*, 2010; Lyons *et al.*, 2012).	Higher Survival of implants sometimes less than 85% and revision may be required just in 5 years. (Tabor and Tabor, 1998; O'Rourke *et al.*, 2005; Vorlat *et al.*, 2006; Goodfellow *et al.*, 2010). Well planned and executed UKA can provide more than 90% of implant survival for 10 years (Murray *et al.*, 1998; Argenson *et al.* 2002; Lyons *et al.*, 2012).
Incision	Larger incision (6-9 inches/150-225 mm). Lateral eversion of patella and dislocation of tibio-femoral joint for maximum joint-space exposure.	Smaller incision (3-4 inches/80-100 mm). Patella is retracted instead of turning it aside. Joint dislocation is avoided or minimised (Marcacci *et al.*, 2000, Leopold, 2009, Pearle *et al.*, 2010).
Blood loss and tissue damage	Higher blood loss and risk of injuries to the surrounding tissues.	Lesser blood loss and risk of injuries to the surrounding tissues thus more preservation of bone stock.
Recovery period	Longer in-patient stay, longer rehabilitation and slower recovery to normal daily activities.	Shorter in-patient stay, quicker rehabilitation and recovery to daily activities, less prolonged pain
Restoration of joint function	Knee kinematics and ROM less improved than UKA.	Superior ROM and knee kinematics than TKA (Newman *et al.*, 1998; Price *et al.*, 2001; Hollinghurst *et al.*, 2006 Goodfellow *et al.*, 2010; Lyons *et al.*, 2012).

2.2.4 Complications of Knee Replacement Surgeries

Large incision size, dissection of high amount of the tibio-femoral joint and surrounding tissues make TKA highly invasive. However, many of the complications arising from knee replacement surgeries are similar for both TKA and UKA.

- The most concerning complication is infection in the joint which can occur at any stage post-surgery. Infection rates after TKA may vary from 0.5%-12% (Blom *et al.*, 2004). In a review study of 4171 TKA surgeries Wilson *et al.* (1990) reported that 67 patients (1.6%), mostly males with previous knee surgeries were followed by infection. Cheung *et al.* (2008) stated the risk factor from infection in 222,684 TKA surgeries was 0.53%. Joint infection after UKA is usually lower and observed as less than 1% of the patients (Knutson *et al.*, 1986; Harwin, 2003).
- Other common clinical complications are deep vein thrombosis and pulmonary embolism, neurovascular injury, wound complications, persistent or recurring pain and stiffness (Harwin, 2003; Lombardi *et al.*, 2007; Cheung *et al.*, 2008).
- Failed planning, malposition, alignment errors and improper placement of implants can lead to loosening of tibial and femoral components, periprosthetic fracture (fracture in the bone around the implant) and mobile bearing dislocation (Voss *et al.*, 1995; Sharkey *et al.*, 2002; Harwin, 2003; Cheung *et al.*, 2008; Leopold, 2009).
- One of the most crucial factors that is responsible for failures and possible complications of UKA is improper patient selection (obese patients or patients with $< 90°$ flexion and varus/valgus deformity $> 15°$) and evaluating the state of the remaining compartment of the knee (Stern *et al.*, 1993; Murray *et al.*, 1998;

Price *et al.*, 2001; Harwin, 2003). Improper patient selection and technical errors contribute to failed and revised surgeries.

- Surgeons have to be adequately trained in order to perform UKA as various tasks apart from cutting of the bones such as implant positioning, fixation and cementing can be difficult to achieve through a small window (Harwin, 2003).
- The malalignment leading to implant failures, technical challenges of the surgery and increasing demand on surgical precision have led researchers to attempt to assist the surgeon with the computerised technology.

2.3 COMPUTERS AND ROBOTICS IN MEDICINE

Computer Integrated Surgery (CIS) and Computer Assisted Surgery (CAS) have emerged as one of the major areas of research from late 1980s leading to Computer Assisted Orthopaedic Surgery (CAOS). Although CIS and CAS are more polysemic terms, they have similar approaches in attaining the ultimate goal of performing surgery with enhanced geometric-ergonomic accuracy and precision.

2.3.1 Medical Robots and CAS

Medical robots are the key element of CIS which are designed to assist surgeons in pre-operative surgery planning, intra-operative registration and execution of the surgery with some systems also assisting in post-operative verification and follow up (Davies, 2000; Sugano, 2003; Taylor and Stoianovici, 2003; Picard *et al.*, 2004; Satava, 2011). Taylor and Stoianovici (2003) classified medical robots based on the manipulator design, level of autonomy, targeted area, technique and operating environment as shown in figure 2.13.

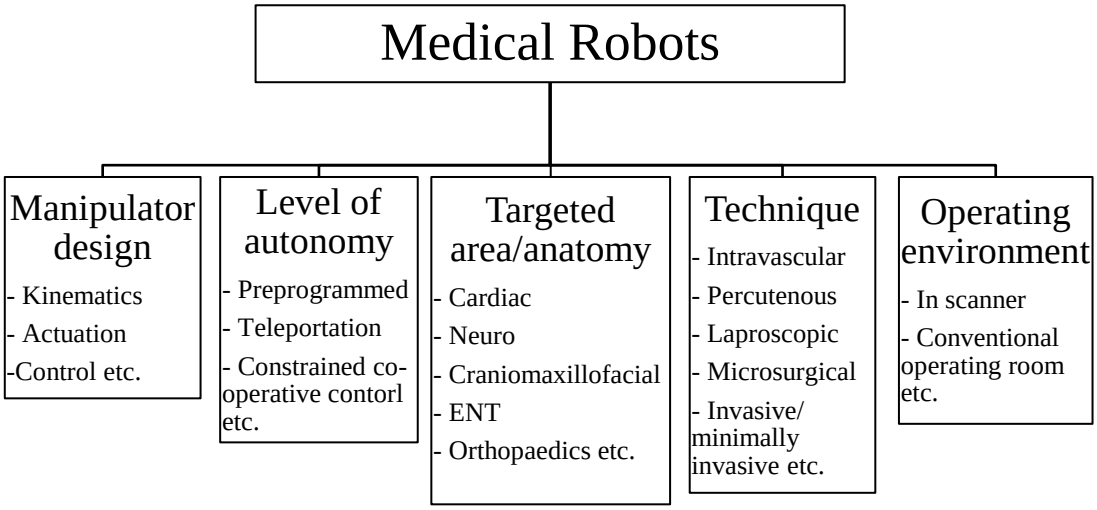

Figure 2.13 Medical robots classification
(Adapted from Taylor and Stoianovici, 2003)

In simple terms, the use of robots and medical robotic information systems in surgery can be reduced to three major phases (figure 2.14): 1) input; 2) analysis or processing; and 3) output (Satava, 2011). The input side uses sensors employed to acquire the required data in order to plan the surgery. These include mechanical pointers, chemical and biological sensors, imagers, etc. In CAS and CIS system, processing and analysis is achieved on the basis of the collected input data and it can be either computer assisted or computer integrated, the former being semi-automatic and the latter an automatic process.

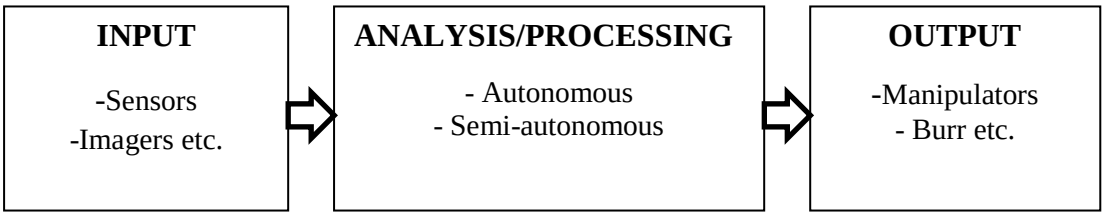

Figure 2.14 Three phases of medical robots
(Adapted from Satava, 2011)

The output end of medical robotic systems is equipped for the surgical execution using manipulators, high energy devices like lasers, electro-coagulators, high speed rotating burrs, etc.

2.3.2 CAS

The important difference between robotic and computer assisted surgery is that robotic surgery implies to a robotic drive controlled by an automated motorized movement whereas for CAS, the control of the movement is with the surgeon (Davies, 2000; Adili, 2004). These terms along with augmented surgery, image guided surgery (IGS), medical robotics, etc. are arranged into a single term by Troccaz (2009) as computer assisted medical interventions (CAMI). CAS systems provide different levels of assistance to the surgeon during training for execution of surgeries. In general, CAS systems can be classified into three major aspects: 1) Image guided surgery systems (IGS CAS); 2) Assistant robots for surgery; and 3) Training simulators for surgery (Cosio and Castaneda, 2003). Apart from improving surgeon's technical capabilities, CAS systems provide better visualisation of the patient's anatomy, better pre-operative planning of the surgery and precise and accurate intra-operative execution of the surgery. A basic approach to any general CIS and CAS system is shown in figure 2.15.

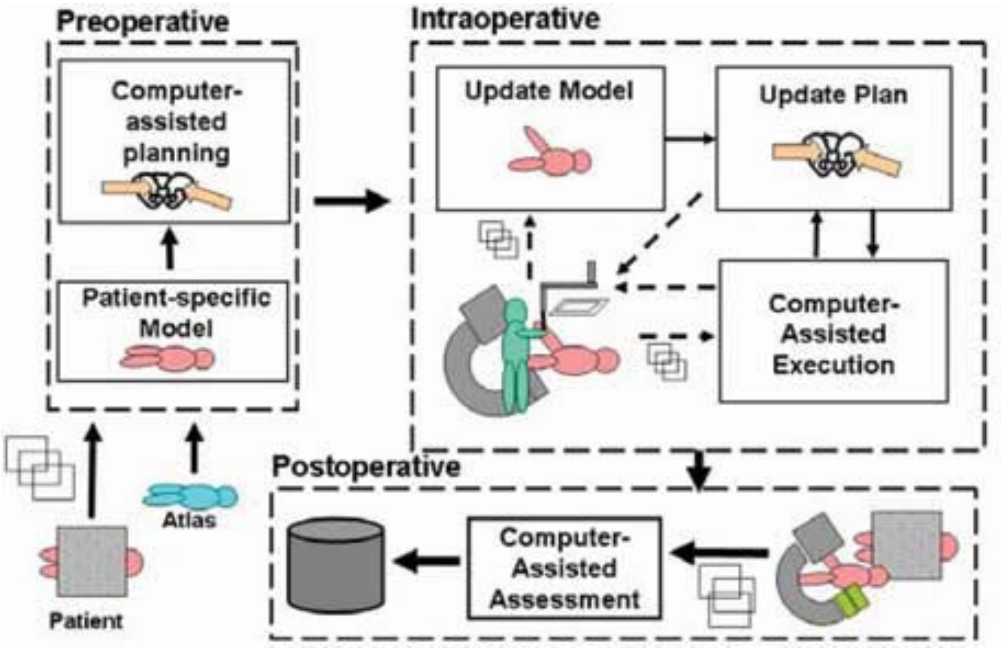

Figure 2.15 CIS and CAS system: Approach and execution
(Reprinted with permission, Taylor, 2006)

Three important and most common phases of CIS and CAS systems:

A. Pre-operative Planning

Initially, before the actual surgery, 1D 2D or 3D data of the patient's anatomy is acquired using different imaging modalities such as CT, MRI, etc. These images are used in conjunction with anatomical concepts and by extracting the required information (segmentation process), a patient specific model of that organ under scrutiny is created which is used to plan the surgery.

B. Intra-operative Procedure

The patient specific model created pre-operatively is first registered with the intra-operative physical anatomy of the patient which is acquired using different sensing techniques to establish a spatial relationship between them. This process is called as 'image registration'. The concept of image registration is further described

in sub-section 2.4. This is followed by the actual surgery such as cutting, electrocuting, burring, etc. with the help of robot in an automatic or semi-automatic way.

C. Post-operative Rehabilitation

Few CAS systems offer post-operative follow up of the patient. Taylor and Stoianovici (2003) refer to the entire process right from creating the patient specific model to the post-operative recovery analysis as ‘surgical CAD/CAM’ (computer aided design/computer assisted manufacturing).

A first attempt on using synergetic partnership of humans/surgeons and machines to record and reproduce 3D haptic information was reported in 1906 using stereotaxis by Clarke and Horsley. But in reality the first practical recorded robotic surgery was performed in 1985, about 8 decades later. Surgeons at the Memorial medical centre, CA, USA used an industrial robot PUMA 200 in a CT guided brain biopsy to place and insert the probe on a 52 year old patient’s brain without damaging any delicate soft tissues (Kwoh *et al.*, 1988). Prior to the surgery, this system was clinically tested for 5 years (1980-1984) which showed accuracy and repeatability of 0.05 mm (Picard *et al.*, 2004). In 1991, a robotic device called Probot was designed and was used in Imperial College, UK to automatically remove large amount of unwanted tissue from the patient in Transurethral Resection Prostate Surgery (TURP) (Davies *et al.*, 1991; Gomes, 2011). The next milestone was in the field of orthopaedics which is elaborated in the next sub-section. So, it can be said that use of robots in the medicine evolved from neurosurgery and moved gradually to other fields such as spine, craniofacial and orthopaedics.

2.3.3 Computer Assisted Orthopaedic Surgery (CAOS)

For many reasons orthopaedics is a natural field to adopt CAS. First of all, pre-operatively it is convenient to plan orthopaedic surgeries as it is easier to evaluate the bones and peri-articular soft tissues using techniques such as CT, MRI, fluoroscopy, etc. and to reconstruct a 3D model of the joint. The rigid structure of bones has made CAS particularly suitable for orthopaedic interventions as the remaining structure of the bones does not deform significantly in spite of drilling and milling (Sugano, 2003; Taylor and Stoianovici, 2003; Taylor, 2006; Hagag *et al.*, 2011). Dynamic reference bodies such as fiducial markers can be inserted and held rigid in the bone which eases the image registration process essential for CAOS (Adili, 2004). In addition, the required accuracy window for fitting the implant in the joint in order to achieve maximum implant longevity is tight making orthopaedic joint replacement surgery more likely to adopt robot assisted surgery (Hagag *et al.*, 2011).

A. Classification of CAOS

CAOS can be classified into active and passive, based on their autonomy and the surgeon's control on the overall surgery (Sugano, 2003; Adili, 2004; Lang *et al.*, 2011). Active systems are pre-programmed to perform the surgical action without surgeon's control. Although in case of emergency, surgeon can use an emergency shut off switch to terminate the robots movement; use of active or automatic system are still under scrutiny for orthopaedic application (Lang *et al.*, 2011). Passive systems are more widely accepted as they assist surgeons in pre-operative planning and intra-operative guidance and execution, peri-operative joint assessment, implant placement guidance; but the ultimate controller of the surgery is the surgeon

(Sugano, 2003). Thus passive systems only provide guidance of the surgery and the surgeon can always override the system's suggestion and take his own action (Lang *et al.*, 2011). Sugano (2003) further classified CAOS into semi-active systems which can perform some activities such as moving a drill guide sleeve or a cutting jig but they are not designed to perform any surgical action.

(i) Active Orthopaedic Robots

Five years after the first recorded robotic surgical operation, the use of robotics and computers entered orthopaedics. In the late 1980s a prototype of a clinical robotic system, ROBODOC®, for total hip replacement (THR) was developed by Integrated Surgical Systems Limited (ISS), Sacramento, USA; now Curexo Technology Corporation, Fremont, USA (parent company being International Business Machine (IBM) (Paul *et al.*, 1992; Davies, 2000; Taylor and Stoianovici, 2003; Adili, 2004; Picard *et al.*, 2004; Taylor, 2006; Gomes, 2011; Hagag *et al.*, 2011; Lang *et al.*, 2011; Sugano, 2013). Although this system had proof of concept, there were barriers to its implementation as it was believed that if the implant cavity was not prepared accurately, even custom made implants could fail. The ROBODOC® (figure 2.16) system was first used to perform THR in 1992 as an autonomous robot (Taylor *et al.*, 1989; Taylor *et al.*, 1994; Kazanzides *et al.*, 1995; Mittelstadt *et al.*, 1996; Taylor and Stoianovici, 2003; Picard *et al.*, 2004; Taylor 2006; Gomes, 2011). ROBODOC® received a CE mark in 1996 and FDA (Food and Drug Administration) clearance for THR in 1998 and TKR in 2009 (Schulz *et al.*, 2007, Gomes, 2011). ROBODOC® was the first active orthopaedic robotic system and used an industrial 5 degree freedom robot SCARA (Selective Compliance Assembly Robot Arm) along with intra-operative surgical CAD/CAM. Pre-

operatively patient's CT images were used by the surgeon to select the implant model and size the placement of each implant with respect to the CT co-ordinates. A separate workstation, called Orthodoc, was used to carry out pre-operative planning (Davies, 2000). Intra-operatively once the registration between the CT and patient's anatomy was achieved, the robot would be brought into action and stationed at an initial position by rigidly attaching it to the patient's bone. Having done this, the robot then cuts the desired surface and creates a precise femoral cavity with the aid of safety sensors, bone motion and force sensor attached between the surgical high speed rotary cutter and robot's tool holder (Taylor and Stoianovici, 2003). This motion would be continuously monitored in real-time by the surgeon, who can stop it if not satisfied.

Figure 2.16 ROBODOC® Orthopaedic surgical system platform
(Reprinted with permission, Beasley, 2012)

Although ROBODOC® was a pioneer in robotic surgery, Hagag *et al.* (2011) stated various glitches of the system; first of all, the system being autonomous, the bone must be rigidly attached to the robot platform in a place during the entire

milling procedure and it cannot be moved post-registration with respect to the base of the robot. This limits the surgeon from manipulating joints for soft tissue balancing and to evaluate ROM which restricts visualisation, access and trials of implant fit. Also, the automated cutting procedure runs very slowly as compared to the current passive systems which adds further delay and automatically stops if any errors such as unexpected forces are encountered. This sometimes results in damage to the surrounding soft tissue and extra blood loss as compared to the conventional orthopaedic systems.

Subsequently, a similar system to ROBODOC® was developed few years later for hip and knee replacement surgeries along with Anterior Cruciate Ligament (ACL) repair. This was called Computer Assisted Surgical Planning and Robotics (CASPAR) initially introduced by Ortho Maquet GmbH and Co., Rastatt, Germany and later acquired by Universal Robot Systems (URS Ortho) (Taylor and Stoianovici, 2003 Picard *et al.*, 2004; Taylor 2006; Gomes, 2011). The CASPAR system with the aid of an industrial PUMA robot was used in 2000 to perform a TKR surgery. CASPAR had similar principles to ROBODOC® but was eventually discontinued in 2004 (Gomes, 2011). In 1999, a system called Compact Robot for Image-Guided Orthopaedic Surgery (CRIGOS), using a parallel link robot as a positioning aid was developed at Helmholtz Institute, Germany (Brandt *et al.*, 1999). Questions regarding the safety of active robots were raised by clinicians even before ROBODOC® was discontinued in Germany because of unwanted surgical effects such as increased time, blood loss and tissue and nerve damage (Davies *et al.*, 2007).

(ii) Assistive Approach

Semi-active surgical robots have a more assistive and co-operating nature than active ones and they reproduce the surgeon's motion in a Master-Slave configuration. A typical example of this is the da Vinci surgical robotic system developed by Intuitive Surgical, Sunnyvale, CA which received initial FDA clearance in 1994 for laparoscopic surgeries and is now used for numerous applications such as prostatectomy, myomectomy, cardiac valve repairs, etc. (Gomes, 2011). Semi-active robotic systems in orthopaedics were not introduced until the 1990s when Moctezuma *et al.* (1994) described a system to perform femoral osteotomies. Based on this, there were other semi-active systems proposed by Davies *et al.*, 1994 and Gotte *et al.*, 1996. However, the first commercial semi-active haptic robotic system for orthopaedics application was developed in London and was named as Active Constraint Robot, ACROBOT®. It was later commercialised in 2001 by The ACROBOT® Company. It provides minimally invasive surgery (MIS) and is a small, low-powered system. ACROBOT® comprises of an interactive device mounted on the spherical manipulator called ACROBOT® Sculptor which has 3 orthogonal axes of motion: yaw, pitch and extension (Jakopec *et al.*, 2003; Gomes, 2011). It has a linear range of 300-500 mm and an angular range of ±30° thus it is much safer to operate as compared to the systems based on industrial robots such as PUMA or KUKA (Jakopec *et al.*, 2003). The kinematic structure of the system is developed in such a way that the mechanical impedance of the axes of the manipulator is low which facilitates surgeon to manipulate it with a low force and thus less physical effort (Jakopec *et al.*, 2003; Gomes 2011).

Figure 2.17 ACROBOT® Orthopaedic surgical system
(Reprinted with permission, Taylor and Stoianovici, 2003)

ACROBOT® is moved by pushing the handle near the tip of the robot which has a six-axis force sensor mounted on it to continuously measure the guided force and torque. At the tip of the robot, a surgical burr is attached which enables precise milling of the bone in a short time using the principle of active constraint control. The quality of cutting in the region being burred is proportional to the stiffness of the robot. Using the patient's pre-operative CT scans and precise implant position planning, a boundary region is created on the virtual model of patient's anatomy. The stiffness of the robot is low when the bone being cut is within the pre-defined safe zone to allow it's free movement and it increases as the tip reaches near the ends of the boundary. At the periphery of the boundary, the robot becomes very stiff to prohibit burring outside the planned resection area (Jakopec *et al.*, 2003; Gomes, 2011). ACROBOT® allows much more preservation of healthy bone as compared to active robotic systems. However, Hagag *et al.* (2011) stated that while using ACROBOT®, the surgeon needs to interact with the force sensors through the handle

for constant feedback. Also, the system is equipped with only three haptic degrees of freedom, which makes it limited to MIS surgeries where limited movement is needed.

A second haptic passive CAOS system called Robotic Arm Interactive Orthopaedic System, RIO® was developed by MAKO Surgical, Fort Lauderdale, FL using MIS approach and entered the clinical market with FDA clearance in 2005 (Gomes, 2011). The approach was targeted towards minimally invasive UKA surgery (Beasley, 2012).

In a typical TKA surgery the incision length can extend to 300 mm, whereas MIS incision length is in the range of 100 mm thus providing a less invasive approach than traditional knee replacement surgeries. Hagag *et al.* (2011) stated that autonomous robots are less suited for MIS where the surgeons view is restricted through the small incision for soft tissue balancing and repositioning of the leg during the surgery. This led to the development of a haptic passive system, RIO® to assist and guide surgeons by improving their technical skill based on intuitive and interactive tools.

The principle elements of haptic rendering technology are a virtual haptic environment and a haptic device. Using these two, the operator's motion is continuously monitored in the physical world to explore the virtual environment and using interacting forces generated in the virtual environment, haptic information is generated by the haptic device to constrain human motion. The kinematic structure of the RIO® is similar to the ACROBOT® where by simulating the mechanical

impedance, position and the orientation of the tools, a force-torque calculation is carried to stiffen the robotic arm at the haptic boundaries (Hagag *et al.*, 2011).

B. MAKO RIO® System

The MAKO RIO® comprises of three major hardware components: The robotic arm, the camera stand system for tracking the surgical tools and the guidance module assembly (figure 2.18). The RIO® manipulator is a backdriveable WAM™ (Whole-Arm Manipulation) arm (Barrett Technology Inc., Cambridge, MA, USA) with six degrees of freedom. It is a passive robotic arm which guides the surgeon in a passive way to accomplish effective and precise joint resurfacing. Similar to ACROBOT®, a virtual safe zone is created by the system based on patient's pre-operative data and the arm moves freely with low friction and inertia within this zone with the help of surgeon's manual movement. Whenever the surgeon approaches the edge of the predefined resection volume, the motors, control system and drive system apply forces to make the arm very stiff in order to restrict the surgeon's movement from cutting the bone outside the surgical plan.

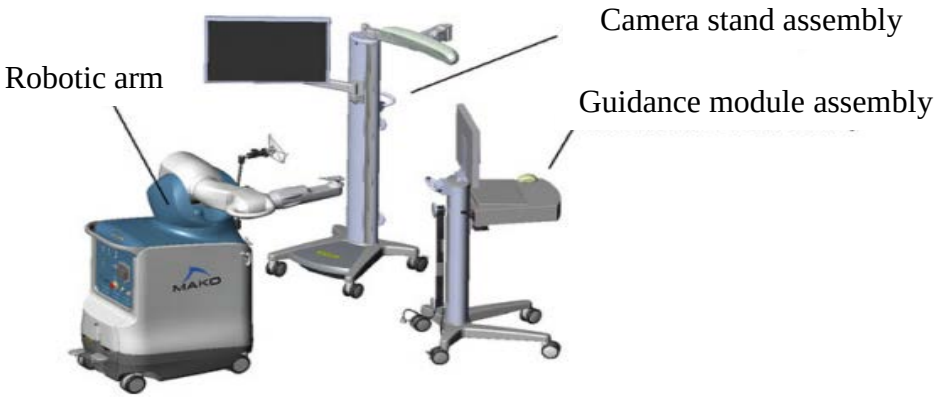

Figure 2.18 MAKO RIO® major hardware components
(Reprinted with permission, Hagag *et al.*, 2011)

The manipulator is driven by 6 joints with the aid of high resolution angular encoders and is designed to accommodate both left and right handed surgeons as shown in figure 2.19. Tools such as the cutting burr are attached as end-effectors of the robot's joint six.

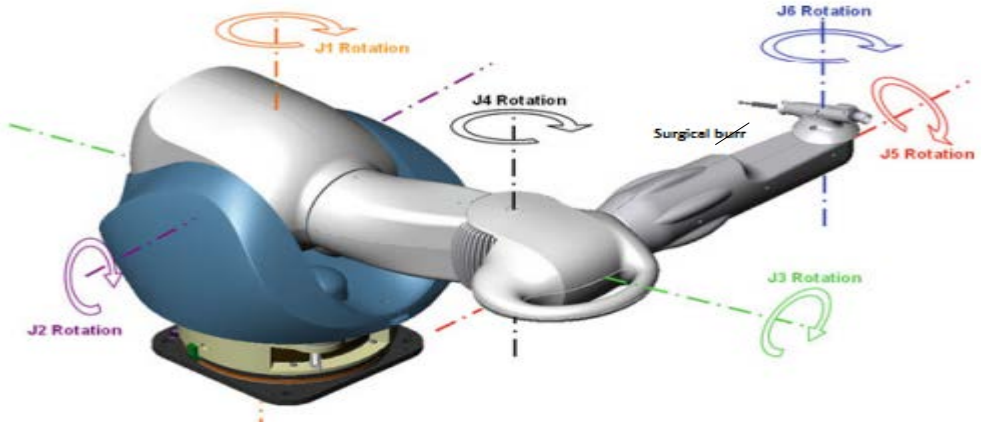

Figure 2.19 RIO® arm with joint motion definitions
(Reprinted with permission, Hagag *et al.*, 2011)

The camera stand system is equipped with two infrared Polaris cameras to track the surgical tools and the patient's anatomy through the mounted checkpoints and tracking arrays. A computer monitor is used to guide the surgeon driving different stages such as registration, bone resection, joint balancing, implant placement, etc. and in real-time. The guidance module is used by the surgical technician to assist the surgery and to guide the surgeon during planning and execution of the surgery.

MAKO's initial application was in UKA surgery but the company has also moved towards patella-femoral arthroplasty (PFA), total hip arthroplasty (THA) and bi-compartmental knee resurfacing (Banks, 2009; Hagag *et al.*, 2011; Tarwala and Dorr, 2011). Like most other passive orthopaedic applications, the MAKO Surgical

system technique can be reduced to three main phases: (i) Pre-operative planning; (ii) Intra-operative execution of the surgery; and (iii) Implant placement and balancing together they are termed as MAKOplasty® (Gomes, 2011; Hagag *et al.* 2011; Lonner and Kerr, 2012).

(i) Pre-operative Planning

Prior to surgery, pre-operative CT scans of the patient's hip, knee and ankle joints are acquired (figure 2.20(a)). Recommended settings are to keep the patient in the supine position with a 'motion rod' attached to the leg to be operated to avoid any artefacts that may appear in the images due to the movement (Pearle *et al.*, 2009; Hagag *et al.*, 2011; Lonner and Kerr, 2012; Cobb and Pearle, 2013). Using bespoke segmentation software, a 3D model of each bone is reconstructed (figure 2.20(b)). Based on the patient's anatomical data, an appropriate implant CAD model is selectively positioned, aligned and a patient-specific surgical plan is developed (figure 2.20 (c)).

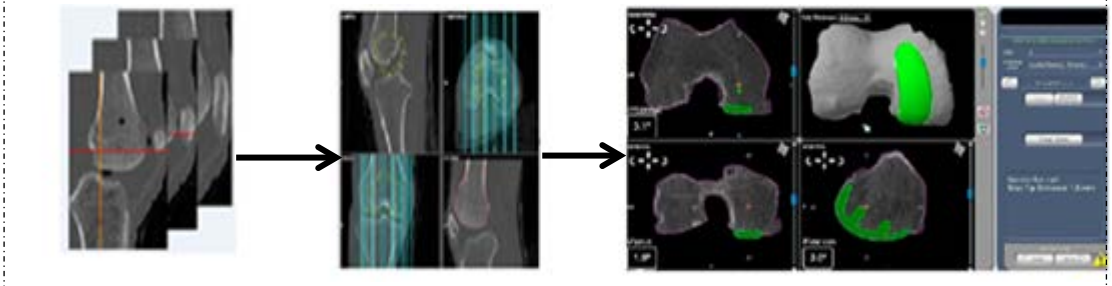

(a) CT acquisition (b) Segmentation (c) Pre-operative implant planning

Figure 2.20 Pre-operative planning in MAKOplasty®

(a): Pre-operative CT data acquisition of patient's knee. (b): Segmentation of the required anatomy using embedded software. (c): Pre-operative planning of the surgery with implant placement.

(ii) Intra-operative Execution

Intra-operatively, MAKOplasty® comprises of six major steps (prior to implant placement) as shown in figure 2.21. The RIO® system is set up before bringing the patient into the operating room. After applying surgical drapes to the RIO®, the robotic arm movement is calibrated through all the six joints and the respective moments via a process called a 'Homing'. Anatomical surface landmarks are registered with the system before the initial incision of around 80-100 mm is made on the patient's knee joint (figure 2.21 (a)). Femoral and tibial reference checkpoints are inserted and bone pins are placed in the femur and the tibia to attach optical arrays which are used to track the patient's leg segments throughout the surgery by the camera system (figure 2.21 (b)). The location of the hip joint centre is evaluated using the functional method (figure 2.21 (c)). The next step is the registration phase (figure 2.21 (d)) used to develop a spatial relationship between the pre-operatively reconstructed patient's anatomical model from the CT scan and the physical patient present in the theatre (the Registration process for MAKOplasty® is further elaborated in the section 2.4.4).

Visualising soft tissues is not possible with CT scans; hence the original plan is then tailored to achieve dynamic soft-tissue gap balancing and long-leg alignment. Post-registration, osteophytes are excised and appropriate varus/valgus forces are applied to tension the affected ligaments. The 3D positions of femur and tibia are captured (Figure 2.21 (e)) throughout ROM to achieve accurate leg kinematics, bone spacing and tissue tension. The surgeon acquires anywhere between 4-15 poses within the full ROM of the knee joint. A spherical surgical burr is then attached to the joint six of robotic arm as an end-effector for effective bone resection.

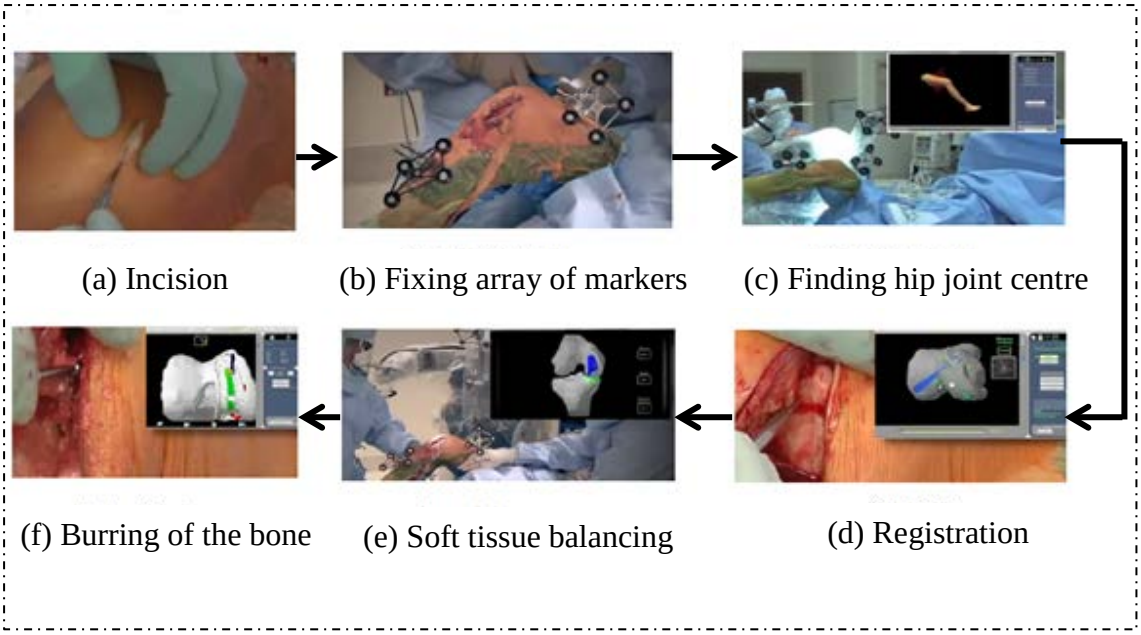

Figure 2.21 Intra-operative execution of MAKOplasty®

(a): Incision on the affected compartment of the knee joint. (b): Fixing checkpoints and arrays on tibia and femur. (c): Rotating the leg in a spiral motion to store the hip joint centre in the system. (d): Registration of femoral condyles and tibial plateaux with the system. (e): Soft tissue balancing. (f): Precise removal of the arthritic bone.

There are different sizes of burrs which can be employed; for example 6 mm diameter burr to remove the majority of the bone material and 2 mm burr to get fine finishing of the edges and corners followed by 1.4 mm router for keel canal preparation (Hagag *et al.*, 2011). Removal of the bone process can be visualised on the monitor in real-time to stay within the safe zone which appears green as shown in figure 2.21 (f). When the surgeon attempts to move outside the planned boundaries by even 0.5 mm, the arm becomes stiff and a red colour appears on the resection area (Hagag *et al.*, 2011). If moved further, the motors spinning the burr stop and user is warned with an audio-visual feedback.

(iii) Implant placement

The level of joint resection including the choice of the implant size and position is decided by the surgeon and can be altered in the surgery (figure 2.22(a)). Family of implants used in MAKOplasty® is termed as the RESTORIS® MCK which can be used for medial UKA, lateral UKA, PFA and bi-compartmental arthroplasty (UKA+PFA) (figure 2.23).

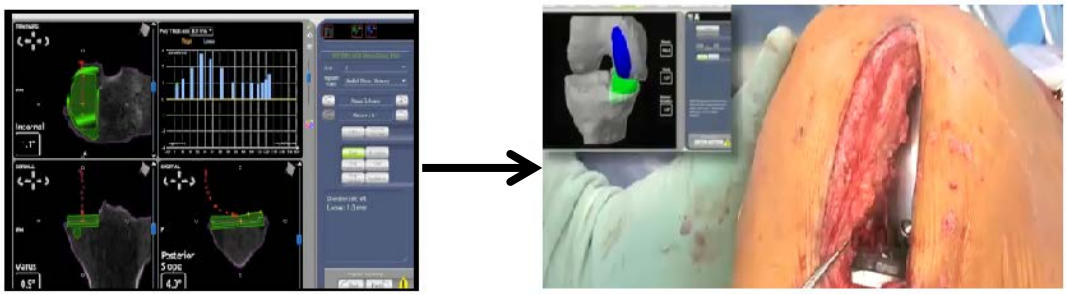

(a) Implant adjustment (b) Implant testing through ROM

Figure 2.22 Implant placement stage of MAKOplasty®

(a): Implant position adjustment to refine the plan. (b): Testing of the position and alignment of the implant

Two designs of tibial prosthetic implants are available. Inlay designs are made of polyethylene and use the patient's tibial subchondral bone bed to support the implant. Onlay prostheses are applied to the patient's cortical rim for support.

Unicompartmental Patellafemoral Bicompartmental

Figure 2.23 RESTORIS® MCK for knee replacement MAKOplasty®

(Reprinted with permission, MAKO Surgical, 2014)

(iv) Post-operative management

Physical therapy begins immediately post-surgery (Hagag *et al.*, 2011). Patients are asked to ambulate immediately with a cane, crutches or walker (Lonner and Kerr, 2012). Patients can be discharged on the same day depending upon whether they can achieve discharge goals such as independent ambulation of 100 feet, active straight leg raise, knee flexion of at least 90°, etc. (Pearle *et al.*, 2009). Roche *et al.* in 2008 conducted MAKOplasty® on 43 patients. The study reported that 3 months post-operatively average flexion ROM increased from 121±8° to 126±6°. Roche *et al.* (2010) also reported outcomes of 73 patients and at two years post-operatively patients saw an increased average ROM of 129° as compared to the pre-operative flexion of 123°. In a cohort study by Coon *et al.* (2008), 18% of patients with inlay implant designs (total n=34) were discharged on the day of the surgery. MAKOplasty® has also resulted in significant amount of improvement in The WOMAC (Western Ontario and McMaster University Osteoarthritis Index) score and KSS (Knee Society Clinical Rating System) score which are used as standard parameters to assess outcome of knee surgeries (Roche *et al.*, 2008; Hagag *et al.* 2011).

C. Other Approaches

BRIGIT, Bone Resection Instrument Guidance by Intelligent Telemanipulator was another robotic system for TKA surgeries developed by MedTech S.A., Montpellier, France and was later acquired by Zimmer in 2006. BRIGIT was a better economic solution when introduced as there was less instrumentation involved with reduced surgery time. Based on the patient-specific plan, by fixing the patient's leg to the robot and by guiding the oscillating saw and

surgical drill, TKA surgeries were performed. In spite of acquiring FDA clearance in 2006, its clinical acceptance by surgeons is still in question (Hagag *et al.*, 2011; Gomes, 2011).

Praxim Inc., Grenoble, France developed a prototype called Praxiteles which is another semi-active approach for TKA with MIS. The next generation called iBLOCK received FDA clearance in 2010 and is a semi-active miniature robot which comprises of universal device (figure 2.24) mounted on the bone to position and orient a saw or milling guide and to prepare distal femoral implant cavity so as to fit in implants of any planar geometry (Plaskos *et al.*, 2005; Hagag *et al.* 2011; Beasley, 2012; Bellemans, 2013).

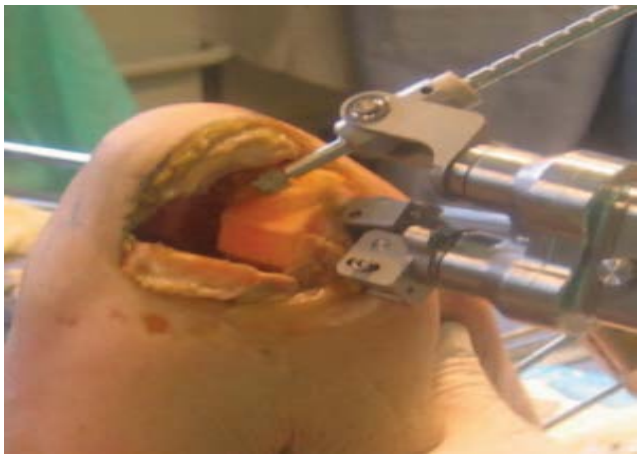

Figure 2.24 iBLOCK by Praxim Inc. mounted on cadaver sample
(Reprinted with permission, Plaskos *et al.*, 2005)

iBLOCK motorized cutting guide positioner was compared with conventional freehand computer-navigated guide positioning in TKR by Koulalis *et al.* (2011) who reported iBLOCK automated guide was more efficient as it indicated relatively shorter surgery time with a significantly lower deviations in the final bone resections from the planned resections.

CAOS systems usually have large robotic arms which take up space in the operating theatre. Consequently, some systems were suggested which utilize small parallel manipulators and are attached either to the surgical table or directly to the bone. An example is CRIGOS which is attached to the surgical table and is employed for multi-tasking operations including milling of the bone. It uses biplane fluoroscopy to register the system and then autonomously positions implants and instrument guides with high accuracy and precision (Brandt *et al.*, 1999; Adili, 2004;). Other parallel manipulators such as Mini Bone-Attached Robotic System for Joint Arthroplasty (MBARS) (figure 2.25) (Plaskos, 2005; Wolf, 2005) and MiniAture Robot for Surgery (MARS) (Shoham *et al.*, 2003; Plaskos, 2005) are mounted on the bone directly such that fixing the bone in a rigid position is no longer required (Brisson, 2008).

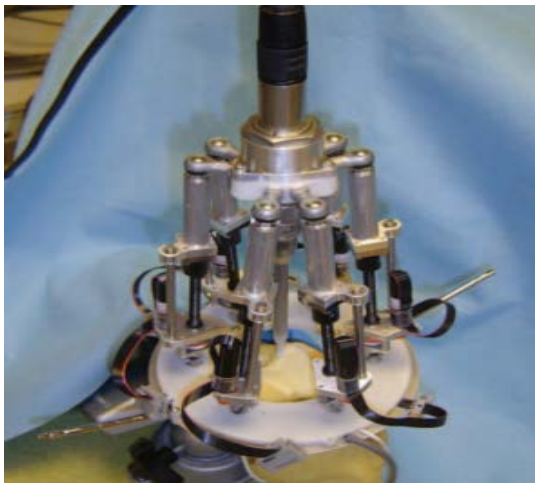

Figure 2.25 MBARS parallel miniature manipulator
(Reprinted with permission, Wolf, 2005)

Another system based on parallel platform design is called modiCAS which works on tracking of the bone with infrared markers attached to it and hence keeping the bone in the same place is no longer required (Crucues and Wahrburg, 2007;

Brisson, 2008). The PI-Galileo Positioning Device (PLUS Orthopaedics AG, Switzerland) is a software controlled electro-mechanical device with a hybrid system of two motorized joints as well as its own navigation system which makes precise femoral cuts (Plaskos, 2005; Hagag *et al.*, 2011). Yen *et al.* (2010) proposed prototypes of unconstrained bone clampers with different designs of medical robots such as Hexaglide Robot (parallel), Hybrid Cartesian Parallel Robot, Serial Robot and Intelligent Tool Module or Milling Tool.

2.3.4 Imageless Navigation

In general, active, semi-active and passive CAOS systems are conceptualised around a similar idea of acquiring the patient's pre-operative data with a CT for planning of the surgery. However, CT scanning induces radiation exposure to the patients as well as additional cost. Newer passive CAOS systems such as NAVIO Precision Freehand Sculptor, PFS® (BlueBelt Technologies, Pittsburgh, USA) are designed on the principle of intra-operative planning of the surgery thus eliminating the need for a pre-operative CT (Brisson, 2008; Beasley, 2012). The NAVIO PFS® which provides image free planning and thus imageless navigation for UKA, acquired CE marking in 2012 with the first surgery performed in late 2013 (Beasley, 2012; Bluebelt Technologies, 2014). PFS® is a hand-held tool (Figure 2.26) which has an array of radio-opaque markers attached to it which gets tracked continuously by an optical tracking system (Polaris). The system does not make use of pre-operative data sets such as CT or MRI to plan the surgery or to navigate the tibio-femoral joint surfaces in the theatre. In turn, it is based on accurate registration of intra-operative knee kinematic assessment, anatomic landmarks and surface mapping of the knee using the PFS device which is constantly tracked by the optical tracking

system (Lonner *et al.*, 2014). Intra-operative surface mapping is achieved by painting or sculpting the condylar surface with the same optical probe. Within the hand tool, there is a high speed rotating burr inside a protective sheath. Similar to RIO® and ACROBOT®, the NAVIO guides the surgeon about the safe zone being burred in real-time but based on intra-operative data planning. Whenever surgeon goes beyond the safe zone, the burr retracts inside the protecting guard hence preventing the surgeon passively from removing unplanned bone (Hagag *et al.*, 2011; Beasley, 2012; Lonner *et al.*, 2014).

Figure 2.26 NAVIO PFS® hand tool with array of radio-opaque markers
(Reprinted with permission, Beasely, 2012)

In general, in most of the prototypes and commercial navigation systems for knee and hip surgery such as OrthoPilot® (B. Braun), Ci (DePuy Orthopaedics), OrthoMap (Stryker), Vector Vision (BraiLab)), OrthoSoft (Zimmer), etc. the bone segments and the surgical tools such as the arrays, sculptor, cutting blocks, etc. are registered and navigated in the same co-ordinate system by infrared camera system (usually Polaris) (Barret *et al.*, 2011; Cheng *et al.*, 2012). In the operating theatre, by acquiring hip, knee and ankle joint centres, mechanical and rotational axes of the limb are found. Then, the anatomy of the articulating surfaces of the tibio-femoral joint is acquired using the navigated device which produces a virtual model of the

knee or hip joint depending upon the surgery. Using this intra-operative data, the surgery is planned in the theatre. After the bone resection is performed, the implants are selected which best fit the size of the condylar surfaces. (Lonner *et al.*, 2014).

Several studies have been implemented to evaluate the accuracy and suitability of imageless navigation based knee/hip replacement surgery. Martin *et al.* (2009) performed CT-based and CT-free TKA surgeries on 44 patients and reported 2 year follow up outcome. Results suggest that the postoperative ROM in both groups (CT-based and CT-free) was increased but showed no statistically significant difference amongst them ($p \leq 0.002$). However, the CT-free imageless navigation showed higher rate of a stable soft tissue situation during examination of ligament balancing in full extension. In addition, CT-free group proved to be better in 30° of flexion, where a better ($p = 0.004$) ligament situation (medially and laterally) was reported. Nogler *et al.* (2008) carried out a comparison study between CT-based and imageless navigation THA where the latter improved the accuracy of acetabular cup placement using the direct anterior approach. In another study (Lonner *et al.*, 2014), a comparison between the planned and the final placement of the implants was carried out using minimally invasive UKA on 25 cadavers. The translational errors and rotational errors were as low as 0.72 mm and 1.04° which indicates that the image less navigation systems can also provide accurate implementation of the surgical plan with minimal errors in the implant placement. This approach of imageless navigation surgery has a lot to offer in terms of reduced radiation, time and cost.

2.3.5 Pearls and Pitfalls of CAOS

Robotics in medicine along with CAS and in particular CAOS offers a large potential to raise the standards of arthroplasty. As compared to the conventional arthroplasty techniques, CAOS provides greater precision, accuracy and reproducibility to the overall outcome of the surgery (Adili, 2004). However, CAOS and digitisation of the surgical environment in general is shaped only to complement humans and not replace them (Hagag *et al.*, 2011) and there are certain aspects which still remain a question mark for their universal acceptance:

- Inherently safe systems are the foundations of the healthcare (Hagag *et al.*, 2011). Manipulator end-effectors are always used in the close proximity to the diseased organ, thus their sterility has to be a top priority (Troccaz, 2009). Also, autonomous robots should be thoroughly assessed and tested before setting up to avoid any unwanted consequences.
- There have been many clinical failures reported with the use of autonomous robots such as ROBODOC® (Davies *et al.*, 2007) as well as with passive systems like MAKO RIO®. Roche *et al.* (2008) reported post-operative complications in a cohort of 223 patients who underwent MAKOplasty®, out of which 6 had to be re-operated and 2 had infections. The long term outcomes of this study are still awaited and need to be compared to those in the conventional surgery.
- Robotic platforms and CAS are usually bulky and take up a large space in the operating room.
- They are expensive to set up and the capital cost can be as high as 1 million pounds. MAKO RIO® costs around $950,000. Other passive surgeries can cost anywhere between $150,000 to $800,000 (Lang *et al.*, 2011).

- The registration process plays a key role in the overall accuracy of the surgery. It directly impacts the surgical navigation and thus errors in the registration process can be also reproduced in the final implant placement (Adili, 2004; Kluge, 2007; Lonner and Kerr, 2012). Therefore, the surgeon has to be adequately skilled and trained in order to achieve accurate registration and perform precise surgery.

CAOS is certainly still a new field and most of the surgeons still prefer conventional joint replacement methods but there are number of early adopters particularly in the private sector. There remain many issues related to the technique and the invasiveness of inserting marker arrays for image registration and navigation. Registration directly affects overall accuracy of the surgery and is usually a lengthy process taking up to 14-20 minutes to achieve the optimum accuracy (Banger *et al.*, 2013). Therefore, there is a need to establish a better and a quicker registration technique to ensure quick and accurate alignment between the pre-operative scan and intra-operative data.

2.4 IMAGE REGISTRATION

Image registration (IR) is a vital aspect in Image Guided Computer Assisted Orthopaedic Surgery (IGS CAOS). IR is a process for aligning two or more images of the same scene taken from different angles, distances and often different devices. These differences in acquiring the image often result in different co-ordinate systems. The IR is done in order to bring two or more images into the same co-ordinate system with the same alignment (Goshtasby 2012). It is often confused in the literature with polysemic terms such as fusion, integration, correlation, matching,

etc. (Maintz and Viergever, 1998). In general, image registration is a process of finding a geometrical transformation that can spatially align and overlay or superimpose 2D and 3D images which are acquired from different viewpoints (Fitzpatrick *et al.*, 2000; Zitova and Flusser, 2003). IR is a key component in remote sensing in the fields of multispectral classification, weather forecasting, environmental monitoring, landscape planning, cartography map updating, image mosaicking/shape fusion, video stabilisation and compression, stereo vision, motion analysis, integrating information into geographic information systems, target localisation and automatic quality control in computer vision (Lucas and Kanade, 1981; Zitova and Flusser, 2003, Wyawahare *et al.*, 2009). Apart from these fields, IR is crucial in the field of medical imaging which is the focus of this section.

2.4.1 Medical Imaging

Medical imaging serves as an important tool in the area of medical diagnostics. It is considered as one of the highest priority research topics as well as one of the fastest developing fields. The pioneer of medical imaging was William Rontgen in 1895 with his ground-breaking work on X-rays (also called as Rontgen rays). Since his invention of X-ray radiography, various different imaging technologies based on other forms of energy have been discovered and developed (Levine III, 2010).

Medical images can be divided into two major groups: 1) ‘Anatomical’ elucidating structural and morphological parameters; and 2) ‘Functional’ depicting real time metabolic process below or within the anatomical structures, as shown in figure 2.27 (Maintz and Viergever, 1998). Anatomical medical imaging comprises the traditional X-rays including CT scanning, a three dimensional X-rays imaging

process developed by stacking several two dimensional X-rays. Landmark anatomical imaging methods such as MRI work on the principle of Nuclear Magnetic resonance (NMR) to visualize internal structures and mostly soft tissues. Techniques such as ultrasound imaging are used to envisage subcutaneous structures for example, joints, tendons, tiny vessels, etc. New and derived imaging techniques such as MRA (magnetic resonance angiography) for magnetic resonance imaging of blood vessels and CTA (computed tomography angiography) used to illustrate blood vessels also constitute anatomical medical imaging. 3D shape acquisition techniques such as laser scanning, whose energy cannot penetrate through the body, are relatively underutilised medical imaging techniques.

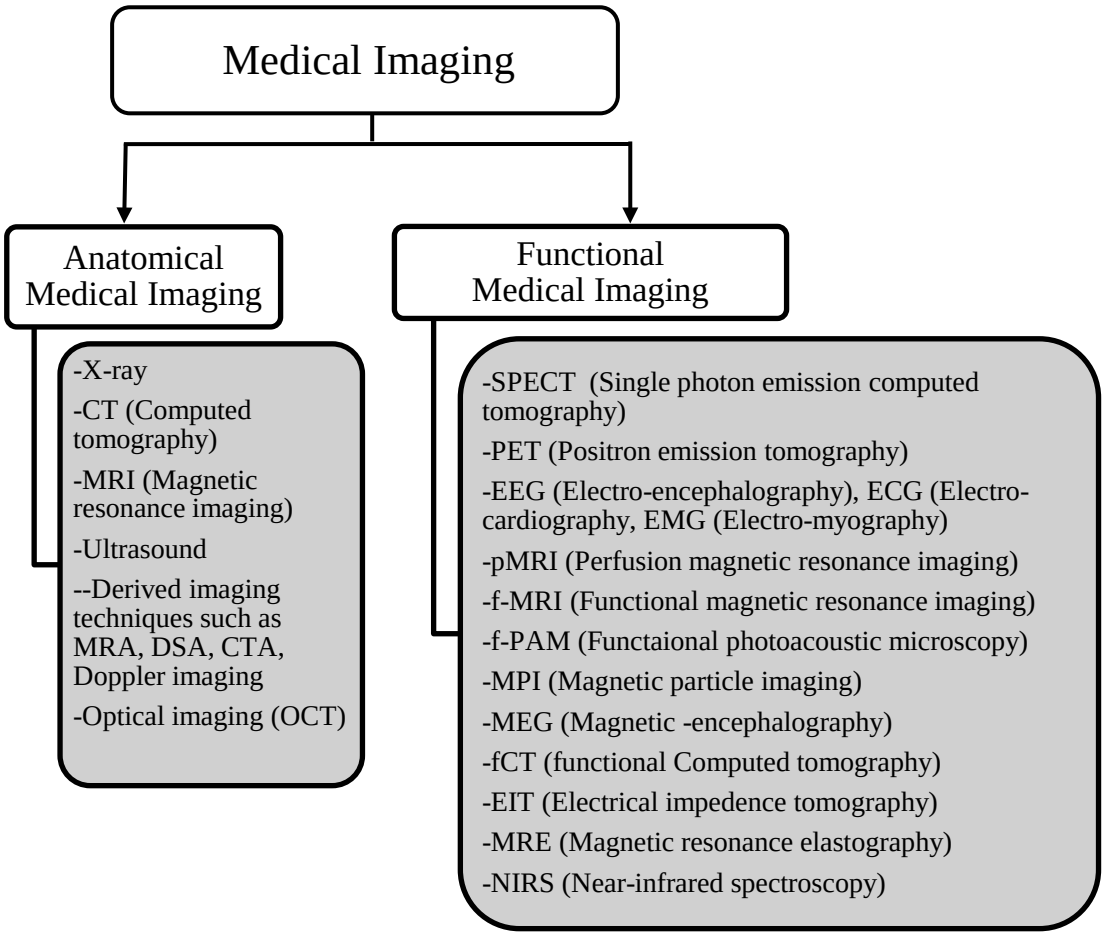

Figure 2.27 Division of medical imaging

Functional medical imaging modalities illustrate real-time metabolic activities of the organs. SPECT imaging which works using gamma camera is extensively used in obtaining 3D information of tumours, myocardial perfusion imaging (MPI), functional brain imaging, etc. PET and multi modal imaging techniques such as modern PET-CT and PET-MRI are widely used in clinical oncology to visualise metastasis of the tumours, musculoskeletal imaging, brain imaging, cardiac imaging, etc. Functional imaging modalities such as f-MRI and f-CT help clinicians visualise real time activity of the tissue or organ under scrutiny. Spatially sparse techniques such EEG (Electro-encephalography), ECG (Electro-cardiography, EMG (Electro-myography) and MEG (Magneti-encephalography) are also included under functional medical imaging (Maintz and Viergever, 1998).

2.4.2 Medical Image Registration

Apart from their extensive diagnostic ability, aligned medical images can help surgeons plan and execute image steered surgeries. IR plays a vital role in the alignment of these images and it is a key component of the execution of computer assisted surgeries including Neurosurgery, Cranio-maxillofacial surgery, ENT (ear, nose and throat) surgery and as explained previously Orthopaedics (Simon, 1997).

In image guided surgery, pre-operative data is acquired to plan, simulate, guide and assist the surgeon while operating (Simon *et al.*, 1995). Medical image registration in CAOS is a process of developing a spatial relationship between pre-operative data such as CT scans or MRI scans and navigation data from the physical patient in the operating theatre. It is possible to visualise a point on patient's femoral medial or lateral condyle in the pre-operated CT scan as well as to locate the same on the actual patient by using intra-operative sensors or probes. However, their spatial

correspondence still remains unknown. IR thus generates this relationship by aligning these images and allows the surgeon to correlate the patient's anatomy in the theatre with the pre-operative data from the scan. Consequently, IR forms a common reference frame between pre-operative volumetric data and the patient physically present in the operating theatre.

A comprehensive classification of medical image registration methods was reported by Elsen *et al.* in 1993. They organized different registration techniques based on the parameters such as dimensionality, origin of images with the properties, domain of transformation, elasticity of transformation, tightness of property coupling, parameter determination and the amount of interaction. Furthermore, in the same year Maurer and Fitzpatrick (1993) defined registration methods and divided them into different techniques such as stereotactic frame systems, point based, curve based methods, etc. Maintz and Viergever (1998) provided an extensive classification of medical image registration based on the criteria formulated by Elsen *et al.* 1993. Since then, many surveys and reviews of methods relating to medical image registration have been published (Lester and Arrige, 1999; Fitzpatrick *et al.*, 2000; Rui and Minglu, 2003; Zitova and Flusser 2003; Salvi *et al.*, 2007; Wyawahare *et al.*, 2009). Maintz and Viergever (1998) divided medical image registration into 9 basic criteria and then subdivided into multiple levels as shown in figure 2.28. The classification is based on decomposition of the registration procedure into three major parameters: The problem statement, the registration paradigm and the optimization procedure.

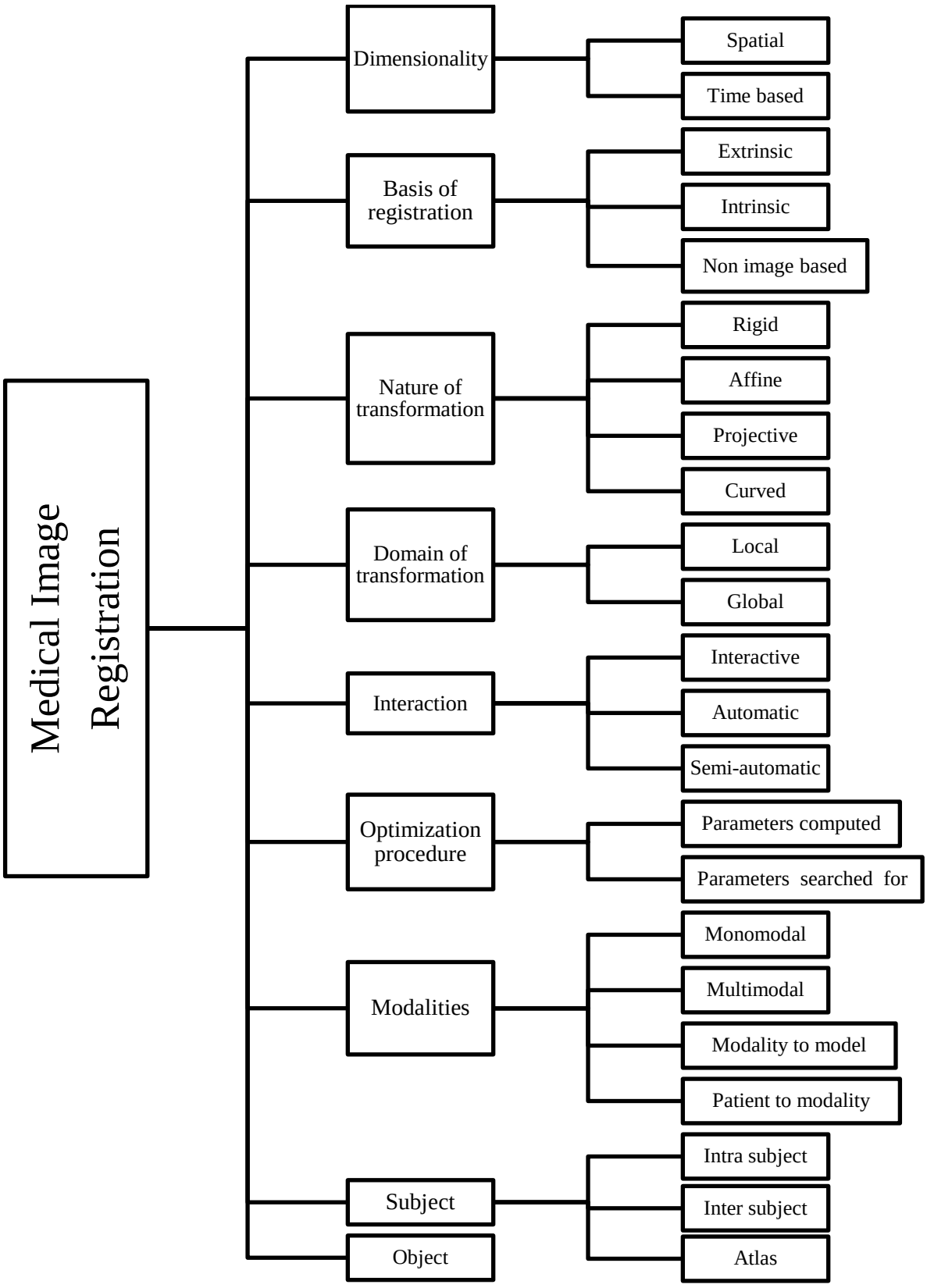

Figure 2.28 Classification of medical image registration

(Adapted from Maintz and Viergever 1998)

Dimensionality in this context refers to 2D-2D, 2D-3D or 3D-3D IR. Extrinsic registration methods rely on introducing reference frames such as invasive fiducials or moulds. Intrinsic registration methods are based on anatomical landmarks present on the alignment of segmented structures (segmentation based), most prominent object surfaces, or directly onto measures computed from the image grey values (voxel property based) which can be located without introducing any external reference object. Non image based registration methods include techniques such as self-calibrating of ultrasound system or registering the position of tools attached as robotic end–effectors. One of the most important foundations of the registration techniques is the way transformation of the co-ordinate system is carried out between methods. If the co-ordinate system is altered by only translation and rotation, then the transformation is said to be rigid. Affine transformations work on mapping parallel lines and if it maps lines onto lines then it is termed as projective transformation. Subsequently, if the transformation maps lines onto curves then it is characterized as curved or elastic transformation (Maintz and Viergever 1998).

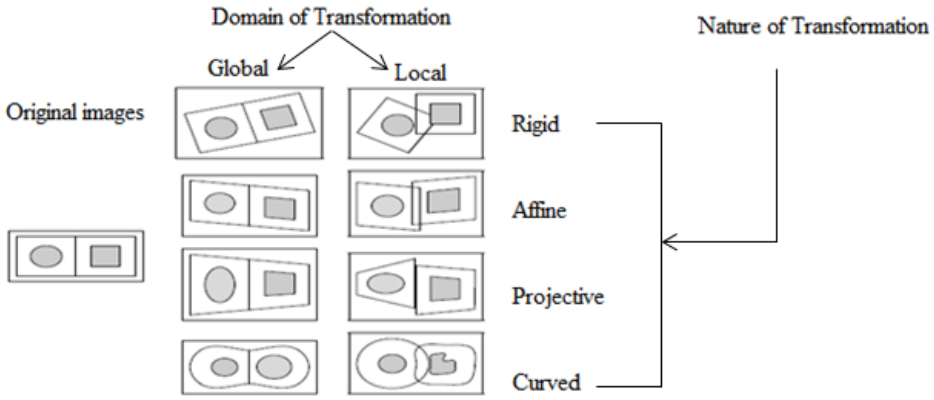

Figure 2.29 Registration methods based on nature and domain of transformation (Adapted from Maintz and Viergever, 1998)

Ashburner and Friston (2003) stated that rigid body transformation is actually a subset of affine transformation. Thus a 3D rigid or affine body transformation can be expressed in terms of old co-ordinates for each point (x_1, x_2, x_3) and new spatial co-ordinates (y_1, y_2, y_3):

$$y_1 = m_{11}x_1 + m_{12}x_2 + m_{13}x_3 + m_{14} \tag{2.1}$$

$$y_2 = m_{21}x_1 + m_{22}x_2 + m_{23}x_3 + m_{24} \tag{2.2}$$

$$y_3 = m_{31}x_1 + m_{32}x_2 + m_{33}x_3 + m_{34} \tag{2.3}$$

When expressed as single constant matrix equation: $y = Mx$

$$\begin{bmatrix} y_1 \\ y_2 \\ y_3 \\ 1 \end{bmatrix} = \begin{bmatrix} m_{11} & m_{12} & m_{13} & m_{14} \\ m_{21} & m_{22} & m_{23} & m_{24} \\ m_{31} & m_{32} & m_{33} & m_{34} \\ 0 & 0 & 0 & 1 \end{bmatrix} \begin{bmatrix} x_1 \\ x_2 \\ x_3 \\ 1 \end{bmatrix} \tag{2.4}$$

(i) Translation

When an old point x is translated by q units, then the new point y will be

$$y = x + q \tag{2.5}$$

In matrix form this can be expressed as:

$$\begin{bmatrix} y_1 \\ y_2 \\ y_3 \\ 1 \end{bmatrix} = \begin{bmatrix} 1 & 0 & 0 & q_1 \\ 0 & 1 & 0 & q_2 \\ 0 & 0 & 1 & q_3 \\ 0 & 0 & 0 & 1 \end{bmatrix} \begin{bmatrix} x_1 \\ x_2 \\ x_3 \\ 1 \end{bmatrix} \tag{2.6}$$

(ii) Rotation

In 2D, let us assume a point at (x_1, x_2) is rotated by a single angle θ to new co-ordinates (y_1, y_2). Then this rotation can be generated by following transformation:

$$y_1 = cos\ (\theta)\ x_1 + sin\ (\theta)\ x_2 \tag{2.7}$$

$$y_2 = -\ sin\ (\theta)\ x_1 + cos\ (\theta)\ x_2 \tag{2.8}$$

Whereas, for 3D, rotations are expressed in terms of three orthogonal planes in which the object has rotated. In the equation 2.9 when an old point is rotated by q_1 radians about X-axis, the rotation is termed as pitch.

$$\begin{bmatrix} y_1 \\ y_2 \\ y_3 \\ 1 \end{bmatrix} = \begin{bmatrix} 1 & 0 & 0 & 0 \\ 0 & cos\ (q_1) & sin\ (q_1) & 0 \\ 0 & -sin\ (q_1) & cos\ (q_1) & 0 \\ 0 & 0 & 0 & 1 \end{bmatrix} \begin{bmatrix} x_1 \\ x_2 \\ x_3 \\ 1 \end{bmatrix} \tag{2.9}$$

Similarly rotation around Y-axis by q_2 radians is called roll (equation 2.10)

$$\begin{bmatrix} y_1 \\ y_2 \\ y_3 \\ 1 \end{bmatrix} = \begin{bmatrix} cos\ (q_2) & 0 & sin\ (q_1) & 0 \\ 0 & 1 & 0 & 0 \\ -sin\ (q_2) & 0 & cos\ (q_2) & 0 \\ 0 & 0 & 0 & 1 \end{bmatrix} \begin{bmatrix} x_1 \\ x_2 \\ x_3 \\ 1 \end{bmatrix} \tag{2.10}$$

And finally, rotation around Z-axis by q_3 radians is called yaw (equation 2.11)

$$\begin{bmatrix} y_1 \\ y_2 \\ y_3 \\ 1 \end{bmatrix} = \begin{bmatrix} \cos(q_3) & \sin(q_3) & 0 & 0 \\ -\sin(q_3) & -\cos(q_3) & 0 & 0 \\ 0 & 0 & 1 & 0 \\ 0 & 0 & 0 & 1 \end{bmatrix} \begin{bmatrix} x_1 \\ \\ x_3 \\ 1 \end{bmatrix} \quad (2.11)$$

Rotations around all three axes are combined by multiplying these matrices together and most importantly in an appropriate order (Ashburner and Friston, 2003).

A domain of transformation is said to be global if the transformation is applied to the entire image, whereas it is called local if only a section or a patch of one or both the images are being registered. The Global registration approach is more often used in medical image registration applications than local transformation as it satisfies rigid body constraints and gives a better approximation.

Medical Image registration techniques can be further classified on the basis of the user interaction with the system. In an interactive registration approach, the user has the control of registration and oversees it himself with the software providing real time accuracy. IR is termed as automatic when user has a minimum control and interaction only supplies the matching algorithm and data to the system. A semi-automatic interaction belongs to both methods in an iterative solution finding process.

Basis of optimization splits registration techniques into two as the parameters chosen for registration are either determined (basis computed) from the available data or they are searched for defining an optimum function (basis searched for).

Furthermore, medical image registration methods are recognized on the basis of the modalities involved as shown in table 2.2.

Table 2.2 Classification of medical image registration methods based on their modality

Monomodal	X-ray/DSA, CT/CTA, MRI, PET, SPECT, Ultrasound, Radiography, Portal, Optical, Catheter based images, video, etc.	All the images to be registered are acquired using same modality. This can be also termed as Intra-modality registration.
Multimodal	X-ray-CT, X-ray-MRI, -ray-portal, X-ray-Ultrasound, MRI-PET, MRI-Ultrasound, CT-Optical, CT-Laser, CT-MRI, CT-PET, CT-SPECT, etc.	Images to be registered are acquired using different modalities. This can be called as Inter-modality registration.
Modality to model	CT, MRI, SPECT, X-ray	Registration is performed between a single modality and a model depicting patient's anatomy or physiology. For example registering MRI of patient's CSF (Cerebrospinal Fluid System) with the hydrodynamic mathematical model.
Patient to modality	CT, MRI, PET, X-ray	Registration is performed between a single modality and the patient itself. For example, registering X-ray simulator images in the radiotherapy treatment with the pre-operative images using patient's position.

Based on the subject, there are three classes in which registration can be subdivided. 'Intra-subject', where acquired images to be registered are of the same subject or patient for medical purposes. 'Inter-subject', when two or more images to be registered are of different patient's or of models. 'Atlas', where registration is achieved between a patient and an image constructed using an information database. IR can be further classified on the basis of segment of the patient being registered.

Primary segments are the head, thorax, abdomen, pelvis and perineum, limbs, spine and vertebrae. There are more parameters based on which IR techniques in medical imaging are further categorized (Elsen *et al.*, 1993; Wyawahare *et al.*, 2009).

Table 2.3 Further classification of Image registration techniques
(Adapted from Elsen *et al.*, 1993; Wyawahare *et al.*, 2009)

Tightness of property/feature coupling	-Interpolating: Complete and exact transformation of features from the reference to the stationary image. -Approximating: Rough transformation of features between two images being registered.
Type of data	-Raw -Features extracted -Introduced markers in

2.4.3 Surface Registration in Medicine

Unlike most of the registration approaches, surface based registration techniques are absolutely free from pre-operative insertion of any markers into the patient's body. In a surface registration approach, a patient specific surface model of the organ under scrutiny is created using the pre-operative scan data. Intra-operatively the same surface is reconstructed using various techniques such as X-ray imagers or fluoroscopy with a C-Arm (Lavallee and Szeliski, 1995, Barrick EF, 2002; Markelj *et al.*, 2008; Otake *et al.*, 2012), optical digitisers (Rohling *et al.* 1994; Dessenne *et al.*, 1995; Lavallee *et al.*, 1995; Simon *et al.*, 1995), video cameras (Betting *et al.*, 1995), etc.

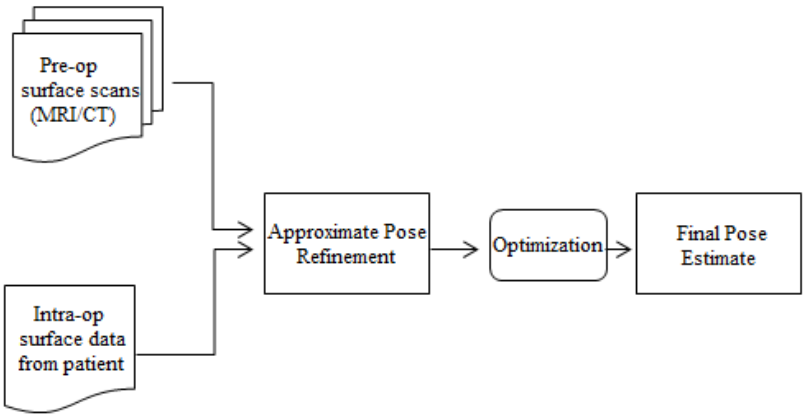

Figure 2.30 Surface registration generalised approach
(Adapted from Simon *et al.*, 1995)

Local surface based registration allows users to align a 'sub-patch' of one image to a larger surface patch of the other which solves the problem of intra-operative entire surface reconstruction when the full operative surface cannot be exposed (Audette *et al.*, 2000). For example, local surface registration is applied where it is possible to acquire an entire surface of the femur from the pre-operatively acquired CT; but it is difficult to reconstruct its shape entirely during the operation using sensors other than X-ray imagers. Audette *et al.* (2000) classified surface registration methods by proposing that best fitting of two surfaces is usually achieved by representing the surface in one of the four ways: Features, Points, Model based and Global similarity. In the feature based methods, set of features such as curves, regions and sparse points expressing salient structures like extremity of curvature, peaks, pits, etc. are used to describe surface topography. Model based methods work on expressing surface identification (segmentation) in one volume or surface tracking over a volume sequence as a model and in global shape methods surfaces are aligned based on the global surface geometry where a rough initial guess of the

transformation is not needed. Point based surface registration method is more commonly used in CAOS applications and is also known as free form matching (Besl and Mackay, 1992; Zhang, 1994). Pelizzari and his associates (1989) instigated a points based surface fitting technique for registration of brain image volumes which is also known as the 'Head and Hat Algorithm'.

More advanced and commonly used point based surface registration techniques are based on repeating iterations to minimize a global function such as sum of squared distance between points to be aligned on the two surfaces (Besl and Mackay, 1992). Fitzpatrick *et al.* (2000) described an ICP (Iterative closest point) algorithm (originally proposed by Besl and Mackay, 1992) as a general-purpose and representation-independent algorithm which can be applied to various geometrical primitives including point sets, line segments, triangle sets, parametric curves and surfaces. Zhang (1994) and Lavallee and Szeliski (1995) proposed similar algorithms based on ICP objective function but without weighting factors to eradicate noise and outliers. Other point based techniques with the minimised distance metric have been suggested (Rangarajan *et al.*, 1997; Soucy and Ferrie, 1997).

2.4.4 Registration in CAOS

The nature of registration in CAOS applications is generally rigid, as deformation in bones is usually negligible (Picard *et al.*, 2004). There are two major types of registration approaches usually accepted in CAOS. The first one is extrinsic fiducial based registration which is a simple approach and the second one a surface based registration which is intrinsic in nature.

Fiducial based registration involves paired point matching (Picard *et al.*, 2004; Sugano, 2013). In order to achieve this, three or more fiducials (physical markers such as titanium screws used in ROBODOC®) are inserted in the patient's bones to determine bone's position and orientation a few days before the surgery and more importantly, before acquiring pre-operative scan data. So, during the actual surgical procedure these markers are used as 3D reference points to align the co-ordinate systems of the physical patient and that of the pre-operative scan data (Sugano, 2013). In 1998, a combination of two screws with an additional pin extension was tried (Sugano, 2013). This type of extrinsic registration is conventionally, conceptually and mathematically simple to execute; however, it requires additional surgery prior to the actual surgery and often results in fiducial site pain (Picard *et al.*, 2004; Sugano, 2013).

The second type of registration in CAOS is surface or shape based registration. The first surface registration in CAOS was achieved in the ROBODOC® system, in 1999 and clinicians reported the accuracy of fit as comparable to the conventional fiducials based method (Sugano, 2013). Newer CAOS systems such as MAKO Surgical's RIO®, run on surface (points-based) registration of the bones by collecting numerous but a pre-set number of points on the bone (figure 2.31). For example, approximately 40 points each on tibial and femoral condyles for UKA or 32 points on the femoral head for THA are acquired intra-operatively. Through image registration, a best fit alignment is formed between the pre-operatively acquired CT-based surface and intra-operatively digitised surface (Tarwala and Dorr, 2011). A probe with a set of markers at a fixed distance is first registered with the camera system. Once this is done, the position of the tip of the probe can be

calculated spatially and thus by touching the probe to the system guided points on the bone, the position of the points on the bone can be calculated in the 3D space to construct a 3D point cloud of the bone surface which is then fitted to the pre-operative patient-specific scan.

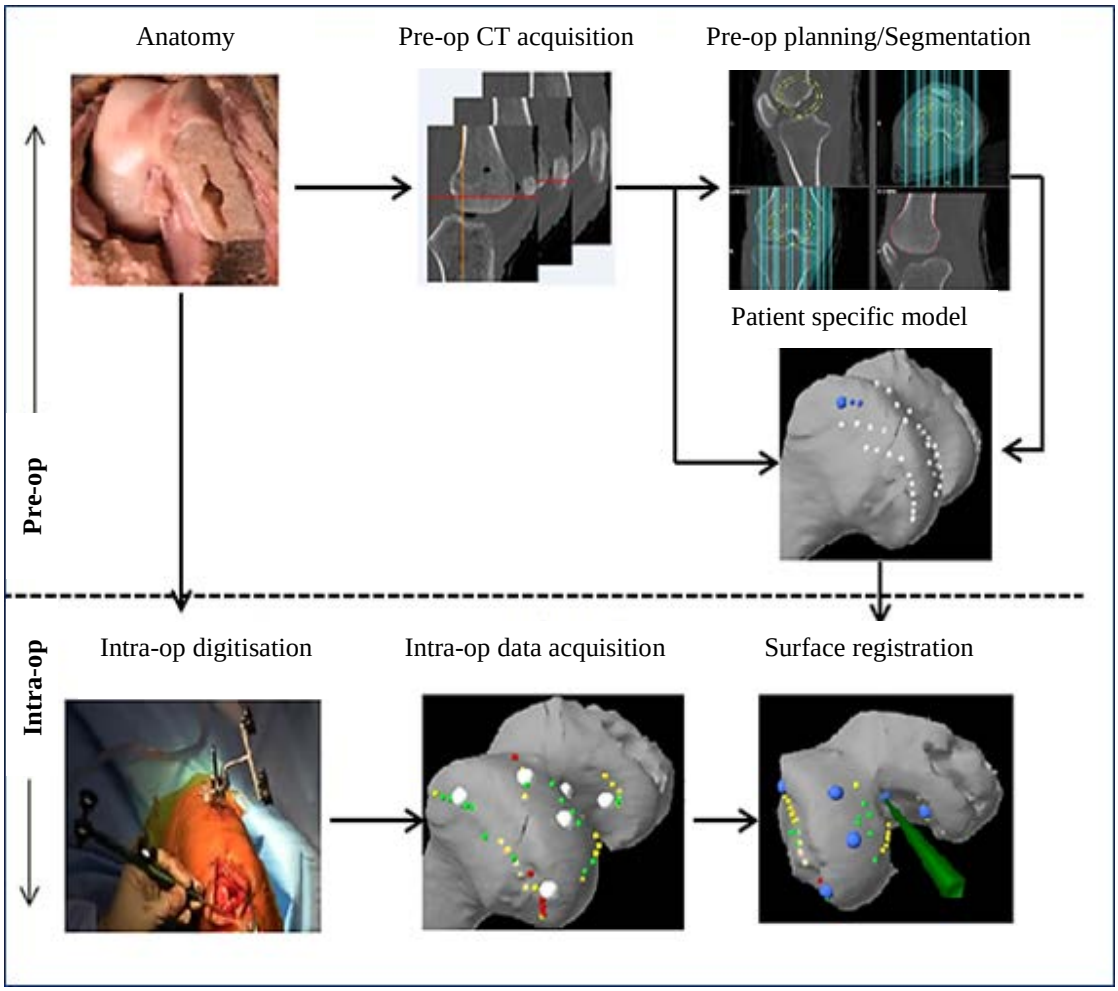

Figure 2.31 MAKO Surgicals surface registration approach

Surface registration is not just limited to UKA or TKA, but it is also widely used in computer assisted hip surgeries as shown in figure 2.32.

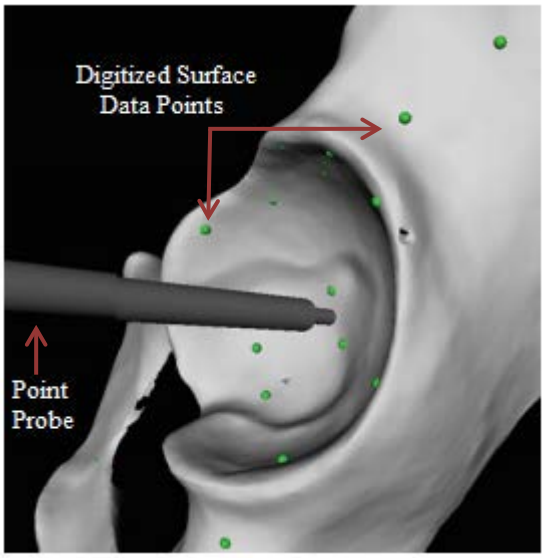

Figure 2.32 Iterative surface matching for acetabular registration in hip replacement surgeries
(Adapted from Ecker *et al.*, 2014)

A common drawback of the surface registration technique is that it is more suitable for rigid body registrations. As soon as the original geometry of the surface being registered is changed or destroyed, re-alignment and re-registration can no longer be achieved within an accepted window of accuracy. This is not only true for soft tissues but also for bones. Therefore, successful surface registration can only be achieved if the surfaces in the pre-operative data set and the intra-operative surgical site remain congruent (Marmulla *et al.*, 2004). Also, the anatomy being registered has to be exposed well which may be difficult in MIS (Ecker *et al.*, 2014).

Thus it can be said that current IR for most application in CAOS is achieved by touching navigated probes along the articulating surface of the anatomy such as

the femoral condyles, the tibial plateau, the acetabulum, etc. The generated digitised data allows a rigid body transformation to be formed which best fits the points on the pre-operative scan to the exposed anatomy. All the current approaches use a probe with a sharp pointer end to touch the bone surface. However, some systems such as the MAKO RIO® provide an option of using different probes for soft and bone tissue.

A time analysis study was performed in the Royal Infirmary of Glasgow in conjunction with the Department of Biomedical Engineering, University of Strathclyde to compare the surgical process of MAKOplasty® UKA vs. OXFORD UKA. In this study, Banger *et al.* (2013) observed 19 MAKOplasty® UKA surgeries and reported that the average time required for the registration process was 14.29 minutes whereas the average time for tibial and femoral burring was only 10.59 minutes. This suggests that although being accurate, surface registration in CAOS is time consuming process which entails extra surgical cost. Thus, the rationale behind this Ph.D. study was to find an alternative method of producing the shape of the articulating surfaces of tibio-femoral joints intra-operatively to be registered with the pre-operative data for CAOS which would be:

- Non-contact
- Markerless
- Less time consuming
- Less costly

Using ultrasound technique to acquire bone profiles is an emerging technique which is non-invasive and cost efficient and is suited for minimally invasive surgery in CAOS (Picard *et al.,* 2004; Barratt *et al.,* 2006). In ultrasound validation studies on phantoms, Amin *et al.* (2003) reported average translation errors and average RMS errors of 1.94 mm and 1.27 mm respectively and average rotation and RMS average rotation errors of 0.9° and 0.59° respectively for the pelvis. Barrat *et al.* reported RMS errors of 1.90 mm for translation and 0.48° for rotation in THR surgery. However, the time taken to acquire these images was between 5 min to 30 min. Also, the resolution of the acquired 3D ultrasound images and the accessibility to some regions around the bone surfaces is still problematic. Imaging the femoral head and neck is crucial in THR. This region is always surrounded by numerous soft tissues, fats, muscles, tendons and ligaments and especially more in obese patients. In addition, occlusion by the acetabulum makes ultrasound probe penetration and depth inadequate (Barratt *et al.*, 2006).

One of the possible and promising techniques for producing 3D surface topology was laser based scanning. The application of lasers in medicine and 3D laser surface scanning techniques are explained in next sections.

2.5 LASERS AND MEDICINE

Phenomenon of laser light was first suggested by Albert Einstein in his paper based on quantum theory of radiation in 1917. The name ‘photon’ was termed in 1926, but Einstein had postulated before that an excited quantum (a theoretically possible state of a gas molecule) returns back to a state with a lower energy (ground

state) at a particular frequency of radiation emitted and if many molecules did the same, the laser light can be emitted.

2.5.1 Laser Applications in Medicine

Since the invention of the Laser-Maser principle, lasers as narrow coherent emissions of light have been extensively used in numerous fields. Lasers have wide applications in industries in material processing, electronic fabrications, holography, spectroscopy, fibre optics and integrated optics, material heat treatment, etc. (Osgood *et al.*, 1983; Hecht *et al.*, 1994; Hariharan, 1996; Ready, 1997; Demtroder, 2003; Koo *et al.*, 2009; Nagabhushana and Sathyanarayana, 2010). In defence, lasers are the foundation of anti-missile, direct energy weapon (Ready *et al.*, 1997; Mallik, 1999). Being fast and precise, laser light is used in measurement, alignment and navigation. Lasers are a preferred choice in geological surveys, archaeology, construction, aviation and shipping industries (Pétillon *et al.*, 1998; Jia-Chong and Hung-Chao, 2007; Doneusa *et al.* 2008). Commercially available laser pointers, compact disc players, laser printers, scanners, etc. are day to day objects and are used comprehensively worldwide, as a result laser technology is well developed.

Lasers have an important role in the field of medicine and their clinical applications are abundant. The first workable medical laser was designed by Theodore Maiman in 1960 (Peng *et al.*, 2008). Soon after, in 1962 lasers entered the clinical field when Lyon Goldman designed and implemented the first laser based medical system in the field of dermatology followed by Francis L Esperance's laser application in ophthalmology (Peng *et al.*, 2008). In 2003, Steiner described therapeutic and diagnostic uses of lasers in medicine which were further elaborated by Peng *et al.* (2008), tabulated in table 2.4 and 2.5 respectively. Lasers for

therapeutic purposes are widely used for tissue ablation, vaporisation and coagulation. Spectroscopic methods, optical coherence tomography, confocal arthroscopy and fibre optic based endoscopic devices are a few of the laser diagnostic applications (Shcherbakov, 2011, Peng, 2008). Recent advances in techniques, such as laser based X-ray imaging (Kieffer *et al.*, 2002) and terahertz laser scanning of soft tissues (Panwar *et al.*, 2002; Yokus *et al.*, 2013) indicate lasers have exciting future applications in the field of medical imaging and diagnosis.

Table 2.4 Medical Therapeutic applications of Lasers
(Adapted from Steiner, 2003 and Peng *et al.*, 2008)

LASER THERAPY	Disruption	Ablation	Vaporisation	Coagulation	Photo-chemical mode	Bio-stimulation
Dermatology	✓	✓	✓	✓	✓	✓
Ophthalmology		✓		✓	✓	
Dentistry		✓	✓	✓	✓	
Oto-laryngology		✓	✓	✓	✓	
Gastro-enterology		✓	✓	✓	✓	
Urology		✓	✓	✓	✓	
Gynaecology		✓	✓	✓		
Cardiovascular		✓	✓	✓	✓	
Neurosurgery			✓	✓	✓	
Orthopaedics		✓		✓		

Table 2.5 Medical Diagnostic applications of Lasers

(Adapted from Steiner, 2003 and Peng *et al.*, 2008)

LASER DIGNOSTICS	Fluorescence spectroscopy	Laser Doppler flowmetry	Optical coherence tomography	Laser scanning confocal arthroscopy
Tumour recognition	✓		✓	✓
Blood flow		✓		
Tissue differentiation	✓		✓	✓
Tissue structures	✓		✓	✓
Metabolic activity and drug concentration	✓			

The use of lasers is relatively limited in orthopaedic imaging as compared to fields such as ophthalmology or dentistry. Most of the laser applications in orthopaedics are localised to therapeutic treatments such as vaporising, ablating or thermally coagulating tissues rather than 3 dimensional imaging (Imhof, 1995; Papagelopoulos *et al.*, 2005; Peng *et al.*, 2008; Garg *et al.*, 2013). For example, patients suffering from herniated discs who are unable to recover with physical therapy are advised to undergo a laser based treatment to vaporise the tissue in the disc in order to create a vacuum (Imhoff, 1995). Arthroscopy is one of the widely used techniques for diagnosing joint disorders. It is also used for therapeutic purposes such as meniscoctomy using holomium lasers (Dillingham *et al.*, 1995).

2.5.2 Lasers for Imaging and Surface Matching

As explained earlier, IR is a vital feature of any computed assisted surgeries. Most of the gold standard methods for best fitting intra-operative patient's anatomy with the pre-operative images are based on markers, external fiducials and frames. However, laser based matching of surfaces has developed in the last decade

particularly in neurosurgery (Miga *et al.*, 2003; Krishnan *et al.*, 2004; Kao and Tarng, 2006), ENT surgery (Ledderose *et al.*, 2007) and Cranio-maxillofacial surgery (Marmulla and Luth 2000; Schlaier *et al.*, 2002; Marmulla *et al.*, 2004 (a); Marmulla *et al.*, 2004 (b); Hoffman *et al.*, 2005). An extensive search of the literature found no evidence in orthopaedic procedures such as knee replacement or hip replacement which would employ producing 3D rigid body models of the knee joint intra-operatively using 3D laser scanning approach. This may be because of the perceived complexity in the anatomy of these joints and/or the potential reflection noise induced by synovial fluid, cartilage and the soft tissues surrounding the joints. 3D laser scanners have been expensive and difficult to set up in the operating theatre. Laser safety is also an additional issue.

Previous investigations by Maramulla and Luth (2000) suggested that the traditional methods of medical image registration which are point based matching of two data sets can be replaced and improved by registering an entire surface of the patient's anatomy. Harmon *et al.* (1994) used a LIDAR (Light detection and Ranging) system and CT scanning to acquire point clouds of the skull and suggested a need for multimodal 3D surface matching. In 2000, Bucholz *et al.* successfully proposed surface matching by evaluating correlation between the CT scan and a laser scan. They developed a hand-held laser scanning technique to acquire surface contours of the patient's head but the accuracy was limited to 10 mm. Using similar approaches, registering patient's intra-operative anatomy with the pre-operative data has been achieved with laser based systems in Cranio-maxillofacial surgery (Marmulla and Luth 2000; Schlaier, 2002; Marmulla *et al.*, 2004 (a); Marmullaa *et al.*, 2004 (b); Hoffman *et al.*, 2005).

Hand-held laser systems such as z-touch by BrainLab, Germany have been used in surface matching for surgical navigation (Schlaier *et al.*, 2002; Marmulla *et al.*, 2004; Hoffman *et al.*, 2005; Ledderose *et al.*, 2007). They are passive, frameless systems (figure 2.33) which work on infrared projection of Class I laser beam onto the surface with a diameter of about 3 mm. This is located and captured by the infrared camera of the Vector Vision^2 (from BrainLab) image guided neuro-navigation surgery system. Best fit alignment is then formed between the pre-operative and intra-operatively acquired surfaces and finally using a partial ICP algorithm and finding the closest difference between the squares of the distances, registration is achieved (Maramulla *et al.*, 2004). Raabe *et al.* (2002) mentioned inaccuracies using the Z-touch system up to 10 mm. Although, Hoffman and co-workers (2005) reported RMS error of 1.21±0.34 mm, with the mean clinical precision of 1.8±0.5 mm.

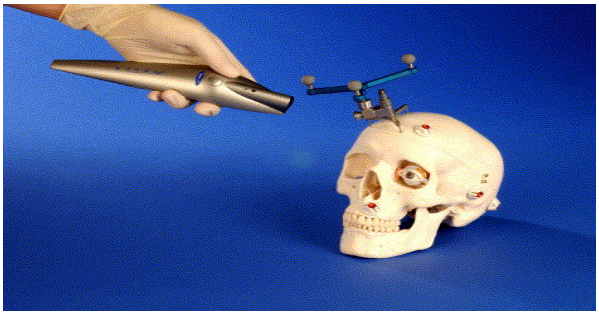

Figure 2.33 Z-touch hand-held laser surface scanner
(Reprinted with permission from, Hoffman *et al.*, 2005)

Alternatively, researchers at the University of Heidelberg developed a surgical navigation system SSN++ (Surgical Segment Navigator) with the support of Carl Zeiss in 1996-98 (Maramulla *et al.*, 2004). This system is equipped with a commercial high-resolution (640 X 480) Class I laser scanner from Minolta, VI-900.

At a distance of 120 cm from the patient, they acquired around 300,000 surface anatomical points in 2 seconds. They collected data in three co-ordinate systems viz pre-operative CT data, intra-operative laser scan data and intra-operative infrared co-ordinate system around the patient's head. Laser scanner data was then aligned by surface matching with the CT (figure 2.35) and the infrared co-ordinate system with a mean precision of 1.1±0.2 mm.

Figure 2.34 Minolta 3D laser digitiser laser scanner with SSN++ navigation system (Reprinted with permission from Maramulla *et al.*, 2004)

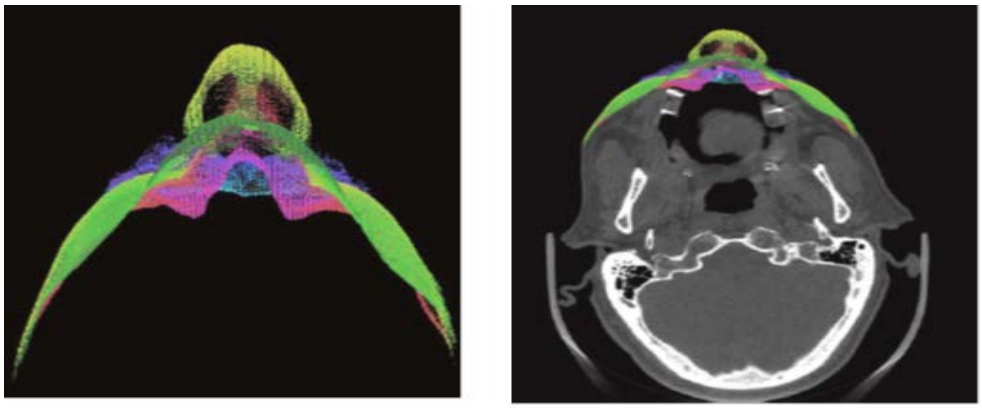

(a) (b)

Figure 2.35 Surface matching of the patient's face in Cranio-maxillofacial surgery (a): Axial view of the laser scan (b): Axial view of the overlay of the laser scan patch on the single CT scan image. (Reprinted with permission, Maramulla *et al.*, 2004)

Miga *et al.* (2003) used a commercial 3D LRS (laser range scanner) developed by RealScan 3D of 3D Digital Corporation, Bedford Hilld, NY for capturing 3D topography of cortical surface (figure 2.36). They registered the intraoperative 3D laser scans of the head with the pre-operated MR scans using point based; ICP based and bespoke SurfaceMI technique which showed satisfactory results.

Figure 2.36 Realscan 3D LRS system
Laser scanner with the laser source in the middle and the CCD camera on the right.
(Miga *et al.*, 2002)

Kao and Tarng (2006) acquired a 3D point cloud of a rubber head phantom using a commercial laser surface scanning system by 3D Family Technology Co. Ltd (figure 2.37). They performed surface registration of CT images to the patient's head using the automated laser scanner and reported position errors in case of symmetric feature, deleting the right side of the feature and spreading fractures of the nose which ranged from 0.8 mm to 6.37 mm.

Figure 2.37 Automated laser scanning system by 3D Family technology
(Kao and Tarng, 2006)

Shamir *et al.* (2009) used a 3D optical surface scanner, faseSCAN II (by Breuckmann) (figure 2.38), to acquire a 3D point cloud of patient faces to match up with the pre-operated CT/MRI images and reported surface registration error of 0.9±0.35 mm.

Figure 2.38 3D surface acquisition of patient's face using faseSCAN II
(Reprinted with permission, Shamir *et al.*, 2009)

The focus of this Ph.D. thesis was intra-operative and thus operating theatre compliant imaging for orthopaedic applications such as knee replacement surgeries.

Being fast, non-invasive, accurate and relatively cheap, lasers seem the preferred choice for the modality. The imaging was to be achieved on a macro scale rather than microscopic level where techniques such as OCT (Optical Coherence Tomography) or confocal laser scanning microscopy would have been preferred (Jones *et al.*, 2005). Acquired 3D scans of the articulating surface of the joints were to be registered with the pre-operatively acquired scan data and a best fit alignment was to be performed. Keeping the cost of the scanner down was a major design aspect. The project requires attention to the rigid body alignment of pre-operative and intra-operative data sets but not the intra-operative navigation of surgical tools. The aim of the study crystallised on an inexpensive laser scanner for intra-operative data acquisition of the tibio-femoral joints for IR in knee arthroplasty. Design and implementation of the developed bespoke scanning technique is described in the Chapter 5 (Building the Equipment) and Chapter 6 (Methodology).

2.6 3D SCANNERS

A 3D Scanner is a device which is used for imaging and analysing the total or partial surface of an object or a scene and more importantly in three dimensions viz length, width and depth. It is employed in order to collect the surface geometry and often the true colour or appearance of the target material. Using 3D scanner, it is possible to collect 3D data such as point co-ordinates of a standard, non-standard, complex or irregular object. With this data, it is then possible to rebuild the 3D model in a computer showing the details of object dimensions using lines formed by a large point cloud which in turn gives a surface and hence the whole body (Chen *et al.*, 2005).

In summary, a 3D scanner generates a 3D point cloud of the object being sensed followed by a reconstruction process where the captured points are combined to extrapolate the shape of the object by means of a mesh or an entire surface pattern. The combination of the sensing phase and the reconstruction phase is called ‘shape acquisition’ or ‘3D digitisation’ (Feng *et al.*, 2005).

2.6.1 Classification of 3D Scanners

Curless B (1999) stated a comprehensive classification of shape acquisition techniques (figure 2.39). In addition, optical techniques for shape acquisition are further classified in figure 2.40.

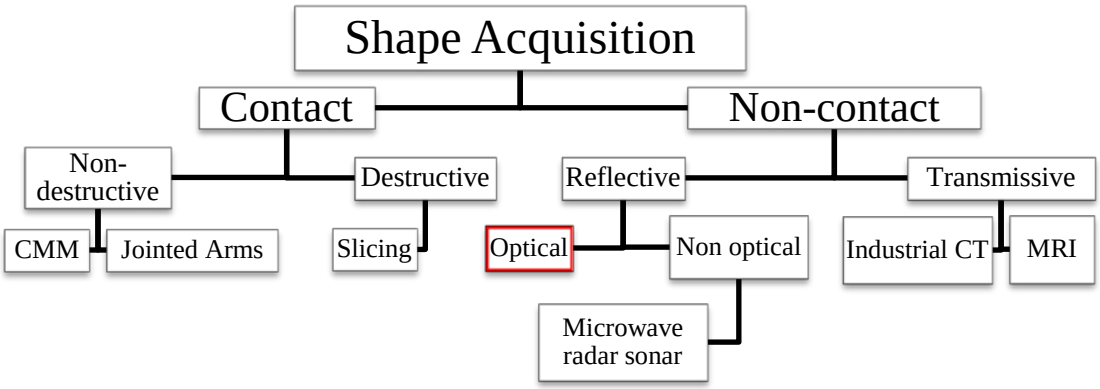

Figure 2.39 Taxonomy of Shape acquisition techniques
(Adapted from Curless B, 1999)

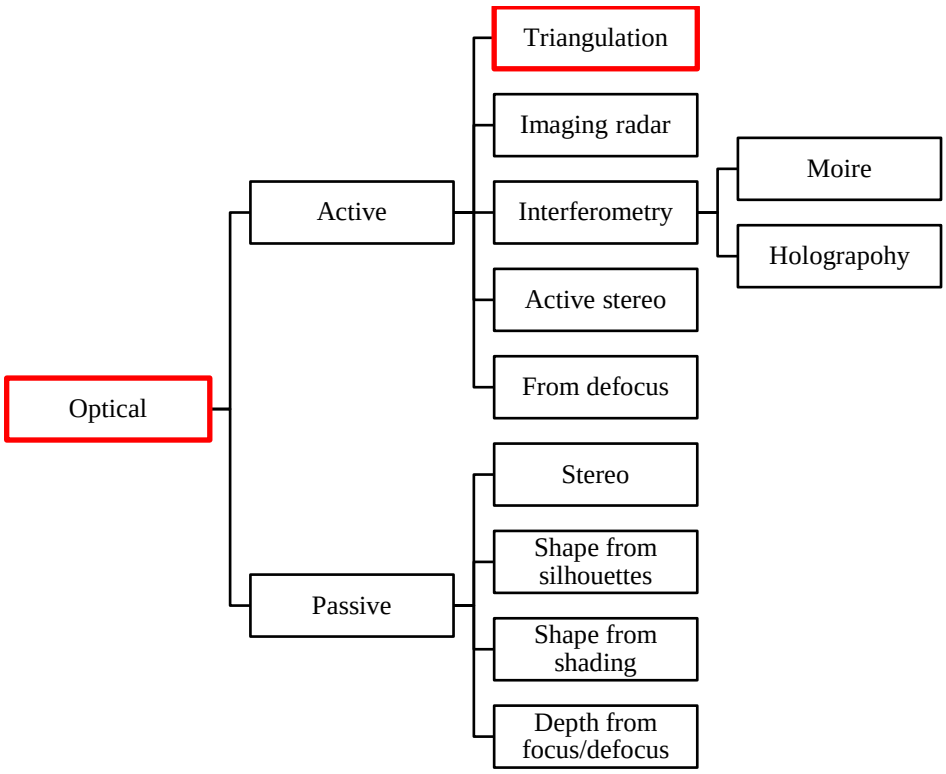

Figure 2.40 Taxonomy of optical shape acquisition techniques
(Adapted from Curless B, 1999)

Contact 3D scanners acquire 3D measurements of the object by physically touching the probe onto the surface. Although they are considered to be very precise in terms of producing accurate dimensions of the object, direct touching of the probe can significantly damage valuable and delicate objects such as historical artefacts or articular cartilage in our case. Contact measurements principally consist of a trilinear coordinates measuring instrument entailing a probe which gathers spatial position of each point on the subject and thus constructing a whole surface (Dongming and Yunhe, 2010). A coordinate measuring machine (CMM) is a common example of a contact 3D scanner. Another major drawback of contact 3D scanning systems is that they are relatively time consuming as compared to the non-contact optical scanning devices (Faxin *et al.*, 2010). In addition, they are much more expensive than simpler

scanning modalities and also require specialised training for setting up, operating and troubleshooting (Webber and Wallace, 2007).

Non-contact optical passive 3D scanners do not emit any light or radiation but use the scene's own lighting and rely on detecting reflected ambient radiation (Zargochev and Goshtasby, 2006; Faxin *et al.*, 2010). These techniques are also termed as shape-from-X techniques where X can be shading, stereo, motion, focus/defocus, texture, etc. (Zhang *et al.*, 1999; Mada *et al.*, 2002). Most of the passive scanners detect visible light while only a few work on infrared radiation detection. They can be extremely cheap as they do not demand specific hardware. However, they are less precise as compared to the active scanners. One of the most common examples of non-contact passive scanning is a stereoscopic system which employs two cameras capturing the image of the same scene from different angles and by taking the difference in these two images, a distance from each point on the target to the cameras and hence thus its spatial coordinates are evaluated. Besides this, photometric system, photogrammetry and Silhouette techniques are some more popular non-contact passive scanning methods (Faxin *et al.*, 2010).

Non-contact active scanners are preferred when high speed and high definition sampling of 3D digitisation of complex shapes is required (Dongming and Yunhe, 2010). These scanners use a source of light or radiation such as X-rays and detect the reflected signal in order to create a 3D point cloud of the target (Faxin *et al.*, 2010). Besl (1988) reported six different optical principles being used for active scanning which included radar, triangulation, Moiré and holographic interferometry, focussing and diffraction. In the phase comparison technique, the phase difference between the transmitted and reflected signal is used to carry out the distance

measurements. However, the necessity of a well-defined reflected signal leads to a short range and poor accuracy (Boehler and Marbs, 2002). Currently, most of the efficient scanning systems work on active scanning principles such as time of flight (TOF) or laser triangulation (Franca *et al.*, 2005; Dongming and Yunhe, 2010). TOF range finders (e.g. the one used in project Natal, Microsoft Corporation (Yangkeun *et al.*, 2010) or TOF laser scanners work on the principle which states that assuming the laser speed and the flight time (time taken by laser scanner to transmit a pulse onto the object until the reflected signal is detected by the sensor) are known, distance between the scanner and the point on the target can be calculated by multiplying the time of flight and the laser speed (Dongming and Yunhe, 2010). A PET scanner works on the principle of TOF (Karp *et al.*, 2005; Surti and Karp, 2008). TOF systems have great range and depth variation and are usually used to scan large structures such as archaeological caves, skyscrapers, etc.; however, their accuracy and precision of distance measurements are relatively low and are in the order of millimetres (Franca *et al.*, 2005; Faxin *et al.*, 2010). On the other hand, scanners based on triangulation principle have a smaller range and depth variation but they are extremely accurate and precise up-to microns. The focus of this study was to acquire intra-operative 3D scans of the tibio-femoral joint. Therefore, it was possible to compromise the range of the scanner in order to produce a more precise system; hence, 3D laser scanner based on the triangulation principle was adopted. There is further ambiguity introduced into the classification scheme as triangulation technique is itself categorized into active and passive subtypes (Karp *et al.*, 2005; Rivas *et al.*, 2008).

2.6.2 Triangulation Principle

As depicted in the taxonomy of the shape acquisition techniques, triangulation mode falls into non-contact/optical/active methodology. The 3D position of the object can be calculated, if the distance between the laser source and the camera (called the baseline) and the angle between the baseline and the laser beam, θ are known (Sinha and Jain, 1994). In figure 2.41, point co-ordinates (*x,y,z*) of an acquired point 'A' can be formulated using the triangulation principle as follows:

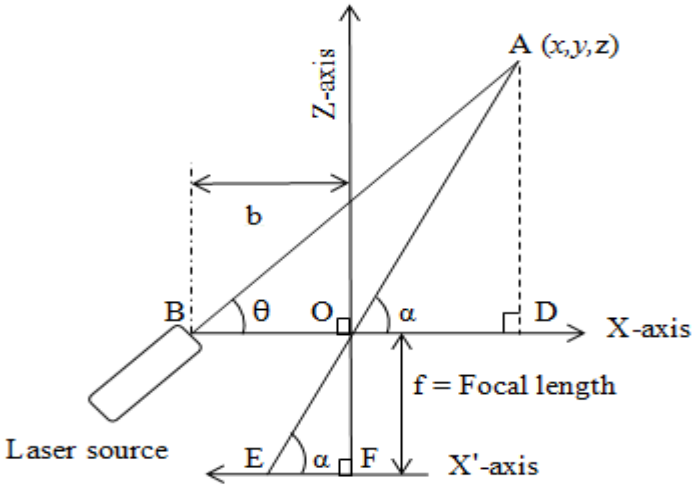

Figure 2.41 Triangulation principle

Camera lens is located at the origin O with the focal length f to the image plane. Distance between the camera and laser source is b (Adapted from Franca *et al.*, 2005).

In figure 2.41, Δ DOA and Δ FEO are similar triangles, therefore by the principle of similar triangles;

$$\frac{DO}{FE} = \frac{OA}{EO} = \frac{AD}{OF} \tag{2.12}$$

But in the Δ DOA, DO = *x*, OA = *y* and AD = *z*

Also, in the Δ FEO, FE = x', EO = y' and OF = f

Therefore by substituting these values in equation (2.12);

$$\frac{x}{x'} = \frac{y}{y'} = \frac{z}{f} \tag{2.13}$$

$$z = \frac{xf}{x'} = \frac{yf}{y'} \tag{2.14}$$

Now considering the Δ DBA, by applying simple trigonometric equation;

$$cot\,\theta = \frac{BD}{AD} \tag{2.15}$$

But BD = BO + BD = $b + x$ also AD = $z = \frac{xf}{x'}$ from equation (2.14)

Hence, by substituting these values in equation (2.15), we get;

$$cot\,\theta = \frac{b+x}{\frac{xf}{x'}} \tag{2.16}$$

By rearranging terms in the equation (2.16), we get;

$$xf\ (cot\,\theta) = x'(b + x) \tag{2.17}$$

Finally, by readjusting equation (2.17) for x, we get;

$$x = \left[\frac{b}{f cot\,\theta - x'}\right] x' \tag{2.18}$$

Similarly, substituting $\frac{x}{x'}$ from equation (2.13) in equation (2.18), co-ordinates y and z will be;

$$y = \left[\frac{b}{f cot\,\theta - x'}\right] y' \tag{2.19}$$

$$z = \left[\frac{b}{f\cot\theta - x'}\right] x' \tag{2.20}$$

In another interesting paper, Zargochev and Goshtasby (2005) stated the simplified triangulation principle (figure 2.42) which shows calculation of the distance, 'd' between the baseline and the image point.

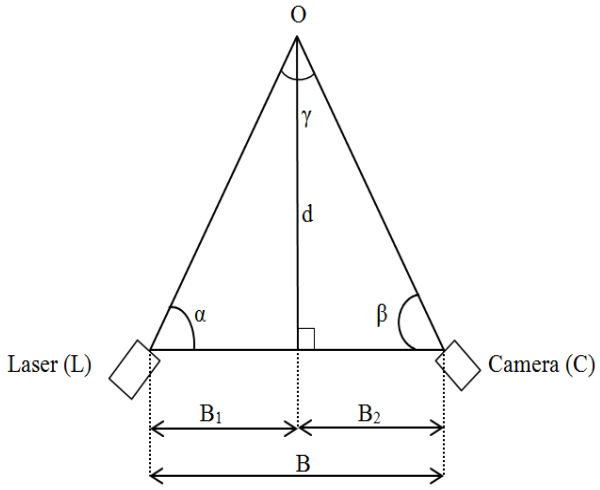

Figure 2.42 Simplified triangulation principle
(Adapted from Zargochev and Goshtasby, 2005)

When the distance B (baseline) between the camera (C) and the light source (L, laser) and the angle made by laser source with baseline, α are known, then the angle β, between the ray from object to the camera and the baseline can be calculated by connecting the lens centre to the image of point O in the image plane. Thus in figure 2.42 when α, β, B_1, B_2 and B are known then, distance 'd' between the point O on the object to the baseline can be determined.

$$tan\ \alpha = \frac{d}{B1}; \quad \frac{1}{tan\ \alpha} = \frac{B1}{d} \tag{2.21}$$

$$tan\,\beta = \frac{d}{B2}; \qquad \frac{1}{tan\,\beta} = \frac{B-B1}{d} \tag{2.22}$$

Adding equation 2.21 and 2.22 we get,

$$\frac{1}{tan\,\alpha} + \frac{1}{tan\,\beta} = \frac{B}{d} \tag{2.23}$$

$$d = B/[cot\,\alpha + cot\,\beta] \tag{2.24}$$

$$d = B\left[\frac{sin\,\alpha * sin\,\beta}{(cos\,\alpha * sin\,\beta)+(cos\,\beta * sin\,\alpha)}\right] \tag{2.25}$$

$$\boxed{d = B\left[\frac{sin\,\alpha * sin\,\beta}{\sin(\alpha+\beta)}\right]} \tag{2.26}$$

The depth resolution is directly proportional to the triangulation angle γ which is the intersection angle between the laser plane and the camera plane. Higher triangulation angle gives higher depth resolution thus greater depth accuracy.

In this paper, Zargochev and Goshtasby proposed a paintbrush laser range scanner where they used a reference double frame comprising front and back surface for initial camera calibration. Using this double frame, the equation of the laser plane as it is moved on an object (analogous to sweeping a paintbrush on painting) was calculated. The co-ordinate system of this double frame was same as that of the world co-ordinate system. As long as the object remains stationary relative to the double frame, it can be scanned from different views and the system would still gather all the data and acquire its point cloud in the same co-ordinate system. The calibration can be carried out before commencing a new scan. If the camera is not stationary and is moved during a scan then the calibration has to be repeated every time before starting a new view. The reference double frame designed by Zargochev

and Goshtasby was equipped with eight markers comprising four markers at the corner of each frame. If the camera is stationary, then these markers need to be registered with the camera position at the beginning of each scan. So every time the scanner is moved, it gets calibrated by the double frame. However, when the camera is being moved, the markers should be visible to the camera at all the times.

2.6.3 DAVID Laserscanner

Based on the paintbrush scanner prototype, Winkelbach *et al.* in 2006 proposed a low cost range scanner using basic components such as a calibration mask, a camera and a laser source with a quicker surface registration method. Their suggested system was free from the reference double frame which had to be adopted relative to the object size. They also stated that using a colour camera may add inaccuracies in the final scans as using a double frame only allows every fourth pixel to capture the light and every three out of four pixels get interpolated. It is very vital to determine the position and orientation of the laser device in real-time to satisfy the principle of triangulation. This is usually achieved by external systems such as electromagnetic sensors, optical LED tracking, mechanical positioning arms, etc. Instead of adding extra components such as an external tracking system, Winkelbach *et al.* provided a real-time self-calibrating hand-held 3D laser scanning system, DAVID Laserscanner. This system is free from markers and works on the basis of sub-pixel analysis of greyscale difference images.

When the data or the scans are captured from different views, it is imperative to establish a spatial relationship between global or world co-ordinate system and co-ordinate system of the scanner. There are various surface registration methods based on ICP suggested by Besl and Mackay in 1992 with more advanced supplementary

methods suggested by Krebs *et al.* (1996) and Dalley and Flynn (2002). All these methods work on predicting an initial guess to find the global optimal. DAVID Laserscanner works with a fast surface registration and an improved random surface matching process based on RANSAC (Random Sample Consensus) algorithm (Fischer and Bolles, 1981). This approach is not only robust and efficient but also can match frames of objects without predicting an initial guess. This allows rotating the object in different views and it can still produce a precise shape fusion of all the frames acquired in different scenes.

A. Camera Calibration

Unlike using the double frame method (paintbrush scanner), Winkelbach *et al.* proposed a background calibration method similar to a camera calibration technique suggested by Tsai (1986). This is a computational method for determining external position and orientation of the camera relative to an object reference coordinate system as well as its different parameters such as effective focal length, radial lens distortion and image scanning parameters. A reference background is two sheets of paper at a right angle with landmark points on it at a fixed distance. The camera calibration process records intrinsic and extrinsic parameters of the camera in the system. It also establishes the spatial relationship between the co-ordinate system of the background calibration geometry and the camera co-ordinate system. The calibration planes used in this study and the camera calibration procedure with the intrinsic and extrinsic parameters of the camera are elaborated in section 5.3 and 5.5.1 respectively.

B. Image Acquisition:

The fundamental concept of image acquisition in the DAVID Laserscanner is that when a laser plane falls on the object being scanned and the reference frame at the same time, their intersection point is used to determine the exact 3D position of the point on the object (figure 2.43). Thus by sweeping the laser line on the object and intersecting it with the projected rays, all such 3D poses, and hence, the 3D co-ordinates of the object can be triangulated. To do this, during camera calibration an image 'I_R' gets recorded without placing an object between the camera and the calibration curves. The object is then placed in between the camera and the calibration curves and the recorded image can be denoted as 'I'. So the final point cloud of the object 'I_d', would be the difference in the two images.

$$I_d = I - I_R \tag{2.27}$$

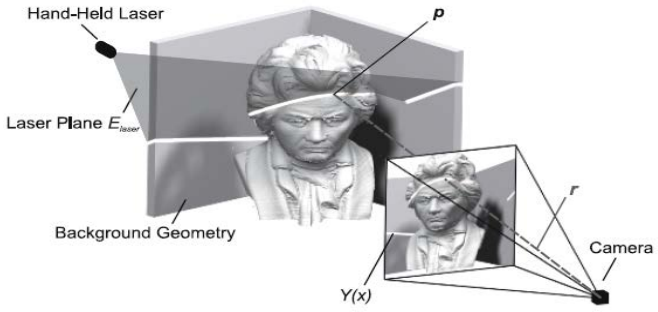

Figure 2.43 Image acquisition in DAVID Laserscanner
The intersection of a projection ray *r* with the laser plane E_{Laser} results in new 3d point *p*. (Reprinted with permission, Winkelbach *et al.*, 2006)

Before obtaining 3D poses of the laser and triangulating 3D co-ordinates of the target, a function $Y(x)$ of the bright pixel co-ordinates is deduced. Once this is achieved, by using the RANSAC method, three random pixels $Y(x_1)$, $Y(x_2)$, $Y(x_3)$ belonging to the calibration mask are selected. Prior to this step, camera would be already calibrated with the calibration mask; thus equations of three light rays r_i for each pixels can be calculated. Once these three rays intersect the known calibration geometry, co-ordinates of these three surface points; p_1, p_2, p_3 can be determined. As the equations of the laser plane, E_{laser} and number of image pixels from $Y(x)$ are found, a new surface point on the object can be calculated by intersection of the light ray r and the laser plane E_{laser}. Multiple points captured for the same image pixel get overlapped and merged using averaging.

$$P = r \cap E_{laser} \tag{2.28}$$

C Practical Issues

The DAVID Laserscanner software package allows users to scan objects using a hand-held laser module with a great accuracy and precision, but to achieve this, the calibration planes need to be placed behind the object at all times during scanning. Complexity in the knee joint and its position was an issue to keep the calibration curves behind it for every scan. Thus, practically it was not possible to use this hand-held technique in the study to scan the exposed knee joint intra-operatively. Moreover, hand-held scanning could be more time consuming due to irregularities in the manual movement by human arm. In this study, an automated 3D laser scanner using DAVID Laserscanner technique was developed. The laser scanning movement was automated and the use of the calibration planes for the actual scanning was eliminated. These developments are further described in Chapter

5. This application of the DAVID Laserscanner for scanning knee joints in situ was novel and showed initial proof of concept both technically and practically.

In general, the literature indicated that by suitable selection of the laser wavelength and by using line scanning technique it should be possible to quantify the 3D shape of the knee cartilage during surgery and therefore, to produce a scanning method to register the pre-operatively acquired scans with the patient's anatomy in the theatre.

CHAPTER 3. STUDY DESIGN

This chapter gives the rationale of the study, key aim of the investigation, objectives which were set up to achieve the aim and the research questions to be answered.

3.1 RATIONALE OF THE STUDY

- Current image registration techniques in CAOS are generally achieved using a navigated probe and by digitising anatomical points on the articulating surface of the knee joint. Using these digitised points a rigid body is formed which is then fitted to the pre-operative scan data using a best fit type minimisation.
- However, this manual digitisation approach is invasive, time consuming and often takes at least 14-20 minutes and is therefore costly.
- The purpose of this study was therefore to design and implement a new, quick, cost effective, contactless and automated 3D data acquisition method for registration in CAOS using a Laser Displacement Sensor.
- The proposed method would be capable of producing accurate rigid body models of articulating surfaces of the knee joint in the operating theatre to register the patient on table with their pre-operative MRI or CT data set.

3.2 AIM OF THE INVESTIGATION

The aim of this project was to develop and validate a quick, cost effective, contactless and automated 3D data acquisition method for registration in CAOS.

3.3 STAGES OF THE INVESTIGATION

- To plan, build and test a bespoke operating theatre compliant, automated 3D laser scanner capable of producing accurate 3D data sets.
- To establish a proof of concept for acquiring and registering pre-operative and intra-operative datasets based on surface matching using cadaveric knee joints.
- To validate the proposed 3D scanning system with standard measurement system.

3.4 RESEARCH OBJECTIVES

- Extensively review the current literature and undertake pilot studies for the selection of a suitable laser sensor based on the important parameters such as wavelength and power (Chapter 2, Chapter 4).
- Scan bovine and porcine knee joints with a commercial laser scanner of the chosen wavelength to test the proof of concept (Chapter 4).
- Perform 3D scanning with the chosen sensor and demonstrate its ability to receive signals from the articular cartilage (Chapter 4).
- 3D scanning of a calibrated dental model using a commercial scanner and the new cheaper hand-held scanning method. Scanning saw bone models for example, atlas cervical vertebrae with the commercial microCT scanner. Segment the CT images and generate the 3D model and scan the same bone with the hand-held

scanning method. Compare the results to check the accuracy and feasibility of the new method (Chapter 4).

- Automate the new laser scanning technique with a geared stepper motor and bespoke Arduino Duemilanove based switch controlled user interface system (Chapter 5).
- Design and assemble an adjustable Aluminium extrusion plate assembly for positioning the scanning modules; stepper coupled laser sensor and the detector camera (Chapter 5).
- In addition, design and implement a parallel scanning system by mounting the scanning modules on the MAKO RIO® system to save space in the theatre and so as to require a single unit (Chapter 5).
- Acquire pre-operative CT and MRI scans of the sample cadaver knee joints and segment them to generate the 3D models of the tibio-femoral joints (Chapter 6).
- Subsequently, acquire intra-operative 3D laser scans of the tibio-femoral joints and register them with their corresponding pre-operative model (Chapter 6).
- Calculate average deviations and maximum deviations with color-coded mapping of the differences between the reference (pre-operative) and the test (intra-operative) models (Chapter 7).
- Perform further statistical analysis to investigate the trends of the errors (Chapter 7, Chapter 8).
- Design and implement a validation study to compare the fixed distance direct measurements acquired using the constructed 3D laser scanner and data from digital vernier callipers (Chapter 6).

- Perform further statistical analysis and evaluate absolute errors and absolute percent errors to support the hypothesis (Chapter 7, Chapter 8).
- Discuss the potentials of the new system to be used for registration in CAOS and the likely benefits this may bring (Chapter 8).

3.5 RESEARCH QUESTIONS

- What are the current pitfalls of CAOS?
- Can this study provide a proof of concept to replace current manual registration approach in CAOS with a quicker and more cost effective 3D scanning system?
- Is a laser sensor capable of generating 3D digitised data of the articular cartilage and the bones in the human tibio-femoral joints? What are the suitable properties of a laser sensor for this application?
- Will the proposed scanning system be safe enough to adopt it in the operating theatre?
- Can this system be validated using a standard measurement system and is it as repeatable and accurate?
- What are the additional advantages and possible applications of the system?

CHAPTER 4. PILOT STUDIES

Before proceeding to the key experiments, a set of pilot studies was carried out. They were designed to solve a few important questions such as specific laser parameters, feasibility and practicality of the project and the most suitable methodology.

4.1 SELECTION OF THE LASER SENSOR

Using 3D laser scanning in theatre to acquire the digitised surface shape of the knee is a novel approach. Thus fundamental laser parameters such as wavelength and power output were crucial in order to obtain a sufficient and undistorted signal from the joint cartilage. Peng *et al.* (2008) stated that choosing the right laser for the right medical application is an important factor. The parameters on which the selection depends are:

1) The absorptive property of the tissue to be observed or destroyed.
2) The wavelength of the laser beam.
3) The power output of the laser emission including applied parameters such as power density, energy density, etc.
4) Mode of operation. Continuous/Pulsed and Contact/Noncontact

Trinh *et al.* (2006) reported on measuring knee cartilage morphology using a 3D laser scanner. They utilised a commercial ShapeGrabber® PLM 300 3D laser scanner with the scan head SG-1000 (Vitana Corporation, Ottawa, Ontario, Canada) to scan dissected cadaveric knee samples, in vitro. This scanner head is equipped

with a laser module of the wavelength, 670 nm (Umeda, 2010). Similar work was later published by the same team in the Osteoarthritis and Cartilage journal (Bowers *et al.*, 2008). Koo *et al.* (2005) demonstrated 3D scanning of resected proximal tibial cartilage placed on a rotating table using a desktop 3D scanner manufactured by Cyberware, Monterey, CA. This system used a Class 2 laser sensor of the wavelength 670 nm (China SouVR Co., Inc, 2008). Furthermore, Class 1 laser scanners of 690 nm from VIVID series (Minolta Co. Ltd, Japan) have been used in Cranio-maxillofacial and dental applications to produce high resolution 3D digitised data (Marmulla *et al.*, 2004; Thiruvenkatachari *et al.*, 2009).

Based on these key investigations, red laser sensors in a visible electromagnetic spectrum were selected. Visible green and blue laser sensors are also available in the marketplace, but their power output is usually more than 5 mW and hence they are classified as Class 3B lasers and are thus hazardous (Health Protection Agency, HPA, 2014).

4.2 POINT LASER SENSORS

Commercial point laser triangulation sensors are available such as Microtrak II from MTI Instruments, Albany, NY, USA as shown in figure 4.1. A Microtrak laser sensor head LTC 200-100 of the wavelength 670 nm and the resolution of ±9 µm was purchased and was interfaced with the National Instruments NI X Series multifunction data acquisition (DAQ) device, PCIe 6321. The laser features state of the art ‘complementary metal oxide semiconductor’ (CMOS) technology to provide precise measurements of displacement, position, vibration and thickness (MTI

Instruments, 2011). This laser sensor confirmed that this wavelength (670 nm) had the potential to digitise bone and cartilage.

(a) (b)

Figure 4.1 Microtrak II laser triangulation sensor

(a): Thickness measurement of an optical disk. (b): Din mountable compact enclosure and a menu driven controller.

However, this system faced some critical practical issues to adopt it for use in the operating theatre environment. Primarily, the laser sensor has a maximum power output of 5.1 mW and falls into Class 3B. According to the HPA and the British Standard user's guide for laser safety; direct viewing and specular reflections from Class 3B lasers are hazardous to the eye. Thus the emission of the laser beam has to be carefully enclosed using engineering controls and safety goggles are mandatory while working with them; although, the extent and severity of injury depends upon the duration of the exposure (HPA, 2014).

This system could generate 3D laser scans of the target object. But in order to achieve this, either the object had to be rotated using a mechanical rotary table or the system had to be moved in a predictable path which proved impractical for CAOS application. Also, it became apparent that using a point laser to map the articulating surfaces of the tibio-femoral joint and acquire digitised data would not save any

significant amount of time as compared to the current data acquisition techniques in the CAOS where each point is measured individually with the probe.

Furthermore, the laser sensor head costs around £9000 with the DAQ system costing around £2000. To work automatically, the system would need additional devices such as linear actuators which would make it more expensive. Thus, this approach of point registration was rejected as a potential future technique. The project concentrated on the development of a more cost- efficient and time-efficient system.

4.3 TESTING THE PROOF OF CONCEPT

To confirm the capability of laser sensors with the selected wavelength (670 nm) to scan the healthy cartilage surface, fresh bovine knee samples were collected from the local abattoir and were scanned using a high definition FARO Laser ScanArm (Quantum V3). This commercial line laser scanner is of Class 2M type with the power output of 1 mW and the wavelength of 660 nm. The results indicated a reasonable output as shown in figure 4.2. Soft tissues on the tibial plateau were not dissected to observe any interference that might be caused in the final scans.

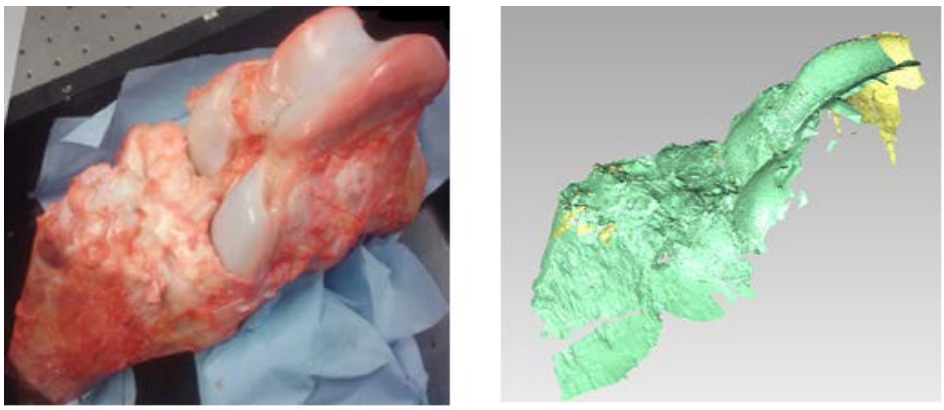

(a) (b)

Figure 4.2 3D scanning of bovine knee joint using FARO LaserArm
(a): Bovine tibio-femoral joint. (b): Corresponding 3D laser scan.

Having established a proof of concept of line scanning technique using a 660 nm laser FARO system, a search was made for a low cost alternative system. An automated, inexpensive and quick 3D laser scanning method was developed in Germany by the DAVID Vision Systems, GmBH as 'DAVID Laserscanner' (Winkelbach *et al.*, 2006). This is a triangulation based self-calibrating 3D laser scanning technique where with the help of a camera and a line laser, a 3D surface model of the target object can be acquired (A detailed explanation of this system is explained in the Chapter 5 and Chapter 6).

A porcine knee sample was collected from the abattoir and was scanned with the inexpensive hand-held laser scanning method using the DAVID Laserscanner technique. The line laser sensor of 1 mW power and 650 nm in wavelength was used in combination with a 1.3 MP Logitech webcam C300 as the detector. Multiple scans of the distal femoral condyle were acquired and were aligned using the shape fusion option in the software package to generate a 3D model of the entire sample (figure 4.3, 4.4 and 4.5).

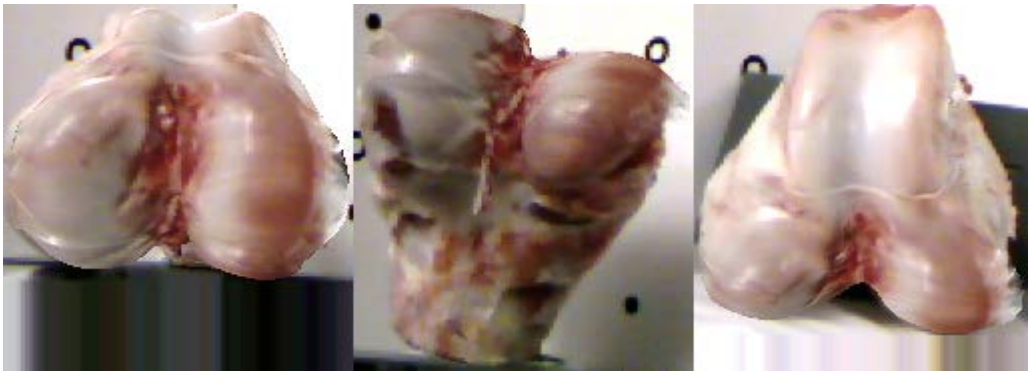

Figure 4.3 Scanning of porcine femur sample from different viewing directions

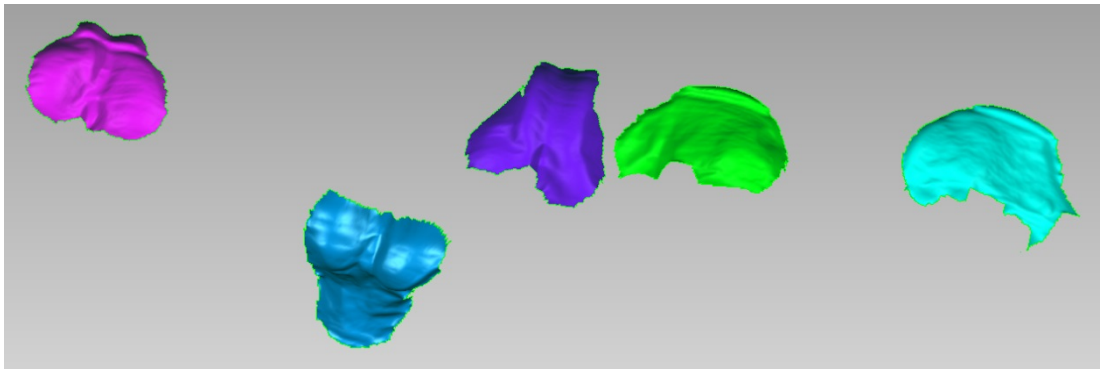

Figure 4.4 Individual scans acquired by rotating the sample manually

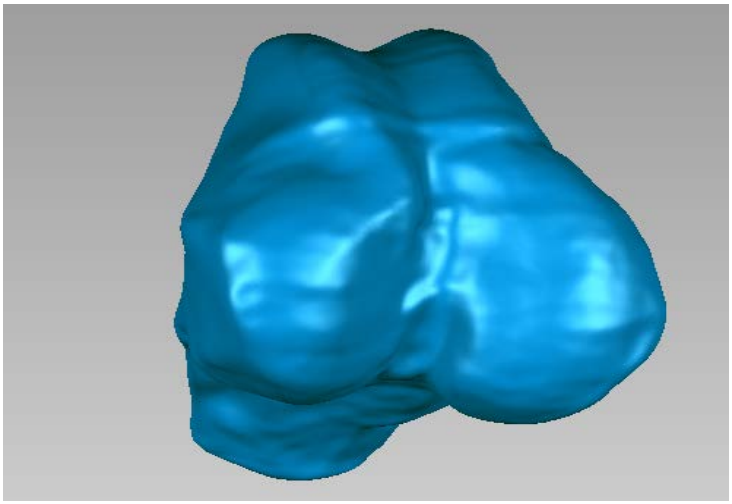

Figure 4.5 Shape fusion to produce a 360 degree 3D model of the femur

4.4 TESTING THE VALIDITY OF THE TECHNIQUE

The validity of the hand-held DAVID laser technique was tested against two imaging techniques.

4.4.1 Mono-Modal Imaging

To assess the validity of the low cost method, an extensively calibrated dental model was 3D laser scanned using the FARO LaserArm (figure 4.6(a)). Furthermore, the same model was scanned using the hand-held DAVID Laserscanner technique from all the sides and the individual scans were merged to generate a single 3D point cloud (figure 4.6(b)). Once this was achieved, the two models were imported to a robust digital image analysis software package, (Geomagic Qualify® 12, now known as Geomagic® Control™) developed by 3D Systems, Rock Hill, USA. The scan acquired with the FARO LaserArm was used as a reference model whereas the scan generated using the hand-held laser technique was treated as a test model. Reference and the test models were first registered manually by selecting 7 common points on the surface of each model.

Post registration, the two models were aligned using the Iterative closest point (ICP) based best fit alignment approach in the Geomagic Qualify® package. Results indicated an average absolute error (AAE) of 0.16 mm with an average positive deviation of +0.11 mm and an average negative deviation of -0.18 mm between the surfaces of the two models.

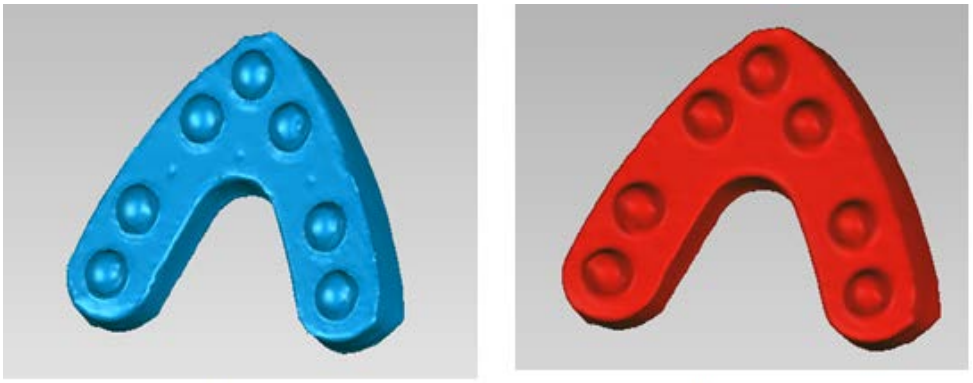

(a) (b)

Figure 4.6 3D laser scanned models of the calibrated dental model
(a): Reference model acquired using FARO LaserArm. (b): Test model acquired using DAVID Laserscanner hand-held technique

4.4.2 Multi-Modal Imaging

Additionally, a saw bone model of the first cervical vertebrae (atlas) was scanned using the SkyScan 1076, a commercial high-performance micro-CT scanner. The spatial resolution (pixel size) for the scanning was 35µm. X-ray settings were 80 kV and 120 µA. With the acquisition time of 59 minutes, in total 2165 slices were acquired. A 3D model (figure 4.7(a)) of the vertebrae was generated by segmenting the data acquired from the micro-CT scanner using advanced clinical software designed for medical image processing (Materialise's Interactive Medical Image Control System known as Mimics 12.01 developed by Materialise, Leuven, Belgium). In addition, this model was 3D scanned (figure 4.7 (b)) from all the sides using the hand-held DAVID Laserscanner technique. Similar to the previous approach, two models were analysed in the Geomagic Qualify software. Results showed an AAE of 0.48 mm with average positive deviation of +0.49 mm and average negative deviation of -0.44 mm.

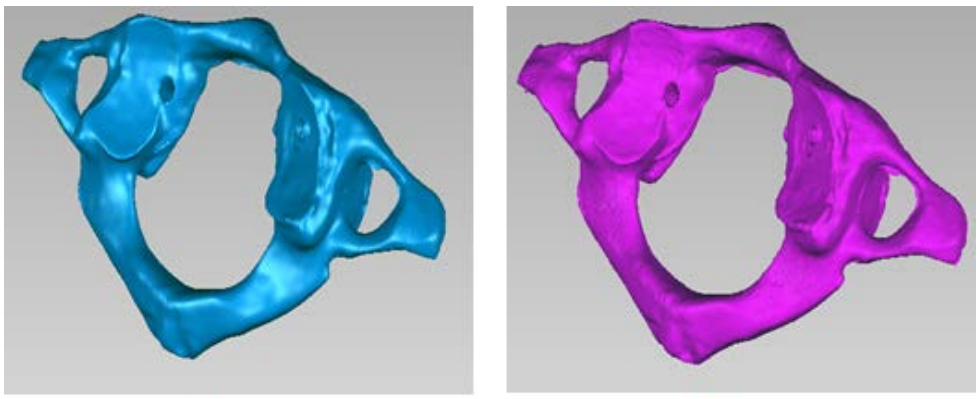

(a) (b)

Figure 4.7 3D scanned models of the atlas cervical vertebrae
(a): Reference model acquired using SkyScan 1076 micro-CT scanner. (b): Test model acquired using DAVID Laserscanner hand-held technique.

Hence, for the major experiments to follow, the laser scanning technique based on DAVID Laserscanner software package was adopted. In order to use this system for knee scanning, the hand-held system needed to be modified to an automated 3D laser scanning system and these developments are explained in detail in Chapter 5 and Chapter 6.

CHAPTER 5. BUILDING THE EQUIPMENT

Pilot studies showed the proof of concept and the validity of the traditional hand-held DAVID Laserscanner technology. This hand-held laser scanning system consists of three main components viz a camera, a laser source and the calibration planes. The quality of the scans using this method was satisfactory (Chapter 4). However, a major drawback of this setup is that after the scanner is calibrated, the object needs to be placed in front of the calibration planes such that when a laser line passes across it, the camera (detector) can triangulate the exact position of the object and thus the 3D point cloud defining the object. In this study the human knee joint was to be scanned in a clinical operating position. So, realistically it would not be possible to place the calibration planes behind the flexed knee joint and then scan it by hand.

An updated version (3.5) of the DAVID Laserscanner enables users to perform the scanning without calibration planes provided that the laser source is moved in a precise and constant motion and the relative distance between the camera and the laser is constant at all times. Thus, the traditional DAVID hand-held scanning method was modified to an automated laser scanning system using a stepper motor controlled by Arduino Duemilanove based stepper controller circuit for a precise automated manoeuvring of the laser module. The modified laser scanning modules (i.e. the stepper motor controlled laser source and the camera) were mounted on two different robust positioners. This chapter elaborates the scanning modules, the automated laser movement controller, the scanning procedure and the bespoke positioners.

5.1 LASER MODULE

Based on the available literature and careful investigation, an inexpensive but high stability and low noise laser module was chosen as a light source. It was a continuous wave laser source comprising a laser diode, lens and driver circuit housed in a metal case. Electrical connections of positive and negative DC voltage supply could be made via flying connecting leads; however these leads were sleeved in a standard 3.5 mm audio jack as a power connector.

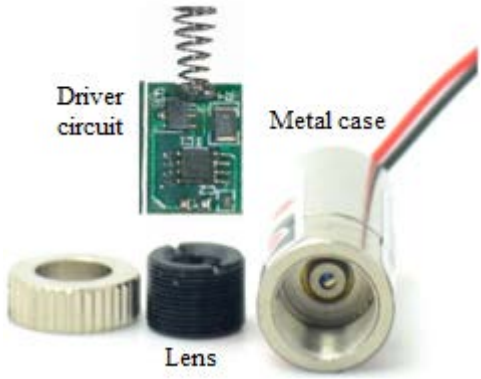

Figure 5.1 Red laser sensor module
Laser diode, lens and driver circuit housed in a metal case

The lens system consists of two major components: A single element of high refractive index glass which focusses the beam and a cylindrical crystal lens which converts that beam into a fine line of light over a long distance. The line generating lens can be rotated to focus the beam in order to produce a very fine and the hence the best possible laser line. In figure 5.2, an example of line laser scanning is shown where a saw bone model of the tibia is scanned.

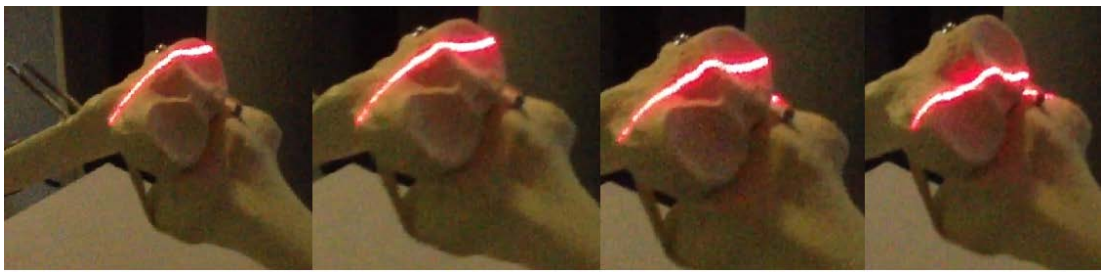

Figure 5.2 Line laser scanning of the saw bone model of the tibia

The laser falls into the safe Class 2 category with the power output of 1 mW and is in a visible range with the wavelength of 650 nm. Optical, electrical and mechanical characteristics of the laser module are listed in table 5.1, table 5.2 and table 5.3 respectively.

Table 5.1 Optical characteristics of the laser module

Parameter	**Value**	**Units**
Power output	1	mW
Power stability	2	%
Wavelength	650	nm
Wavelength stability	3	%
Noise	<0.5	% RMS
Laser operation	Continuous	-
Laser structure	Single mode	-
Line thickness	Adjustable	-
Fan angle	60	° (Degrees)
Spot size (minimum diameter)	<50	µm

Table 5.2 Electrical characteristics of the laser module

Parameter	Value	Units
Operating Voltage	3.3-5	V (DC)
Operating current	25-55	mA
Operating temperature	-15 to 35	°C
Storage temperature	-20 to 35	°C
Electrical connections	Red +ve, Black –ve	-

Table 5.3 Mechanical characteristics of the laser module

Parameter	Value	Units
Dimension (Diameter * Length)	12 x 36	mm
Cable length	1150	mm

5.2 CAMERA

Choosing the right detector is an important step when building any data acquisition scanner. In general, a camera which can record or stream a video can be used for a DAVID Laserscanner. Even old analog cameras which can acquire the frames in an Audio Video Interleave (AVI) video file can be used with the DAVID Video Grabber. The modern option however, was to use a standard PC-camera i.e. a standard webcam in ‘live’ mode.

The resolution and the frame rate are the two most important aspects of the camera when being used as a detector in a 3D laser scanner system. They are in competition to each other. High resolution cameras yield high quality and more accurate images but compromise the frame rate. Higher frame rates result in reduced scanning time but consequentially in lower resolution. Usually, for objects which are

vivid and tend to move, higher frame rate is advised as the scanning needs to be done as quickly as possible. For targets which are stationary a high frame rate is less important and high resolution scans can be achieved. For the current study a C525 Logitech HD Webcam was used with the frame rate of 20 fps and the resolution of 1280x720 (720p). The specifications of this camera are as follows:

Table 5.4 Specifications of the camera

Connection type	USB 2.0
Focus type	Auto
Optical resolution	2MP, True; 8.0 MP software enhanced
Diagonal field of view	69°
Image Capture (4:3 SD)	320x240, 640x480, 2MP, 8.0MP
Image Capture (16:9 W)	360p, 480p, 720p
Video Capture (4:3 SD)	320x240, 640x480, 2MP
Video Capture (16:9 W)	360p, 480p, 720p
Frame Rate (max)	30fps@640x480
Dimensions	68.5 * 40.4 * 31.75 mm (Length*Width*Height)

5.3 CALIBRATION PLANES

Calibration is a key issue in 3D scanning as it can affect the accuracy and the overall quality of the output. In general, it is a process of determining the intrinsic and the extrinsic properties of the camera along with its distance from the calibration planes. The size of these planes depends on the size of the object being scanned. For relatively small targets such as a coin or a ping pong ball, A4 size planes can be used. In this study, a human tibio-femoral joint was to be scanned and more importantly in a clinical situation on an operating table. A larger volume was therefore needed and

hence calibration planes were printed in A2 sizes. These were fixed on rigid wooden planes held exactly at 90°.

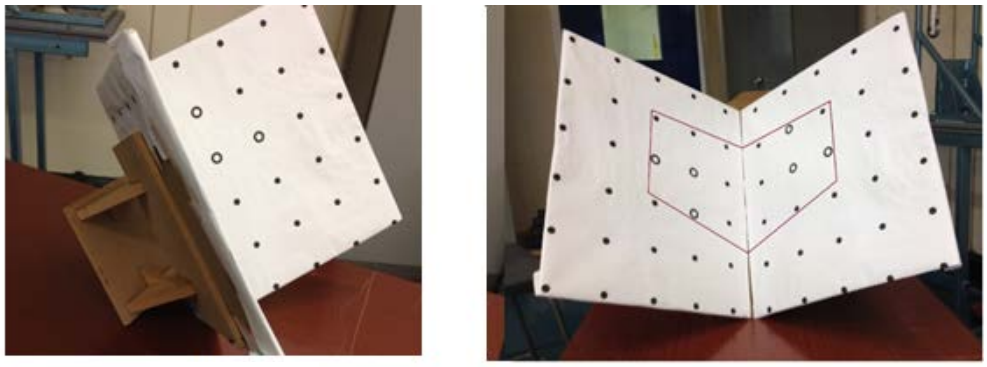

(a) (b)

Figure 5.3 Calibration mask used for camera and laser calibration
(a) Mounted on wooden fixture (b): Area within the red line is the actual zone used for calibration

In a traditional DAVID setup, calibration planes consist of two sides at 90° each consisting of 35 dots including 3 landmark points (big hollow circles). It was found by experimentation that as long as the camera could see both sides of the planes and the 6 landmark points, calibration could be achieved successfully. Therefore, instead of using an entire A2 sized mask, only a section of dimension 270 x 230 mm with 8 points on each side was used for the calibration. This area can be seen in figure 5.3 (b) enclosed by a red solid line.

5.4 AUTOMATED LASER MOVEMENT CONTROLLER

As explained earlier, to achieve the 3D scans using the traditional DAVID hand-held scanning setup the object has to be placed in front of the calibration planes which would be impractical for the current study. Hence, this method was modified to an automated 3D scanning method using a stepper motor and a controller circuit.

This section is focussed on the components used to build the stepper controller. The main constituents are a geared stepper motor, controller, stepper driver and the user interface.

5.4.1 Stepper Motor

The NEMA-17 motor with a planetary gearbox of 99.5:1 ratio was used and the laser module was attached to its shaft with a bespoke machined T-joint slot made of plastic as shown in figure 5.4 (a), figure 5.4 (b), and figure 5.4 (c). This stepper motor when coupled with the gearbox can produce a torque of 250 kg-cm at the maximum current (1.6 A). It is rated for 48 kg-cm of continuous torque and 100 kg-cm for brief overloads. The motor has a step angle of 1.8° and thus with the gear ratio of 99.5:1 it generates a step angle of approximately 0.018° at the output (Robotshop, 2011)

(a) (b) (c)

Figure 5.4 Geared stepper motor with the mounted laser module
(a): 99:1 geared stepper motor. (b): Stepper motor with the T-slot at the shaft. (c): Stepper motor with the laser module attached through the T-slot at the shaft

General, electrical and physical properties of the motor as well as gearbox properties are shown in table 5.5, table 5.6, table 5.7 and table 5.8 respectively.

Table 5.5 General properties of the stepper motor

Motor type	Geared bipolar stepper
Step angle at the output	0.018°
Step accuracy	5%
Holding torque	48 kg-cm
Related torque	48 kg-cm

Table 5.6 Electrical properties of the stepper motor

Operating voltage	12-30 V DC
Rated current	1.7 A
Coil resistance	1.7 Ω

Table 5.7 Physical properties of the stepper motor

Shaft diameter	8 mm
Weight	568 g (Without the gearbox)
Number of leads	4

Table 5.8 General properties of the gearbox applied on the stepper motor

Gearbox type	Planetary
Gear ratio	99:5:1
Backlash error	1 ½°
Maximum strength of gears	48 kg-cm
Shaft maximum Axial load	49.1 N
Shaft maximum Radial load	98.1 N

5.4.2 Controller

A high performance, low power ATmega 328 based Arduino Duemilanove controller was used to control the stepper movement. This controller is designed around the 8-bit Atmel AVR® microcontroller with the complementary components

to facilitate interface with other circuits. It consists of 14 digital input/output pins out of which 6 can be used as PWM outputs. It was powered using PC USB connection without any other external power supply. Specifications of the controller are as follows.

Table 5.9 Specifications of the controller

Operating voltage	5-12 V
Digital I/O pins	14
Analog Input pins	6
Clock speed	16 MHz
Flash program memory	32K
EEPROM	1K
SRAM	2K
PWM channels	6
Timer/counters	Two 8-bit, one 16-bit
Dimensions	68.5*53.3 mm
Temperature range	-40°C to 85°C

5.4.3 Stepper Driver

Basic stepper drivers such as EasyDriver and Pololu were first considered to drive the motor. However, the chips would overheat even at lower currents and in spite of applying heat sinks; the required stability could not be achieved. Thus a much more stable M542 microstepping driver controller was selected which is based on pure-sinusoidal current control technique patented by Leadshine Technology Co. Ltd. With this technology and the 3-state self-adjust current control parameters for different motors, the drive motors can run with smaller noise, lower heating, smoother movement and have better performances at a higher speed at a reasonable

price. It is suitable for running stepper motors from NEMA 17 to 34 and microstepping resolution can be selected by pressing the switches on the dual-in-line-package (DIP). Dynamic current was kept at 1.91A, (1.36A, RMS) with the microstepping resolution of 64 providing 12800 steps/revolution. The specified input voltage is between 20-50 V DC (Leadshine, 2015). Thus, instead of an external power supply, the driver was powered using Hewlett-Packard (HP) laptop charger with 20.5V DC. Specifications are tabulated in table 5.10.

Table 5.10 Specifications of the stepper driver

Input Voltage	20-50V DC, 36V typical
Output current	1- 4.2 (3.0 RMS)A
Logic signal current	7-16 mA, 10mA typical
Pulse input frequency	0-300 KHz
Operating temperature	0°C-70°C
Dimensions	118*75.5*33 mm
Weight	280gm

5.4.4 User Interface

All the circuit components were housed into a standard plastic case with all the control switches on the top panel and all the connecting leads attached on the front panel. Top panel is equipped with four switches namely, Laser ON-OFF, Motor ON-OFF, Motor direction UP-DOWN and STEPPER RESET as shown in figure 5.5. Laser ON-OFF and Motor ON-OFF switches are used to switch the laser source and the stepper motor on-off respectively. Motor UP-DOWN is a toggle switch which is used to select the direction in which the motor and thus the laser can be panned. STEPPER RESET is a push button switch which resets the motor position such that

the motor and hence the laser comes back to the exact same position from where it had started (zero step). This is the initial position of the motor after plugging in.

Figure 5.5 User interface of the controller box
Switches in the top from left: Laser ON-OFF, Motor ON-OFF, Stepper reset, Direction UP-DOWN. Two knobs for changing motor speed and laser intensity. LCD showing the current state of scanning

On the top panel, there are two potentiometer controlled knobs to control the motor speed and the laser intensity. Motor speed can be varied depending upon the object being scanned. Usually, a very slow speed would gather maximum number of points from the object to generate its point cloud but this results in higher acquisition time. From practice, a suitable motor speed was selected for scanning of bone and cartilage. Similarly, the input voltage and the current settings were optimized for a sufficient laser intensity to acquire the surface shape of the bone and the cartilage. A low intensity can lead to missing points and gaps in the scan whereas a very bright

laser line can cause reflectance from the surroundings. A 16x4 LCD display shows speed of the motor, number of step and frequency in real-time.

In this prototype, the user has to manually press the control switches on the user interface to initiate the scanning procedure. However, with modification these switches could be digitally controlled on the computer. The motor speed and the laser intensity were selected prior to the studies with respect to the object being scanned and were kept constant throughout the studies. Thus, there will not be any need of switches and knobs on the panel to control the scanning procedure of a future device. This would save cost and time and the system would be more portable and fully automatic.

The front panel consists of Din mount connecting leads for the motor. The power supply leads for the laser module, the controller and the stepper driver are also attached through the front panel as shown in figure 5.6.

Figure 5.6 Connections for the controller box
From left: 180° Din mount chassis for motor, laser power supply, D socket USB connector for the controller, power supply unit (PSU) for the motor.

5.5 TAKING A SCAN WITH DAVID LASERSCANNER

The basic principle behind the DAVID Laserscanner system has already been discussed in Chapter 2 (section 2.6.3). The traditional DAVID hand-held scanning setup consists of two major stages; camera calibration and 3D scanning. Whereas, the modified automated DAVID scanning system in this study consists of an additional stage of 'laser movement calibration' or 'reference scanning'. As mentioned earlier, the hand-held DAVID scanning system was adopted to undertake the pilot studies and the modified automated (motorized) scanning system was used for the major experiments. After choosing the hardware setup type (hand-held/ motorized) on the software screen, the calibration can be started. The camera calibration phase for both the methods (hand-held/motorized) was exactly the same.

5.5.1 Camera Calibration

Careful and accurate camera calibration is the foundation of the scanning and can directly affect the accuracy and precision of the output. The calibration planes were kept exactly at right angles to each other. The camera was placed facing the planes to the front without placing any object in between them.

In this study, prior to the calibration, camera parameters such as focus, white balance, brightness, contrast, etc. were kept on AUTO mode so that the camera would adjust to its optimum properties to suit the particular light condition in the room. Once they were set, the AUTO mode was unchecked as altering these values post calibration disturbs the scans. It was found that disconnecting the camera after calibration and then connecting it again for actual scanning resulted in inaccurate object geometries. When this happened, the camera needed to be recalibrated. Once the camera parameters were set and the planes were placed at the correct position, the

calibration can be achieved by clicking the Calibrate button on the user interface of the DAVID software (figure 5.7). The camera calibration results are stored in the file calibpoints.dat.

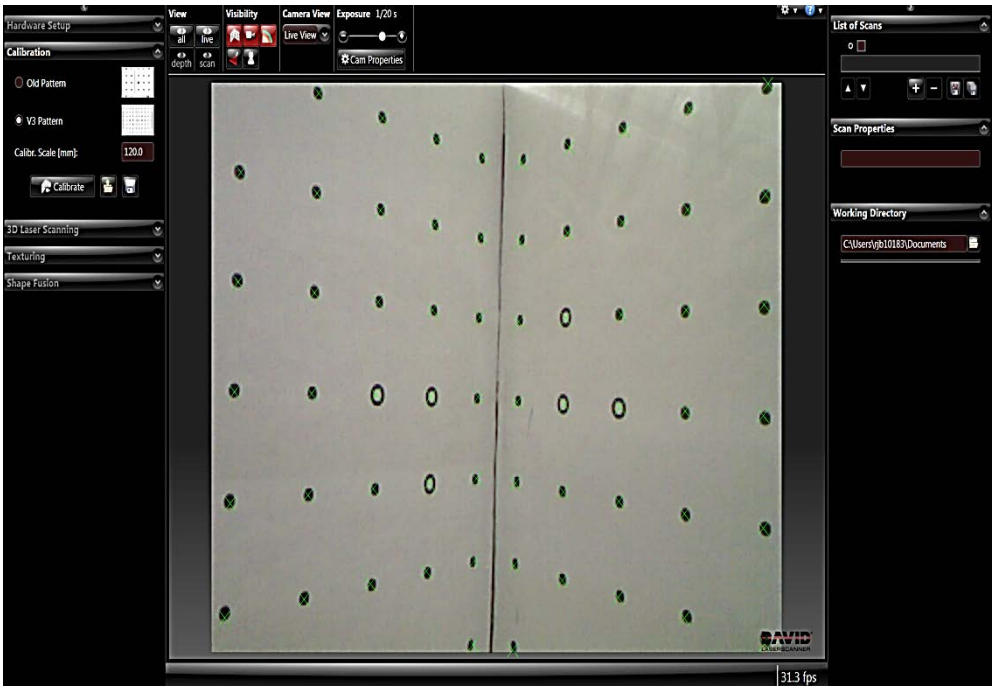

Figure 5.7 User interface of the DAVID Laserscanner for camera calibration

In general, Camera calibration is a process of determining intrinsic and extrinsic properties of the camera as well as its distance from the calibration planes at the zero position (Winkelbach *et al.*, 2006). It also establishes a spatial relationship between the co-ordinate system of the camera and the calibration mask.

A. Extrinsic Camera Parameters

a) T_x, T_y, T_z – Position of the calibration mask, thus the world co-ordinate system with respect to the camera co-ordinate system.

b) R_x, R_y, R_z – Rotation from the camera to the world system. (Around X, Y, Z axes.)

B. Intrinsic camera parameters

a) Focal length, ‘f’.

b) Physical pixel aspect ratio (on the CCD-Chip)

c) Image coordinates of the centre of radial lens distortions, C_x, C_y

d) Radial lens distortion

The calibration planes act as the world co-ordinate system with its centre being the origin of the co-ordinate system. So by inverting the transformation given by the camera parameters (T_x, $T_{y,}$ $T_{z,}$ R_x, R_y, R_z), the camera position with respect to the calibration planes (global reference frame) is acquired.

5.5.2 Laser Movement Calibration (Reference Scanning)

In the traditional DAVID system, once the camera calibration is achieved, the 3D scanning can be commenced by placing the object between the camera and the calibration planes. In this way the camera uses the back planes to work out its position in relation to the global co-ordinate system with respect to its translation and rotation.

However, in the modified scanning system the next step after camera calibration was to calibrate the laser movement (also termed as ‘reference scanning’) with respect to the camera and the calibration planes. Background filter factor has to be set to -1 to acquire the reference scan. In this stage, the laser line source gets identified by the camera and the system. During the reference scanning, the calibration planes are scanned with the laser source without placing any object between the planes and the camera. Thereafter, the user can then remove the calibration planes for the actual 3D scanning. The principle behind this is during the

reference scanning, a scan of the calibration planes is stored virtually in the software in an internal file called laser.xml. Thus, while 3D scanning of the target, the calibration planes can be removed as the detector camera uses the stored reference scan (laser.xml) as if it were the actual calibration planes placed behind the object being scanned (analogous to traditional hand-held scanning). With the reference scanning, the system stores the camera parameters, camera position and position of the laser with respect to the camera. Therefore, unlike the traditional hand-held DAVID system, the modified automated system facilitates 3D scanning of the target without the physical use of calibration planes. Figure 5.8 shows an example of the reference scan of the calibration planes.

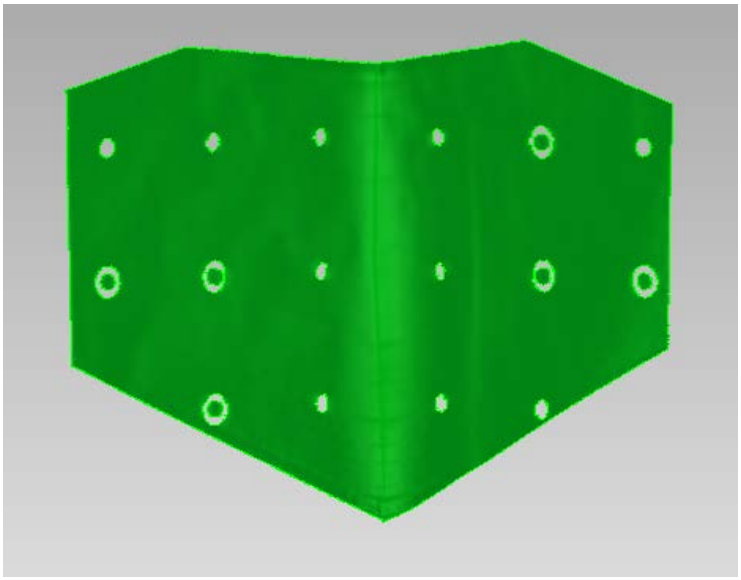

Figure 5.8 Laser calibration reference scanning result

Reference scans were acquired after the camera calibration stage without changing the position and orientation of the camera and the calibration planes. The

user interface for reference scanning is shown in figure 5.9. The depth map of the scan can be seen in real time.

Figure 5.9 User interface of the DAVID Laserscanner for reference scanning

The following procedure was followed in the same order to acquire the reference scans:

1) On the software screen check the box, Record New Motion and select the laser colour (Red).
2) Turn ON the laser module from the controller panel making sure a thin and ambient bright laser line is pointing at the calibration planes and adjust its position at the top or at the bottom of the planes (This was kept at the TOP and laser was panned in UP to DOWN motion).
3) Initiate the laser scanning by pressing Start on the computer screen and then turn the MOTOR ON switch on the controller box. At this point the motor starts moving and thus the laser line starts sweeping on the calibration planes. As stated

earlier, the required motor speed was selected on the controller panel and it was kept unchanged throughout.

4) Once the laser line reaches the end of the calibration planes, click Stop on the computer screen and then STEPPER RESET on the controller box and then Motor OFF. The laser source can be turned OFF if no other scan is to be acquired. At this moment the STEPPER RESET switch brings the motor and thus the laser source back to the exact same position from where it had started to acquire the reference scan. This concludes the reference scanning.

5.5.3 3D Scanning

The 3D scanning for the traditional hand-held DAVID setup can be begun after the camera calibration. For the automated DAVID setup the 3D scanning procedure was started after the camera calibration and the reference scanning.

A. Hand-Held 3D Scanning

For the traditional hand-held DAVID setup, after the camera calibration the object was placed in between the camera and the calibration planes with its surface being scanned facing the camera. The laser source was connected to a 3.3 V DC power supply. Figure 5.10 shows the user interface on the computer screen for hand-held DAVID Laser scanning technique. Following steps were applied in order to acquire the scans:

1) Turn the power supply ON to switch on the laser source.
2) Press the Start on the computer screen and move the laser source on the surface of the target object like a paintbrush.

3) Scanning can be seen on the computer screen in real-time. Once the area under inspection is scanned Stop the scanning on the computer screen, then turn the power supply OFF to switch off the laser source.

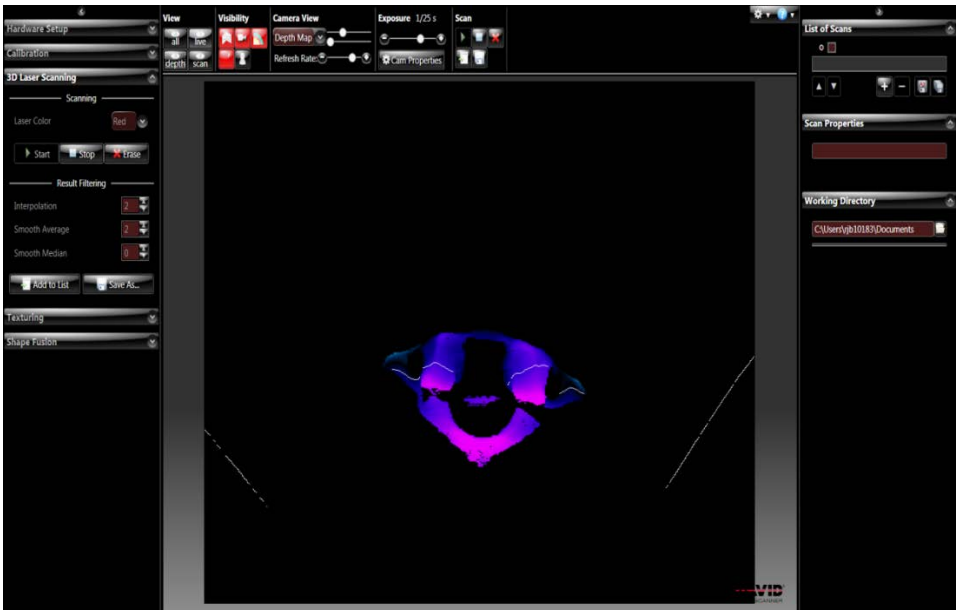

Figure 5.10 User interface of the DAVID Laserscanner for the hand-held 3D scanning

B. Automated 3D Scanning

The generic procedure for taking a scan for a modified automated scanning was very similar to that of the reference scanning (section 5.5.2). The only change was to remove the calibration planes and manipulate the scanner (mounted on the positioners, explained in the next section, 5.6 and 5.7) towards the object so that the area under scrutiny lied about centre of the camera screen. The path followed by the laser source in the reference scanning is replicated in the 3D scanning. The virtually stored calibration planes would be the reference frames for the scanning. It should be noted that at this point the laser would be at the same position with zero steps from where it had started in the reference scanning. Alternatively, by pressing the

STEPPER RESET switch on the front panel of the controller box, the laser can be moved back to its original position. The procedure for the 3D scanning is described in steps as follows:

1) Remove the calibration planes and move the scanner towards the object being scanned. Adjust its position to cover the surface being scanned.
2) On the software screen Uncheck the box, Record New Motion.
3) Turn ON the laser from the controller panel, then press Start on the computer screen. Turn the Motor ON to start acquiring the data.
4) Scanning can be seen on the computer screen in real-time (figure 5.11). Once the required area is scanned, STOP the scanning on the computer screen, then press RESET STEPPER and then Motor OFF.
5) Turn the laser OFF if no further scan is to be acquired.

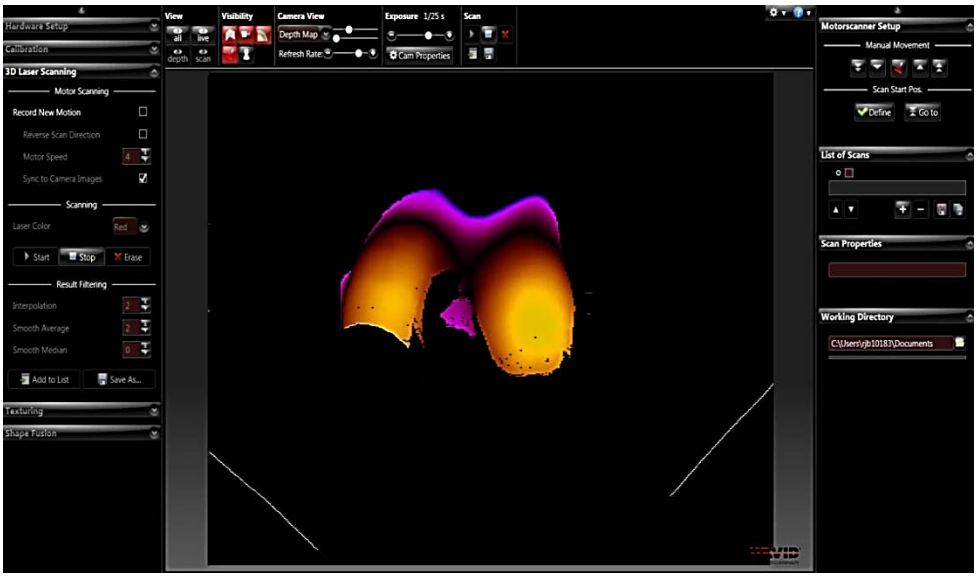

Figure 5.11 User interface of the DAVID Laserscanner for the automated 3D laser scanning

5.5.4 Storing the Data

The acquired scans for each session were added on the right hand side (List of Scans) of the software interface screen (figure 5.11). All the scans were exported in the Stereolithography (.STL) format to the computer hard drive. [.STL file format stores the required information within a small sized file and is widely accepted in CAD/CAM, rapid prototyping and majority of the 3D scanning systems].

5.6 POSITIONING THE SCANNER ON AN ASSEMBLY

The automated scanning modules; geared stepper coupled laser sensor and the detector camera were mounted on a robust positioner assembly constructed using Aluminium Extrusion plates.

This structure comprises T-slotted (figure 5.12) aluminium extrusion plates. These are easy to connect using the adjustable profiles and are preferred over other structures to build an economical but stable framework.

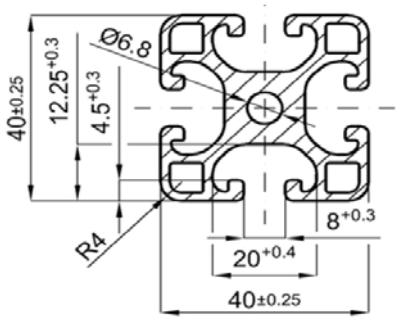

Figure 5.12 T slot of the aluminium extrusion frames
(Reprinted with permission, Valuframe, 2013)

A 40 mm aluminium profile was used with custom-made T and L connectors. All the attachments on the extrusion plates were made using standard M8 screws and sliding slot nuts. The stepper motor coupled with the laser sensor and the camera were attached at an approximate distance of 450 mm on an angular adjustable stream with the help of self-machined mounting plates shown in figure 5.13.

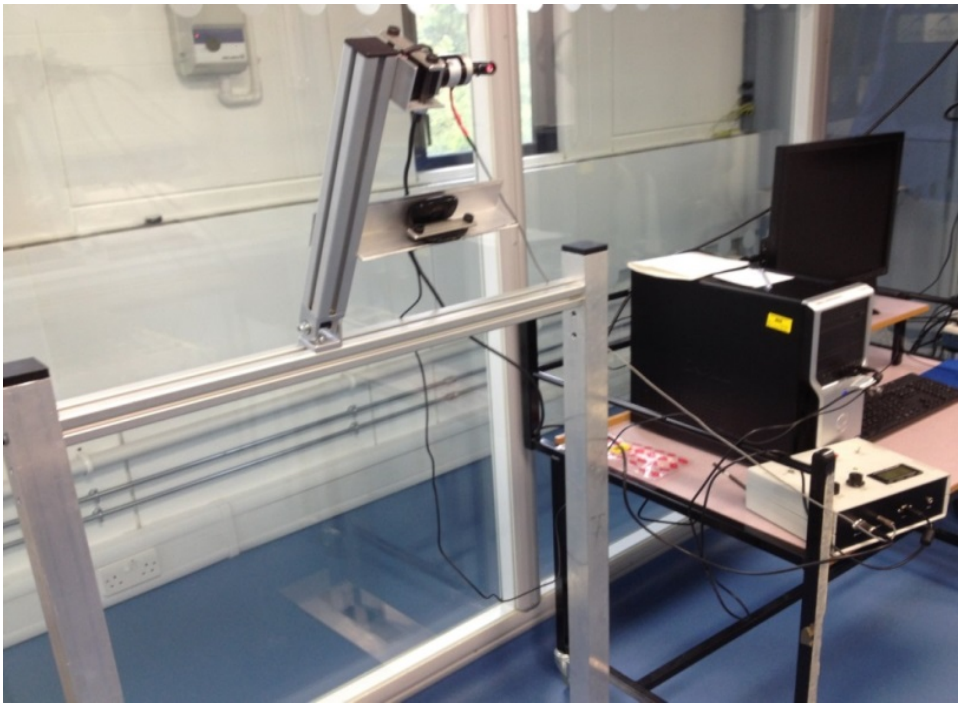

Figure 5.13 3D laser scanner mounted on the aluminium extrusion framework

5.7 MAKO RIO ARM AS POSITIONER

In addition to the first setup, the scanning modules were mounted as an end-effector on the MAKO Surgical Corps's RIO® arm shown in figure 5.14. This would mimic the setup which would be possible if this robotic surgical system was in use.

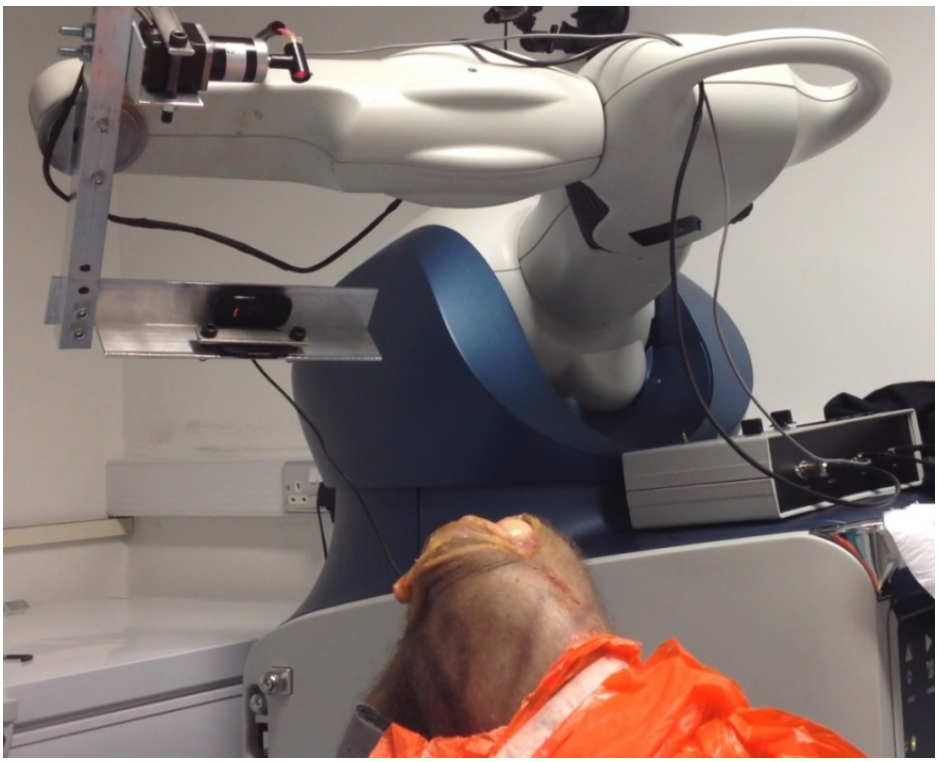

Figure 5.14 3D laser scanner mounted on the joint six of the MAKO RIO® arm

The key purpose of coupling the laser scanner to the RIO system was to save space in the operating theatre so as to require just a single unit. Also, the RIO arm features six joints and six degrees of freedom which facilitates precise movement and high stability to position the system.

After calibrating the scanner, any small deviation from the original positions and orientations between the camera and the laser source would create measurement errors. However, provided the relative movement between the camera and laser source did not occur, the position assemblies could be moved or rotated after calibration to any position. So once the camera calibration and laser movement calibration is achieved, the scanner can be moved anywhere to undertake the scan.

5.8 SUMMARY OF SCANNING

Acquiring a 3D scan using DAVID Laserscanner technology is a quicker and an inexpensive approach. The traditional hand-held setup comprises of camera calibration and the 3D scanning phases whereas the modified automated system consists of an additional procedure of laser movement calibration (also known as reference scanning). Camera calibration process in both the setups is exactly the same. In the hand-held system, 3D scanning was commenced once the camera was calibrated with respect to the calibration planes and hence the global co-ordinate system.

In the modified automated 3D laser scanner, after the camera calibration, reference scanning was performed where laser movement was calibrated with the camera by acquiring a scan of the calibration planes. The laser line source was directed at the calibration planes and by pressing the appropriate switches and the controls on the computer screen (in the same order as sub-section 5.5.2), a reference scan of the calibration plane was acquired. This data gets stored in the software and for the actual 3D scanning the system considers the virtually stored calibration scan as the actual planes placed behind the object. This allows users to acquire 3D scans of the object without using the calibration planes. At the end of the reference scanning, by pressing the STEPPER RESET button, the stepper motor and the laser source get back to their original position where they had started. For the actual 3D scanning, the calibration planes were removed and the scanner was positioned on the target using the two positioner setups. The scans were acquired by pressing the appropriate switches and digital controls on the computer (in the same order as sub-sub-section 5.5.3 B). The data files were stored in .STL format.

CHAPTER 6. METHODOLOGY

This chapter explains the methods applied for the experiments of the study. The demography of the samples utilised in the study is elaborated. The pre-operative planning, intra-operative 3D laser scanning and the data analysis methods using a single example are explained. Before performing the intra-operative 3D laser scanning of the samples, a standard registration approach used in MAKO Surgical Corps' system was applied.

6.1 SAMPLES

Ten fresh frozen cadaver knee joints were used for the study. Eight out of the ten samples were obtained from the Anatomy Gift Registry, 7522 Connelley Drive, Suite L, Hanover, MD 21076. The remaining two samples were collected from the Clinical Anatomy Skills Centre (CASC), Glasgow University, Glasgow, UK. One female and nine male cadaver legs were utilised and all the samples had their anatomical structure present from hemi-pelvis to the toe. All the legs were stored in the freezer at -19.5 °C.

Prior to these studies, nine of the cadaver legs had been operated on post donation. A medial UKA surgery had been performed using the NAVIO PFS® system developed by BlueBelt Technologies, INC. Hence, all these nine legs had their medial compartment milled and were left with the burred and rough bone surface. Lateral compartments of all samples were intact with the smooth articular cartilage. One cadaver leg was not operated and its knee joint was intact. This

yielded nine operated (medial) and eleven intact (ten lateral + one medial) knee joint compartments. The demography of the samples is illustrated in table 6.1.The samples were pre-operatively CT scanned to visualise and acquire 3D models of the bone surface from their medial compartments. Furthermore, the samples were MRI scanned to obtain articular cartilage 3D models from the un-operated compartments. The CT scans were acquired in axial plane whereas MRI was performed sagitally.

Table 6.1 Demography of cadaver legs

Knee joint compartments utilised for the study: eleven intact, nine operated.

Cadavers	**Knee Joint Compartments**	
	Medial	**Lateral**
1	Operated	Intact
2	Operated	Intact
3	Operated	Intact
4	Operated	Intact
5	Operated	Intact
6	Operated	Intact
7	Operated	Intact
8	Operated	Intact
9	Operated	Intact
10	Intact	Intact

6.2 PRE-OPERATIVE PLANNING

As stated earlier, nine knee joints were operated post donation on the medial compartment. All these samples were CT scanned and were segmented to generate

the 3D models of the nine medial compartments comprising a bone surface. In addition, all the samples were MRI scanned to generate eleven 3D models of the (10 lateral + 1 medial) articular cartilage. Thus, pre-operatively nine 3D bone and eleven 3D articular cartilage compartmental models were generated.

6.2.1 MRI Protocol

MR imaging pulse sequences are usually preferred to comprehend the state of the articular cartilage (Eckstein *et al.* 1995, Cohen *et al.* 1999, Sonin *et al.* 2002, Roemer *et al.* 2011). The most important criteria while imaging articular cartilage are SNR (Signal to Noise Ratio), CNR (Contrast to Noise Ratio), spatial resolution and image acquisition time (Eckstein *et al.* 2006). 3D FLASH (Fast Low Angle Shot) MR imaging technique invented in 1985 at the Max-Planck-Institut für biophysikalische Chemie, Germany (Haase *et al.* 1986) provides better SNR and CNR to adequately set apart critical sites such as cartilage to bone interface and the articular interface in healthy as well as arthritic knee joints (Kornaat *et al.* 2005, Eckstein *et al.* 2006). Various MRI manufacturers use different names for this MR sequence technique. Where Siemens terms it 3D FLASH, GE (General Electric) use the term 3D Spoiled Potential Gradient Recoiled (SPGR) and Philips call it Contrast-Enhanced Fast Field Echo (CE-FFE-T1) or T1-FFE (Nitz 1999, Eckstein *et al.* 2006) [This will be referred as 3D FLASH throughout the thesis as the MR scans were acquired on Siemens station]. Slice thickness was kept at 1 mm as the articular cartilage is 1.3-2.5 mm thick in healthy knees (Eckstein *et al.* 2006).

Although 3D FLASH MR imaging technique has drawbacks of providing poor contrast between synovial fluid and cartilage and high sensitivity to the artefacts, it still makes the segmentation of the articular cartilage much easier and is

still considered as a standard MR imaging technique for depicting articular cartilage morphology (Recht 1993, Eckstein *et al.* 2005, Kornaat *et al.* 2005, Eckctein *et al.* 2006, Roemer *et al.* 2011). Using radio frequency (RF) pulses with low flip angles allows optimization of better SNR and spatial resolution. Usually a low TE (time of echo) and TR (time of repetition) are employed and by randomly changing the phase of the RF pulse, FLASH sequence spoils the transverse steady state to produce the phase shift (Haase *et al.* 1986). Combination of 3D FLASH along with radial data sampling can also be used for real time MR imaging (Zang *et al.* 2010).

All ten cadavers were defrosted 48 hours prior to the MR imaging and were scanned on a standard Siemens MRI station at 1.5 T. A standard protocol (table 6.2) presented in the literature was followed (Kornaat *et al.* 2005, Eckstein *et al.* 2006, Stahl *et al.* 2009). This was also approved by a highly skilled clinical research team in the Western Infirmary, Glasgow where the scanning was performed. The sagittal MRI was performed (figure 6.1) and using 3D volume, images were reformatted in the coronal and the axial planes. Optimal parameters were chosen to keep the SNR, CNR and the overall quality of the scans high. TR/TE were optimized to 17/8.4 ms along with a low flip angle 12° to achieve maximum contrast between articular cartilage, synovial fluid and menisci (Stahl *et al.* 2009). Scans were acquired using an acquisition matrix of 512 x 512, 16 cm of field of view (FOV), 120 Hz/pixel bandwidth signal averaging with the number of excitations (NEX) of 1 and 1 mm slice thickness. 120 slices were acquired for 8 knee joint samples whereas for two slim legs the number of slices was 104, both without any inter-slice gap which yielded 0.3 mm in plane resolution. Acquisition time for 8 legs with 120 slices was 12 minutes 46 seconds while for the two slim samples it was 11 minutes 52 seconds.

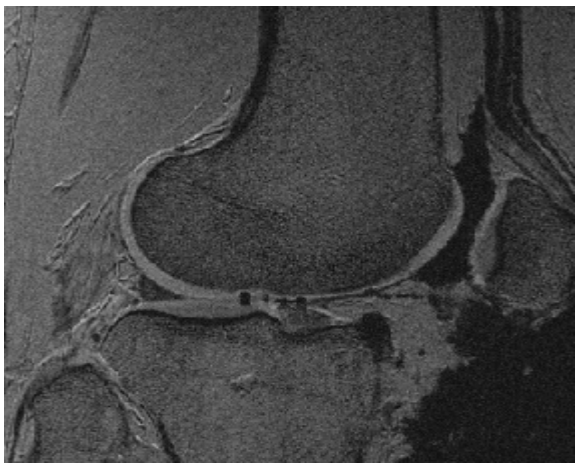

Figure 6.1 A sample MRI scan of the right knee joint
MRI acquired at 1.5 T using 3D FLASH which shows excellent contrast between the cartilage and the rest of the structure

Table 6.2 Synopsis of the 3D FLASH sequence MRI protocol

Workstation	1.5 Tesla Siemens
Pulse sequence	3D FLASH
TR	17 ms
TE	8.40 ms
NEX	1
Slice thickness	1 mm
BW	120 Hz/pixel
Gap	0
Number of slices	104/120
FOV	160 mm
Flip angle	12°
In plane resolution	0.3 mm x 0.3 mm
Acquisition matrix/ Base resolution	512 x 512
Reconstruction matrix	512 x 512
K-space sampling	0
TA	11.52/12.46 min.

6.2.2 CT Protocol

The samples were also CT scanned in order to generate 3D models of the cut bone surface of the nine medial compartments. The samples were in a frozen state and were scanned on the Philips Brilliance 64 CT scanner.

A standard CT protocol (table 6.3) for the knee segment recommended by MAKO Surgicals Corps was followed which was also validated by the clinical research team at the Western Infirmary, Glasgow (Hagag *et al.* 2011). An aluminium motion rod was strapped to the leg to keep the leg straight in the supine position as well as to mark the reference for anatomical landmarks. Initially, a standard topography was acquired to check for the presence of any metal implants and the condition of the tissue using 120 kV, 50 mA settings with acquisition times ranging from 10.27 ms to 12.93 ms. A variable FOV ranging from 64.5 cm to 39.5 cm with 512 X 512 matrix was utilized. Variability depended upon the size and the length of the leg. Slice thickness was kept at 0.6 mm.

For the actual knee CT scans, the parameters were 120 kV, 100 mAs, 56 mA with the acquisition time of 17.7 seconds. A FOV of 35 cm with 512 X 512 matrix was used. Slice thickness was 1 mm with 350 slices**.** An example of a CT of a left knee joint is shown in figure 6.2.

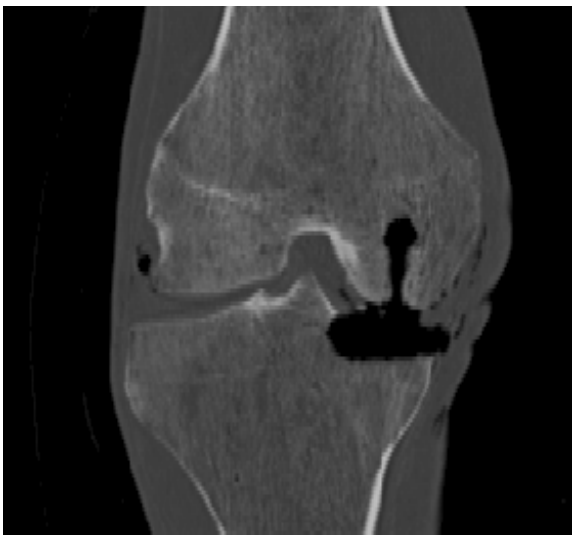

Figure 6.2 A sample of CT scan of the left knee joint
Medial compartment is operated and milled

Table 6.3 Synopsis of the CT protocol adapted from MAKO Surgicals Corps

Workstation	Philips Brilliance 64 CT scanner
kV	120
mAs	100
TA	17.7 seconds
FOV	35 cm
Slice thickness	1 mm
Number of slices	350
Gap	-
Acquisition matrix/ Base resolution	512 X 512

6.2.3 Segmentation

All the MRI and CT scans were acquired in the DICOM (Digital Imaging and Communications in Medicine) format. The segmentation was performed using advanced clinical software specially designed for medical image processing, Mimics (Materialise's Interactive Medical Image Control System). This software package

enables users to interpret medical images acquired in various formats such as DICOM, JPEG (Joint Photographic Experts Group), BMP (Bitmap), etc. Mimics can be used for the visualisation and the segmentation of scans acquired from various modalities such as CT, MRI, ultrasound and confocal microscopy including 3D rendering of objects. The Hounsfield Units histogram represents an immediate visualization of the pixels distribution for setting an appropriate threshold, which provides faster definition of the threshold values. Thus, the user can select a particular area of interest such as bone or soft tissue (for example 1.5-2 mm thick articular cartilage) to act as a boundary on the acquired MR images. Once this is achieved, the boundary can be visualised in 3D format which in turn can be exported in STL or CAD format which are the standard file formats for reverse engineering, rapid prototyping and Finite element analysis (FEA) (Materialise, 2014). Steps involved in segmenting MRI and CT scan digital images of the cadavers using MIMICS are elaborated in this section.

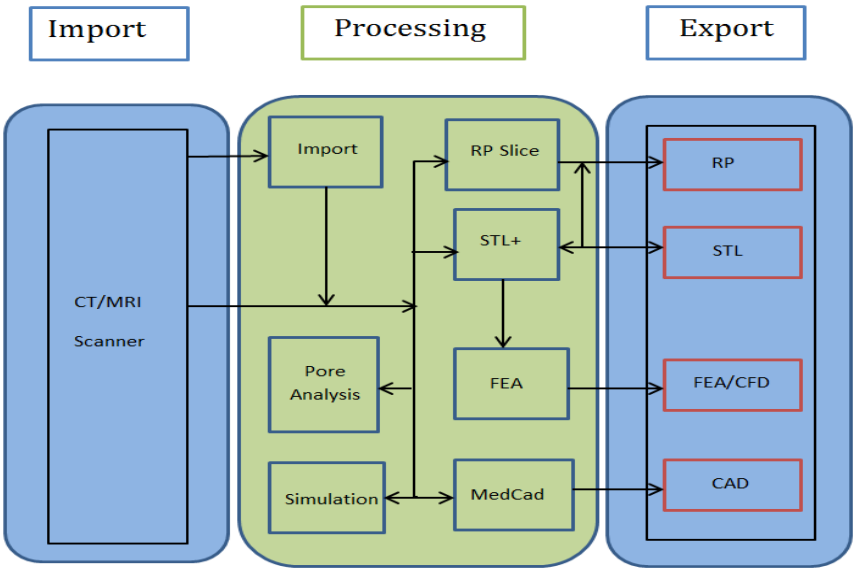

Figure 6.3 Mimics module overview
(Adapted from Materialise, 2011)

The Import module in MIMICS allows users to insert MRI or CT data into the software which can be accessed from CD, Flash drives, Portable hard drives, optical disks, etc. (figure 6.3). It comprises of seven major modules in the processing unit. The RP slice module interfaces from MIMICS to rapid prototyping systems via sliced files to build models. Pore analysis provides in depth delineation of the characteristics of porous materials. MedCad acts as a bridge to CAD systems whereas FEA module is a link to FEA systems such as Abaqus and Ansys.

1) Import: It was observed that importing data from a CD or a flash drive consumed considerable amount of Random Access Memory (RAM), hence the DICOM data was copied to the computer hard drive first and was then imported. While importing, the user has to select the orientation of the images in order to visualise the scans in the correct orientation as shown in figure 6.4.

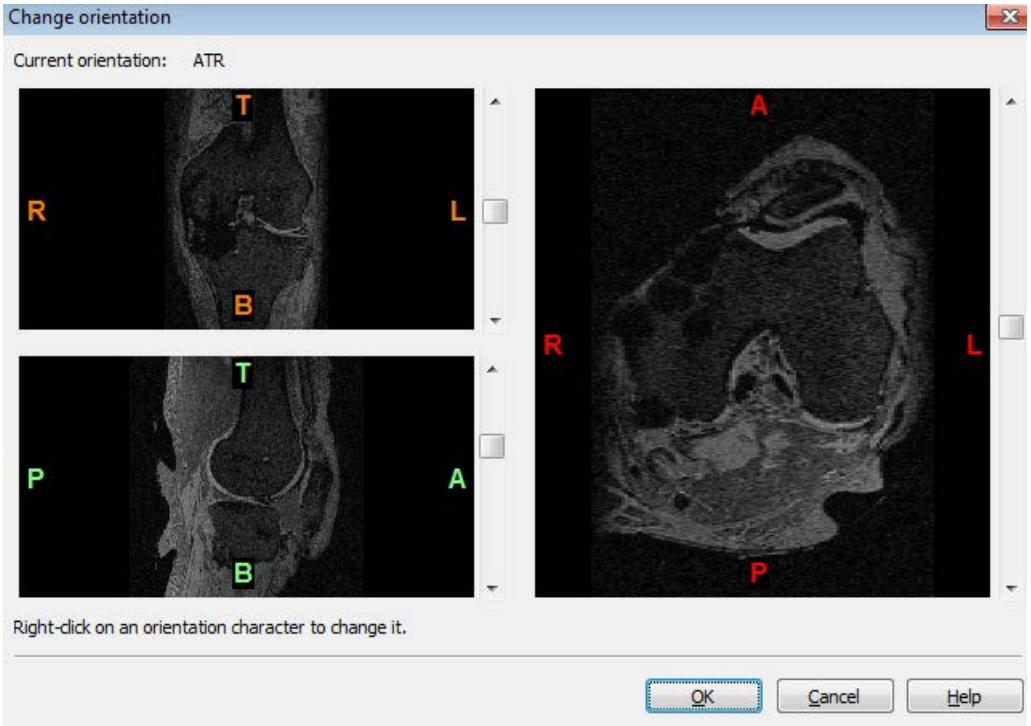

Figure 6.4 Orientation selections for importing scans into MIMICS

2) Thresholding: Once the images were imported, the area of interest such as cartilage or bone had to be masked. Thresholding option produces Hounsfield histogram which allows users to define a particular object based on low threshold or high threshold. Threshold value can be selected based on predefined units for bone, fat tissue, etc. or can be chosen manually. Throughout the studies, threshold values were picked manually to select the required area with minimum external outliers (figure 6.5).

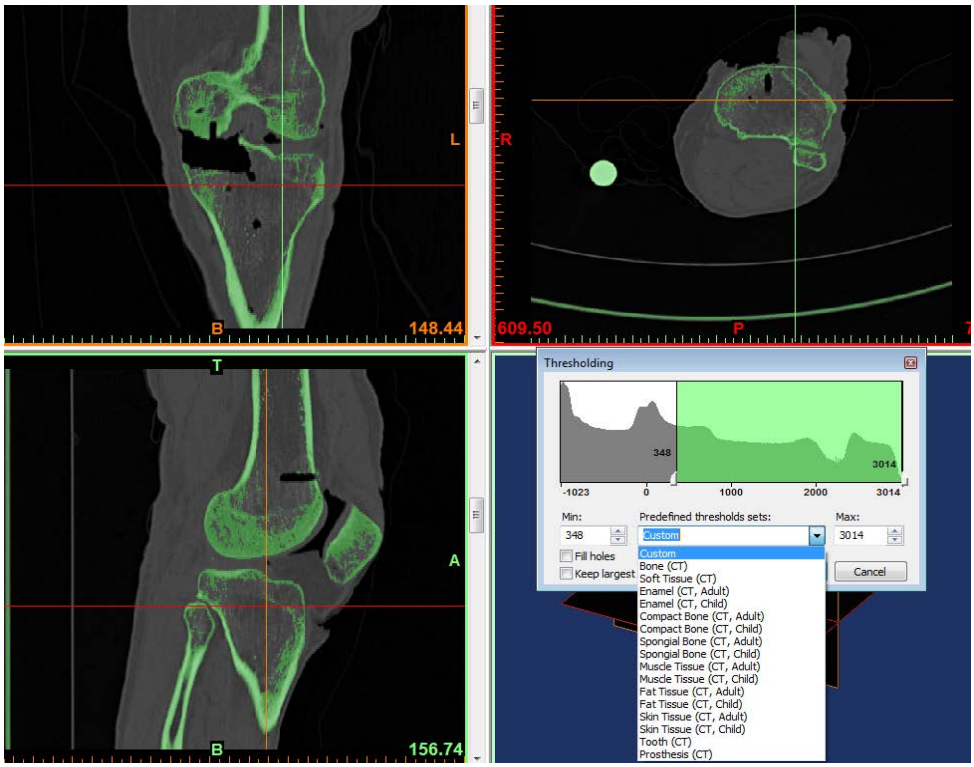

Figure 6.5 Setting up threshold of CT scan for segmenting bone in MIMICS

Unwanted regions and thus pixels can be deleted by zooming the area especially around the edges by choosing edit masks option. Also, missing regions can be redrawn using the same tool.

3) Region growing: As shown in figure 6.5, by using the thresholding tool, the region of interest can be selected. The region growing tool can be used to bifurcate the segmented area to select a particular object. In figure 6.6, only the femur is selected.

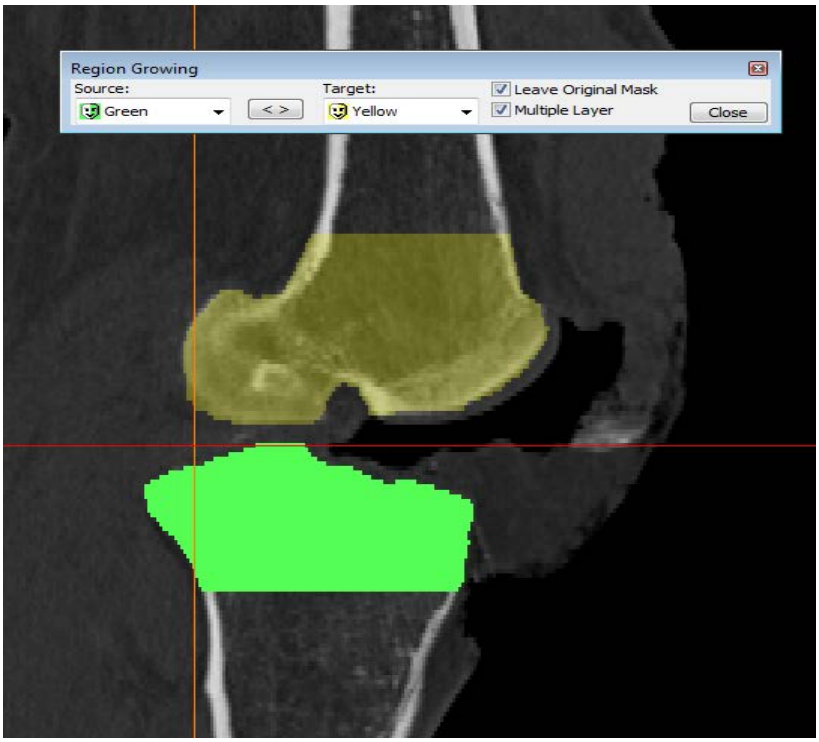

Figure 6.6 Region growing to select a particular object in the segmented area

4) Calculate 3D: Once the required area is selected and all the unnecessary pixels are removed, a 3D volume can be calculated. To speed up this process on a standard computer, models can be acquired with a low or a medium quality; however, this resulted in inaccurate dimensions of the models because of extensive matrix reduction. On the other hand, high quality option yielded high resolution model, but it did so by adding extra smoothing factors. During the current studies, all the 3D models were generated at an optimal quality to ensure dimensional accuracies

of the surfaces. Example of an acquired 3D model using a CT scan is shown in figure 6.7.

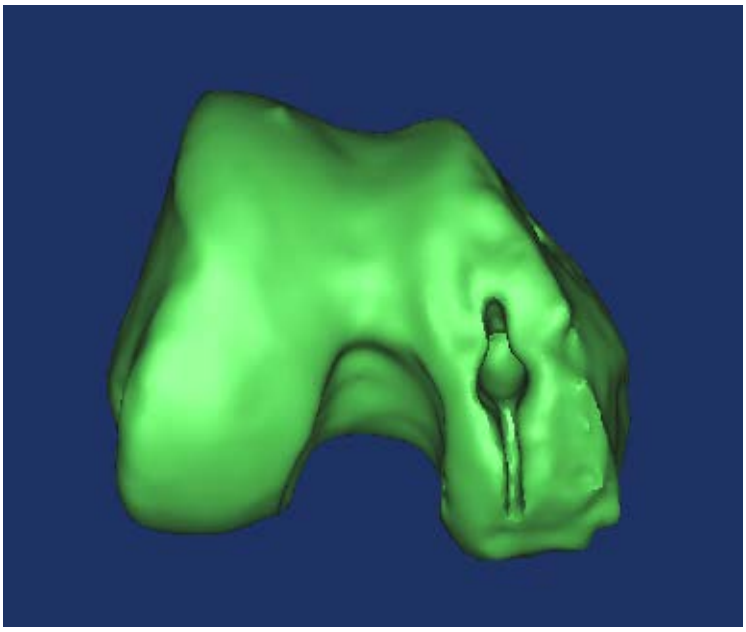

Figure 6.7 CT generated 3D model of the femur of the left knee acquired in MIMICS

5) Remeshing and smoothening**:** The connectivity and the distribution of the triangles over the model needed to be improved prior to exporting it. This was done using Remesh wizard tool in the FEA module. This tool allows users to specify the tolerance variation from the original data (Magne 2007). Usually, the mesh geometry display of the object prior to remeshing looks similar to figure 6.8 where the histogram shows the triangular distribution. Triangles closer to the factor of 1.0 on the right end of the histogram are equilateral triangles of the mesh. Values such as edge length, geometrical errors or even number of iterations depend upon various factors such as the size, shape of the model as well as how finely the user wants to refine the model.

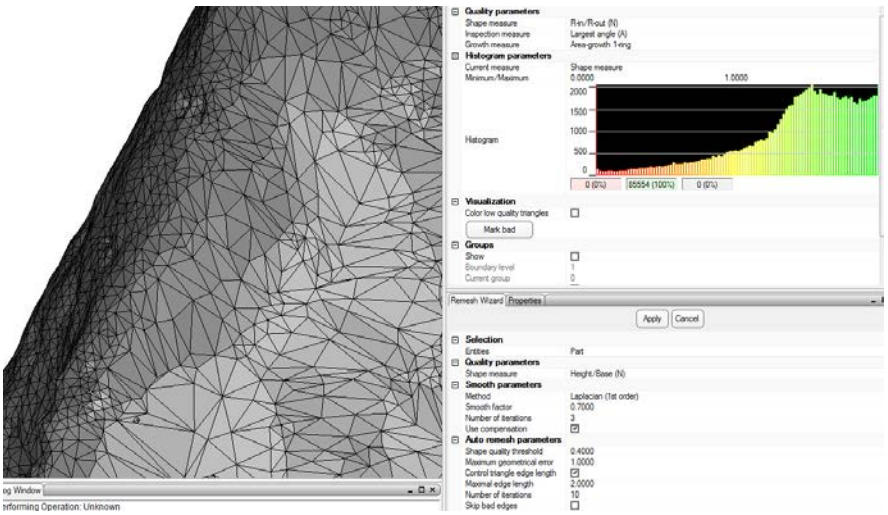

Figure 6.8 Remeshing wizard interface in the FEA module of MIMICS

In this study, maximum geometrical error of 1 mm (with 10 iterations) was applied. The global triangle quality can be visualized via a histogram. Once the remeshing was performed, the histogram distribution and thus the quality of the triangle based on shape measures, inspection measures and growth measures improved (figure 6.9).

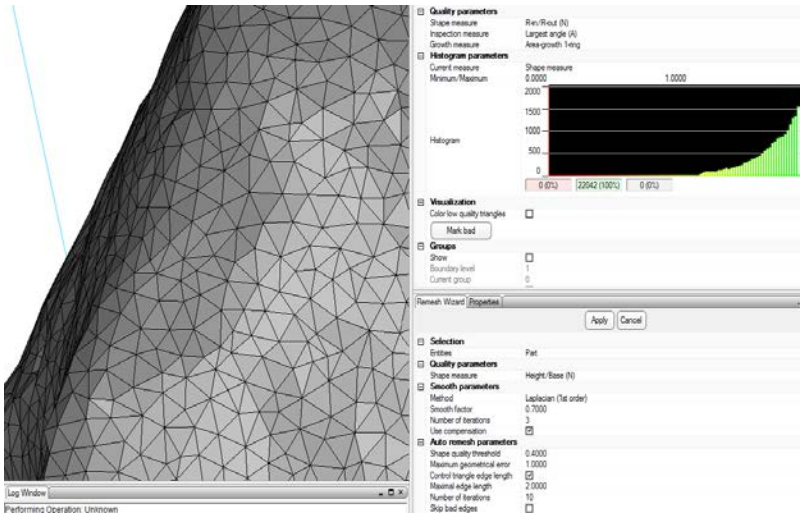

Figure 6.9 Remeshing wizard interface in the FEA module of MIMICS indicating improved model quality

6) Smoothing: The final part of the segmentation process prior to exporting the model was to smoothen it by reducing the noise in the mesh. In this study, Laplacian 1st order basic smoothing algorithm was used over Laplacian 2nd order as although the latter resulted in better looking model, it changed the dimensions of the model by adding extra smoothening effects. Smoothing factor was kept only 0.7 (with 3 iterations) and an example result in shown in figure 6.10. It was observed that smoothing improved the triangle distribution in the histogram. 'Use compensation box' in the menu was always checked to compensate for volume losses.

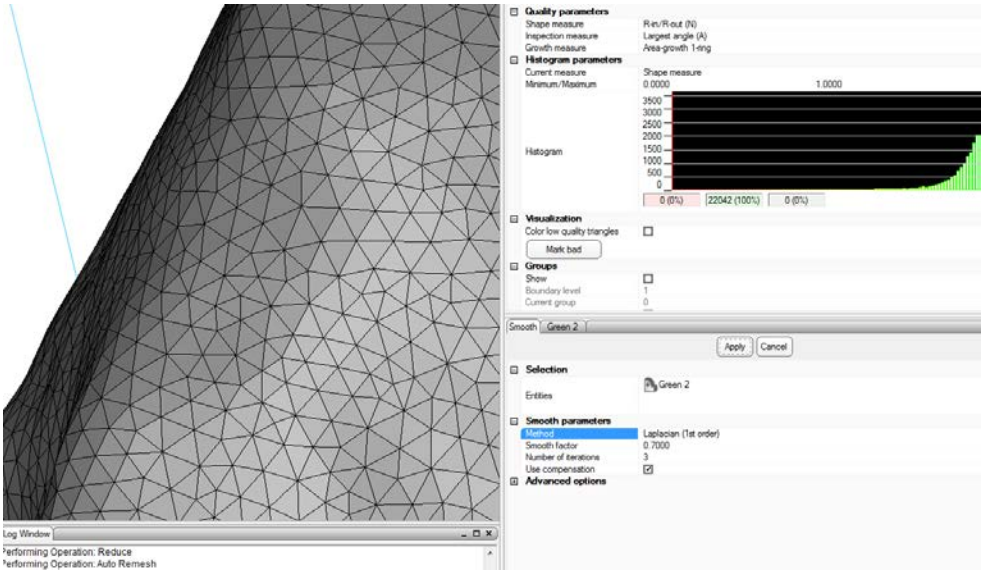

Figure 6.10 Smoothening tool in the FEA module of MIMICS

7) Exporting the model: The ultimate goal of the segmentation was to extract the required information from the CT and MRI scans by selecting the regions of interest and to create 3D models which were to be registered with the 3D laser scans. STL+ module provides interface options to export the model in various formats such as Binary STL (Stereolithography), ASCII STL (American Standard

Code for Information Interchange Stereolithography), DXF (Drawing Interchange Format), etc. In this study '.STL' (binary) file format was preferred so as to match up with laser scans acquired.

6.3 MAKO SURGICAL CORP'S REGISTRATION

As mentioned in the literature review, MAKO Surgical Corps's UKA procedure is termed as MAKOplasty® (Hagag *et al.* 2011). Before undertaking the intra-operative 3D scanning using our 3D laser scanning method, each sample was registered using standard MAKOplasty® registration process. Prior to the experiments, the preoperative image space models were constructed by segmenting the CT of the lateral (un-operated) compartments of all the cadavers. Each segmentation plan was loaded into the MAKO system before starting the session and registration was achieved through a minimally invasive UKA incision. The registration in MAKOplasty® is achieved with ICP based surface matching algorithm where bespoke pointers are used to register cartilage (green) and bone surfaces (blue) separately.

1) First, trackers (marker clusters) were attached to the green and the blue probes, the tibia, the femur, and the robot so each component can be tracked throughout the procedure.
2) Then each tracked component was registered using an infrared camera which stereoscopically detects the trackers. This allows the robot to understand its position relative to the patient.
3) Next step was to attach checkpoints to the femur and the tibia. These points were again registered against the camera using the green and the blue probes.

4) The femoral and the tibial registrations were performed separately but one after another. The system generates around 40 points across the femoral condyles which were acquired by pressing a foot switch. Acquisition is achieved by touching the condylar surface with the end of the probe with its markers facing the camera. This initial rough registration was followed by registering 6 key landmarks points on the condyles again in real-time.

5) Similarly, for tibial registration 40 points indicated roughly by the system (figure 6.11) were registered using the probe and then 6 landmarks points were captured (figure 6.12).

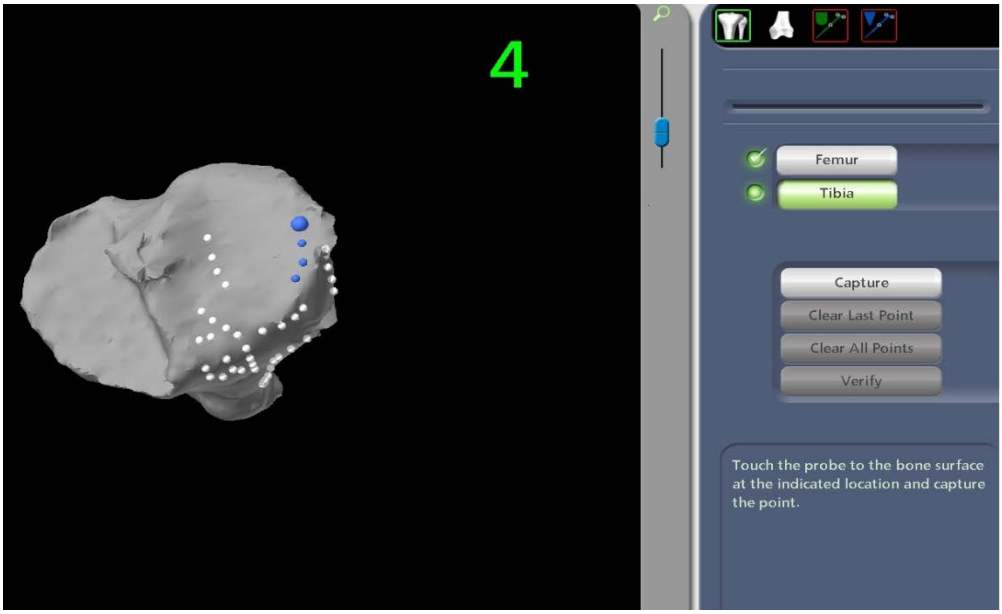

Figure 6.11 MAKO System generated 40 points for lateral tibial registration

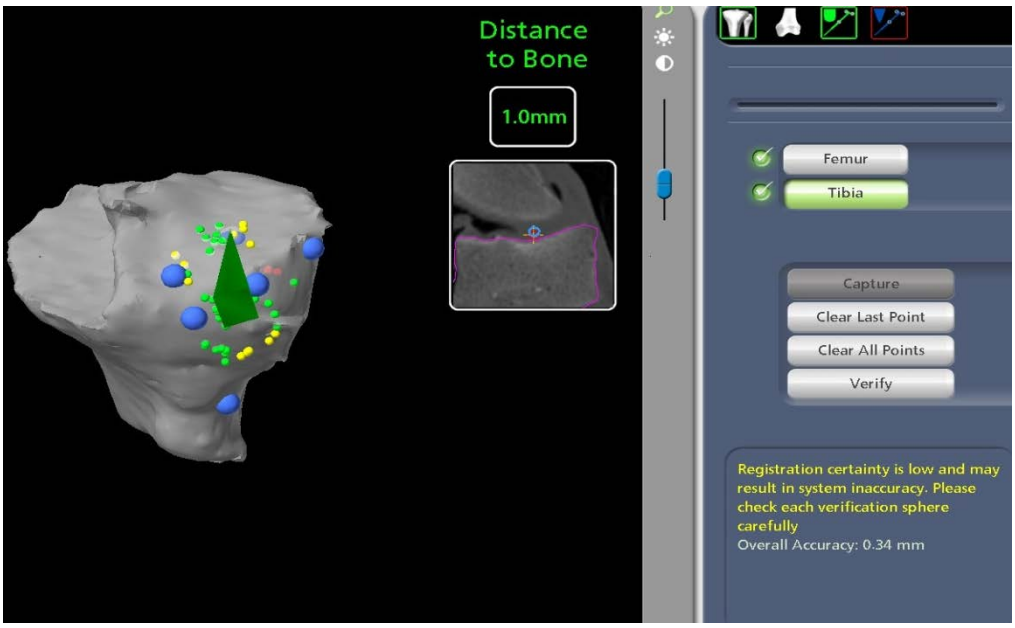

Figure 6.12 MAKO System generated 6 landmark points for lateral tibial registration

6) After the registration, the system displays distances from the end of the probe to the surface of the bone and to the reference point to be captured. Registration can only be achieved if both these values are below 1 mm.
7) Time required to register each bone was noted down.

6.4 LOGISTICS OF THE 3D LASER SCANNING

After achieving MAKOplasty® registration, intra-operative 3D scanning was commenced. The Logistics of the 3D scanning is briefly elaborated in this section. Figure 6.13 and figure 6.14 demonstrate the logistics of the methodology.

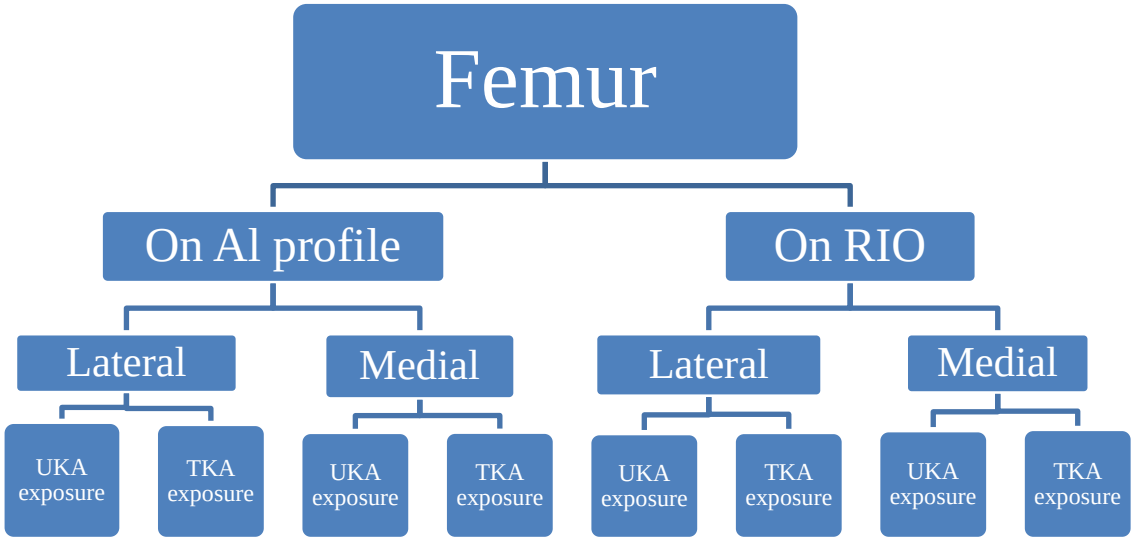

Figure 6.13 Logistics of the intra-operative 3D scanning (of femur)

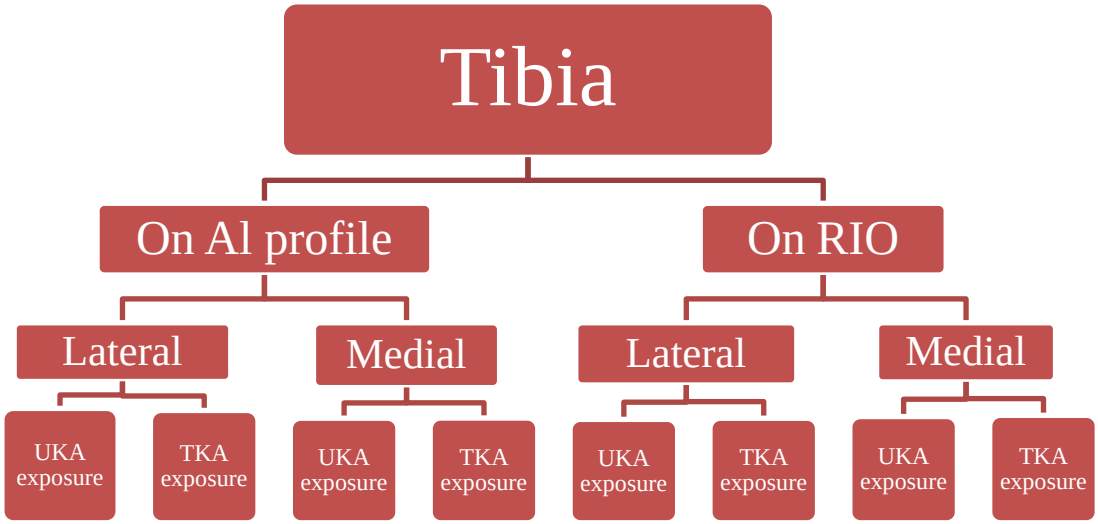

Figure 6.14 Logistics of the intra-operative 3D scanning (of tibia)

1) Intra-operatively, the 3D laser scanner was first calibrated with the scanning modules (motor, laser and camera) mounted on the first setup, the Aluminium extrusion assembly. With this setup, each femoral and tibial condyles (lateral and medial separately) were scanned individually with ten repeats. Each sample was

scanned through a minimally invasive UKA exposure (around 90 mm) in a clinical flexed position, figure 6.15).

Figure 6.15 Incision of around 90 mm. on the medial side of the right knee

2) In the next step, the MAKO RIO arm was calibrated to ensure all the joints of the arm are working accurately. This procedure is also known as “Homing” of the arm. The MAKO arm was placed in the desired position and the emergency brakes were applied to lock all the joints.
3) The scanner was then removed from the Aluminium extrusion assembly and was mounted on the MAKO RIO arm. The scanner was moved and oriented to the desired position by releasing the brakes on the MAKO RIO arm. All the joints were then locked again by pressing the brakes.
4) Next, the camera calibration was performed followed by the laser scanner calibration. Lateral and medial, femoral and tibial condyles with minimally invasive UKA exposure were scanned with this setup providing four groups with ten scans each.
5) In the next stage the joint was exposed completely by making an incision of 150-180 mm (analogous to TKA) in the centre thereby exposing tibial and femoral

condyles completely (figure 6.16). The menisci were completely dissected including some fatty tissues surrounding the joint.

Figure 6.16 Incision of around 160 mm on the left knee joint
Lateral eversion of patella for maximum joint-space exposure (Leopold, 2009)

6) Using the same setup (On RIO) once again ten repeating scans were acquired for medial and lateral compartments of the femoral and the tibial condyles. This order was followed to save the extra time which would have required for recalibrating the scanner.
7) In the final stage, all the scanning components were positioned back on the Aluminium assembly and recalibrated. Again as with step (5) and (6), ten scans were acquired each for exposed femoral and tibial articulating surface with the same TKA exposure.

Thus, each compartment of the articulating surfaces of the femur and the tibia was scanned ten times using two different setups (Aluminium assembly, MAKO RIO arm) and through two different exposures (minimally invasive UKA, exposed TKA), thereby providing 160 scans for each leg (figure 6.13 and figure 6.14). Hence, in total 1600 separate 3D laser scans were acquired in ten sessions (a session each for a

sample) to be surface matched with their corresponding pre-operatively acquired models. Time required to acquire each scans was noted.

6.5 INTRA-OPERATIVE WORKING PROCEDURE

Intra-operatively, the cadaveric legs were placed in a clinical position and were scanned using the modified automated 3D laser scanning method.

6.5.1 Sample Setup

Each cadaveric leg was thawed 48 hours prior to the intra-operative experiments. The bed was covered with the surgical drapes to prevent spillages before placing the leg. All the donated samples had their structure from hemi-pelvis to toe. They were attached to the bed in a clinical knee flexed position using straps around the hemi-pelvis as shown in figure 6.17. The foot was attached to a sliding foot holder to allow variable knee flexion.

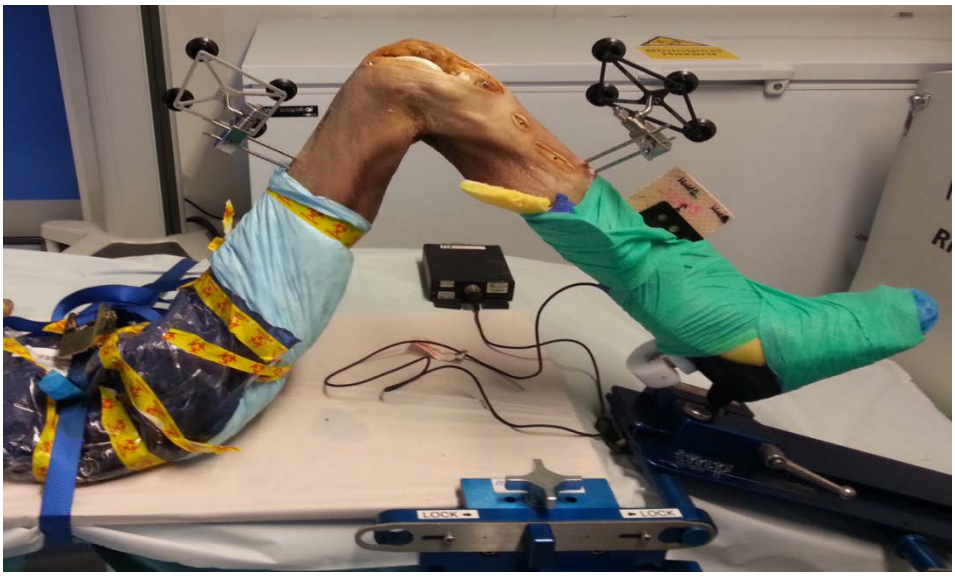

Figure 6.17 Sample cadaver set up on the bed with the attached arrays for MAKO registration

Operated medial compartments were already sutured and closed. As explained in section 6.4 (Logistics of scanning) an incision of 80-100 mm was made on each lateral compartment of the knee joint to mimic the UKA exposure size followed by a TKA exposure of 150-180 mm.

6.5.2 Scanning

Before proceeding to the 3D scanning, the lights directly overhead over the area being scanned were switched off. This routine was also checked by keeping the lights ON but by covering the scanning area, camera and the laser source with a non-reflective cloth. In both the methods, the process of scanning was unaffected. The optimization of the illumination was done in order to avoid any stray light or external interference and noise in the final results. Articulating surfaces of the joint (tibia and femur) were mopped with gauze to avoid any reflectance that may arise due to the body fluids. The skin around the joint was stretched using the retractors to allow the camera for maximum area exposure of the articulating surfaces of the joint and the scanning was begun.

As explained in section 5.5, the camera calibration and the reference scanning was first done to calibrate the scanner followed by the actual scanning.

1) Camera calibration

The calibration planes were kept exactly at right angles to each other. The camera was placed facing the planes. Camera parameters such as Auto Focus, Auto white balance and Auto brightness were optimized to the illumination in the room before the calibration. The camera calibration results were stored in the file calibpoints.dat.

2) Reference scanning

A stated in the previous chapter (sub-section 5.5.2), the modified automated system comprises of camera calibration followed by the reference scanning. Following the camera calibration, the position of the calibration planes and the camera parameters were kept unchanged. A reference scan of the calibration plane was acquired and stored in the software in an internal file called “laser.xml”. The reference scan can be acquired by pressing the proper switches on the user interface of the scanner and the appropriate commands on the computer screen. A step by step procedure has already been explained in the sub-section 5.5.2. At the end of the reference scan, a virtual 3D image of the calibration planes is stored in the software which allows users to scan the object without the use of the planes.

3) 3D scanning

Once the scanner was calibrated, the calibration planes were removed and scanner was manipulated towards the leg to scan tibial and femoral condyles. Extreme precaution was taken while assembling the scanning modules on the positioning setups, as a slight movement between them could cause large errors in the scans. The 3D scans were acquired similarly as the reference scanning using the scanner user interface and the commands on the software user interface. The scanning was performed with respect to the order specified in the section 6.4, logistics of the scanning. The step by step procedure as explained in the sub-section 5.5.3 (B) was followed and the scans were stored in the .STL format on the computer hard-drive. Furthermore, true colours for few scans were acquired in the ambient light conditions making sure that the object had not moved from the last scan.

6.6 DATA ANALYSIS

All the scans were post processed and cleaned using a robust digital image software package, Geomagic Qualify® 12. The software is certified and has received very high accuracy certification from widely accepted organisations such as Physikalisch-Technische Bundesanstalt (PTB) institute and National Institute of Standards and Technology (NIST) in the area of least squared surface and curve fitting (Accurate up to 0.1 µm in length and 0.1" [1/36,000 of a degree] in angle) (Geomagic.com, 2011).

It provides comprehensive 3D metrology solution to complex 3D comparisons, first-article inspection and product inspection with high accuracy and speed. It also provides automatic algorithms for shape correction such as filling up holes, removing dents, spikes, non-manifold edges; but it should be noted that these options only improve connection topology and do not change the position of the points which are already present (Popat *et al.* 2008). In this study no automatic algorithm was applied and spurious edges and surfaces captured while scanning the knee joints were deleted manually.

6.6.1 Alignment Analysis

Once the scans were cleaned for each data set, every scan was first registered and then aligned using a best fit alignment algorithm with the corresponding pre-operatively (CT/MRI) acquired 3D model. An example process for a left lateral tibial cartilage model is elaborated here. The following steps were applied.

A. Manual Registration

1) MRI or CT generated model (MRI for this particular example) was set as a reference model whereas the 3D laser scan was designated as the test frame.

2) Reference and the test models were first registered using the Manual Registration option where three to nine operator-chosen common points are selected. The models were aligned based on the selection of overlapping section of the objects. Prominent points such as ones with high curvatures; condylar centres, etc. were selected which were spread all over the test surface as shown in figure 6.18**.**

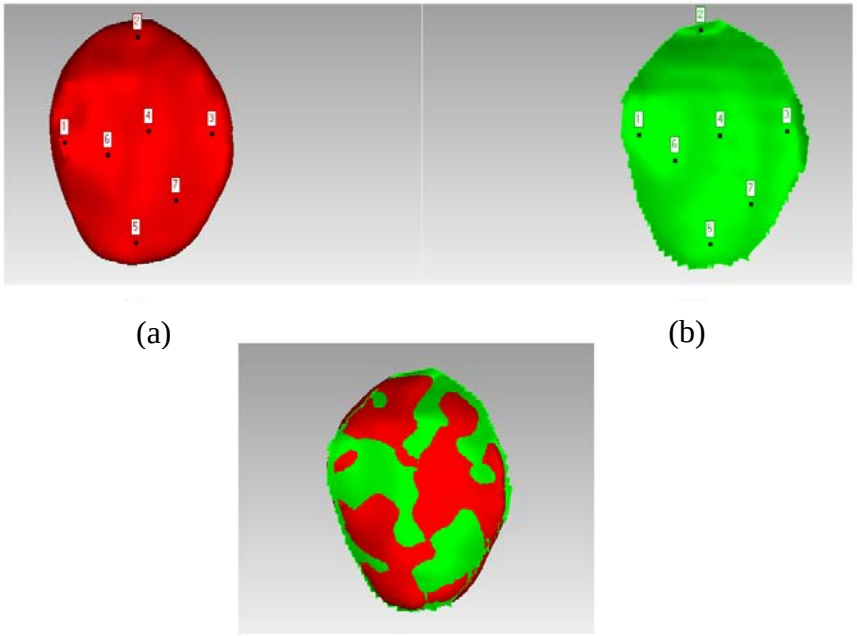

(a) (b)

(c)

Figure 6.18 Manual registration by selecting random points over the left lateral tibial surface

(a): MRI generated 3D model of the articular cartilage (in red), set as a reference model. (b): Corresponding 3D laser scan of the same cartilage acquired intra-operatively, set as a test model. (c): Rough manual registration between two surfaces

3) This is the type of surface (point based registration or free-form surface matching) registration that works closely on the Iterative Closet Point (ICP) algorithm where

the two surfaces are aligned with respect to the closest points leading to the segments and the triangles (Besl and Mackay 1992, Audette *et al.* 2000, Jasson *et al.* 2006; Geomagic, 2013).

4) After manual registration, global registration was performed where the alignment between the models is automatically fine-tuned using ICP algorithm based on their spatial position. The main difference in the manual registration and the global registration is in the former the reference scan is kept still and the test scan is rotated and translated to align with the reference scan whereas in the global registration all the scans are simultaneously shifted together. The number of points used for the registration can be chosen depending upon the size of the model. Using maximum number of points would increase the accuracy of the registration.

B. Error Evaluation

Once the models were roughly registered, the next stage was to align the test model with the reference model using a 'best fit' type of minimisation.

1) The software enables users to set a tolerance level of error which controls the average tolerance at which the best fit goes from its gross alignment algorithm to the fine adjustment algorithm (Geomagic, 2013).
2) However, as the objects were aligned already using manual and global registration, only fine adjustment was performed using best fit alignment option. This provided better alignment and was also a quicker option.
3) During this process, the test object is sampled based on the size specified and the closest corresponding points are computed on the reference model. Alignment statistics provides an average absolute error (AAE) between two models. Each

deviation between the two closest points is a Euclidean distance in a three dimensional space. The distances between the sample pairs are minimized over all the rigid motions that could realign the two objects.

For example, if the point on the reference model R_1 (r_x, r_y, r_z) is the closest computed point for the point T_1 (t_x, t_y, t_z) on the test model, then the deviation between them is calculated by the equation 6.1.

$$d_1(R_1, T_1) = \sqrt{((r_x - t_x)^2 + \left(r_y - t_y\right)^2 + (r_z - t_z)^2)} \quad (6.1)$$

AAE is a ratio of the sum of all the deviations ($d_1 \ldots\ldots d_n$) and the total number of points (*n=total number of points of the test model*) used for matching.

$$AAE = \frac{d_1 + d_2 \ldots\ldots\ldots + d_n}{n} \quad (6.2)$$

4) Initially, the closest points on the reference surface are computed for each point on the test surface and a new transformation matrix is established. This process is repeated in an iterative manner similar to the ICP algorithm suggested by Besl and Mackay (Besl and Mackay 1992, Geomagic, 2013).

C. 3D Comparison

1) Once the surfaces were registered, 3D comparison was performed in order to inspect the deviations between the surfaces of the reference and the test scan.
2) A three dimensional color-coded mapping of the differences between the surface models was acquired to visualise the spatial distribution of the errors. Colour-coded map of the example of tibial cartilage used earlier is shown in figure 6.19, figure 6.20 and figure 6.21.

3) The colour map on the left indicates the deviation (AAE) between the reference model and the test model in millimetres representing the range for each specific colour. After the alignment, when the point on the aligned test model falls above the corresponding point on the reference model in the depth axis of the 3D space, the deviation is reported as the positive deviation. Similarly, when the point on the test model is below the point on the reference model, the deviation is negative.

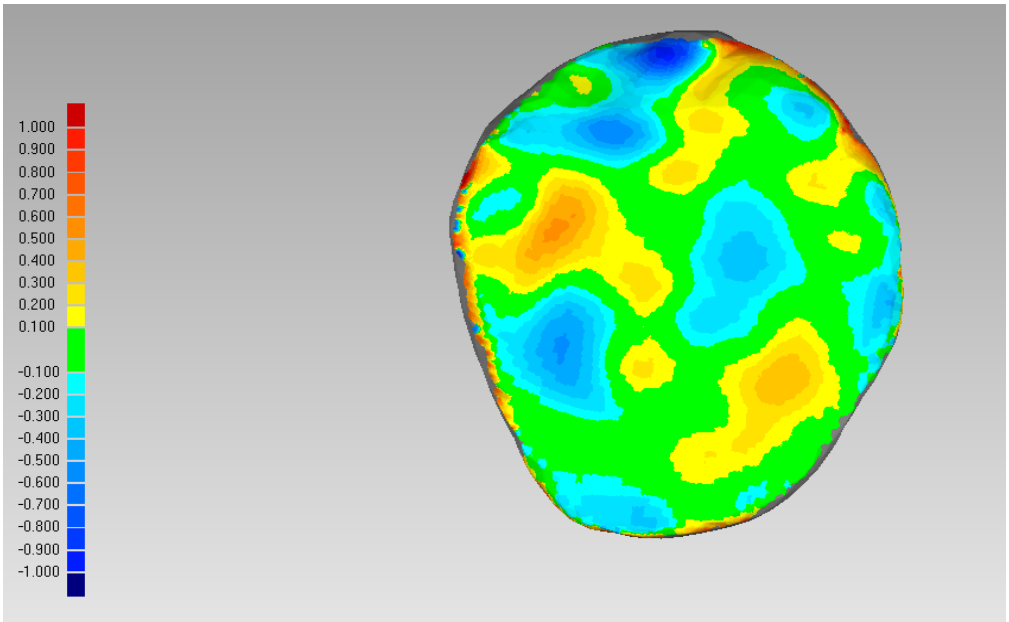

Figure 6.19 Top view of the colour deviation map for the spatial distribution of the deviations between the reference (MRI) and the test (laser) model of an example left tibial lateral cartilage

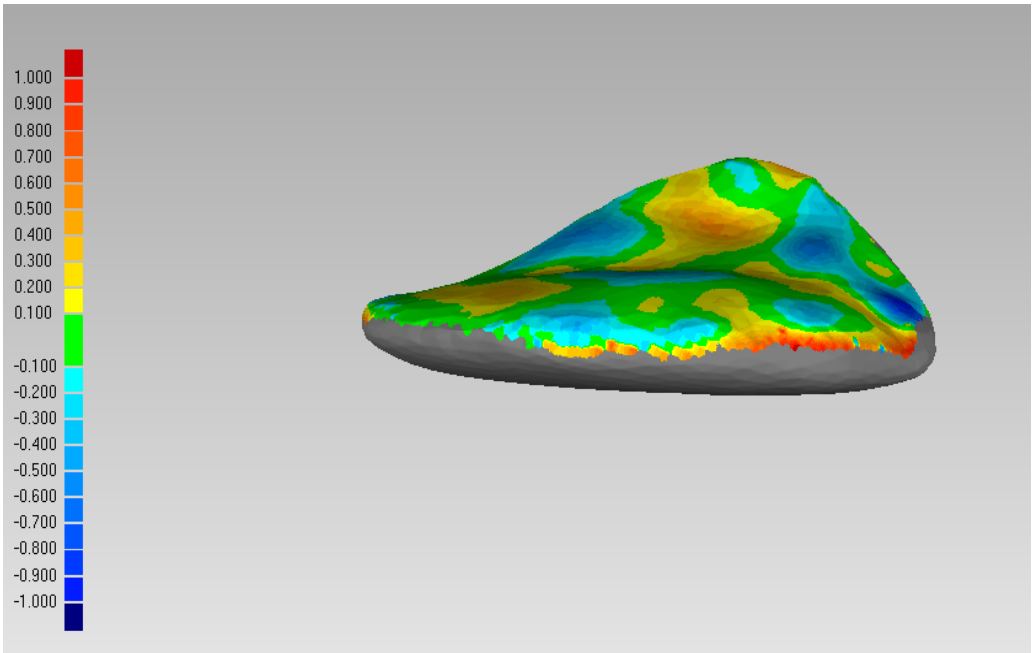

Figure 6.20 Right isometric view of the colour deviation map for the spatial distribution of the deviations between the reference (MRI) and the test (laser) model of an example left tibial lateral cartilage

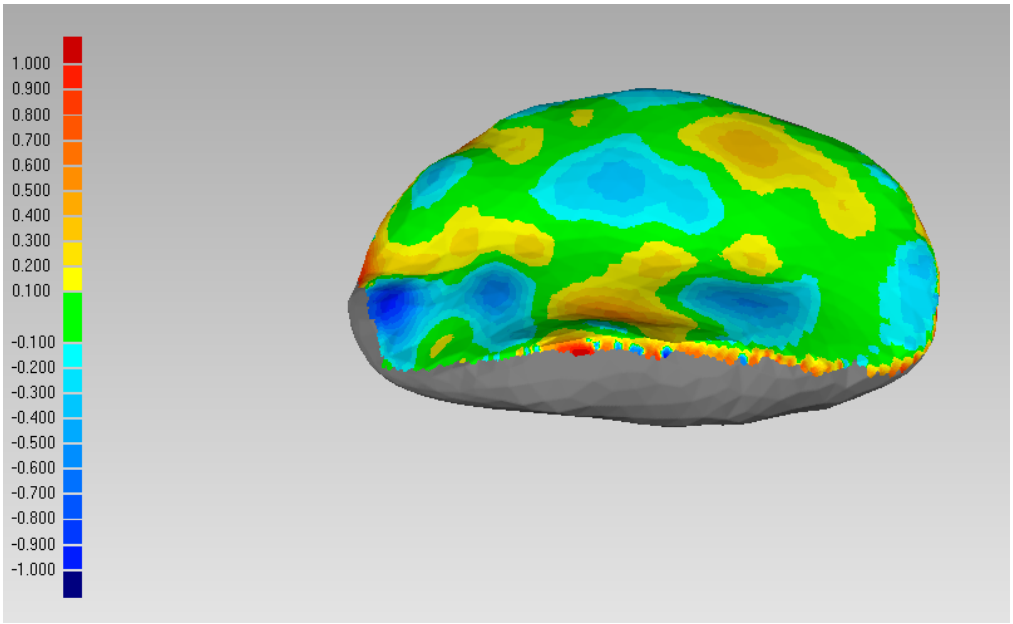

Figure 6.21 Left isometric view of the colour deviation map for the spatial distribution of the deviations between the reference (MRI) and the test (laser) model of an example left tibial lateral cartilage

D. Reports

1) Having done the alignment and comparison, the final step was to extract the analysed data for further investigation.
2) A customized report of the inspected data can be generated in Geomagic Qualify® which gives the elaborated results for each point pair at a time.
3) Additionally, the reports can be generated visually as alone in a 3D pdf format, which can allow users to inspect the fit of the models spatially.

Alignment statistics computed for the left lateral tibial cartilage example are shown in table 6.4.

Table 6.4 Alignment statistics for the example tibial cartilage

Parameter	**Units (mm)**
Average absolute error (AAE)	0.17
Standard Deviation of absolute error (SD_{AE})	0.25
Maximum deviations (d_{max})	+1.51, -0.97

Throughout the alignment process, the reference model is kept still and the test model is rotated to find the best fit between the two models. As stated earlier, AAE is a ratio of the summation of all the absolute deviations divided by the number of points used for pair matching. The standard deviation is a measure of the dispersion of the AAE (deviation) values from their mean. A low standard deviation indicates that majority of the deviations are close to the mean deviation. Figure 6.22 illustrates frequency histogram of the standard deviation and figure 6.23 shows the normal distribution (Gaussian bell) curve overlaid on the histogram.

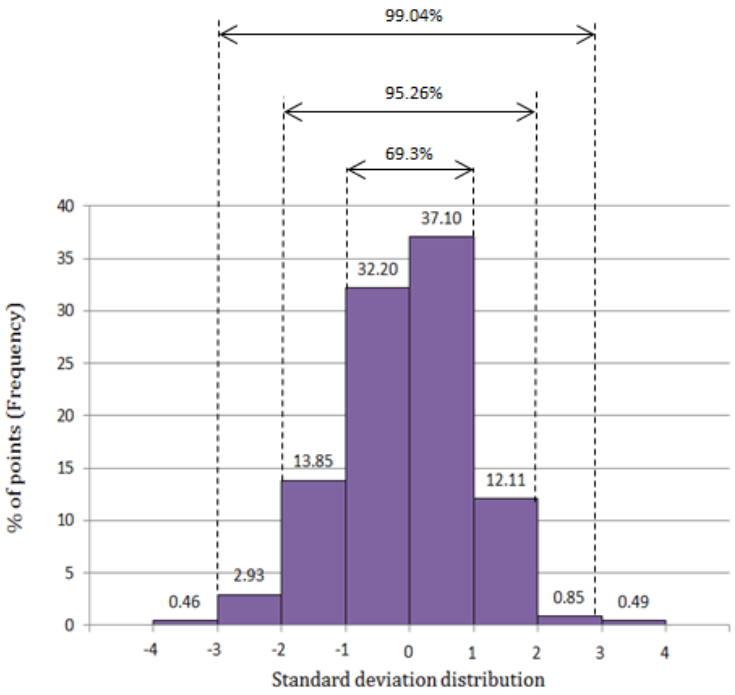

Figure 6.22 Standard deviation distribution frequency histogram

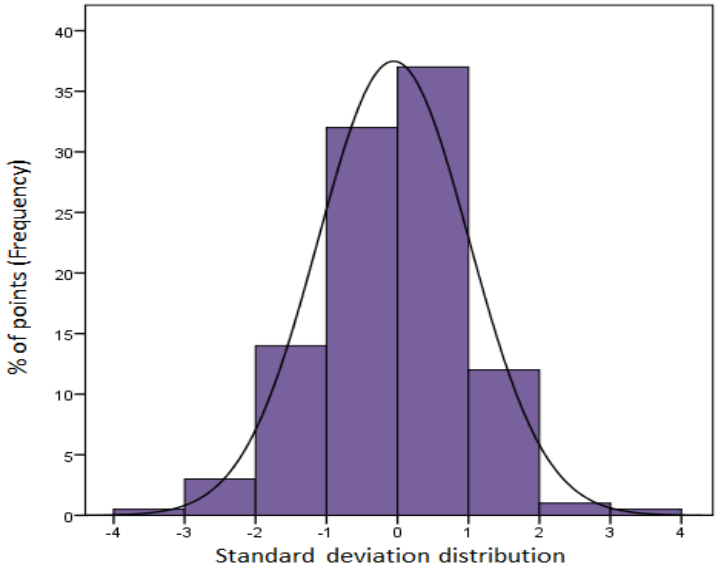

Figure 6.23 Standard deviation distribution frequency histogram with the overlaid Gaussian bell curve

Figure 6.22 shows that 69.3% of the values fall between ± one standard deviation from the mean. Furthermore, 95.26% of the values are between ± two

standard deviation and 99.04% of the values are between ± three standard deviation which indicates the deviations are approximately normally distributed. The maximum positive and negative deviations are the furthest points computed between two models. Table 6.5 illustrates the deviation distribution of all the point pairs for the given example.

Table 6.5 Deviation distribution between point pairs of MRI and laser scan for example model

Range (Minimum) mm	**Range (Maximum) mm**	**Number of points**	**% of points**
<-1	-0.9	5	0.13
-0.9	-0.8	13	0.34
-0.8	-0.7	15	0.40
-0.7	-0.6	15	0.40
-0.6	-0.5	32	0.85
-0.5	-0.4	87	2.30
-0.4	-0.3	159	4.21
-0.3	-0.2	371	9.82
-0.2	-0.1	461	12.21
-0.1	0.1	1408	37.28
0.1	0.2	598	15.83
0.2	0.3	289	7.65
0.3	0.4	128	3.39
0.4	0.5	80	2.12
0.5	0.6	45	1.19
0.6	0.7	21	0.56
0.7	0.8	20	0.53
0.8	0.9	15	0.40
0.9	>1	8	0.21

Figure 6.24 shows the deviation distribution frequency histogram. X-axis indicates maximum and minimum range of the deviations whereas on the Y-axis percentage frequency of the point within a particular range is plotted. This relates to the colour-coded map shown previously in figure 6.19, figure 6.20 and figure 6.21.

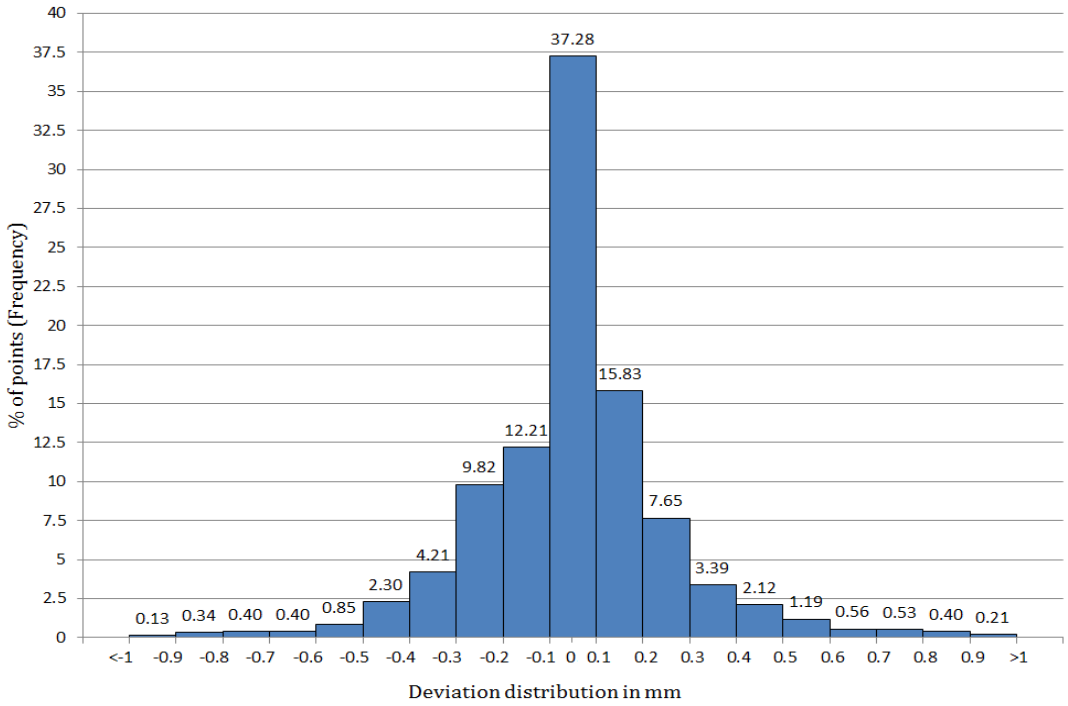

Figure 6.24 Deviation distribution histogram between point pairs of MRI and laser scan for example model

Deviation in mm is plotted against the percentage of points within the range of deviations

In the colour maps, maximum and minimum nominal values (±0.1) are shown by the green colour which occupies majority of the central area of the model. Figure 6.24 and table 6.5 indicate that more than 37% of the deviations were in the range of ±0.1 mm. In addition, more than 94% of the deviations were between ±0.5 mm. Majority of the higher deviations were seen on the peripheral region of the condyles (figure 6.19, figure 6.20 and figure 6.21). This was observed in all the 3D

comparisons. This is suspected as a result of the viewing direction of the detector camera with respect to the articulating surface being scanned. This effect is explained in detail in Chapter 8, sub-section 8.2.2 A. In the rest of majority of the scans, the AAE between the surfaces was less than 1mm. Having established the proof of concept, a more extensive experiment was undertaken.

Each femoral and tibial compartment of each sample was scanned ten times using two different positioners (Aluminium assembly and MAKO RIO) and with two different exposures (UKA and TKA), thus providing 1600 test models. All the test models were registered, aligned and compared with their corresponding reference model. A detailed inspection analysis is elaborated in the Chapter 7 and Chapter 8.

6.6.2 Statistical Analysis

For every scan (1600 in total), average absolute error (AAE), standard deviation of the absolute error (SD_{AE}) and maximum deviations ($\pm d_{max}$) were reported. In general, there were two factors which could affect the accuracy of every scan namely, the exposures (UKA, TKA) and the positioner setup (Aluminium assembly, MAKO RIO). After analysing all the scans for the first set of a sample, it was suspected that discrepancies between the laser scans and the CT/MRI models were higher on the femoral surfaces than on the tibial surfaces. Besides, each femoral and tibial surfaces (lateral and medial separately) were scanned separately. Hence, to investigate whether the type of the surfaces produces any significant effect on the AAE between the laser and CT/MRI models, a third variable (type of the surface: tibia and femur) was introduced for further analysis. Hence, in total there were eight possible combinations in which the scans were acquired.

1. Al extrusion with UKA exposure of Tibial surface
2. RIO with UKA exposure of Tibial surface
3. Al extrusion with TKA exposure of Tibial surface
4. RIO with TKA exposure of Tibial surface
5. Al extrusion with UKA exposure of Femoral surface
6. RIO with UKA exposure of Femoral surface
7. Al extrusion with TKA exposure of Femoral surface
8. RIO with TKA exposure of Femoral surface

The null hypotheses were set as follows:

$H0_1$: 'Setup' effect is not significant

$H0_2$: 'Exposure' effect is not significant

H03: 'Surface' effect is not significant

$H0_4$: Two way 'Interaction' effect is not present between the setup and the exposure

$H0_5$: Two way 'Interaction' effect is not present between the setup and the surface

$H0_6$: Two way 'Interaction' effect is not present between the exposure and the surface

$H0_7$: Three way 'Interaction' effect is not present between the setup, the exposure and the surface.

The AAE here is the dependent variable whereas the setup, the exposure and the surface are the independent variables. A Repeated measures ANOVA test was

performed using a standard statistical software package, SPSS (developed by IBM Corporation, NY, USA) to investigate the effects of the independent variables on the AAE. Significance of the independent variables was tested at α=0.05 level. The results are reported in the Chapter 7. Additionally, to support the ANOVA analysis a post statistical analysis was performed in the SPSS software package. Individual effects of the independent variables on the AAE were assessed separately using a paired t-test at α=0.05 level. The interpretations of the outcomes are discussed in the Chapter 8.

6.7 VALIDITY STUDY

An additional validity study was conducted for every cadaveric sample which assessed the distance measurements acquired by the laser scanner against the direct distance measurements acquired using a standard digital vernier calliper. This approach is widely accepted in research and industry to assess the technical performance of 3D imaging system for geometric accuracy (Moss *et al.*, 1989; Motohashi and Kurdoa, 1999; Bell *et al.*, 2003; Zilberman *et al.*, 2003; Winder *et al.*, 2008; Nouri *et al.*, 2009; Thiruvenkatachari *et al.*, 2009; El-Katatny *et al.*, 2010; Fleming *et al.*, 2011).

6.7.1 Design of experiment

As stated previously, 10 cadaveric knee joint samples were employed in the study. The tibial and the femoral articulating condyles were treated as a separate surface thereby providing 20 set of surfaces. On each surface, 7 M2 screws were inserted in a random pattern but with a good spread as shown in figure 6.25(a). The

distances between the centres of the each screw with the centres of every other screw were measured thus providing 21 different distance measurements on each surface as shown in figure 6.25(b).

1-2 2-3 3-4 4-5 5-6 6-7
1-3 2-4 3-5 4-6 5-7
1-4 2-5 3-6 4-7
1-5 2-6 3-7
1-6 2-7
1-7

(a) (b)

Figure 6.25 Distance measurements between the screw markers on the tibial condyle (a): Placement of seven screws over the surface (b): Total (21) number of measurements computed between every pair of the points.

First, all the distances were measured using the digital vernier calliper (figure 6.26). In the next stage, 3D laser scans of the surfaces with the inserted markers were acquired with 10 repeats using the developed laser scanning system. All the scans were then imported to Geomagic Qualify® 12 software package for further analysis. The distances between the pairs of screws on every scan were then measured using the distance calculation tool of the software package. As explained in the previous section (equation 6.1), the distance calculations in Geomagic Qualify® are computed using Euclidean metric distance calculation in the 3D space. In addition to the Euclidean distances between two points (X_1,Y_1,Z_1) and (X_2,Y_2,Z_2), absolute distances

between the Cartesian co-ordinates of two points [(X_1-X_2), (Y_1- Y_2) and (Z_1-Z_2)] are provided on the software screen (figure 6.27).

Figure 6.26 Direct distance measurement acquired using digital vernier calliper on the tibial condyle of the cadaveric knee joint

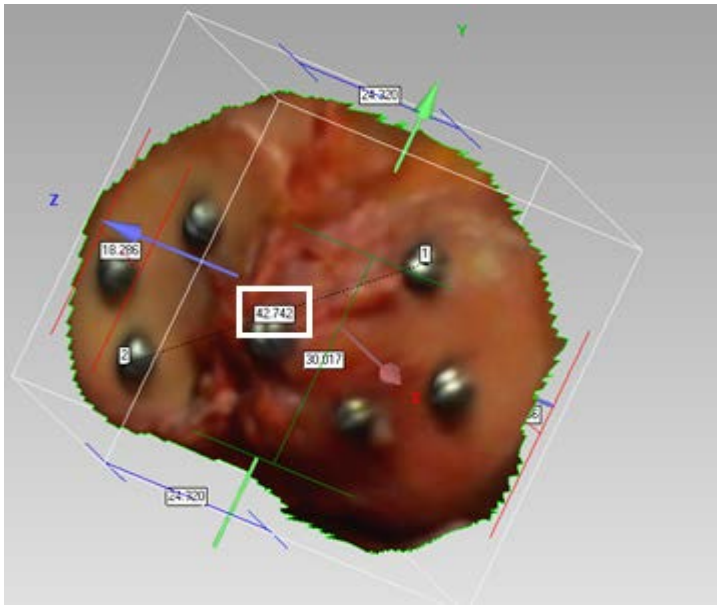

Figure 6.27 Distance measurement (in the white box) acquired on the corresponding digitised 3D laser scan and formulated using Geomagic Qualify® on the tibial condyle of the cadaveric knee joint

So 21 measurements for each of the 20 surfaces were calculated, thereby providing 21*20 = 420 different measurements. For every surface, ten 3D laser scans were acquired. Thus in total 4200 distance measurements acquired from laser scans were compared with the corresponding 420 digital vernier calliper measurements.

6.7.2 Data Analysis

For every set of measurement (i.e. distance measured by the digital vernier calliper and the 3D laser scan for every pair of the screws), an absolute error (AE) and absolute percent error (APE) were computed followed by average absolute error (AAE) and average absolute percentage error (AAPE, also known as MAPE, mean absolute percentage error). The absolute error is the absolute difference between the two measurements. Thus for example, if the digital calliper measured the reading as 15 mm and same distance appeared on the laser scan was measured 15.4 mm, then the absolute error (AE) will be; |(15-15.4)| = 0.4 mm. The absolute percent error (APE) expresses accuracy as percentage. If M_V is the measurement shown by the digital vernier calliper and M_L is a measurement calculated on the laser scan then the APE can be defined as:

$$APE = \frac{M_V - M_L}{M_V} * 100 \qquad \text{Equation 6.3}$$

The null hypothesis was set as there is no significant difference in the measurements acquired using either technique. If μ_v is the mean measurement for the vernier calliper and μ_L is mean measurement recorded on the laser scan, then

$$H0: \mu_v = \mu_L$$

$$H1: \mu_v \neq \mu_L$$

A two sample (independent t-test) student t-test was performed to check if any statistical significance is present between them (Bell *et al.*, 2003). Results for this validity study are reported in the next chapter, section 7.2.

CHAPTER 7. RESULTS

In order to achieve the objectives of the study, various types of experiments were designed and conducted (Chapter 6, Methodology) throughout the development of the research program. The key findings of these studies are reported in this chapter. The framework of this section is divided into two sub-sections. The first comprising the major developmental experiments and the second depicting a final validity study. In the major experiments, surface geometries of the tibio-femoral joints were scanned using standard pre-operative MRI/CT technology followed by intra-operative 3D laser scanning. Each laser scan was then compared with the corresponding reference model from MRI/CT to evaluate the average deviation between the two models. The outcomes of this sub-section are divided into four different groups each depicting different surface matching: 1) tibial cartilage; 2) femoral cartilage; 3) tibial bone; and 4) femoral bone. For every group, a single scan comparison example is explained in detail with its deviation distribution, standard deviation distribution and spatial distribution of the deviations in a colour coded pattern. This is followed by a summary table of all the samples for that specific group.

To analyse the trends in Average Absolute Error (AAE) between comparison groups, a careful statistical analysis was performed. Primarily, the experimental designs consisted of one dependent variable i.e. AAE and three independent variables: 1) Type of setup (Aluminium extrusion, RIO); 2) Type of exposure (UKA, TKA); and 3) Type of surface (Tibia, Femur) each with two levels. A three way repeated measures ANOVA was performed for cartilage and then separately for bone

surfaces to understand if any of the independent variables (alone or with the combination of other independent variables) affected AAE significantly. Main effects and the interaction effects of the independent variables are presented using profile plots. Additionally, where indicated by repeated measures ANOVA, individual effects of each variable pair on AAE were tested separately using paired t-test which is illustrated using box and whisker plots and error bars.

The second section of this chapter includes the findings of the validation experiment entailing fixed distance measurement comparisons between vernier calliper data and digitised 3D laser model data. AAE (average absolute error) and AAPE (average absolute percentage error) for the laser readings were calculated against the corresponding reference vernier callipers measurements. A single example of measurements acquired on one surface is reported in this sub-section in full using bar graph and error bars which is followed by a summary table of all the surfaces.

7.1 CONCURRENT VALIDITY STUDY 1

As explained in the previous chapter, intra-operatively acquired laser scans were registered with the pre-operatively acquired models (segmented using MRI/CT scans) using Geomagic Qualify® 12, a digital image software package. The results are grouped into 4 sets.

7.1.1 Reference-Test model analysis

A. Tibial Cartilage Scanning

The following example is of the right tibial lateral cartilage. The test (laser) scan was acquired using Aluminium extrusion setup and with UKA exposure. The

test model was then registered with the reference model (MRI) and the results are shown in table 7.1.

Table 7.1 Alignment statistics between reference (MRI) and test (laser) models for an example right tibial lateral cartilage.

AAE; average absolute error between two models, SD_{AE}; standard deviation of the AAE, $+d_{max}$ and $-d_{max}$; maximum positive and negative deviations respectively

Parameter	Units (mm)
AAE	0.20
SD_{AE}	0.27
$+d_{max}$	1.31
$-d_{max}$	-1.24

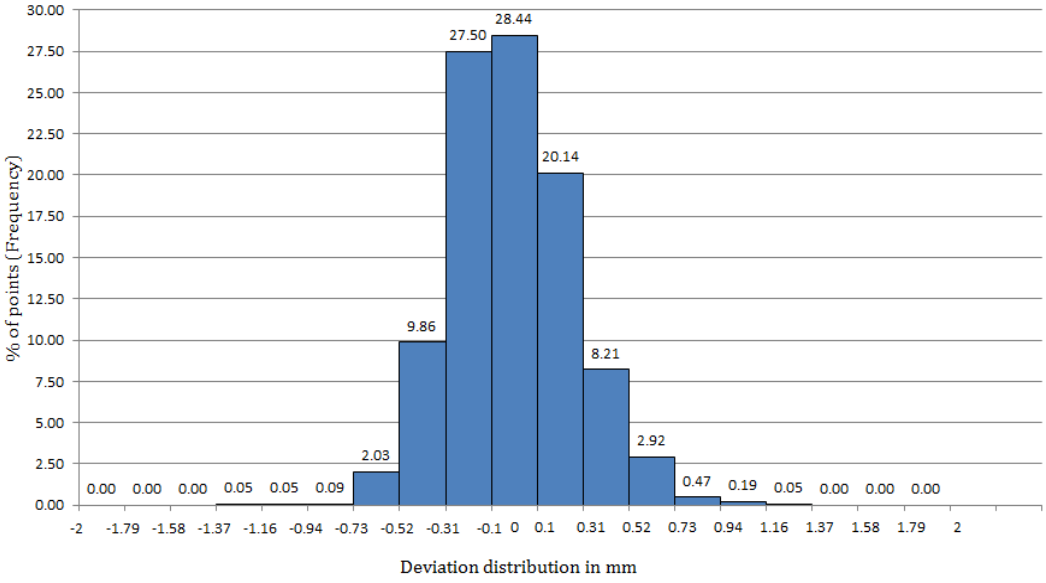

Figure 7.1 Deviation distribution between reference (MRI) and test (laser) model of an example right tibial lateral cartilage

Deviation in mm is plotted against the percentage of points within the range of deviations

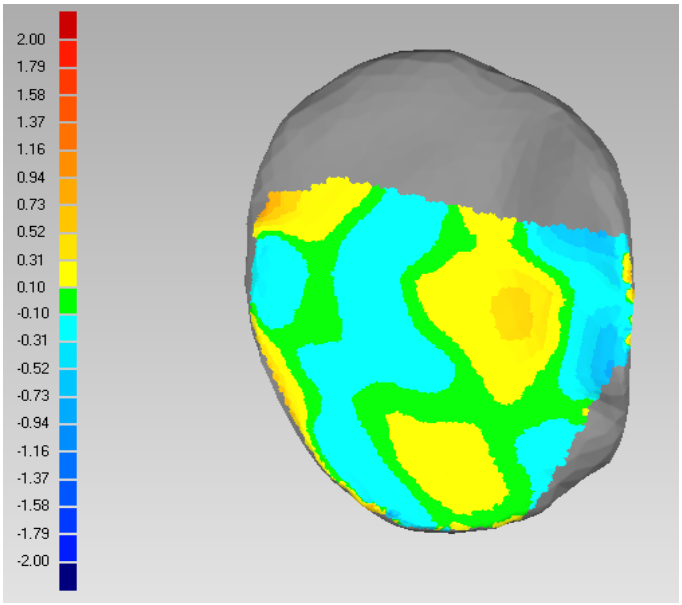

Figure 7.2 Top view of the colour deviation map for the spatial distribution of the deviations between the reference (MRI) and the test (laser) model of an example right tibial lateral cartilage

The posterior region is clipped as the laser scan was acquired with a minimal exposure (90 mm, mimicking UKA). Note: Errors in excess of 1 mm are only found at the scan periphery

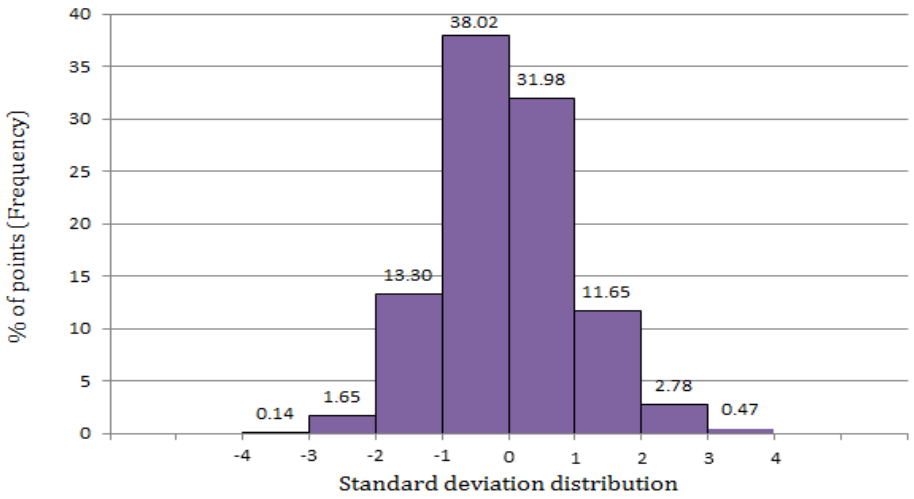

Figure 7.3 Standard deviation distribution between reference (MRI) and test (laser) model of an example right tibial lateral cartilage

Standard deviation distribution is plotted against the percentage of points

Table 7.2 Summary of the alignment statistics between reference (MRI) and test (laser) models of tibial cartilaginous surface of all the samples

AAE; average absolute error between the models, SD_{AE}; standard deviation of the AAE, $+d_{max}$ and $-d_{max}$; maximum positive and negative deviations respectively. Average and standard deviation of all the parameters is shown at the bottom of the table. Note: d_{max} values consistently related to the periphery of the scans.

	UKA Exposure								**TKA Exposure**							
	On Al Extrusion				On RIO				On Al Extrusion				On RIO			
Samples	AAE (mm)	SD_{AE} (mm)	d_{max} (mm)		AAE (mm)	SD_{AE} (mm)	d_{max} (mm)		AAE (mm)	SD_{AE} (mm)	d_{max} (mm)		AAE (mm)	SD_{AE} (mm)	d_{max} (mm)	
			+	-			+	-			+	-			+	-
1	0.21	0.31	1.44	-1.40	0.21	0.37	1.59	-1.66	0.28	0.42	1.82	-1.57	0.36	0.51	1.80	-1.71
2	0.25	0.37	1.24	-1.34	0.24	0.33	1.23	-0.81	0.36	0.52	1.79	-1.71	0.31	0.47	1.72	-1.66
3	0.21	0.39	1.41	-1.51	0.22	0.40	1.46	-1.50	0.29	0.47	1.76	-1.81	0.38	0.57	1.85	-1.91
4	0.16	0.23	1.34	-1.15	0.17	0.24	1.52	-1.33	0.19	0.28	1.50	-1.33	0.20	0.30	1.63	-1.48
5	0.17	0.28	1.29	-1.23	0.17	0.34	1.18	-1.42	0.18	0.28	1.33	-1.44	0.21	0.29	1.33	-1.18
6	0.18	0.37	1.23	-1.66	0.17	0.35	1.55	-1.42	0.25	0.46	1.64	-1.60	0.27	0.48	1.81	-1.70
7	0.16	0.24	1.21	-1.13	0.17	0.24	1.21	-0.90	0.22	0.33	1.69	-1.51	0.24	0.34	1.63	-1.25
8	0.19	0.25	1.20	-0.65	0.15	0.22	1.10	-0.64	0.28	0.38	1.52	-1.23	0.29	0.39	1.48	-1.25
9	0.18	0.39	1.56	-1.25	0.23	0.32	1.61	-1.49	0.23	0.33	1.88	-1.58	0.17	0.22	1.00	-0.88
10	0.15	0.22	1.23	-1.13	0.16	0.23	1.11	-0.94	0.22	0.31	1.62	-1.41	0.20	0.31	1.72	-1.51
11	0.21	0.26	1.36	-1.09	0.23	0.39	1.51	-1.47	0.27	0.38	1.63	-1.45	0.29	0.42	1.71	-1.59
Average	0.19	0.30	1.32	-1.23	0.19	0.31	1.37	-1.23	0.25	0.38	1.65	-1.51	0.26	0.39	1.61	-1.46
SD	0.03	0.07	0.11	0.26	0.03	0.07	0.20	0.34	0.05	0.08	0.16	0.17	0.07	0.11	0.25	0.30

B. Femoral Cartilage Scanning

The following example is of the right femoral lateral cartilage. The test (laser) scan was acquired with the RIO robot setup and UKA exposure. The test model was registered with the reference model (MRI) and the results are shown in table 7.3.

Table 7.3 Alignment statistics between reference (MRI) and test (laser) model for an example right femoral lateral cartilage

AAE; average absolute error between two models, SD_{AE}; standard deviation of the AAE, $+d_{max}$ and $-d_{max}$; maximum positive and negative deviations respectively. Note: $\pm d_{max}$ again occurred at the periphery

Parameter	Units (mm)
AAE	0.21
SD_{AE}	0.32
$+d_{max}$	1.88
$-d_{max}$	-1.38

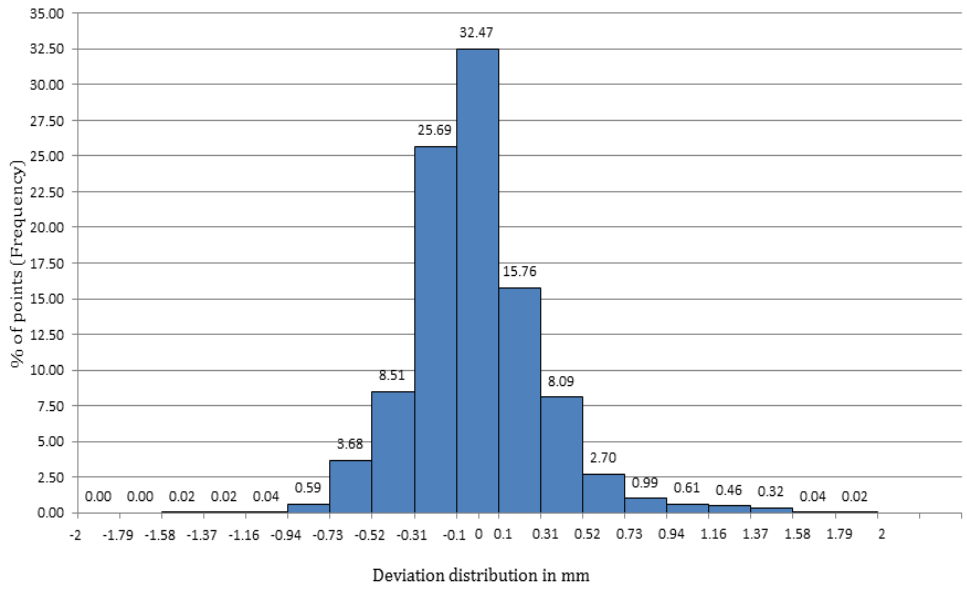

Figure 7.4 Deviation distribution between reference (MRI) and test (laser) model of an example right femoral lateral cartilage

Deviation in mm is plotted against the percentage of points within the range of deviations. Note: $\pm d_{max}$ occurred at the periphery

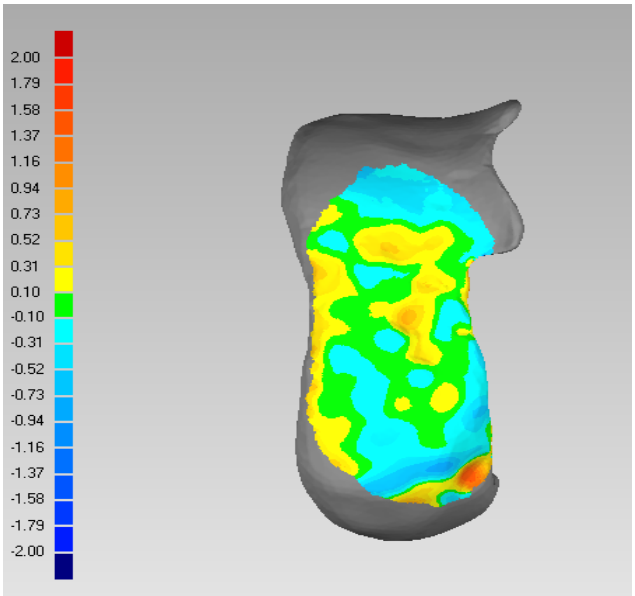

Figure 7.5 Top view of the colour deviation map for the spatial distribution of the deviations between the reference (MRI) and the test (laser) model of an example right femoral lateral cartilage

The posterior and superior condylar region is clipped as the laser scan was acquired with a minimal exposure (90 mm, mimicking UKA). Note: Large errors ($\pm d_{max}$) at the periphery of the scan

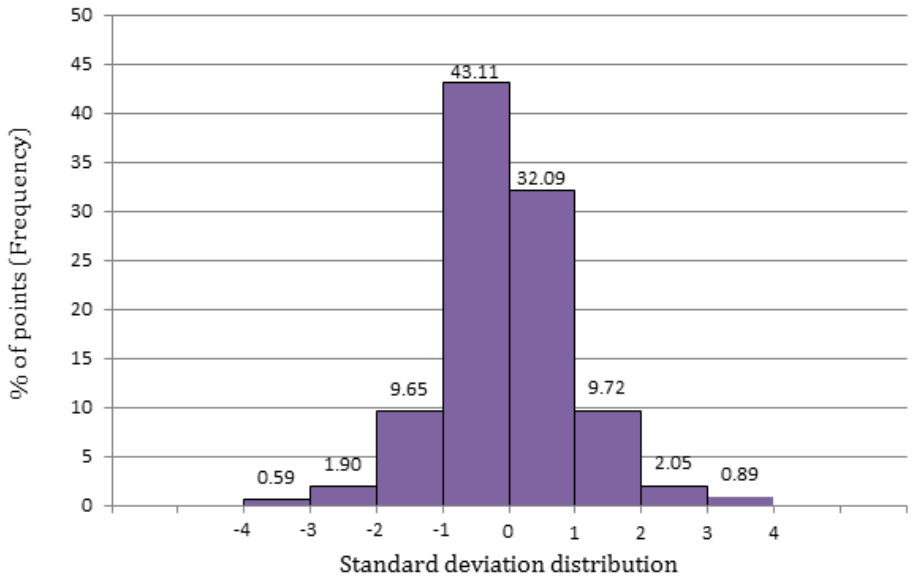

Figure 7.6 Standard deviation distribution between reference (MRI) and test (laser) model of an example right femoral lateral cartilage

Standard deviation distribution is plotted against the percentage of points

Table 7.4 Summary of the alignment statistics between reference (MRI) and test (laser) models of femoral cartilaginous surface of all the samples

AAE; average absolute error between the models, SD_{AE}; standard deviation of the AAE, $+d_{max}$ and $-d_{max}$; maximum positive and negative deviations respectively. Average and standard deviation of all the parameters is shown at the bottom of the table. Note: d_{max} values occurred at the periphery of the scan zones.

	UKA Exposure								**TKA Exposure**							
	On Al Extrusion				On RIO				On Al Extrusion				On RIO			
Samples	AAE (mm)	SD_{AE} (mm)	d_{max} (mm)		AAE (mm)	SD_{AE} (mm)	d_{max} (mm)		AAE (mm)	SD_{AE} (mm)	d_{max} (mm)		AAE (mm)	SD_{AE} (mm)	d_{max} (mm)	
			+	-			+	-			+	-			+	-
1	0.23	0.33	1.84	-1.50	0.26	0.42	1.51	-1.67	0.28	0.42	1.81	-1.82	0.27	0.44	1.85	-1.94
2	0.20	0.29	2.07	-1.37	0.18	0.28	1.30	-2.03	0.35	0.68	2.15	-2.47	0.33	0.61	2.30	-2.24
3	0.28	0.40	1.49	-1.60	0.28	0.44	1.51	-1.86	0.33	0.46	1.49	-1.69	0.32	0.47	1.87	-1.89
4	0.23	0.33	1.84	-1.50	0.26	0.42	1.51	-1.67	0.28	0.42	1.81	-1.82	0.27	0.44	1.85	-1.94
5	0.21	0.28	1.15	-0.99	0.24	0.33	1.34	-1.31	0.25	0.46	2.73	-2.20	0.27	0.37	2.72	-1.97
6	0.25	0.58	1.43	-1.91	0.25	0.53	1.79	-1.88	0.29	0.66	2.53	-2.20	0.30	0.60	2.46	-2.54
7	0.21	0.31	1.75	-1.39	0.23	0.33	1.72	-1.37	0.28	0.32	1.74	-1.25	0.29	0.38	2.52	-1.46
8	0.26	0.44	1.36	-1.97	0.26	0.46	1.32	-2.19	0.28	0.59	1.97	-3.03	0.30	0.64	2.56	-2.46
9	0.29	0.38	1.23	-1.57	0.28	0.40	1.43	-1.56	0.32	0.45	1.63	-1.73	0.33	0.54	1.93	-2.32
10	0.24	0.36	1.66	-1.65	0.23	0.31	1.31	-1.13	0.30	0.40	2.18	-1.63	0.27	0.40	2.61	-2.50
11	0.29	0.43	1.45	-1.44	0.29	0.45	1.82	-1.43	0.34	0.53	1.72	-1.72	0.33	0.48	2.47	-2.38
Average	0.24	0.37	1.57	-1.54	0.25	0.40	1.50	-1.64	0.30	0.49	1.98	-1.96	0.30	0.49	2.29	-2.15
SD	0.03	0.09	0.29	0.27	0.03	0.08	0.19	0.32	0.03	0.11	0.38	0.49	0.03	0.10	0.34	0.34

C. Tibial Bone Scanning

The following example is of the resurfaced left medial tibia comprising only bone. The test (laser) scan was acquired using RIO setup and TKA exposure which was registered with the reference model (CT). The results are shown in table 7.5.

Table 7.5 Alignment statistics between reference (CT) and test (laser) model for an example left tibial medial bone

AAE; average absolute error between two models, SD_{AE}; standard deviation of the AAE, $+d_{max}$ and $-d_{max}$; maximum positive and negative deviations respectively. Note: $\pm d_{max}$ values again occurred at the periphery

Parameter	Units (mm)
AAE	0.31
SD_{AE}	0.46
$+d_{max}$	1.93
$-d_{max}$	-2.19

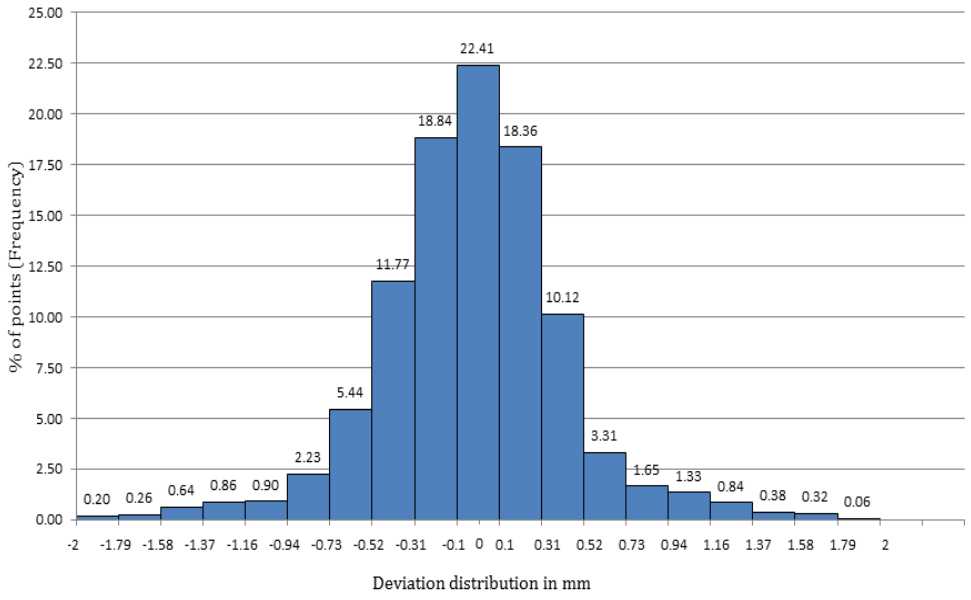

Figure 7.7 Deviation distribution between reference (CT) and test (laser) model of an example left tibial medial bone

Deviation in mm is plotted against the percentage of points within the range of deviations. Note: Larger tail in the ± distribution when scanning with larger exposure

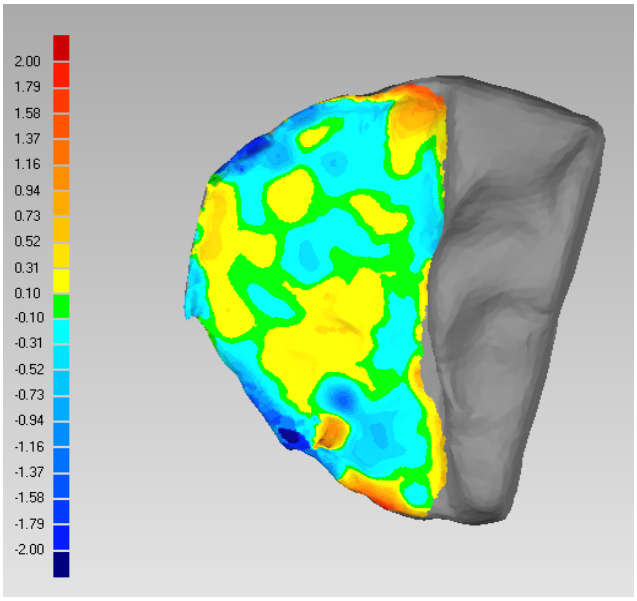

Figure 7.8 Top view of the colour deviation map for the spatial distribution of the deviations between the reference (CT) and the test (laser) model of an example left tibial medial bone

The scan was acquired with a large exposure thus a maximum exposure (180 mm, mimicking TKA). Note: Larger area scanned resulting in larger errors especially towards the periphery

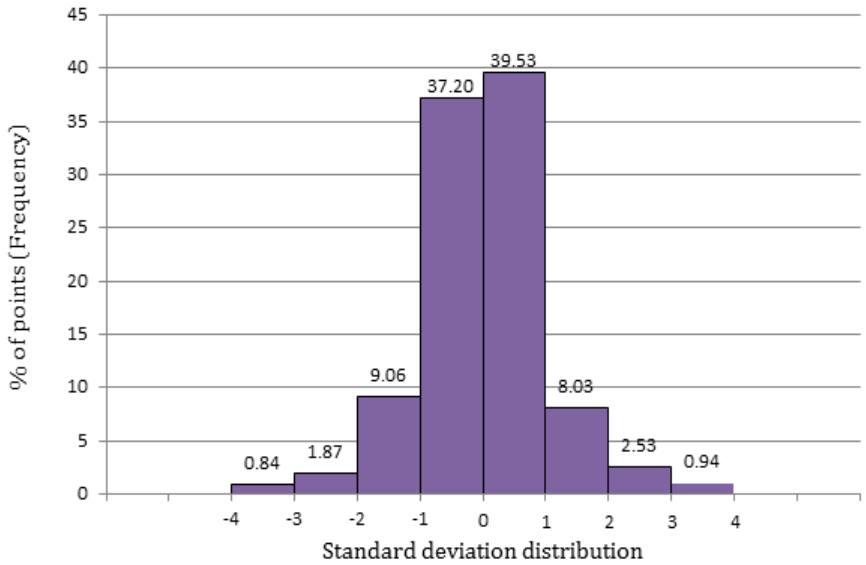

Figure 7.9 Standard deviation distribution between reference (CT) and test (laser) model of an example left tibial medial bone

Standard deviation is plotted against the percentage of points

Table 7.6 Summary of the alignment statistics between reference (CT) and test (laser) models of tibial bone surface of all the samples

AAE; average absolute error between the models, SD_{AE}; standard deviation of the AAE, $+d_{max}$ and $-d_{max}$; maximum positive and negative deviations respectively. Average and standard deviation of all the parameters is shown at the bottom of the table. All the d_{max+} values again occurred at the periphery of the scans.

Samples	**UKA Exposure**								**TKA Exposure**							
	On Al Extrusion				On RIO				On Al Extrusion				On RIO			
	AAE (mm)	SD_{AE} (mm)	d_{max} (mm)		AAE (mm)	SD_{AE} (mm)	d_{max} (mm)		AAE (mm)	SD_{AE} (mm)	d_{max} (mm)		AAE (mm)	SD_{AE} (mm)	d_{max} (mm)	
			+	-			+	-			+	-			+	-
1	0.28	0.38	1.57	-1.43	0.28	0.38	1.40	-1.56	0.32	0.45	1.97	-1.74	0.30	0.41	1.84	-1.93
2	0.32	0.47	1.80	-1.59	0.32	0.47	1.56	-1.63	0.34	0.52	2.36	-1.99	0.35	0.57	2.19	-2.27
3	0.31	0.40	0.79	-1.75	0.30	0.38	1.04	-1.60	0.34	0.50	1.68	-2.10	0.35	0.49	1.30	-2.06
4	0.28	0.39	1.50	-1.85	0.26	0.38	1.70	-1.28	0.27	0.37	1.77	-1.97	0.28	0.41	1.39	-1.57
5	0.25	0.34	1.61	-1.46	0.25	0.38	1.61	-1.78	0.26	0.36	1.62	-1.94	0.27	0.38	1.29	-1.73
6	0.29	0.42	1.48	-1.43	0.31	0.41	1.69	-1.29	0.32	0.45	1.44	-1.82	0.32	0.43	1.66	-1.96
7	0.28	0.39	1.60	-1.34	0.29	0.41	1.50	-1.43	0.31	0.43	1.66	-2.06	0.32	0.45	1.32	-1.86
8	0.28	0.44	1.80	-1.73	0.30	0.45	1.74	-1.74	0.31	0.46	1.88	-1.95	0.31	0.47	1.93	-1.97
9	0.28	0.44	2.37	-1.72	0.29	0.41	1.72	-1.53	0.32	0.45	1.89	-1.74	0.33	0.45	1.72	-1.75
Average	0.28	0.41	1.61	-1.59	0.29	0.41	1.55	-1.54	0.31	0.44	1.81	-1.92	0.31	0.45	1.62	-1.90
SD	0.02	0.04	0.41	0.18	0.02	0.03	0.22	0.18	0.03	0.05	0.26	0.13	0.03	0.05	0.32	0.21

D. Femoral Bone Scanning

The following example is of the resurfaced left medial femur. The test (laser) scan was acquired using Aluminium extrusion setup and TKA exposure which was registered with the reference model (CT). The results are shown in table 7.7

Table 7.7 Alignment statistics between reference (CT) and test (laser) models for an example left femoral medial bone

AAE; average absolute error between two models, SD_{AE}; standard deviation of the AAE, $+d_{max}$ and $-d_{max}$; maximum positive and negative deviations respectively. Note: $\pm d_{max}$ was at the periphery of the scan

Parameter	Units mm
AE	0.33
SD_{AE}	0.47
$+d_{max}$	1.94
$-d_{max}$	-1.99

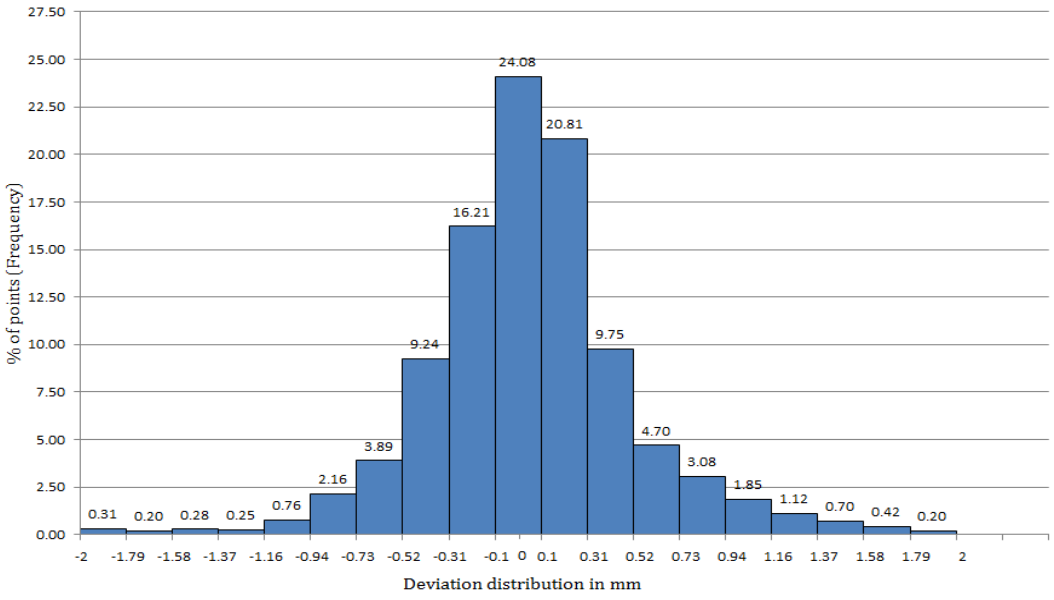

Figure 7.10 Deviation distribution between reference (CT) and test (laser) model of an example left femoral medial bone

Deviation in mm is plotted against the percentage of points within the range of deviations. Note: Greater tails to the distribution with larger exposure.

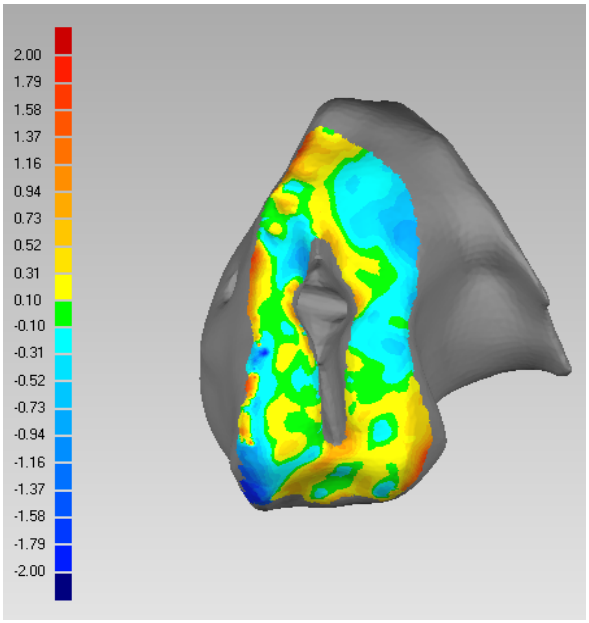

Figure 7.11 Top view of the colour deviation map (in mm) showing the spatial distribution of the deviations between the reference (CT) and the test (laser) model of an example left femoral medial bone

The scan was acquired with a large exposure thus a maximum exposure (180 mm, mimicking TKA). Note: The maximum error values at the periphery

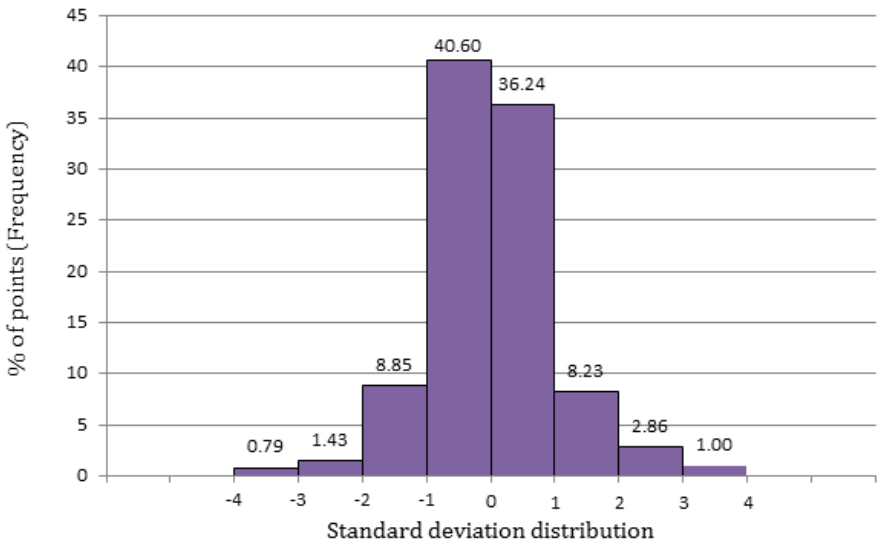

Figure 7.12 Standard deviation distribution between reference (CT) and test (laser) models of an example left femoral medial bone

Standard deviation is plotted against the percentage of points within the range of standard deviations

Table 7.8 Summary of the alignment statistics between reference (CT) and test (laser) models of femoral bone surface of all the samples

AAE; average absolute error between the models, SD_{AE}; standard deviation of the AAE, $+d_{max}$ and $-d_{max}$; maximum positive and negative deviations respectively. Average and standard deviation of all the parameters is shown at the bottom of the table.

	UKA Exposure								**TKA Exposure**							
	On Al Extrusion				On RIO				On Al Extrusion				On RIO			
Samples	AAE (mm)	SD_{AE} (mm)	d_{max} (mm)		AAE (mm)	SD_{AE} (mm)	d_{max} (mm)		AAE (mm)	SD_{AE} (mm)	d_{max} (mm)		AAE (mm)	SD_{AE} (mm)	d_{max} (mm)	
			+	-			+	-			+	-			+	-
1	0.32	0.45	2.12	-2.31	0.32	0.45	1.74	-1.78	0.37	0.49	1.66	-1.78	0.37	0.49	1.66	-1.82
2	0.29	0.39	2.01	-2.00	0.34	0.47	1.94	-1.77	0.37	0.51	2.08	-2.01	0.36	0.50	2.00	-2.13
3	0.36	0.47	1.73	-1.52	0.35	0.45	1.57	-1.38	0.37	0.52	2.27	-1.93	0.37	0.53	2.65	-1.99
4	0.33	0.45	1.95	-1.65	0.34	0.47	2.14	-1.86	0.37	0.50	2.05	-1.95	0.37	0.51	2.13	-1.89
5	0.26	0.37	2.41	-2.22	0.28	0.37	1.76	-1.73	0.31	0.45	2.25	-1.56	0.30	0.43	2.55	-2.31
6	0.32	0.42	1.53	-1.76	0.33	0.42	1.74	-1.78	0.36	0.48	1.97	-1.99	0.36	0.49	2.07	-2.02
7	0.35	0.46	1.68	-1.74	0.36	0.47	1.56	-1.73	0.38	0.51	2.38	-2.39	0.40	0.55	2.19	-2.19
8	0.35	0.46	2.10	-2.31	0.36	0.45	1.99	-2.29	0.40	0.51	2.00	-2.30	0.40	0.50	2.17	-2.47
9	0.33	0.45	2.12	-1.97	0.32	0.45	2.08	-1.92	0.35	0.49	2.30	-2.12	0.37	0.52	2.25	-2.17
Average	0.32	0.44	1.96	-1.94	0.33	0.44	1.84	-1.81	0.36	0.50	2.10	-2.00	0.37	0.50	2.19	-2.11
SD	0.03	0.03	0.27	0.29	0.02	0.03	0.21	0.24	0.02	0.02	0.22	0.25	0.03	0.03	0.29	0.21

7.1.2 Effects of the Independent Variables

The first stage of the statistical analysis of the results comprised of evaluating the AAE between the reference (MRI/CT) models and the corresponding test (laser) models. In the next stage, the effects of three independent variables i.e. type of setup (Aluminium extrusion, RIO), type of exposure (UKA, TKA) and type of surface (Tibia, Femur) on the dependent variable, AAE were studied. In this sub-section, the main effects and the interaction effects of the independent variables on AAE are reported by profile plots. Additionally, each independent variable was tested separately to investigate differences within them using paired t-test and their comparison is shown using bar chart with error bars (for 95% confidence limits) and box and whisker plots. The effects for the cartilaginous region and the bone region are analysed separately as:

- Pre-operative data acquisition of the cartilage and bone was performed using two different techniques; 3D FLASH MRI and CT respectively.
- Sample size for the cartilaginous surface and the bone surface comparison were different (11 and 9 respectively).
- The bone region was milled using NAVIO PFS® technique prior to the experiments of this study whereas the cartilaginous surfaces were intact.

A. Cartilaginous Surface

Statistical analysis of the effects of the independent variables on the AAE between the reference MRI and test laser (cartilage) scans.

1) Type of Setup

Table 7.9 Descriptive statistics of the effect of type of setup on the AAE for cartilaginous surface

Type of Setup	Average AAE	Std. Error	95% Confidence Interval	
			Lower Bound	Upper Bound
Al	.246	.009	.227	.265
RIO	.253	.008	.233	.270

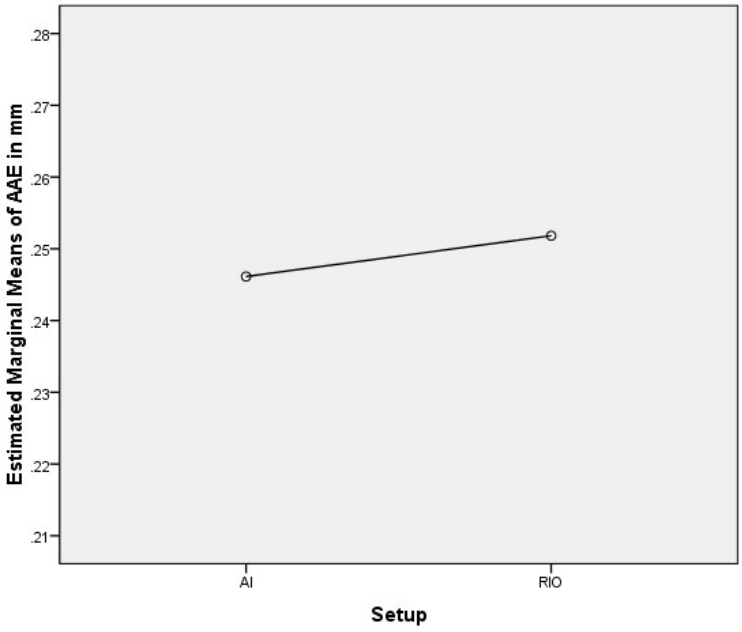

Figure 7.13 Profile plot for the effect of the two types of the setups on the AAE of cartilaginous surface

No statistically significant difference in the means, $F(1,10) = 1.495$; $P=0.25$

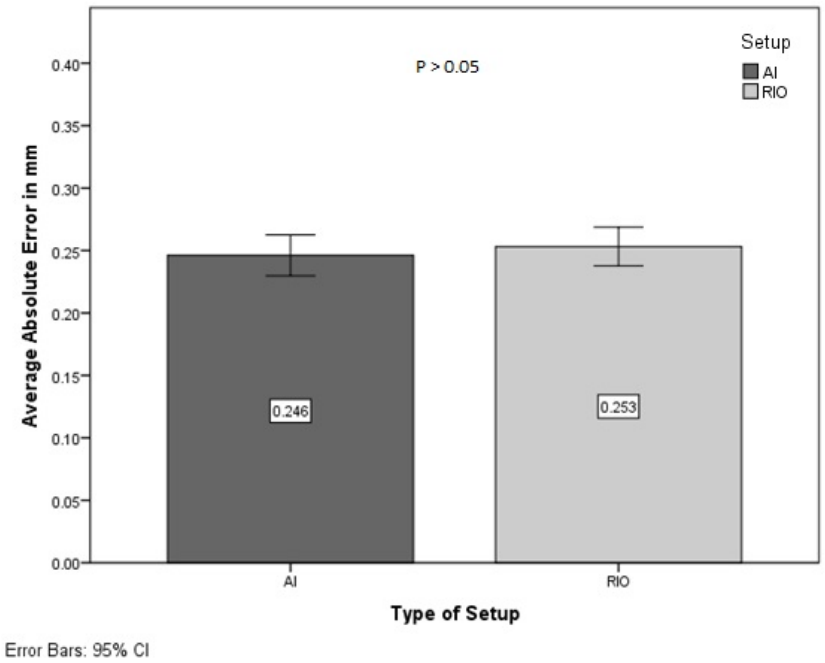

Figure 7.14 Bar graph with error bars for 95% confidence limit for the effects of two types of setups on the AAE of cartilaginous surface

No statistically significant difference; P>0.05

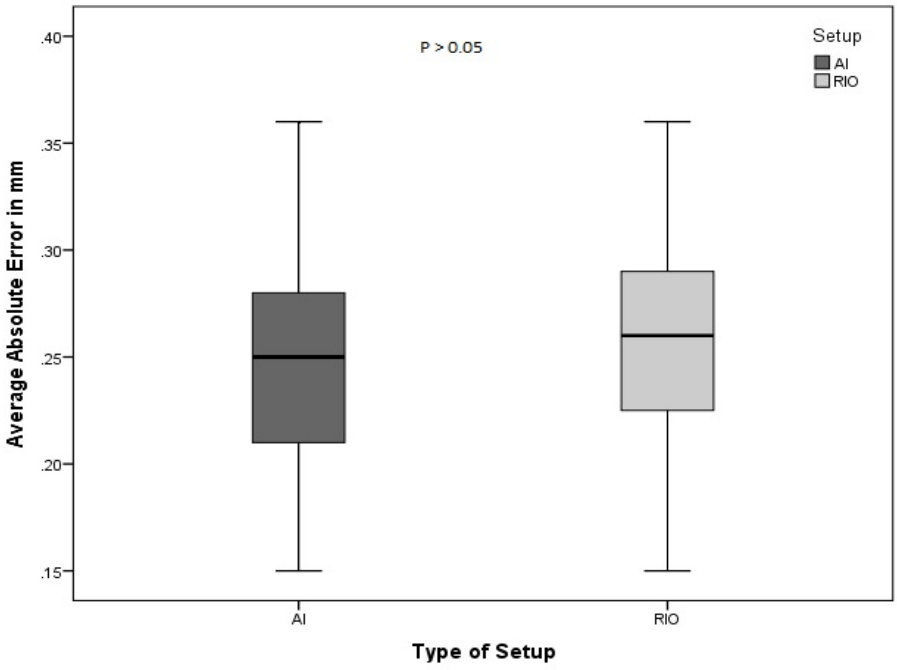

Figure 7.15 Box and whisker plot for the effect of the two types of setups on the AAE of cartilaginous surface.

No statistically significant difference; P>0.05

2) Type of Exposure

Table 7.10 Descriptive statistics of the effect of type of exposure on the AAE for cartilaginous surface

Type of Exposure	Average AAE	Std. Error	95% Confidence Interval	
			Lower Bound	Upper Bound
UKA	.219	.007	.204	.234
TKA	.279	.011	.254	.304

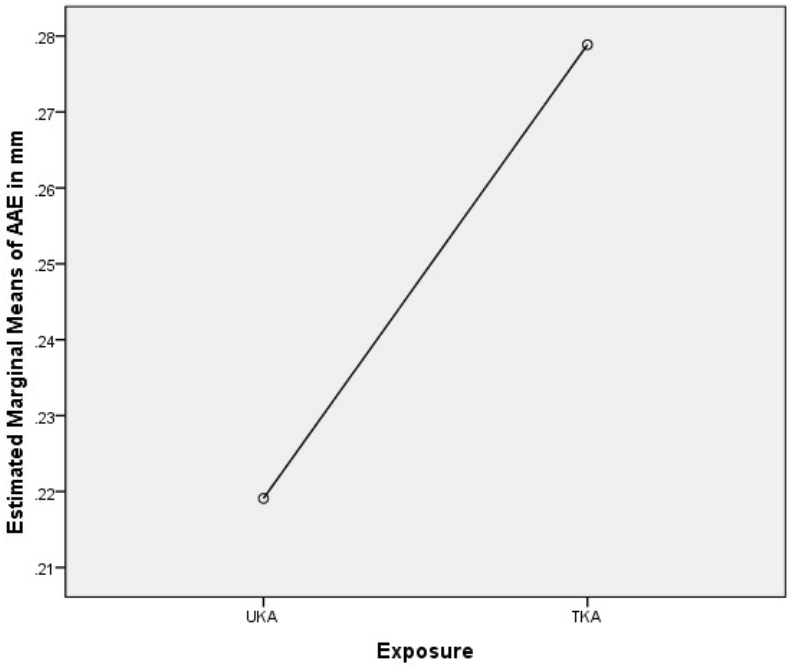

Figure 7.16 Profile plot for the effect of the two types of the exposures on the AAE of cartilaginous surface

Statistically significant difference was found in their means, $F(1,10) = 48.336$; P= 0.0004. Errors slightly larger with TKA exposure

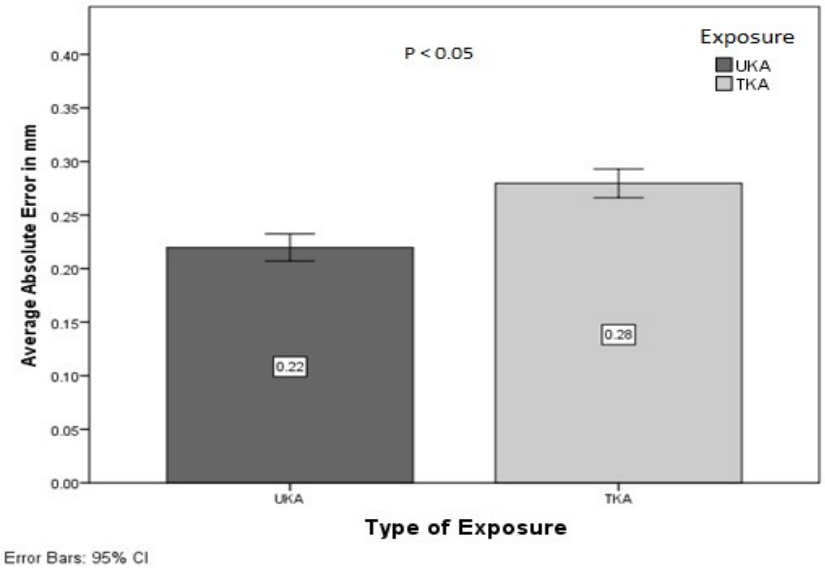

Figure 7.17 Bar graph with error bars for 95% confidence limit for the effect of the two types of exposures on the AAE of cartilaginous surface

Statistically significant difference was found; P<0.05. Errors slightly larger with TKA exposure

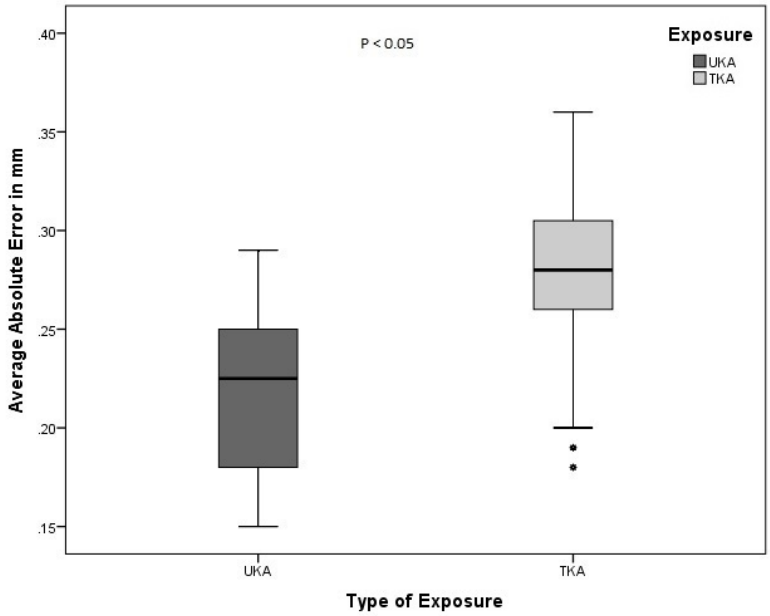

Figure 7.18 Box and whisker plot for the effect of the two types of exposures on the AAE of cartilaginous surface

Statistically significant difference was found; * indicates outliers; P<0.05. Errors slightly larger with TKA exposure

3) Type of Surface

Table 7.11 Descriptive statistics of the effect of type of the surface on the AAE for cartilaginous surface

Type of Surface	Average AAE	Std. Error	95% Confidence Interval	
			Lower Bound	Upper Bound
Tibia	.225	0.012	0.198	0.251
Femur	.273	0.007	0.258	0.289

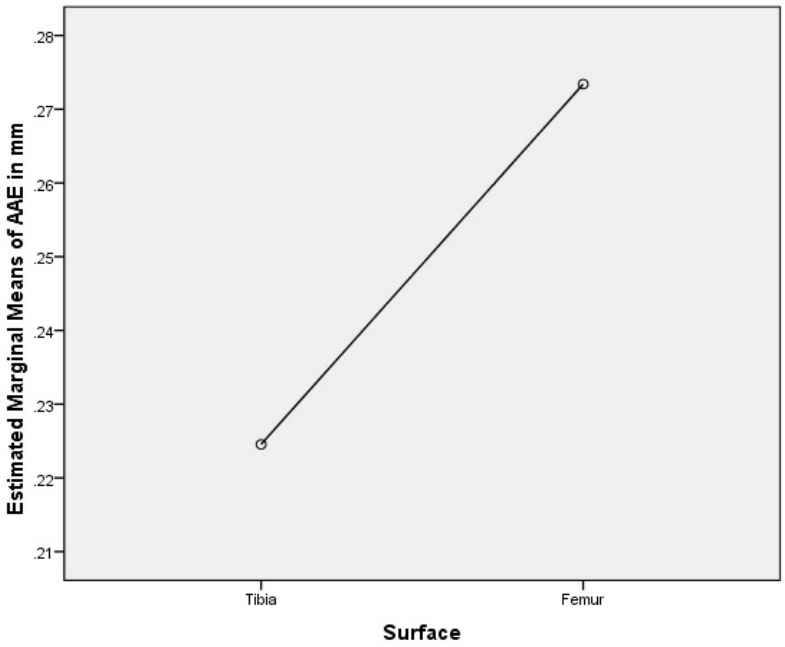

Figure 7.19 Profile plot for the effect of the two types of the surfaces on the AAE of cartilaginous surface

Statistically significant difference was found, $F(1,10) = 18.940$; P = 0.01. Errors slightly larger in the femoral surfaces

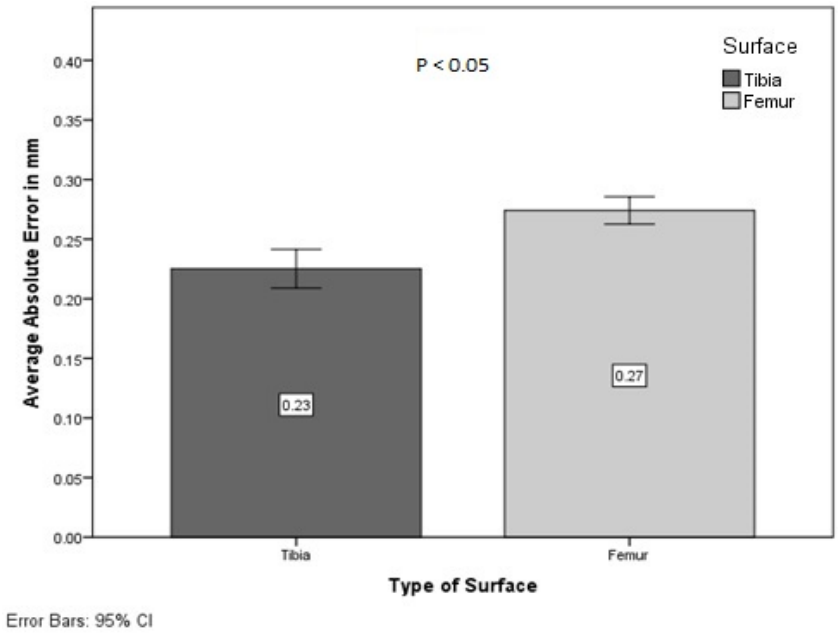

Figure 7.20 Bar graph with error bars for 95% confidence limit for the effect of the two types of surfaces on the AAE of cartilaginous surface

Statistically significant difference was found; P<0.05. Marginally larger errors in femoral scans

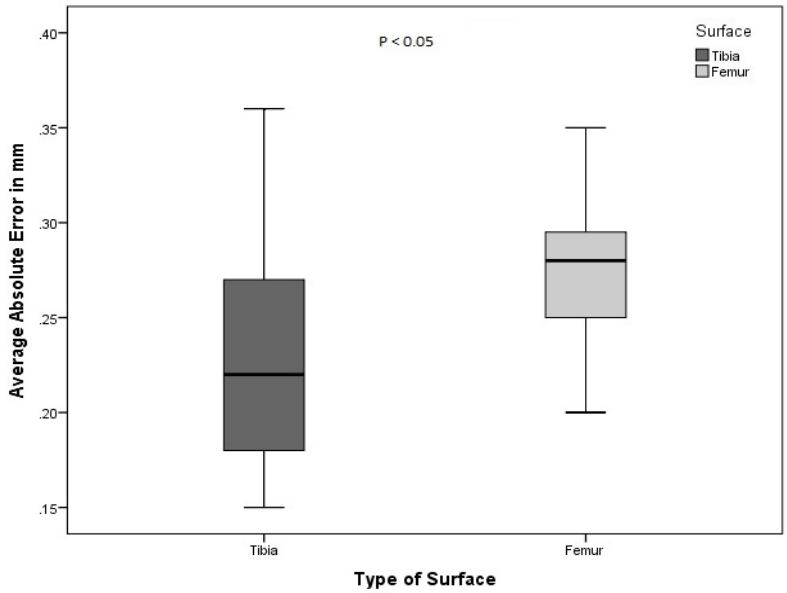

Figure 7.21 Box and whisker plot for the effect of the two types of surfaces on the AAE of cartilaginous surface

Statistically significant difference was found; P<0.05. Slightly larger errors in femoral scans.

Interaction of independent variables

Table 7.12 Descriptive statistics of the interaction between independent variables for cartilaginous surface

Independent variables: Type of setup (Aluminium extrusion, RIO), type of exposure (UKA, TKA) and type of the surface (Tibia, Femur)

Interaction of independent variables	Average AAE	Std. Deviation
Aluminium Extrusion + UKA + Tibia	.1882	.02960
Aluminium Extrusion + UKA + Femur	.2445	.03236
Aluminium Extrusion + TKA + Tibia	.2518	.05154
Aluminium Extrusion + TKA + Femur	.3000	.03098
RIO + UKA + Tibia	.1927	.03319
RIO + UKA + Femur	.2509	.03081
RIO + TKA + Tibia	.2655	.06832
RIO + TKA + Femur	.2982	.02601

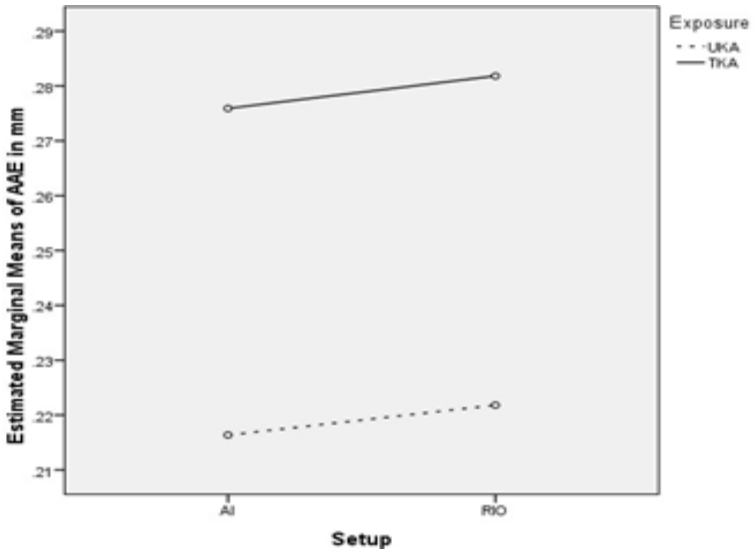

Figure 7.22 The two way interaction between the type of setup and the type of exposure for cartilaginous surface

No statistically significant difference; $F(1,10) = 0.03$; $P = 0.955$. Note: No statistically significant interaction effect so we can rely on the single variable analysis with no need to do multivariate analysis.

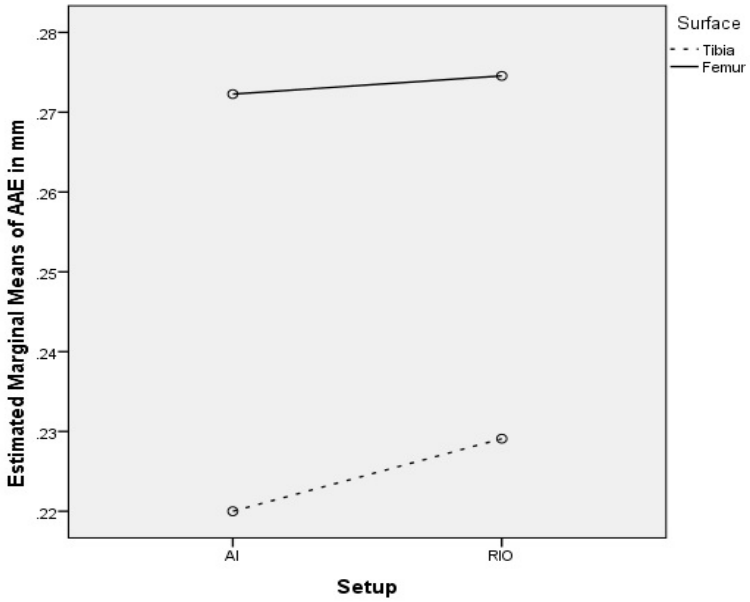

Figure 7.23 The two way interaction between the type of setup and the type of surface for cartilaginous surface

No statistically significant difference; $F(1,10) = 1$; P= 0.341. Note: As above

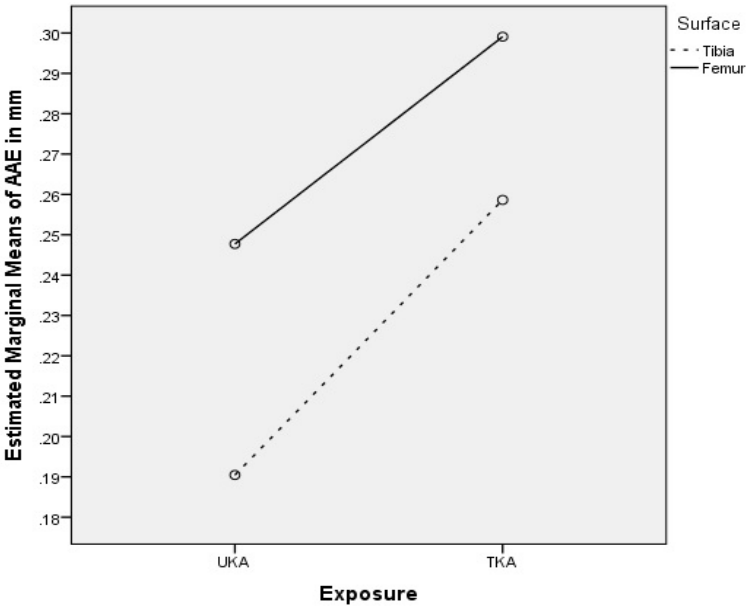

Figure 7.24 The two way interaction between the type of exposure and the type of surface for cartilaginous surface

No statistically significant difference; $F(1,10) = 1.312$; P= 0.279. Note: As above

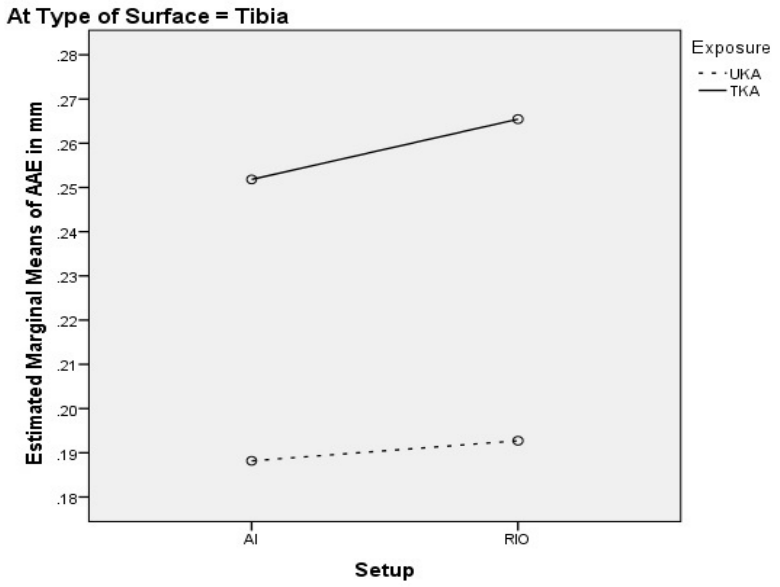

Figure 7.25 The three way interaction (A difference in the pattern of a 2-way interaction at levels of the third factor, tibia) between the type of setup, the type of exposure and the type of surface for cartilaginous surface

No statistically significant difference; $F(1,10) = 0.766$; P = 0.402. Note: As above

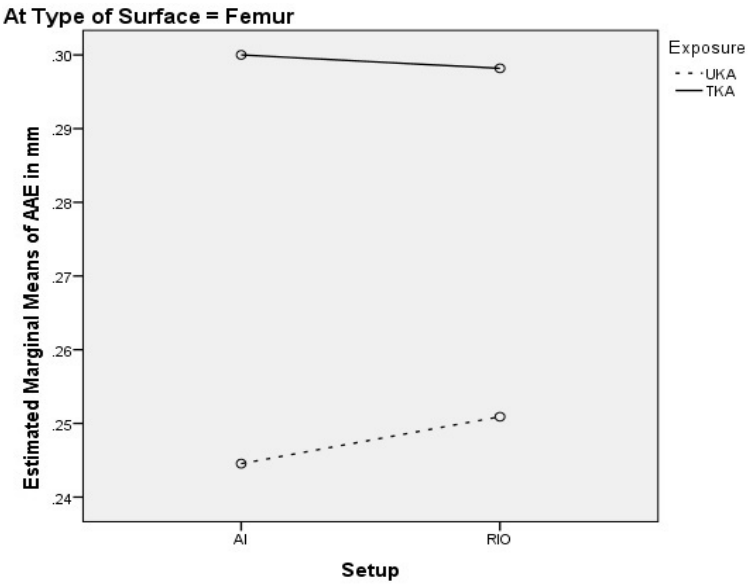

Figure 7.26 The three way interaction (A difference in the pattern of a 2-way interaction at levels of the third factor, femur) between the type of setup, the type of exposure and the type of surface for cartilaginous surface

No statistically significant difference; $F(1,10) = 0.766$; P = 0.402 . Note: As above

B. Bone Surface

Statistical analysis of the effects of the independent variables on the AAE between the reference CT and test laser (bone) scans

1) Type of Setup

Table 7.13 Descriptive statistics of the effect of type of setup on the AAE for bone surface

Type of Setup	Average AAE	Std. Error	95% Confidence Interval	
			Lower Bound	Upper Bound
Al	.321	.007	.304	.337
RIO	.326	.007	.309	.343

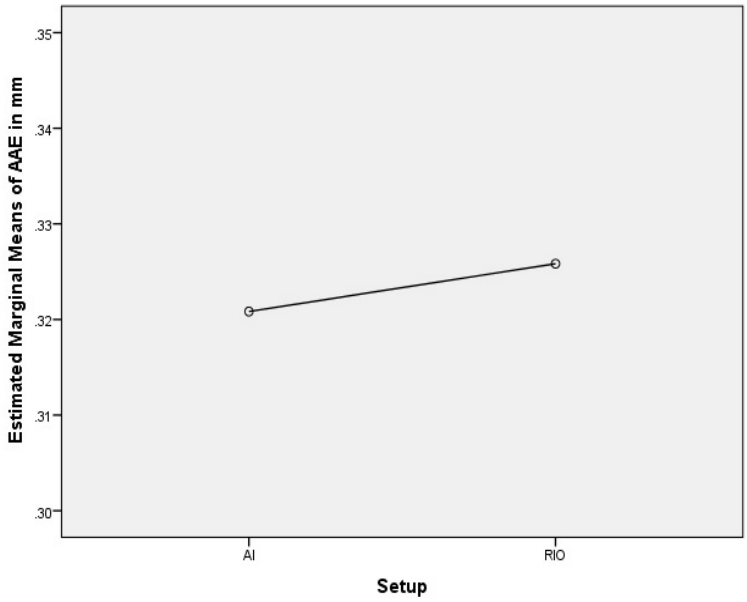

Figure 7.27 Profile plot for the effect of the two types of the setups on the AAE of bone surface

No statistically significant difference, $F(1,8) = 5.76$; P = 0.073.

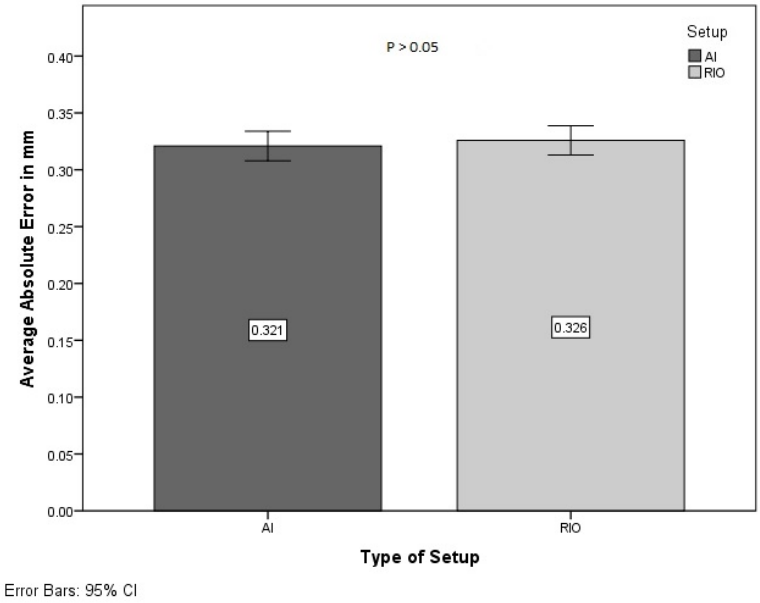

Figure 7.28 Bar graph with error bars for 95% confidence limit for the effect of the two types of setups on the AAE of bone surface

No statistically significant difference; P>0.05.

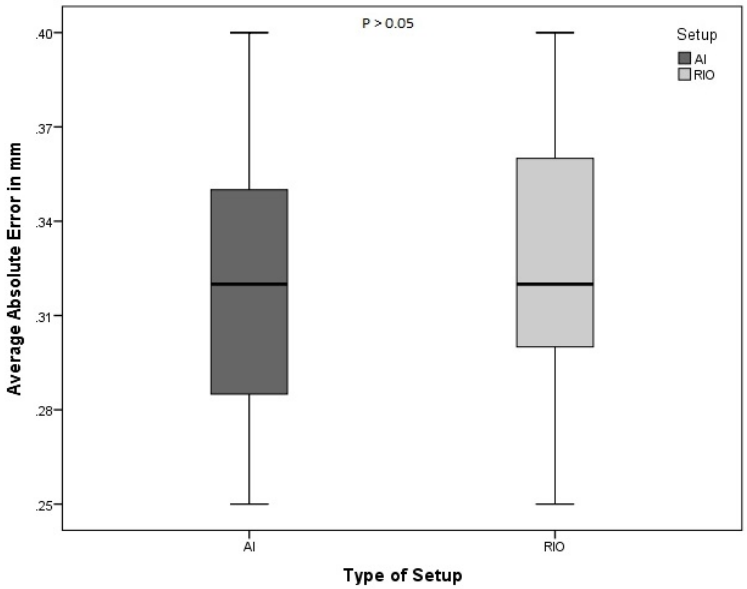

Figure 7.29 Box and whisker plot showing the effect of the two types of setups on the AAE of bone surface

No statistical significant difference P>0.05

Type of Exposure

Table 7.14 Descriptive statistics of the effect of type of exposure on the AAE for bone surface

Type of Exposure	Average AAE	Std. Error	95% Confidence Interval	
			Lower Bound	Upper Bound
UKA	.308	.007	.292	.324
TKA	.339	.008	.321	.357

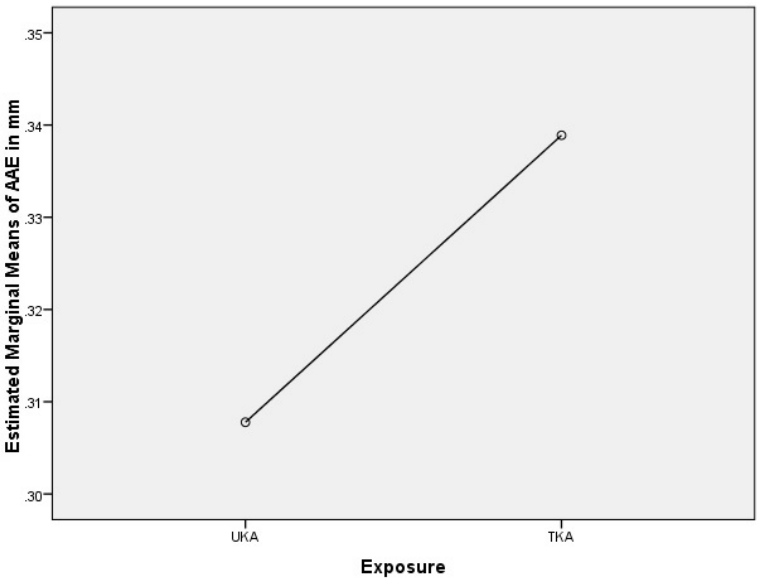

Figure 7.30 Profile plot for the effect of the two types of the exposures on the AAE of bone surface

Statistically significant difference was found, $F(1,8) = 198.32$; P = 0.00001. Slightly larger errors with larger exposure

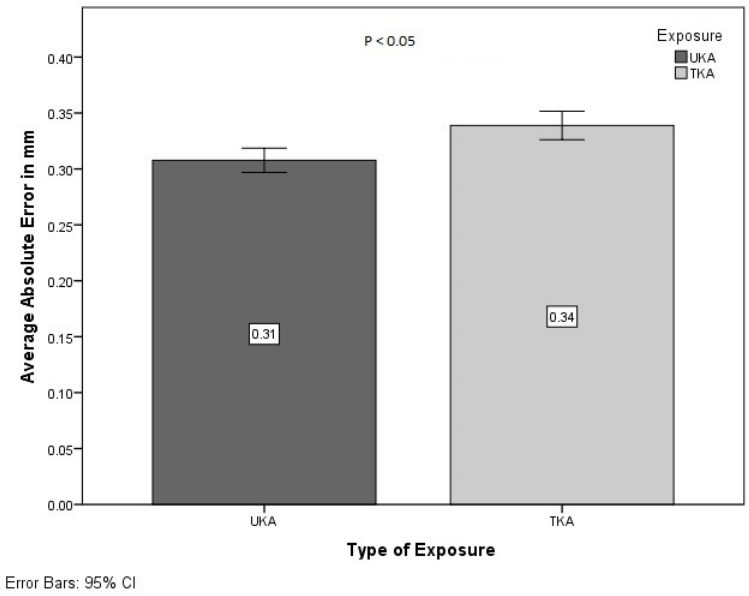

Figure 7.31 Bar graph with error bars for 95% confidence limit for the effect of the two types of exposures on the AAE of bone surface

Statistically significant difference was found; P<0.05. Slightly larger errors with larger exposure

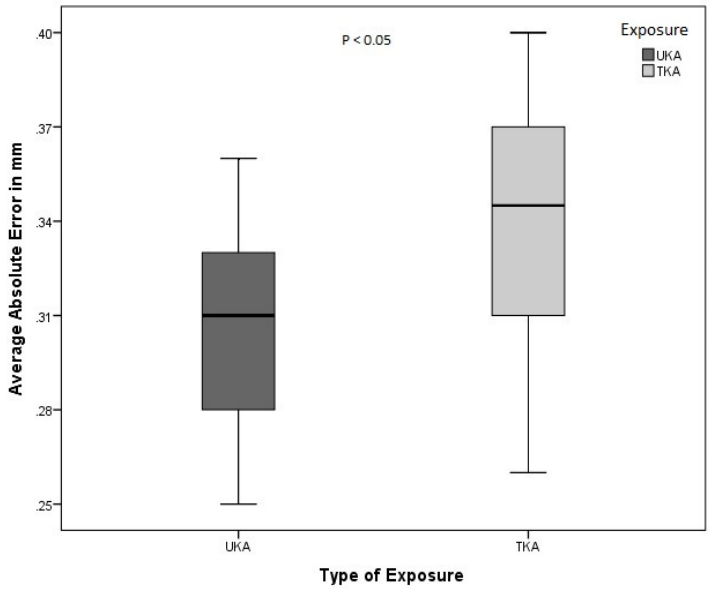

Figure 7.32 Box and whisker plot for the effect of the two types of exposures on the AAE of bone surface

Statistically significant difference was found; P<0.05. Slightly larger errors with larger exposure

Type of Surface

Table 7.15 Descriptive statistics of the effect of type of the surface on the AAE for bone surface

Type of surface	Average AAE	Std. Error	95% Confidence Interval	
			Lower Bound	Upper Bound
Tibia	.300	.008	.282	.318
Femur	.347	.009	.327	.367

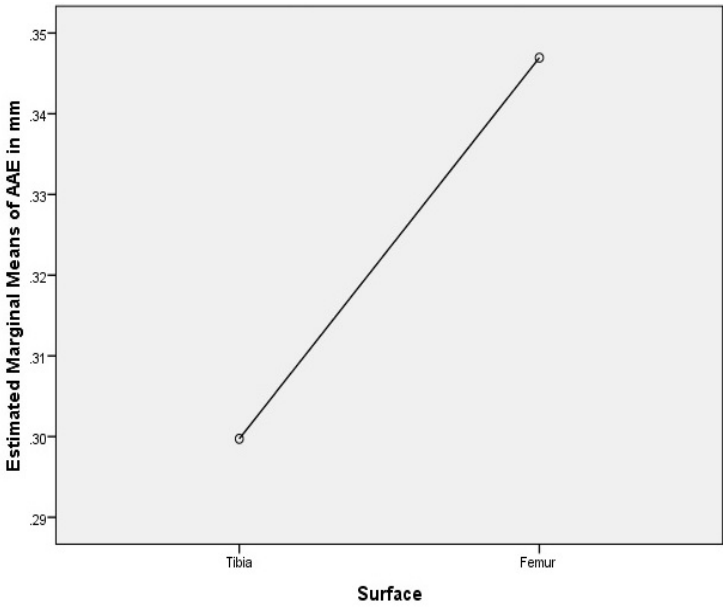

Figure 7.33: Profile plot for the effect of the two types of the surfaces on the AAE of bone surface

Statistically significant difference was found, $F(1,8) = 32.646$; P = 0.00044.

Slightly larger errors on femoral surfaces

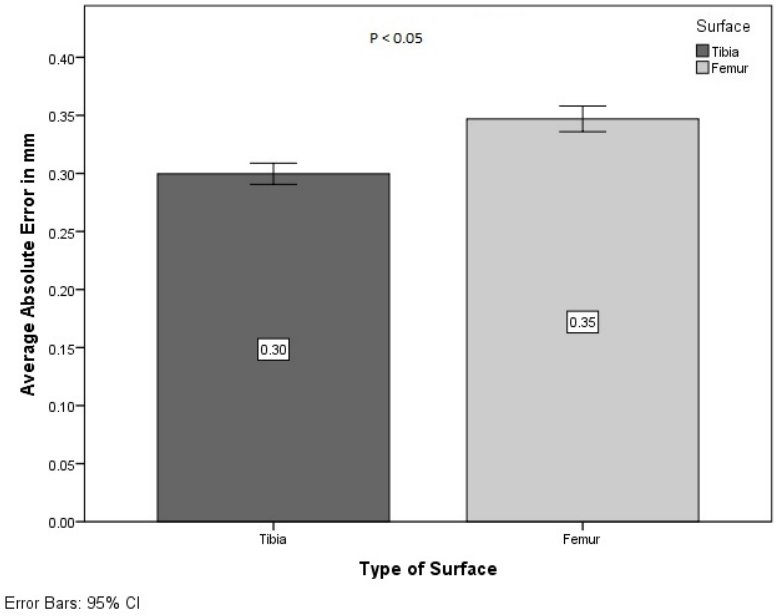

Figure 7.34 Bar graph with error bars for 95% confidence limit for the effect of the two types of surfaces on the AAE of bone surface

Statistically significant difference was found; P<0.05. Slightly larger errors on femoral surfaces

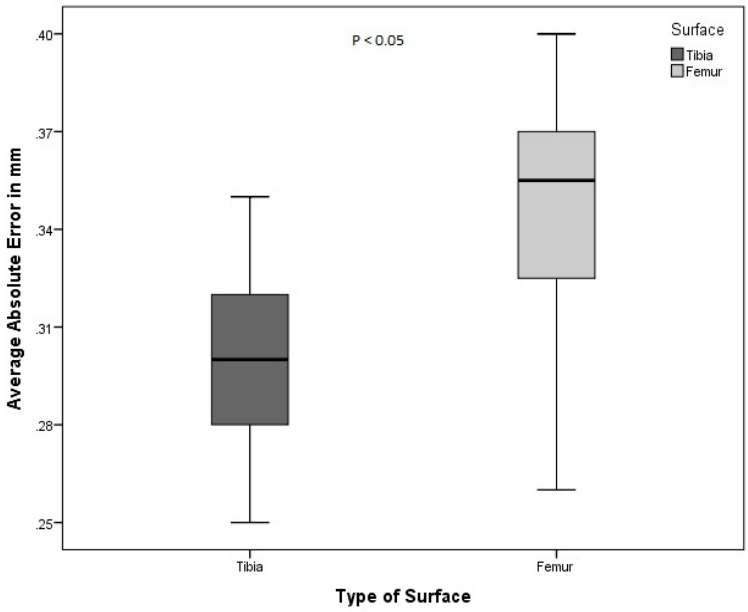

Figure 7.35 Box and whisker plot for the effect of the two types of surfaces on the AAE of bone surface

Statistically significant difference was found; P<0.05. Slightly larger errors on femoral surfaces

Interaction of independent variables

Table 7.16 Descriptive statistics of the interaction between independent variables for bone surface

Independent variables: Type of setup (Aluminium extrusion, RIO), Type of exposure (UKA, TKA) and Type of the surface (Tibia, Femur)

Interaction of independent variables	Average AAE	Std. Deviation
Aluminium Extrusion + UKA + Tibia	.2856	.02007
Aluminium Extrusion + UKA + Femur	.3233	.03162
Aluminium Extrusion + TKA + Tibia	.3100	.02784
Aluminium Extrusion + TKA + Femur	.3644	.02455
RIO + UKA + Tibia	.2889	.02261
RIO + UKA + Femur	.3333	.02500
RIO + TKA + Tibia	.3144	.02789
RIO + TKA + Femur	.3667	.02915

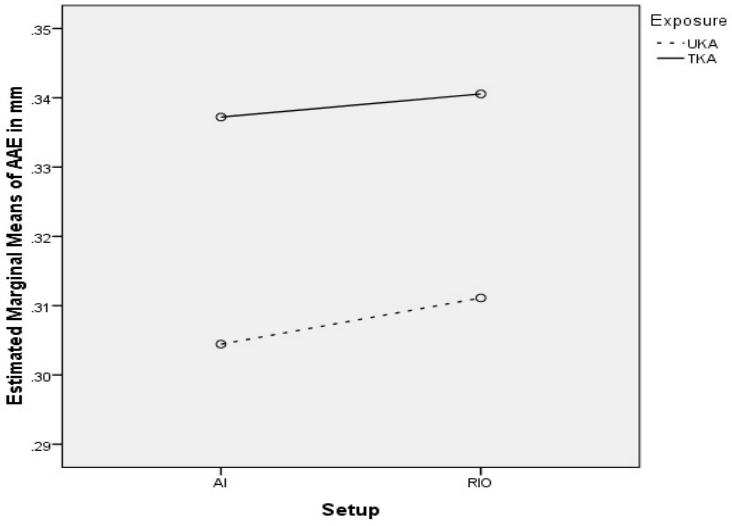

Figure 7.36 The two way interaction between the type of setup and the type of exposure for bone surface

No statistically significant difference, $F(1,8) = 0.457$; $P = 0.518$. Note: No statistically significant interaction effect so we can rely on the single variable analysis with no need to do multivariate analysis.

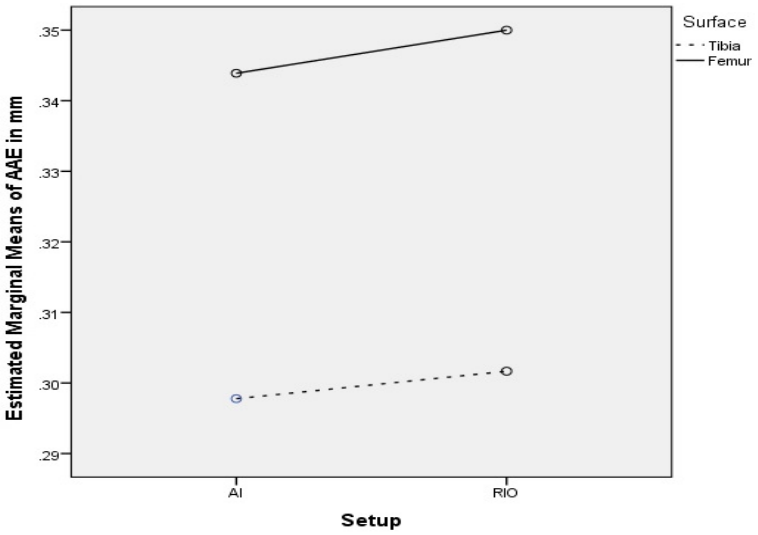

Figure 7.37 The two way interaction between the type of setup and the type of surface for bone surface

No statistically significant difference; $F(1,8) = 0.703$; P = 0.426. Note: As above

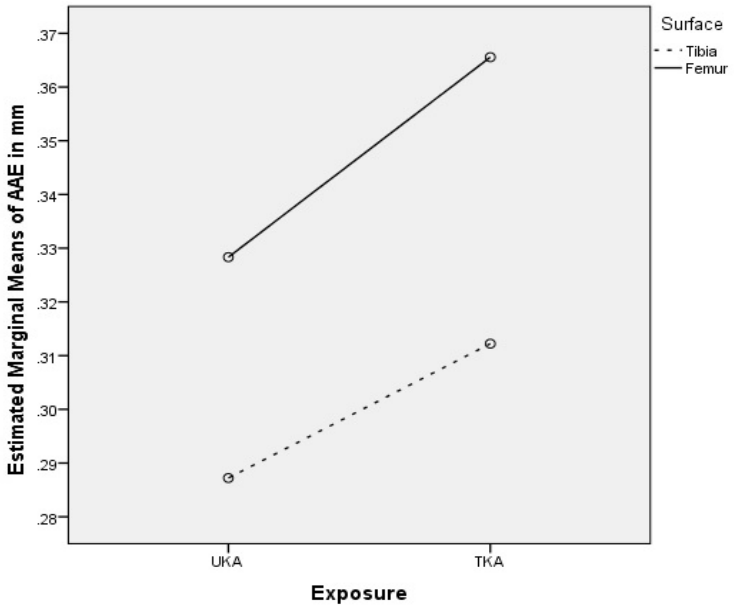

Figure 7.38 The two way interaction between the type of exposure and the type of surface for bone surface

No statistically significant difference; $F(1,8) = 4.293$; P = 0.072. Note: As above

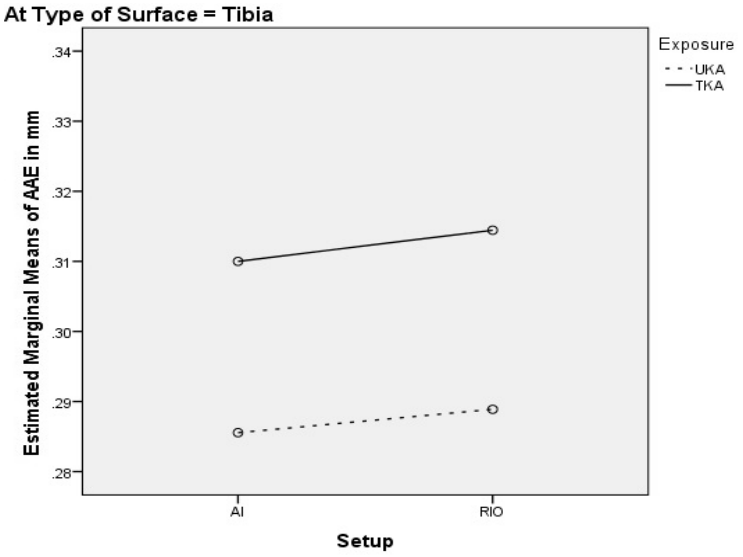

Figure 7.39 The three way interaction (A difference in the pattern of a 2-way interaction at levels of the third factor, tibia) between the type of setup, the type of exposure and the type of surface for bone surface

No statistically significant difference; $F(1,8) = 0.626$; P = 0.452. Note: As above

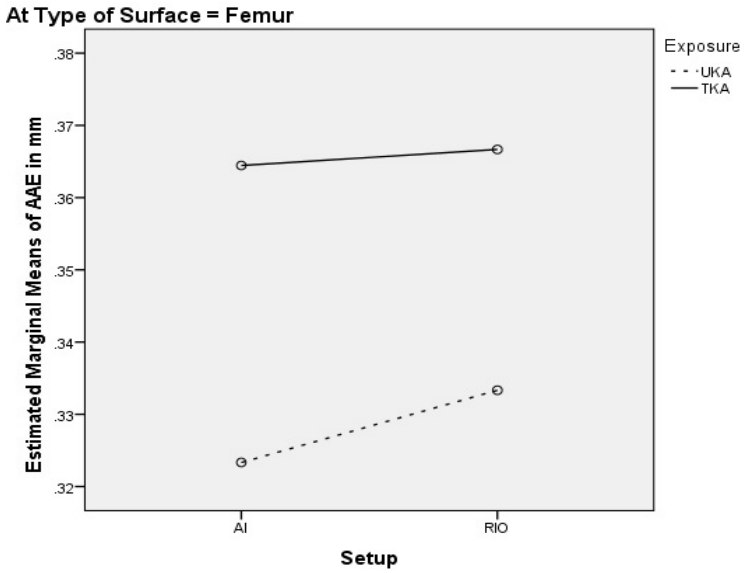

Figure 7.40 The three way interaction (A difference in the pattern of a 2-way interaction at levels of the third factor, femur) between the type of setup, the type of exposure and the type of surface for bone surface

No statistically significant difference; $F(1,8) = 0.626$; P = 0.452. Note: As above

Table 7.17 Summary of the effects of the independent variables on AAE between reference MRI and test laser scans for cartilaginous surface

The main and interaction effects of the independent variables indicating the P-value statistics, the significance of the statistics and the interpretation of the results.

Effects	**Independent variables**	**Cartilage**		
		P-value statistics	Significance	Interpretation
Main Effects	Type of Setup (Al, RIO)	$F(1,10) = 1.495$; $P = 0.25$	Not significant	No difference in two types of setup
	Type of Exposure (UKA, TKA)	$F(1,10) = 48.336$; $P = 0.0004$	Significant	Errors slightly larger with TKA exposure
	Type of Surface (Tibia, Femur)	$F(1,10) = 18.940$; $P = 0.01$	Significant	Errors slightly larger on femoral surface
Interaction Effects	Seup*Exposure	$F(1,10) = 0.03$; $P = 0.955$	Not significant	No interaction between setup and exposure
	Setup*Surface	$F(1,10) = 1$; $P = 0.341$	Not significant	No interaction between setup and surface
	Exposure*Surface	$F(1,10) = 1.312$; $P = 0.279$	Not significant	No interaction between exposure and surface
	Setup*Exposure*Surface	$F(1,10) = 0.766$; $P = 0.402$	Not significant	No interaction between setup, exposure and surface

Table 7.18 Summary of the effects of the independent variables on AAE between reference CT and test laser scans for bone surface

The main and interaction effects of the independent variables on AAE between reference CT and test laser scans indicating the P-value statistics, the significance of the statistics and the interpretation of the results.

Effects	**Independent variables**	**Bone**		
		P-value statistics	Significance	Interpretation
Main Effects	Type of Setup (Al, RIO)	$F(1,8) = 5.76$; $P = 0.073$	Not significant	No difference in two types of setup
	Type of Exposure (UKA, TKA)	$F(1,8) = 198.32$; $P = 0.00001$	Significant	Errors slightly larger with TKA exposure
	Type of Surface (Tibia, Femur)	$F(1,8) = 32.646$; $P = 0.00044$	Significant	Errors slightly larger on femoral surface
Interaction Effects	Seup*Exposure	$F(1,8) = 0.457$; $P = 0.518$	Not significant	No interaction between setup and exposure
	Setup*Surface	$F(1,8) = 0.703$; $P = 0.426$	Not significant	No interaction between setup and surface
	Exposure*Surface	$F(1,8) = 4.293$; $P = 0.072$	Not significant	No interaction between exposure and surface
	Setup*Exposure*Surface	$F(1,8) = 0.626$; $P = 0.452$	Not significant	No interaction between setup, exposure and surface

7.2 VALIDITY STUDY 2

The design of the validity study has already been explained (Methodology, section 6.7). In this section, bar graph (figure 7.41 and figure 7.42) along with error bars showing the variation in the measurements is shown for one of the 20 surfaces. In addition, a complete summary of all the 4200 measurements is reported in table 7.19.

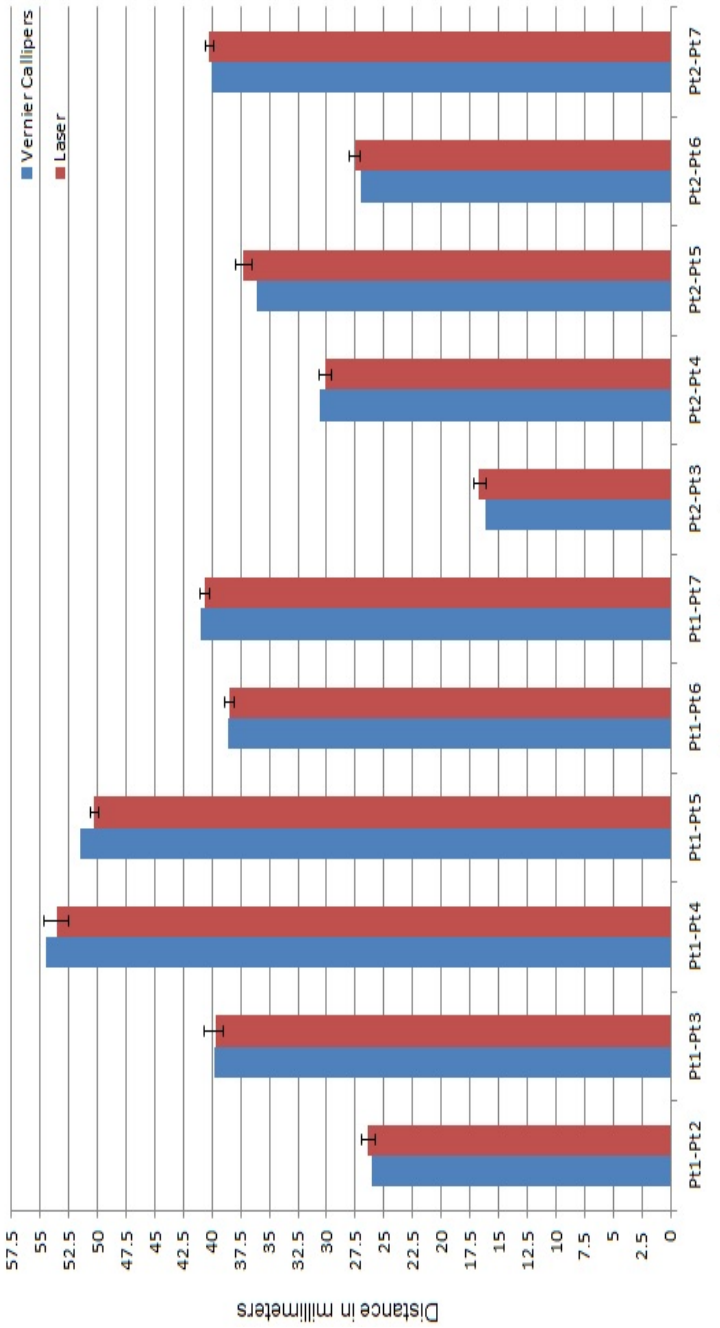

Figure 7.41 Bar graph for the comparison for the distance calculations (for first 11 pairs of screws) between vernier calliper and 3D laser scans.

Note: Blue bar is the measurement recorded by the vernier calliper, whereas red bar is the mean value of the measurements on the laser scan models. Error bars indicate the range of values (minimum and maximum values). All the measurement differences between vernier calliper and laser were statistically not significant; P>0.05

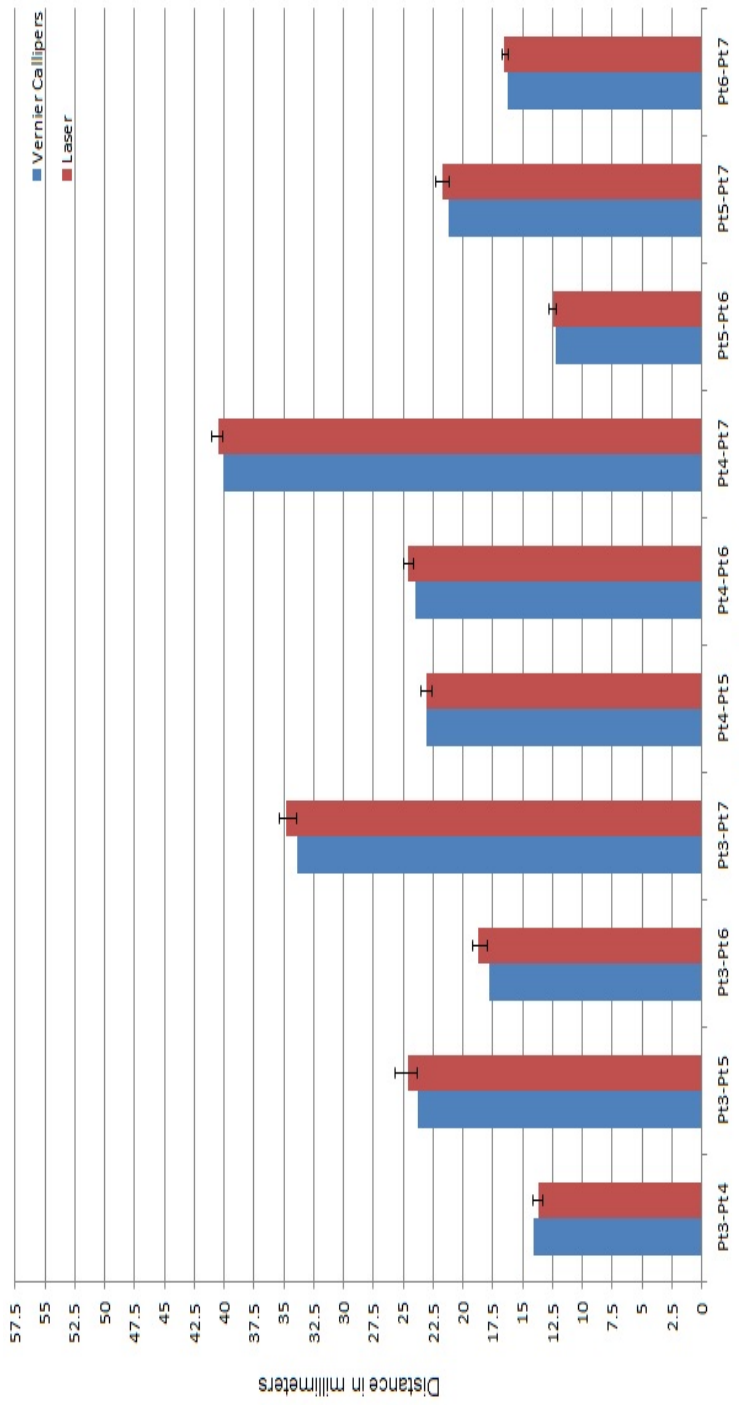

Figure 7.42 Bar graph for the comparison for the distance calculations (for last 10 pairs of screws) between vernier calliper and 3D laser scans

Note: Blue bar is the measurement recorded by the vernier calliper, whereas red bar is the mean value of the measurements on the laser scan models. Error bars indicate the range of values (minimum and maximum values). All the measurement differences between vernier calliper and laser were statistically not significant; P>0.05

Both the methods (laser and vernier calliper) were responsive so changing the differences between the screws and inter measurement system differences were small with 95% of the scanned measurements within 1 mm of the vernier callipers.

Table 7.19 Summary of the assessment of the distance calculations performed using direct measurements (vernier calliper) and those made on the 3D laser scans AAE; average absolute error between measurements, SD_{AE}; standard deviation of the absolute error, AAPE; average absolute percentage error, SD_{APE}; standard deviation of the absolute percentage error. Average and standard deviation of all the parameters is shown at the bottom of the table. Note: NS= Not significant. All the measurement differences between vernier calliper and laser were statistically not significant; P>0.05

Surface	AAE (mm)	SD_{AE}	AAPE (%)	SD_{APE}	P-value	Significance
1	0.49	0.17	1.66	0.65	0.930	NS
2	0.61	0.23	2.45	1.40	0.923	NS
3	0.44	0.12	1.66	0.91	0.972	NS
4	0.43	0.14	1.88	1.00	0.987	NS
5	0.48	0.13	1.72	0.63	0.993	NS
6	0.41	0.09	1.49	0.73	0.999	NS
7	0.38	0.13	1.47	0.76	0.992	NS
8	0.47	0.17	1.47	0.62	0.934	NS
9	0.50	0.12	1.55	0.67	0.996	NS
10	0.46	0.11	1.37	0.54	0.993	NS
11	0.49	0.12	1.88	0.80	0.967	NS
12	0.62	0.27	2.17	1.34	0.966	NS
13	0.59	0.23	2.18	0.97	0.986	NS
14	0.47	0.14	1.70	0.82	0.964	NS
15	0.43	0.20	1.50	0.65	0.976	NS
16	0.49	0.25	1.51	0.81	0.965	NS
17	0.39	0.14	1.49	1.10	0.978	NS
18	0.38	0.08	1.40	0.64	0.991	NS
19	0.30	0.09	1.19	0.70	0.974	NS
20	0.43	0.13	1.54	0.67	0.954	NS
Mean	0.46	0.15	1.66	0.82		
SD	0.08	0.05	0.31	0.24		

The average of the deviations (Average AAE) for all the 20 surfaces was less than 0.5mm (0.46mm) with an average SD_{AE} of 0.15 implying that 95% of the deviations (4200 measurements) lay within 0.46±0.3 (2 SD) i.e. within 0.16-0.76 mm absolute deviation which is suitable for orthopaedic surgeries. The inference of the outcomes is reported in the next chapter (section 8.3).

CHAPTER 8. DISCUSSION

Over the last decade, Computer Assisted Orthopaedic Surgery (CAOS) has emerged particularly in the area of minimally invasive UKA surgery. With the more conservative approach of UKA (as compared to TKA), which have been reenergised with the development of the advanced robotic systems, only the affected compartment (medial/lateral) is resected and an implant is placed to facilitate normal joint function. In robotically assisted surgeries, such as MAKOplasty® by MAKO Surgical Corps, patients' pre-operative CT scans are acquired and using a bespoke software package, the scans are segmented to generate a patient specific 3D knee model particularly emphasizing on the articulating surfaces of the tibio-femoral joint. Using this model and patient specific information, the surgery is planned on the computer well before the actual day of the surgery. One of the most important phases of the computer assisted surgical process in theatre is to develop a spatial relationship between this pre-operatively acquired patient specific model and the physical patient present in the operating theatre. It is possible to visualise key anatomical points around patient's knee joint in the pre-operated CT scan as well as to locate the same points on the actual patient during surgery using intra-operative sensors or probes. However, their spatial correspondence remains unknown until image registration is achieved. Image registration is the process that generates the relationship between the scan and the patient and allows the surgeon to visualise the 3D pre-operative scan data in-relation to the patient's anatomy in the operating theatre.

Current image registration techniques for CAOS involve using of a navigated hand-held probe and laborious digitisation of points along the articulating surface of

the knee joint. This intra-operative model is then fitted to the pre-operatively acquired CT scans and image registration is achieved. However, this surface digitisation approach is invasive and time consuming and adds further extra cost. The aim for this study was to develop a new, quick, cost effective, contactless and automated technique for CAOS using laser displacement sensor which could be used to produce 3D models of the human tibio-femoral joint in the operating theatre.

The first major stage of the study as explained in the Chapter 3 (Study Design) was to plan, build and test an automated 3D laser scanner capable of producing 3D models of the patients knee joint intra-operatively and specifically tuned to the optical properties of the cartilage and bone. Once the automated 3D laser scanning system was designed and developed, the extensive set of experiments were planned and implemented. The major investigation comprised of comparison between the pre-operative CT and MRI data with the intra-operative 3D laser scans on the cadaver knee joints. The second experiment was a validation study to compare the fixed distance measurements acquired using digital vernier callipers and the 3D scanning system. But before this, to understand the likelihood success of the technique, a set of pilot studies was carried out.

8.1 DISCUSSION OF PILOT STUDIES

De Vaus (1993) stated that “Do not take the risk. Pilot test first.” Pilot studies have a major role in the success of the research studies. They not only test the feasibility but also provide the effectiveness of the proposed methods especially if the approach is novel and innovative (Leon *et al.*, 2011). They are one of the most

important aspects of the study design and can be called ‘mini-versions’ of the full scale study which effectively deliver a pre-testing of the research instrument (Teijlingen and Hundley, 2002). For example, in social studies the research instrument can be questioners or sample interviews. In technologically novel studies, the research instrument can be a methodological approach or designs of devices. There are many definitions of pilot studies available which were listed by Thabanel *et al.* (2010). In general, it can be said that pilot studies are the preliminary studies which in hindsight demonstrate the potential of the proposed methods and instruments used to solve the research problem.

Pilot studies can be also termed as pass/fail tests. Practically they may not necessarily provide or identify the correct methodology or design to be applied for the larger studies; however, they certainly strike out the ones which would not be suitable. Teijlingen and Hundley (2002) stated the rationale to conduct the pilot studies. A few of the important factors can be classified as:

- Practicality: Assessing whether the proposed methods and designs can be applied in practice and are realistic and safe.
- Feasibility: Evaluating and analysing the potential of the proposed large scale study.
- Effectiveness and validity: Identifying the likelihood of the success of the actual studies and the validation of the method.
- Study design and analysis: Developing research questions, research hypothesis and research plan and working out the possible data analysis approach.
- Resource estimation: Estimating resources such as budget, time and manpower needed for the studies.

- Convincingness: Assuring funding bodies the competency of the research team to achieve the research goals.

A very important goal of the current studies was to acquire geometry of the articulating surfaces of the tibio-femoral joint and most importantly in clinical surgical conditions. As explained in the Chapter 4, the practicality of the studies was assessed a priory. Possible methods such as those based on ultrasound technology were first considered but were later discarded because of their limited resolution and accessibility issue within the complicated joint structures. After selecting laser as the potential shape acquisition sensor, an appropriate wavelength of light to use on bone and cartilage was found from the literature and was reused in practice. Suitable point laser sensors such as Microtak II were tested for precise distance measurements. Although they were highly accurate and precise when used on bone and cartilage, practically this point laser approach would have been quite time consuming, costly and due to the high power of lasers, clinically unsafe.

After an extensive review of the relevant literature, possible laser emitters of suitable wavelength and reduced (safe) power output were found which could give a safe and undistorted output (Marmulla *et al.*, 2004; Koo *et al.*, 2005; Trinh *et al.*, 2006; Bowers *et al.*, 2008; Thiruvenkatachari *et al.*, 2009; Umeda, 2010). A commercial FARO Laser ScanArm (Quantum V3) was used to scan the tibio-femoral joint of the bovine knee to mimic this approach. The scans acquired using this 660 nm laser arm showed satisfactory output of the soft tissues and most importantly of the articular cartilage and the bone surrounding the condyles as shown in figure 4.2 (a) and figure 4.2 (b). This section of the pilot studies established the feasibility of

the laser scanning method for acquiring 3D surface geometry of the tibio-femoral joints and a proof of concept for the data was so obtained.

In the past three decades, many attempts have been made to achieve precise, contactless measurement and 3D reconstruction of object surfaces. However, most of these approaches are impractical to use in the surgical environment and require complex and expensive equipment. In contrast, Winkelback *et al.* (2006) proposed a hand-held laser scanning technique (later commercialised as the DAVID Laserscanner) which is simpler, quick and inexpensive. The effectiveness of this line rather than point based laser scanning method was assessed by this prospect when scanning surface geometry of the porcine distal femoral condyles. Using 1 mW, 650 nm laser emitter (Price = less than £3) and 1.3 MP Logitech webcam (Price = £17.66), the target was scanned from multiple angles and the individual scans were merged to reconstruct an entire 3D model as shown in figure 4.3, figure 4.4 and figure 4.5. The time required to acquire each scan was less than 20 seconds. Post-processing of the data and merging of all the scans required less than 5 minutes even without automation and optimization. The shape fusion option in the DAVID Laserscanner allows the users to choose between seven different registration modes (free rotation, rotation around x-axis, rotation around y-axis, rotation around z-axis, manual alignment, and fine tuning options using pairwise fine registration and global fine registration). The scans were aligned using the free registration option in which a coarse registration between two scans at a time is achieved, without any constraints regarding rotation or translation. This approach cannot be applied on the scans acquired with low resolution or with minimum relative pose and contact between them. Once the scans were aligned, the fusion of scans was optimized by pairwise

fine registration. The software assumes reference co-ordinate systems are the same as those of the calibration planes. In our case, the object was stationary but if in case the object is rotated around the axis parallel to the X, Y or Z axis of the reference coordinate system, then shape fusion options such as rotation around X, Y or Z axes can be applied.

So by performing a series of Up-Down line scans of the condylar surface (using laser of correct wavelength) from different viewpoints and merging these scans using shape fusion based on pair wise free registration, a fused model of the exposed bone and the cartilage surface could be acquired without significant discontinuities between the scan segment or section of the bone surface. Armed with this proof of concept, we proceeded to implement a programme of study to confirm the suitability of this approach.

Having established the proof of concept and the capability of the scanning modules and the overall system, calibrated and phantom bone models were 3D laser scanned and were compared with commercial and conventional imaging techniques in the professional software package, Geomagic Qualify® 12. At first, an extensively calibrated dental model was scanned using commercial FARO laser arm as well using the DAVID Laserscanner hand-held technique. Multiple scans were combined to create a single surface as explained previously and shown in figure 4.6 (a) and figure 4.6 (b). The registration process has already been explained in the Chapter 4 and Chapter 6 and discussed early in the Chapter 7. After registering the models, a 3D deviation analysis was performed and an analysis report was generated. The overall average positive deviation of the test model (DAVID Laserscanner) with respect to the reference model (FARO) was 0.11 mm whereas the average negative

deviation was -0.18 mm. An average absolute error (AAE) of 0.16 mm with a standard deviation (SD_{AE}) of 0.2 mm was reported. The purpose of this mono-modal testing was to evaluate the discrepancy between the data obtained from an inexpensive hand-held laser scanning method and an expensive but highly accurate (±0.035 mm) commercial FARO LaserArm (FARO, 2015). The hardware cost for the hand-held technique was less than £30 whereas commercial arms such as FARO LaserArm or PLM 300 cost approximately £50,000.

During a short sabbatical as part of Sino-UK research student exchange program run by University of Strathclyde, a brief study was conducted at Beihang University, Beijing. An artificial (polyurethane) bone model of the first cervical vertebrae (atlas) was scanned using a high-performance micro-CT scanner, the SkyScan 1076. Similar to the previous approach, the model was scanned using the hand-held laser scanning technique and two models were registered in the Geomagic Qualify® 12. Post-alignment the deviation analysis indicated AAE of 0.48 mm, SD_{AE} of 0.32 mm, average positive deviation of +0.49 mm and average negative deviation of -0.44 mm. Taking into consideration that the reference model was acquired using an expensive and a very high performance micro-CT scanner, the average deviation between the reference model and the test model scanned using the DAVID Laserscanner technique was still less than a half millimetre.

This mono-modal and multi-modal imaging comparison confirmed that in spite of using very inexpensive components, high resolution scans of the target could be achieved. Based on these strategic pilot studies and the extensive literature review (Chapter 2) an automated 3D laser scanning system was developed using inexpensive

but optimum components. The following section elaborates the key findings of the designed validity experiments using fresh frozen human cadaveric tissues.

8.2 DISCUSSION OF CONCURRENT VALIDITY STUDY 1

In the experimental design, concurrent validity was explored between the intra-operative laser scans of the cadaveric knee joints and the pre-operative MRI/CT based models. As mentioned in the section 6.4, a total of 1600 separate laser scans were generated with two different variables each with two levels (Setup: Aluminium Extrusion, RIO and Exposure: UKA, TKA). The prime reason behind the 'setup' variable was to check whether there is a need of a bulky extrusion based setup or can we replace it with a more compact setup such as by mounting the scanning modules on the end of the RIO robotic arm or some other similar positioners. The scans were acquired with two different exposures to check whether the proposed methodology would work for both; UKA and TKA surgeries. Additionally, as stated in section 6.6.2, after analysing first proof of concept, we suspected that the methodology might produce higher deviations on the femoral condyles than on the tibial surfaces. Thus a third independent variable (Surface: Tibia, Femur) was included for the analysis to find out if this was so.

The results section 7.1 is divided into two sub-sections: 1) Reference scans from existing medical imaging methods taken pre-operatively compared to test scans acquired intra-operatively using established laser scanning method; and 2) Effects of the independent variables (setup, exposure and surface of the joint) on the dependent

variable (AAE). Similarly, this section of the discussion is divided into two sub-sections.

8.2.1 Reference-Test Model Analysis

The results presented in the section 7.1.1 are discussed here. They are divided into four groups: tibial cartilage scanning, femoral cartilage scanning, tibial bone scanning and femoral bone scanning.

A. Tibial Cartilage Scanning

At first, a detailed data analysis of single laser scan with a pre-operatively acquired MRI scan is depicted. The laser scan for this right lateral tibial surface was acquired using Aluminium extrusion setup through UKA exposure. The results displayed in table 7.1 show the alignment statistics between two models. It can be seen that average deviation (AAE) between the two models was only 0.20 mm with a standard deviation (SD_{AE}) of 0.27 mm. Figure 7.1 illustrates the AAE distribution and thus the spread of the deviations between the two models which indicates that errors were approximately normally distributed. Out of 2120 data pairs used for the alignment, 28.44% of pairs between the two models were within the deviation of ±0.1 mm. Moreover, deviations for 99.7% of all the data pairs were less than ± 0.94 mm. Figure 7.2 shows the spatial distribution of the AAE between the two models with a colour coded deviation bar. The green colour represents the ±0.1 mm of the deviation which is predominant in the central region along with the first yellow and first blue colour code (representing -0.31 mm and +0.31 mm respectively). It can be clearly seen that the absolute errors tend to increase as we go towards the edge of the scan area. This issue is further discussed and explained in the sub-section 8.2.2 A. Figure 7.3 shows the standard deviation distribution of the errors. 70 % of all the

deviations were within 1 standard deviation of the mean value, 94.95% within 2 standard deviation and 99.38% within 3 standard deviation which roughly follows the golden (68-95-99.7) three sigma rule for a normal distribution. The remaining of all the scans followed the same trend hence, we can conclude that the errors were normally distributed and parametric statistical tests such as Repeated measures ANOVA and t-tests are appropriate.

The summary of alignment statistics between the laser and MRI models of tibial cartilages for all the samples is shown in table 7.2. The results are divided into two different setups and two different exposures where each row represents the average of the scan repeats. The average of AAE with UKA exposure on both setups (Al extrusion and RIO arm) was 0.19 mm where the average SD_{AE} was 0.30 mm and 0.31 mm respectively. The average maximum ± deviations (d_{max}) for both the setups with UKA exposure were similar. On the other hand average AAE, SD_{AE} and d_{max} with the TKA exposure using the two setups were different and slightly higher than UKA exposure. However, this difference was of the order of a few millimetres ($1/100^{th}$ of a mm) and while statistically detectable, clinically it is not relevant in knee arthroplasty surgery. It can be also seen that the maximum SD of the average AAE was 0.07 mm which indicates the high concentration of values around the mean value.

B. Femoral Cartilage Scanning

Analogous to the tibial cartilaginous surfaces, laser scans for femoral surfaces were compared with the pre-operatively acquired MRI models. An example of the alignment statistics of one of the data comparisons is reported in table 7.3. The laser scan of this right femoral cartilage was acquired with a UKA exposure using the RIO

arm setup. The maximum deviations were slightly higher; the deviation distribution spread was slightly greater (1.88 mm and -1.38 mm). The total number of pairs used for the data comparison was 5266 out of which 32.47% were within ±0.1 mm of the deviation (the model value) and 98.48% were within ±0.94 mm. The colour coded map of the deviation distribution in figure 7.5 shows a similar pattern to that of previous tibial cartilage analysis. The central region is concentrated by green (±0.1mm) and the first yellow (0.31mm) and blue colours (-0.31mm). As before, the deviations were higher on the peripheral regions especially at the posterior medial region of the condyle. Standard deviation distribution of the absolute errors (figure 7.6) approximately follows the normal distribution curve with a distribution of 75.2%, 94.57%, and 98.52% for 1, 2 and 3 standard deviations respectively. Once again, the similar trend was followed by the rest of the scans but they generally showed higher AAE, SD_{AE} and d_{max} values as compared to the tibial surfaces. These trends were statistically analysed and are reported in the next section (8.2.2). However, some statistically significant differences were found in the context, they were again of the order of a few $1/100^{th}$ of a millimetre and hence clinically not relevant for arthroplasty surgery.

The summary of the alignment statistics for all the femoral cartilage MRI/laser alignment comparison is reported in table 7.4. As expected, the average of the AAE, SD_{AE} and d_{max} for all the four groups were higher in the femur as compared to the tibial surfaces. Average AAE for scans acquired with UKA exposures on Al extrusion and RIO setup as well as average SD_{AE} were still very similar. AAE, SD_{AE} and d_{max} for TKA exposures again appeared slightly higher. The average maximum deviation for femoral cartilage was higher (+2.73 mm and -2.54 mm). This higher

level of errors appeared to be clinically relevant. But these deviations were again located on the extreme edge of the surface. SD for the average AAE for all four groups was 0.03 mm.

C. Tibial Bone Scanning

Contrary to the intact cartilaginous surfaces, the bone surfaces had been exposed using a NAVIO PFS® burr as part of Robotic Surgical Training in our faculty. Thus, they were rougher than normal bone with drilled holes to fix implants. Table 7.5 displays the alignment statistics between a laser scan of the left medial tibia (acquired with RIO arm and TKA exposure) and the pre-operative CT based scan. An AAE of 0.31 mm and SD_{AE} of 0.46 mm indicate higher deviation values with longer tail for rough bone than smooth cartilage as would be expected but on average were still less than 0.5 mm. The deviation distribution shown in figure 7.7 indicates a cruder normal distribution of the errors with 22.41% of the total 4979 pairs in ±0.1 mm (the model value), 94.13% within ±0.94 mm and 99.08% within ±1.58 mm. Figure 7.8 illustrates that deviation distribution colour coded bar. The maximum absolute errors were increased to -2.19 mm near the dark blue region towards the edge of the model. However, once again errors in the central region were much less with green (±0.1 mm), light yellow (0.31 mm) and light blue (-0.31 mm) being predominant. The standard deviation distribution shown in figure 7.9 indicates 76.73% of the values were within 1 standard deviation, 93.82 within 2 standard deviations and 98.22 in 3 standard deviations and thus shows a general normal distribution.

For cartilaginous surfaces, the total number of scans was 440 (each for femur and tibia) whereas for bone regions, this number was 360 (each for femur and tibia)

due to two less samples. The alignment statistics presented in table 7.6 includes a summary of the 9 cadaveric samples for the tibial bone surfaces. The average of the AAE in this set appeared slightly higher as compared to the tibial and femoral cartilaginous surfaces. However, similar to the cartilaginous surfaces, the AAE, SD_{AE} and d_{max} for the scans acquired through UKA exposures looked less than those acquired through TKA exposures. Again, these differences were of the order of a few $1/100^{th}$ of a mm.

D. Femoral Bone Scanning

Similar to the previous three surfaces, an alignment statistics for one of the 360 scans for femoral bone surfaces is provided in table 7.7. The laser scan of the resected left medial femoral condyle was acquired with aluminium extrusion and through TKA exposure. The AAE and SD_{AE} between the laser and CT model were slightly higher than for cartilaginous surfaces with maximum deviations of 1.94 mm and -1.99 mm. Figure 7.10 shows the deviation distribution of the absolute errors which once again display a normal distribution. Model errors (24.08%) were concentrated within ±0.1 mm of deviation. More than 6% points were on the extremes of ±0.94 mm of deviation which validates higher value of AAE. The colour coded deviation map is displayed in figure 7.11 which once again demonstrates higher absolute errors between the laser and the CT model towards the edge of the surface. The hole of the surface could not be acquired due to the interference of the surrounding surface. The higher errors near the region of the hole indicate that absolute errors would probably increase if we were able to acquire the missing region and that peripheral regions are prone to larger errors whether at the edge of the surface or cut into it. Standard deviation distribution of the absolute errors in figure

7.12 shows 76.84, 93.92% and 98.21% of the values within 1, 2 and 3 standard deviation respectively which again indicates the approximate normal distribution.

The summary of the alignment statistics of all the 360 scans is presented in table 7.8. Results indicated similar trend as of the previous three surfaces. Average of AAE for UKA exposure with Al extrusion and RIO were 0.32 mm and 0.33 mm with average SD_{AE} of 0.44 mm each. Average AAE, SD_{AE} and d_{max} appeared higher for the scans acquired through TKA exposure.

8.2.2 Effects of the Independent Variables

The next stage of data analysis was to assess the effects of the three independent variables (setup, exposure and surface) on the AAE formulated between the laser scanned data and the pre-operative data (MRI/CT). As explained in section 7.1.2, cartilaginous and bone surfaces were analysed as separate groups as their pre-operative data acquisition methods were different (3D FLASH MRI for cartilage and CT for bone). From table 6.1, there were nine (operated) bone and eleven (intact) cartilaginous compartments. Furthermore, the interactions between the independent variables were studied and the results were reported in the section 7.1.2. The research hypotheses have already been presented in the Chapter 6, section 6.2.2.

A. Cartilaginous Surface

The results for the effects of independent variables on AAE are shown in Chapter 7 with the help of descriptive statistics, profile plots, bar graphs with error bars and box and whisker plots. The error bars in the bar graph specify the range of the readings within 95% confidence limit acquired in that particular set of measurements. Standard error is an indicator of the dispersion of the variability of

the sample mean from the population mean. In other words, standard error is a measure of the average by which the sample means vary from the population mean (Howitt and Cramer, 2008). The formula to calculate the standard error SEM is shown in the equation 8.1

$$SEM = \frac{SD}{\sqrt{N}} \tag{8.1}$$

Where SD is the standard deviation and N is the total number of samples. Thus, the standard error reduces as the sample size increases. The confidence intervals for the normal population are calculated by μ± SEM*1.96, where μ is the mean for all the samples. Standard error also provides a measure of how well the selected sample represents the actual population.

Table 7.9 shows the effect of the two types of setup on average AAE. The average AAE with Aluminium extrusion was reported as 0.246 mm and with RIO setup as 0.253 mm. Low standard errors indicate that each sample fairly represents the actual population. The ANOVA results throughout the thesis are reported in the same format as $F(df_{time}, df_{error})$ = *F*-value, P = P-value. Where df_{time} is the total number of levels of the factor minus 1 and df_{error} is the total number of samples minus 1. The SPPS output from the repeated measures ANOVA provides a profile plot (e.g. figure 7.13) displaying the mean values of AAE obtained using Al and RIO setup for cartilaginous surface. There was no statistically significant difference on AAE within two types of setups (Al and RIO), $F(1,10) = 1.495$; P=0.25 which indicates that the bulky Aluminium extrusion setup can be replaced with the positioning RIO arm which in our case would be already present in the theatre. Thus, it would be possible to make one compact system consisting of the robot and the

scanner which would save a lot of space in the operating theatre. Alternatively, an inexpensive positioning arm can be used in non-robotic surgery.

Additionally, the AAE obtained through the Al and RIO setup were analysed with a paired t test. Figure 7.14 and figure 7.15 illustrate the difference between the AAE with Al and RIO setup with the help of a bar chart including error bars for 95% confidence limit and a box and whisker plot respectively. Although, AAE obtained from RIO arm setup were slightly higher, the difference was statistically not significant, $P>0.05$ and the differences were sub-millimteric. The box plot for both the setups seemed symmetrical in nature. Hence, either setup was acceptable for accurate surgery.

The main effect of the type of the exposure is displayed in table 7.10. The average AAE with UKA exposure was 0.219 mm while with TKA exposure it was 0.279 mm. The profile plot obtained from ANOVA of the effects of two exposures on AAE is shown in figure 7.16. It indicates that the AAE with TKA exposure was significantly higher than UKA exposure, $F(1,10) = 48.336$; $P= 0.0004$. Figure 7.17 (bar graph with error bars) and 7.18 (box and whisker plot) represent the main effect of the type of the exposure on AAE. The AAE between the laser and MRI models with the TKA exposure was significantly higher than that with the UKA exposure, $P<0.05$. The box and whisker plot suggests that the group with UKA exposure was skewed slightly towards left. The group with TKA exposure was showed two outliers. It may seem that greater errors occurred with greater exposure but this was caused by exposing more edges to the scan where the surface was at a greater angle to the incident laser light and hence, the errors in depth perception produced larger

errors between the laser scan and the MRI/CT images. However, these errors remained sub-millimetric.

The results for the main effect of the third independent variable, type of the surface (tibia and femur) are presented in table 7.11. The average AAE for the tibial surfaces and the femoral surfaces were 0.225 mm and 0.273 mm respectively. The outcomes of the repeated measures ANOVA in figure 7.19 indicate that the AAE on the femoral surfaces was significantly higher than on the tibial surfaces, $F(1,10) = 18.940$; $P = 0.01$. Figure 7.20 shows the bar graphs with error bars which indicate a better spread of the AAE values for tibial surfaces than femoral surfaces. Box and whisker plot in figure 7.21 suggests a slightly right skewed distribution for tibial surfaces and left skewed distribution for femoral surfaces. The AAE reported on the femoral surfaces were significantly higher than the tibial surfaces, $P<0.05$. As above, this can be explained as the end of the femoral condyles contains more regions where the profile of the bone surface is at a greater angle to the incident laser light and hence where errors in depth perception produced larger errors between the laser scan and MRI/CT images. However, these errors were again sub-millimetric.

In other words, reason for the higher errors with TKA exposure (as compared with UKA exposure) and on femoral surfaces (as compared to tibial surfaces) is the ‘edge effect’ which affects most triangulation systems. This ‘edge effect’ can be seen in the colour coded deviation distribution maps (figure 7.2, figure 7.5, figure 7.8 and figure 7.11) where the higher % of the larger deviations appeared on the edges of the surfaces. 3D scanners and particularly laser based scanners tend to produce errors at the spatial discontinuities or edges of the surfaces being scanned. When the laser hits the surface edges, only a certain part is reflected from the actual point and some

reflection is always induced by the adjacent surfaces or the surface behind the object. Thus, the final signal is a mixture of the signals from the foreground and the background. This phenomenon is called as ‘mixed-pixel effect’ or ‘edge effect’. Due to the higher slope on the edge of the surface and the viewing direction of the scanner, the laser plane falls almost tangentially on the edge which leads to errors in location of these points in the cloud and thus causes inaccuracies and distortions in the scan (Herbert and Kortkov, 1992; Huising and Pereira, 1998; Bao and Yao, 2001; Boehler *et al.*, 2003; Zeibak and Filin, 2008; Tang *et al.*, 2009; Sanz *et al.*, 2011).

During the scanning, the scanner was always positioned such that the surface (tibial and femoral condyle) being scanned was in the centre of the camera image. With a greater incision, there is more exposure of the edges of the surface to the detector camera i.e. the additional surface exposure provided by the TKA incision is usually towards the peripheral region of the surface. Also, femoral condyles are more non-uniform and curved in their surface topography when compared to the tibial plateau. So, while scanning the femoral condyles, there is a higher slope of the target around the edges and around the curved region which causes higher deviations in those areas. Due to this, the laser plane E_{laser} (Chapter 2, section 2.6.3 B) incidents more tangentially on the femoral condyles as compared to the tibial plateau and thus the edge effect results in higher deviations. This could be a potential problem as in general, the laser scanner will eventually produce more errors on the curved surfaces than on the flat planes. However, optimising the scanning angle will help reduce this error. In this study, all the scans were acquired within the similar scanning angle. As stated earlier, the scanner and thus the scanning modules (laser and camera) were positioned in such a way that the centre of the camera and the centre of the target

(femoral condyle or tibial plateau) would approximately coincide. For every target, only one scan was acquired. But there is always an option of acquiring multiple scans from different angles and merging them to create a single model. The scanner can be positioned so that the centre of the scanner and hence the camera would overlap with the centre of the peripheral area being scanned. Thus, multiple scans can be acquired for every surface from different angles and can be fused to make a full model of that particular condyle. This would reduce the relative tangential planes as well the relative slope of the target with respect to the camera and the laser plane, E_{laser}.

Another simpler way of controlling the edge effect could be removing the peripheral region which is most likely to add higher magnitude of absolute deviations in the resultant average absolute error, AAE. However, in order to achieve this, a minimum percentage of the surface area needs to be standardised to successfully align the pre-operative CT/MRI and intra-operative laser models which would be as close as the original alignment. Also, manually removing the edges may add additional time in the data post-processing phase. But, this approach seems practical if it can be automated. A prototype for the mathematical model attempt to reduce the edge effects is explained in the section 8.5.

The interaction between the independent variables is reported in table 7.12. Figure 7.22 illustrates no significant interaction between type of setup (Al, RIO) and type of exposure (UKA, TKA), $F(1,10) = 0.03$; $P = 0.955$. The interaction between the type of setup (Al, RIO) and the surface type (Tibia, Femur) is shown in figure 7.23. The F-statistic suggests that there is no significant interaction between the two setups and surfaces, $F(1,10) = 1$; $P = 0.341$; however, it can be seen from the plot that perhaps with greater sample size this outcome may change. This is the type of

ordinal interaction which indicates higher errors with femoral surfaces and RIO setup. F-statistics for the type of exposure (UKA, TKA) and the type of surface (Tibia, Femur) indicates no significant interaction, $F(1,10) = 1.312$; P= 0.279 (figure 7.24).

The three way interaction between all three independent variables is presented in figures 7.25 and 7.26. The F-statistic shows that there is no significant interaction between the variables, $F(1,10) = 0.766$; P = 0.402; however, this is also a type of an ordinal interaction. When the interaction is disordinal i.e. when the lines of the cell-means plot cross each other, then the main effects of the variables become redundant. Ordinal interactions where lines in the plot do not cross over are not as pronounced as disordinal interactions and are usually not easy to interpret unless provided with enough statistical power thus researchers are permitted to examine and interpret the main effects of the variables (Loftus, 1978; Newman and Newman, 1994; Stevens, 1999; Andrew *et al.*, 2011). Therefore, in both cases of the ordinal interactions where the lines did not cross, it can be said that the interactions were not significant and main effects of the independent variables can be accepted. The summary of the effects of independent variables (setup, exposure, surface) on the dependent variable (AAE) for cartilaginous surface is reported in table 7.17.

The repeated measures ANOVA is an extension of paired t-test and is applied when measurements are made using more than one independent variable repeatedly over the sample and on the same dependant variable. A paired t-test can be used when all the sample participants are measured with a same one pair of independent variable (in 2 separate conditions) to assess the differences in the dependent variable (Singh *et al.*, 2013). Thus, when the interaction effects of the variables are not

significant, a paired t-test can be applied to check the individual effect (difference in the mean) of each independent variable on the dependent variable.

B. Bone Surface

A similar analysis approach was applied for cut bone surfaces i.e. the surfaces which were operated using NAVIO PFS® technique. The sample size was reduced to nine as compared to the eleven samples of the cartilaginous surfaces. Table 7.13 shows the main effects of the type of the setup on the AAE between the laser models and the CT models. The average AAE reported with Al setup was 0.321 mm whereas with the RIO it was 0.326 mm. The standard error was only 0.007 mm for both the setups which suggests that the samples fairly represent the population from where they come from. The profile plot acquired using repeated measures ANOVA is presented in figure 7.27 which states that although the deviations with the RIO setup were higher as compared with the Al setup, the main effect of the type of the setup on AAE between the laser and the CT models was not significant, $F(1,8) = 5.76$; $P = 0.073$. The bar graph in figure 7.28 indicates symmetric distribution of the deviations. The box and whisker plot in figure 7.29 shows a nearly symmetric distribution with Aluminium setup whereas the box plot of the RIO setup was right skewed. The main effect of the setup was found statistically not significant, $P>0.05$.

From table 7.14, the average AAE obtained through UKA exposure and TKA exposure were 0.308 mm and 0.339 mm. The ANOVA results for the main effects of the type of the exposure are shown in figure 7.30. The main effect of the TKA exposure was significantly higher than the UKA exposure. Thus, AAE between laser scanned models and CT based models for bone surface with the TKA exposures were significantly higher than the UKA exposures, $F(1,8) = 198.32$; $P = 0.00001$. The bar

graph in figure 7.31 and the box and whisker plot in figure 7.32 indicate that the AAE between the laser and CT models was significantly higher with TKA exposures than the UKA exposures, $P<0.05$. The box plots for both the exposures were nearly symmetric. The interquartile range for the TKA exposure was around 0.06 mm whereas for the UKA exposure it was around 0.05 mm.

Furthermore, the AAE between the CT and laser data was assessed with respect to the type of the surface (tibia and femur) being scanned (table 7.15). The profile plot in figure 7.33 from the Repeated measures ANOVA indicates that the AAE between the laser and CT models on the femoral surfaces were significantly higher than the tibial surfaces, $F(1,8) = 32.646$; $P = 0.00044$. The bar graphs in figure 7.34 and the box and whisker plot in figure 7.35 clearly indicate higher deviations on the femoral condyles than the tibial plateau. The box plot of the tibial surface was symmetrical whereas for the femoral surfaces it was slightly left skewed. The deviations on the femoral surfaces were found to be significantly higher than the tibial surfaces, $P<0.05$.

Similar to the cartilaginous surfaces, it can be predicted that the higher deviations between the laser and CT data with TKA exposures (as compared to the UKA exposures) and femoral surfaces (as compared to the tibial surfaces) were due to the edge effect which also indicates that the edge effect is inevitable in both the surfaces, the cartilage and the bone. The errors in the cut bone samples were fractionally higher than when the bone was covered with cartilage but again the deviations were marginal and sub-millimetric.

The descriptive statistics of the interaction between the independent variables on AAE for bone surfaces is reported in table 7.16. The maximum reported average

AAE was on the femoral surfaces with RIO setup and TKA exposure. The two way interaction between the two types of setups and the two types of exposures shown in figure 7.36 was statistically not significant, $F(1,8) = 0.457$; P = 0.518. The interactions between the type of the setup and the type of the surface (figure 7.37) was a type of an ordinal interaction (where the lines do not cross) in which the deviations on the femoral surfaces with the RIO setup seemed higher, but were statistically not significant, $F(1,8) = 0.703$; P = 0.426. Similarly, the two way interaction between the type of exposure and the type of surface (figure 7.38) was ordinal (again not as pronounced as disordinal as the lines do not cross) and showed higher deviations on the femoral surfaces with TKA exposure but it did not show any statistically significant difference, $F(1,8) = 4.293$; P = 0.072. The lines in the cell-means plot for the three way interaction between the type of the setup and the type of the exposure at tibial plateau (figure 7.39) were parallel and hence there was no significant interaction, $F(1,8) = 0.626$; P = 0.452. There was an ordinal interaction between the two setups and the two exposures at the femoral condyles (figure 7.40) which showed higher deviations with the TKA exposure acquired using RIO setup. For UKA exposures, deviations were higher on the RIO setup than the Al setup, but all these effects were statistically not significant, $F(1,8) = 0.626$; P = 0.452, allowing the results of the t-tests to be accepted.

The summary of the effects of independent variables (setup, exposure, surface) on the dependent variable (AAE) for bone surface is reported in table 7.18.

8.2.3 Inference of the Results

The research hypotheses stated in the Chapter 6, section 6.6.2 were assessed as follows and were identical for cartilaginous and bone surfaces.

1) Fail to reject the null hypothesis: There is insufficient evidence that the 'Setup' effect is present.
2) Reject the null hypothesis: The 'Exposure' effect is statistically significant where the deviations with TKA exposures were higher than the deviations with UKA exposures.
3) Reject the null hypothesis: The 'Surface' effect is statistically significant where the deviations on the femoral condyles were higher than the deviations on the tibial plateaux.
4) Fail to reject the null hypothesis: There is insufficient evidence that the two way 'Interaction' effect is present between the 'Setup' and the 'Exposure'.
5) Fail to reject the null hypothesis: There is insufficient evidence that the two way 'Interaction' effect is present between the 'Setup' and the 'Surface'.
6) Fail to reject the null hypothesis: There is insufficient evidence that the two way 'Interaction' effect is present between the 'Exposure' and the 'Surface'.
7) Fail to reject the null hypothesis: There is insufficient evidence that the three way 'Interaction' effect is present between the 'Setup', the 'Exposure' and the 'Surface'.

8.3 VALIDITY STUDY 2

The second stage in the experimental design was to assess the automated distance measurements acquired using the developed laser scanner with the manual measurements acquired using digital Vernier calliper. As mentioned in Chapter 6, section 6.7, 10 samples providing 20 surfaces (10 tibial and 10 femoral) were employed for this study. Instead of plotting the graphs for all the surfaces, a bar graph with error bars for one surface is presented in figures 7.41 and 7.42. The rest of the surfaces followed similar patterns. The red and blue bars in the graph represent the mean values of the distance measurements acquired using laser scanner and digital vernier calliper respectively. The error bars indicate the range (minimum and maximum) of the reported values. For example, the first bar in figure 7.41 for the measurement parameter Pt1-Pt2 shows that the mean vernier calliper (blue) reading was 26.08 mm whereas the mean laser reading was 26.38 mm with the max value of 26.90 mm and min value of 25.72 mm.

The statistical analysis for each surface for the measurements acquired by the laser scanner and the digital vernier calliper is reported in table 7.19. The average absolute error (AAE) values ranged from 0.3 mm to 0.62 mm with a mean of 0.46 mm and SD of 0.08 mm. The standard deviation of AAE (SD_{AE}) within each surface was also analysed which showed a mean of 0.15 mm with the SD of 0.05 mm. Furthermore, for every set of data, average absolute percentage error (AAPE) was reported which ranged from 1.19% to 2.45% with the mean of 1.66% and SD of 0.31%. The mean standard deviation of AAPE within each surface (SD_{AAPE}) was 0.82% with SD of 0.24% and min/max values of 0.54% and 1.40%. The measurements between two systems were analysed using two sample (independent

sample) t-test (Bell *et al.*, 2003). The P-values for each surface are reported in table 7.19. None of the differences were statistically significant, P>0.05 and in fact the P-values were very close to 1. Hence, we fail to reject the null hypothesis (Chapter 6, section 6.7.2) and can conclude that there is no evidence to suggest that the laser readings and vernier calliper distance measurements were different.

Normality tests were run using The Shapiro-Wilk Test in SPSS which showed normal distributions of the deviations for all the surfaces. In the paper provided by Bell *et al.* (2003), there were 22 samples with 15 measurements each whereas in this study there were 20 samples with 21 measurements each. To ensure the validity of the data analysis approach, the sensitivity to the assumption of normality of the validity data was tested by applying a non-parametric Mann–Whitney U test. It should be noted that in this test, medians which are more suitable for non-normal distributed data than the means are used, as means can be vulnerable to outliers whereas medians remain unaffected in spite of the presence of extreme data points in the data. The results showed no statistically significant difference between the laser and the Vernier calliper measurements, P>0.05.

8.4 TYPES OF ERRORS

In general, the digitising errors arising from laser scanning systems can be grouped into systematic errors and random errors (Huising and Pereira, 1998; Feng *et al.*, 2001; Xia *et al.*, 2009). Random errors are difficult to predict but systematic errors are usually constant and follow a similar pattern thus can be minimised to a

great extent if not eliminated. These errors from the context of this study are explored in this section.

8.4.1 Random Errors

Random errors are usually inherent, uncertain and difficult to control. They are usually beyond the control of the experiments and can be tedious to eliminate. Random errors can arise either due to the changes in the instruments or in the environmental conditions. They are generally small, scattered around the mean value and compensate for each other. Below is the list of possible random errors that occur in the laser triangulation systems.

- Speckle noise: This is the most common reason behind the random errors which occurs in the triangulation based laser scanners (Baribeau and Rioux 1991; Feng *et al.*, 2001). Speckle noise is usually due to the coherent illumination in combination with rough surfaces (Dorsch *et al.*, 1991). In other words, when the object is being scanned, then the image of the each point in the cloud is the result of the summation of contributions from all the scattering points of the object. For relatively rough objects, random phasors can pose effects on this summation which can lead to dark and bright speckles in the image (Baribeau and Rioux, 1991).
- Specular reflections from highly reflective surfaces and noises added by stray lights or unusual lighting conditions lead to measurement errors in the scans.
- Choosing wrong laser parameters such as wavelength, power, intensity and beam length for the surface being scanned can affect the quality of the scan.

8.4.2 Systematic errors

Systematic errors typically impose a predictable or a deterministic deviation from the true measurement value. So, as long as the external conditions remain unchanged, the systematic errors have a fixed value. Thus once known, systematic errors can be minimised or even eliminated using mathematical modelling or a similar approach (Feng *et al.*, 2001; Isheil *et al.*, 2011). These errors arise due to either a fault or a limitation of the instrument or a faulty handling of the instrument. Following is the list of systematic errors which generally affect the quality of the laser triangulation systems:

- Improper scanner design and components with inaccurate technical specifications can lead to overall inaccuracy of the system.
- As mentioned in the Chapter 5, section 5.3, calibration of the scanner is an important phase of the scanning and improperly calibrated scanner directly adds systematic errors.
- Misalignment of the scanning modules (camera and laser sensor), accidental deviation between their relative distance and/or incorrect measurement of the distance between them leads to artifacts in the scans.
- Edge effect results in higher deviations around the edges of the surfaces.

8.5 MINIMISING THE ERRORS

As mentioned before, due to their unpredictable nature, random errors are difficult to avoid. However, with proper logistics and attention, their likelihood can be minimised. On the other hand, systematic errors can be minimised using mathematical models and better design of the devices.

There are various methods which are designed to reduce the speckle noise in laser scanners. These include illumination of laser with a single fibre or a fibre bundle, superimposition of a pulse laser, fibre or fibre bundles with different lengths or refractive indices, liquid crystals, ultrasonic waves and other methods (Wang *et al.,* 1998). As explained in the Chapter 4 (Pilot Studies), the laser source was selected after extensive literature review and a set of pilot studies. Thus it is very unlikely that the laser had unsuitable parameters for the current application.

The systematic errors arising from the design of the scanner and components were not evaluated in the current study, thus they could not be modelled. However, sub-millimetric accuracies were achieved with an in-house robust bespoke prototype device. Edge effect can contribute to large errors from millimetres to decimetres (Boehler *et al.*, 2003). But in this study, all the maximum errors were sub-millimetric due to the relatively smaller size of the surfaces being scanned. Edge effect can be minimised by using an extremely well-focused laser sensor. Furthermore, a mathematical model for minimising the edge effect appearing on the laser scanned data could be developed such that the edges of the scan can be found automatically and a perimeter of the scan can be excluded. This would be a novel approach for eliminating the edge effect which would include following steps:

- Acquire the full scan of the model.
- Calculate the centroid of the model by averaging all the x, y and z co-ordinates.
- Find the Euclidean distance between the centroid and all the points on the model.
- Find the maximum value of this distance and use for example 90% (needs to be standardised) of that maximum value as a radius of the circular region which would be the area of interest (figure 8.2(a)).

- Similarly, the area of interest can be selected in different shapes, for example elliptical with corresponding parameters (figure 8.2(b)).
- Remove the area outside this region from the scan data.
- Use the remaining area for the alignment.

The reference co-ordinate system of the DAVID Laserscanner setup is always with respect to the calibration planes. Thus, the acquired scans (figure 8.1(a)) are in the same co-ordinate system as the calibration planes. Hence, before the edge points are deleted, the model needs to be aligned to a new co-ordinate system such that its centroid and the origin of this co-ordinate system coincide.

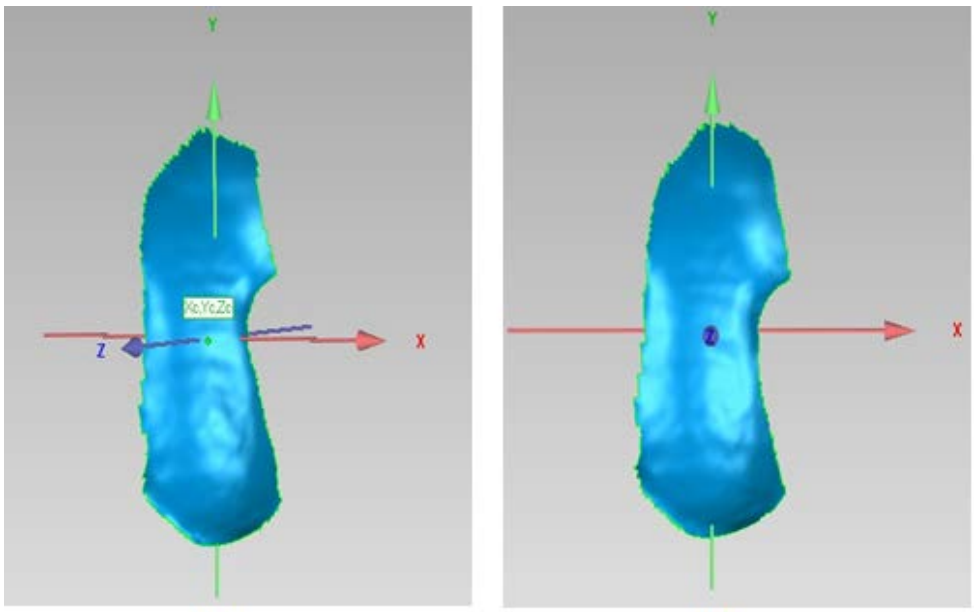

(a) (b)

Figure 8.1 Edge effect removal approach

(a): Right femoral laser scan aligned with the reference calibration planes co-ordinate system, Xc,Yc,Zc: Centroid of the model (b): Scan aligned with the world co-ordinate system with its centroid as the origin

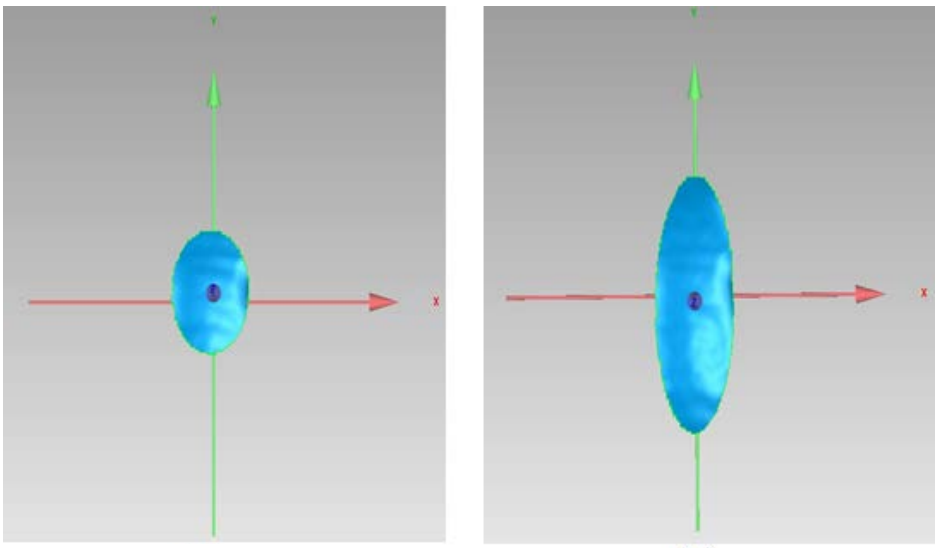

(a) (b)

Figure 8.2 Edge effect removal, area of interest
(a): Circular surface (b): Elliptical surface

This also means that the model needs to be translated and rotated in the space such that X and Y axes lie on the surface of the model and a perpendicular Z axis passes through the model as a depth axis (figure 8.1(b)). Thus by finding a cross product between X and Y axis co-ordinates, new Z axis co-ordinates can be formulated. After standardising, simulation software such as Matlab or even Microsoft Excel with the aid of Macro files can be utilised and can be run for all the scans as a stage of post-processing of the data. Further work needs to be done to decide how much surface area of the intra-operative scan would be enough to successfully register it with the pre-operative data. However, elimination of the edge effect would seem possible using this method. Even without this, the errors are sub-millimetric and hence, laser scanning as developed would appear suitably accurate for CAOS surgery.

8.6 RESEARCH LIMITATIONS

This sub-section discusses the overall limitations of the study and offers prospective for future research. Moreover, limitations of device and technique, experimental design and data collection methodology and data analysis approach are explored.

8.6.1 Limitations of Device and Technique

3D laser scanners have obvious advantages such as high speed, accuracy, precision and reproducibility. However, their strength depends on various factors. Stray light or an unidentified light source can affect the quality of the scans. Therefore, care has to be taken to avoid such light sources and most importantly any proximal light source which might enter the triangulation plane i.e. the plane formed by the camera, the laser source and the object being scanned. Shadow of the surrounding structures can produce gaps in the scans. Due to the awkward and complex structure of the tibio-femoral joint, occultation effect arises, especially produced by the femoral condyles on the tibial plateaux. Hence, the joint has to be flexed to its maximum limit in order to acquire the undistorted scan. Also, to avoid possible hindrance, the skin surrounding the incision needs to be retracted, especially in smaller UKA exposures to allow the detector camera to completely visualise the area under scrutiny.

In order to operate the prototype of automated controller (developed to control the laser movement), appropriate switches have to be pressed in a specific order and the user has to be adequately trained (section 5.5). As explained in the section 5.6, any small deviation in the relative position of the detector camera and the laser source can produce large measurement errors. Throughout all the experiments,

this occurred only twice but compromised the quality of the results. Thus, the scanner had to be recalibrated which in practice can affect the flow of the actual surgery. The laser and the camera module should be rigidly attached to a sub frame and housed firmly so they cannot be knocked. The scanner is suitable for the current application, but to scan extremely smaller structures and internal complex geometries, more advanced systems such as co-ordinate measuring machines (CMM) would need to be used.

The detector used in the study was an inexpensive webcam. The image acquisition was performed at a lower frame rate of 20 fps with a compromised resolution of 720p. This undoubtedly reduced the quality of the scans with increased acquisition time.

As explained in the literature review, surface matching approach can produce large errors if the original geometry of the surface being registered changes. Hence, this technique can only be reliable if the patient has not had any significant anatomical changes on the surface of the tibio-femoral joint between the time of the pre-operative scanning and the actual surgery.

8.6.2 Limitations of Experimental Design and Data Collection Methods

Currently, CT scanning is the most common method for acquiring pre-operative data in CAOS to be registered with patient's anatomy in the surgical theatre. The 3D models generated using CT scans depict the bone surface of the tibio-femoral joint, whereas in reality these surfaces are covered with the articular cartilage. Different approaches are employed to overcome this problem, for example, during MAKOplasty®, two different types of probes are used: A soft probe for

registering the cartilage and a sharp probe which penetrates through the cartilage to touch the bone surface. In the proposed study, a laser scanner would only provide the surface of the cartilage on the bone surfaces, thus instead of CT, MRI would be a preferred choice. Ultimately, the in-theatre scanner could be navigated and hence, could produce the articular surface on which the surgery can be planned and carried out. This imageless navigation would be very effective in terms of reduced cost, time and radiation dosage and would provide convenience to patients and clinicians.

The sample size in the study was limited, but the type of the sample (cadaver leg) was clinically realistic. In the experiments, for every combination of the independent variables, ten scan repeats were performed on each specimen and no significant differences were found between the repeats. More number of samples would strengthen the conclusion.

In the validity study, the distances between the landmark points were measured manually by pointing the digital vernier callipers positioning tips on their centres. This approach may be subject to intra and inter operator variation. As all the readings were taken by the same operator, inter operator variation is eliminated. This issue also applies while performing the distance measurements on the computer screen.

8.6.3 Data Analysis Approach

Due to the limited number of the samples, a normality tests such as Kolmogorov-Smirnov Test or Shapiro-Wilk Test would not have assured the normal distribution. After performing the deviation analysis between pre-operative and intra-operative models, it was observed that the errors were all normally distributed in general, thus the repeated measures ANOVA was justified. Some researchers have

used Friedman test as a nonparametric equivalent for one way repeated measures ANOVA (Marsh and Blair, 2008; Ellis *et al.*, 2012; Atzmueller *et al.*, 2014). However, there is no non-parametric equivalent for multiple factors repeated measures ANOVA (Mowles *et al.*, 2011; Wobbrock *et al.*, 2011). After analysing the results in the first study, it was observed that due to the edge effect, deviations between the pre-operative CT/MRI models and intra-operative laser models were higher on the edges of the surface. This effect could have also been analysed and eliminated in the validity study with an improved processing algorithm.

8.7 FUTURE RESEARCH

In the previous section, the limiting factors of this study are reported. This section of the thesis focuses on finding solutions and alternative options for these limitations. In addition, various innovative methods such as a hybrid approach of the multiple scanning modalities, navigating and optimizing the laser scanning system are discussed.

8.7.1 Device and Technique

As stated in the previous sub-section, stray light sources can produce large amount of noise in the output scans. During this study, the overhead lights were switched off. Also, for three samples the scans were acquired by covering the knee joint surface by a non-reflective black cloth. In both the methods, the scan quality was unaffected by any unwanted light source. With better designing of the assembly, a convex non-reflective plane covering the surface can be affixed to the scanner which would always avoid any possible interference of other light sources. In addition, this interference effect can also be supressed by controlling the exposure of

the camera. If in spite of the maximum flexion, the shadow of the femoral condyles obstructs the complete exposure of the tibial plateau to the detector camera, then a controlled external light source can be used to light up the darkened area and its interference can in turn be controlled by reducing the camera exposure.

As explained in the Chapter 5, sub-section 5.4.4 the use of switches and knobs from the user interface of the controller box can be digitised to be controlled on the computer. The motor speed and the laser intensity can be pre-set to eliminate the need of the controller box and thus of the extra person to take the scan. With an advanced setup such as using gyroscopes, the positioning of the scanner modules can be made very robust which would avoid any possible deviation and thus the need of the recalibration. Also, the current Arduino controlled setup can be modified to an advanced controller for better stability (Sven, 2011).

Currently, the laser sensor module being used in the study is of very low-price costing less than £3 and is of a very low power, 1 mW. Understandably, with an expensive and slightly high powered output laser sensor, the overall resolution of the system can be improved which would allow users to acquire scans of more complex and smaller surfaces. The surface registration approach can only be applied if the patients' anatomical geometry has not changed between pre and intra-operative procedure. With better management and logistics, the time between the pre-operative scanning and intra-operative surgery can be reduced to avoid possible implications.

8.7.2 Improving Experimental Designs and Data Collection Approach

Instead of using MRI as the pre-operative data acquisition method, a different approach can be applied. Using a simultaneous ultrasound method such as A-mode

ultrasound, if the cartilage thickness difference at the subchondral bone-articular cartilage interface can be worked out, then it can be possible to superimpose the surface of the cartilage on the bone surface acquired using the pre-operative CT. Thus, it would be possible to align the cartilage surfaces acquired using two techniques (laser and CT). Similar hybrid scanning approaches are explained in the sub-section 8.7.4 in detail.

Further scanning of more cadaver legs should be undertaken and more independent variables should be explored such as the distance between the centre of the scanner and the surface being scanned, sex of the patient, cross sectional area of the surface, etc. For the validity study, inter operator variation was eliminated but intra operator variation should be investigated by repeating the same measurement of the digital vernier calliper acquired by the same operator to check the variation.

8.7.3 Data Analysis

As the sample size and the scan repeats will increase, the standard error will reduce. In the validity study, eight to ten markers can be inserted around the peripheries of the surface and similarly at the central region. Then the distance variation within the peripheral markers and the central markers can be compared. This would justify the fact that the deviation around the peripheral region of the surface is higher than that of the central region as per the camera plane due to the edge effect.

8.7.4 Hybrid Approach

As explained in the Chapter 2 (literature review), ultrasound methods to acquire bone profiles for CAOS applications are developing techniques. Although it

offers obvious benefits such as non-invasiveness and cost effectiveness, its suitability in terms of resolution, time, penetration and accessibility is still under scrutiny (Amin *et al.,* 2003; Barrat *et al.,* 2006). While ultrasound technique is unlikely to scan shape sufficiently and accurately, there is no question about the ability of ultrasound and indentation based techniques to comprehend the biomechanical properties of the articular cartilage and subchondral bone. Researchers have successfully quantified the articular cartilage to differentiate between healthy and damaged arthritic cartilage using techniques based on A-mode ultrasound, UBM (Ultrasound Biomicroscopy), intravascular ultrasound, ultrasound indentation, etc. The parameters include mechanical properties of the cartilage for e.g. Young's modulus, thickness, volume as well as its acoustic properties such as apparent integrated backscatter (AIB), ultrasound roughness index (URI) and integrated reflection coefficient (IRC). (Toyras *et al.*, 1999; Saied *et al.*, 2000; Hattori *et al.*, 2003; Laasanen *et al.*, 2003; Saarakkala *et al.*, 2003; Saarakkala *et al.*, 2004; Laasanen *et al.*, 2006; Wang *et al.*, 2007; Kuroki *et al.*, 2008; Huang and Zhen, 2009; Aula *et al.*, 2010; Niu *et al.*, 2012).

In all these studies, high frequency ultrasound transducers (usually between 12-55 MHz) were used to examine articular cartilage properties whereas 0.1-1 MHz ultrasound frequency range was applied to study the degeneration of bones. However, Aula *et al.* (2010) demonstrated the feasibility of 5 MHz ultrasound for simultaneously measuring acoustic properties of articular cartilage and subchondral bone.

A similar methodology could be applied to the methods in the current study by using a hybrid approach of simultaneous scanning using laser and ultrasound

modalities. For example, the 3D model of the right femoral condyles shown in figure 8.3 (a) was acquired using the developed scanner. A degenerated cartilage can be clearly seen on the lateral side which is marked in figure 8.3(b).

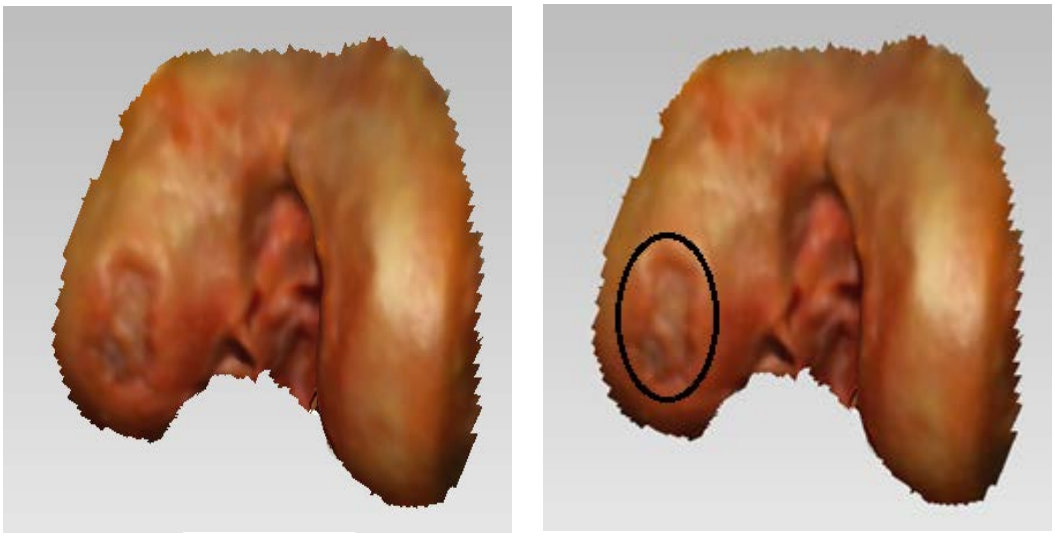

(a) (b)

Figure 8.3 Coloured 3D laser scans of the right femoral condyle
(a): Lateral condyle showing the articular cartilage lesion (b): Degenerated cartilage pointed within the border

So using the laser scanner, the 3D model of the surface as well as the true colour of the surface can be acquired in less than 10 seconds. This scan would then be registered with the pre-operative scan or could be used as a standalone measure for imageless navigation. With the help of the laser scan, it would be possible to narrow down the region of interest. In the registered scan, the degenerated cartilage, subchondral bone and the surroundings can then be assessed using a simultaneous high frequency ultrasound modality. A pulse-echo ultrasound system working at 5 MHz suggested by Aula *et al.* (2010) would be ideal for this purpose. In addition to this, an ultrasound indentation technique proposed by Toyras *et al.* (1999) can be used to estimate the mechanical properties of the articular cartilage such as the Dynamic modulus and Young's modulus. Using this method, only selected area can

be dissected making the CAOS and UKA a more conservative methodology. Instead of using one modality alone, the simultaneous scanning by laser and ultrasound can be a more effective and quicker solution for quantitative assessment of the degenerated tissues in situ.

8.7.5 Navigating the Devices

In addition to the quantitative assessment of the tissues, the hybrid approach also has the potential of eliminating the need of the pre-operative planning. Using standard optical tracking system such as Vicon Bonita (Vicon Motion Systems Ltd. UK), the scanning devices can be navigated in 3D space. This can be done by defining a rigid body comprising a set of passive markers onto the scanning module and by knowing the geometry of the laser sensor module and by correlating the output voltage reading to the distance between the centre of the module and the surface being scanned. Similarly, once if the ultrasound system is also navigated in the 3D space, then the surgery can be planned intra-operatively. Although this may add extra time in the actual surgery, the entire pre-operative CT scanning stage inducing the radiation dose can be eliminated so reducing the cost and improving the patient experience.

8.7.6 Miniaturizing the System

In the current study, the scanner comprises of the scanning modules (the laser sensor and the detector camera), a controller box and a positioner. A bespoke positioner used in this study was constructed using an aluminium extrusion assembly. Additionally, the MAKO Surgical RIO® arm was used as the positioner. It has already been demonstrated that changing the setup had no significant difference on the AAE between the laser scans and the pre-operative (CT/MRI) models. Thus,

the extrusion positioner can be replaced with the robotic arm which would save space in the surgical theatre.

As explained in the section 5.2, there is a trade-off between the resolution and the frame rate of the camera. Current image acquisition was performed with the resolution of 720p and a frame rate of 20 fps. To reduce the scanning time, either the speed of the motor has to be increased to acquire more points in a lesser time or the camera frame rate has to be increased. Increasing the motor speed with this frame rate would distort the quality of the scans as the camera would be unable to acquire sufficient number of points in the one panning direction of the laser. Also, there is a high possibility that increasing the frame rate would result in reduced resolution which might increase the average absolute error (AAE) between the models. Similarly, compromising on the frame rate would increase the resolution but also increase the time of acquisition. Commercially available high speed CMOS cameras such as Phantom can provide resolution up to 1600p or even 2304p with frame rates of 1450 and 940 respectively (Vision Research, 2015). Certainly, these cameras would not only increase the frame rate but also provide high resolution images resulting in high quality scans in a much reduced acquisition time.

In addition, wireless cameras can be used instead of the webcam used in the study which will minimise the accidental unplugging of the camera from the system. The current laser module can be switched with the smaller modules or even with a fibre optic laser system. Furthermore, even the process of sweeping of the laser line over the surface of the object can be replaced with an advanced approach such as by introducing laser mirrors in the system. For example, dielectric laser mirrors can be used to reflect the laser beam on the surface of the object. Thus, instead of moving

the laser beam over the surface of the object, precise deflections of the beam by mirrors can accomplish the task which would save additional time.

However, despite of all these possible improvements, the current system proved to be suitable for scanning knee joint surface geometry in theatre and to an accuracy suitable for CAOS knee surgery.

CHAPTER 9. CONCLUSION

Computer Assisted Orthopaedic Surgery (CAOS) has proven to be one of the landmarks in the knee replacement surgery especially for treating knee Osteoarthritis (OA). Although CAOS systems are usually expensive and bulky to set up in the operating theatre environment, they have raised the standards of the overall outcome of arthroplasty techniques in terms of accuracy, precision and reproducibility (Adili, 2004). As relatively new, there are still only a few surgeons who have adopted CAOS and its long term outcomes are still awaited.

This study has addressed an important issue by providing a 'proof of concept' to replace the current invasive, time consuming and costly manual intra-operative surface acquisition and image registration process of CAOS using 3D laser scanning. After an extensive literature review and a set of pilot studies, a clinically safe laser sensor with suitable parameters (650 nm, 1 mW) was chosen to acquire the 3D digitised data of the articular cartilage and bones in the human tibio-femoral joints. Using this laser sensor a quick, inexpensive, contactless and automated 3D laser scanner was developed. The total cost of the scanning hardware was less than £200. The overall time for scanning, post-processing and the registration required less than 4 minutes for every model. On the other hand, registering each bone surface using MAKO Surgical registration approach required more than 8-10 minutes. In this study, the feasibility of using a novel laser scanning technique was demonstrated where by acquiring scans of the tibio-femoral joint in theatre, complete 3D models of the geometry and true surface colour can be developed which can be registered with the pre-operative scan.

A series of experiments (Concurrent Validity Study 1) showed that the average deviations between the pre-operative CT/MRI models and the intra-operative 3D laser scans were in general less than half a millimetre. This suggests that the system can repeatedly acquire accurate 3D scans of the tibio-femoral cartilage and bone and most importantly in the operating theatre environment. The second validity study has proven that the developed laser scanner measurements were accurate, precise and repeatable as compared to the standard measurement system (the vernier calliper). The sample size of 20 surfaces should be born in mind with the sub-millimetric size of the deviations.

REFERENCES

Abdeen AR, Collen SB, Vince KG (2010). Fifteen-year to 19-year follow-up of the Insall-Burstein-1 total knee arthroplasty. J Arthroplasty. 25:173-178

Adili A (2004). Robot-assisted orthopaedic surgery. Surgical Innovation 11(2):89-98

Aglietti P, Buzzi R, De Felice R, Giron F (1999). The Insall-Burstein total knee replacement in osteoarthritis: a 10-year minimum follow-up. J Arthroplasty. 14:560-565

Akizuki S, Mueller JK, Horiuchi H, Matsunaga D, Shibakawa A, Komistek RD (2009). In vivo determination of kinematics for subjects having a Zimmer Unicompartmental High Flex Knee System. J. Arthroplasty. 24:963-971

Alphonso B (2013)
http://www.studyblue.com/notes/note/n/kins-chapter-13-knee-/deck/8533161
DOA: 16-03-2011, 15.50

Altman RD (1995). The classification of osteoarthritis Rheumatol Suppl. 43:42-43

American Academy of Orthopaedic Surgeons (2014)
http://orthoinfo.aaos.org/topic.cfm?topic=a00325
DOA: 02-02-2011, 15.00

Amin D, Kanade T, DiGioia A, Jaramaz B (2003). Ultrasound registration of the bone surface for surgical navigation. Comput. Aided Surg. 8:1-16

Andrew DPS, Padersen PM, McEvoy CD (2011). Research Methods and Design in Sport Management, Champaign, IL: Human Kinetics

Arámbula FC, Padilla MAC (2003). Computer Assisted Surgery AIP Conference Proceedings. 682:38-45

Argenson JN, Chevrol-Benkeddache Y, Aubaniac JM (2002). Modern uni-compartmental knee arthroplasty with cement: a three to ten year follow-up study. J Bone Joint Surg Am. 84:2235–2239

Arthritis research UK (2013). Osteoarthritis in General Practice Data and Perspectives.
http://www.arthritisresearchuk.org/arthritis-information/data-and-statistics/osteoarthritis.aspx
DOA: 05-01-2015, 14.00

Artro (2008)
http://www.artro.lt/en/knee_joint_arthroscopy_
DOA: 18-03-2014. 15.05

Ashburner J, Friston KJ (2003). Rigid body registration in Frackowiak RSJ, Friston K, Frith C, Dolan R, Price CJ, Zeki S, Ashburner J (Eds.) "Human brain function" (2nd Ed). Boston. Elsevier Academic Press. pp-1144

Athanasiou KA, Rosenwasser MP, Buckwalter JA, Malinin TI, Mow VC (1991). Interspecies comparisons of in situ intrinsic mechanical properties of distal femoral cartilage. J Orthop Res. 9(3):330-40.

Atzmueller M, Ernst A, Krebs F, Scholz C, Stumme G (2014). On the evolution of social groups during coffee breaks in Proceedings of the companion publication of the 23rd international conference on World wide web companion (WWW Companion '14). International World Wide Web Conferences Steering Committee, Republic and Canton of Geneva, Switzerland. 631-636

Audette MA, Ferrie FP, Peters TM (2000). An algorithmic overview of surface registration techniques for medical imaging. Medical Image Analysis. 4:201–217

Aula AS, Toyras J, Tiitu V, Jurvelin J (2010). Simultaneous ultrasound measurement of articular cartilage and subchondral bone. Osteoarthritis and Cartilage. 18:1570-1576

Banger M, Rowe PJ, Blyth M (2013). Time Analysis of MAKO RIO UKA Procedures in Comparison with the OXFORD UKA. Bone Joint J 95(B): Supp. 28 89

Banks SA (2009). Haptic robotics enable a systems approach to design of a minimally invasive modular knee arthroplasty. Am J Orthop. 38(2):23-27

Bao J, Yao Y (2001). Analysis and Prediction of Edge Effects in Laser Bending. Journal of Manufacturing Science and Engineering. 123:53-61

Baribeau R, Rioux M (1991). Influence of speckle on laser range finders. Applied Optics. 30:2873-2878

Barratt DC, Penney GP, Chan CSK, Slomczykowski M, Carter TJ, Edwards PJ, Hawkes DJ (2006). Self-Calibrating 3D-Ultrasound-Based Bone Registration for Minimally Invasive Orthopedic Surgery. IEEE Transactions on Medical Imaging. 25(3):312-322

Barrett WP, Mason JB, Moskal JT, Dalury DF, Oliashirazi A, Fisher DA (2011). Comparison of radiographic alignment of imageless computer-assisted surgery vs conventional instrumentation in primary total knee arthroplasty. J Arthroplasty. 26(8):1273-1284

Barrick F (2002). Fluoroscopic image guided orthopaedic surgery system with intraoperative registration; Google Patents. US Patent 6,477,400

Bashir A, Gray M, Hartke J, Burstein D (1999). Non-destructive Imaging of Human Cartilage Glycosaminoglycan Concentration by MRI. Magnetic Resonance in Medicine 41:857–865

Baucer DC, Hunter DJ, Abramson SB, Atturx M, Corr M, Felson D, Heinega˚rd D, Jordan JM, Kepler TB, Lane NE, Saxne T, Tyree B, Kraus VB (2006). Classification of osteoarthritis biomarkers: a proposed approach. Osteoarthritis Cartilage. 14(8):723–727

Beasley RA (2012). Medical Robots: Current Systems and Research Directions Journal of Robotics. 1-14

Bell A, Ayoub AF, Siebert P (2003). Assessment of the accuracy of three-dimensional imaging system for archiving study models. Journal of orthodontics. 30:219-223

Bellemans J (2013). Robotic in TKA in Catani F, Zaffagnini S (Eds.) "Knee Surgery using Computer Assisted Surgery and Robotics". Springer, London. pp 57-61

Benjamin CMa (2011)
http://www.nlm.nih.gov/medlineplus/ency/presentations/100225_1.htm
DOA: 13-03-2014, 13.00

Besl PJ (1988). Active, Optical Range Imaging Sensors. Machine Vision and Applications. 1:127-152

Besl PJ, Mckay ND (1992). A method for registration of 3D shapes. IEEE transactions on pattern analysis and machine intelligence. 14(2):239-256

Betting F, Feldman J, Ayache N, Devernay F (1995) in Ayache N. (Ed.) "A New Framework for Fusing Stereo Images with Volumetric Medical Images". Proc. CVRMed '95, Springer-Verlag, Nice, France. pp. 30-39

Beuf O, Ghosh S, Newitt DC, Link TM, Steinbach L, Ries M, Lane N, Majumdar S (2002). Magnetic resonance imaging of normal and osteoarthritic trabecular bone structure in the human knee. Arthritis & Rheumatism. 46: 385–393

Bhosale AM, Richardson JB (2008). Articular cartilage: structure, injuries and review of management. Br Med Bull. 87:77-95

Bian Q, Wang YJ, Liu SF, Li YP (2012). Osteoarthritis: genetic factors, animal models, mechanisms, and therapies. Frontiers in Bioscience (Elite Edition). 4:74-100

Blackburn T, Craig E (1980). Knee Anatomy: A Brief Review. Phys Ther. 60:1556-1560

Blackburn WD Jr, Chivers S, Bernreuter W (1996). Cartilage Imaging in Osteoarthritis. Semin. Arthritis Rheum. 25:273-281

Bland JM, Altman DG (1986). Statistical methods for assessing agreement between two methods of clinical measurement. Lancet. 8476:307-310

Blom AW, Brown J, Taylor AH, Pattison G, Whitehouse S, Bannister GC (2004). Infection after total knee arthroplasty. J Bone Joint Surg Br. 86(5):688-691

Bluebelt Technologies (2014)
http://www.bluebelttech.com/blue-belt-technologies-announces-first-NAVIO-unicondylar-knee-replacement-performed-in-france/
DOA: 04-03-2014, 20.36

Boehler W, Bordas VM, Marbs A (2003). Investigating laser scanner accuracy. International Archives of Photogrammetry. Remote Sensing and the Spatial Information Sciences. 34(5):696-701

Boehler W, Marbs A (2002). 3D Scanning Instruments at 'Proceedings of the CIPA WG 6 International Workshop on Scanning For Cultural Heritage Recording', Corfu

Bowers ME, Trinh N, Tung GA, Crisco JJ, Kimia BB, Fleming BC (2008). Quantitative MR imaging using "LiveWire" to measure tibiofemoral articular cartilage thickness. Osteoarthritis Cartilage. 6(10):1167-1173

Brandt G, Zimolong A, Carrat L, Merloz P, Staudte HW, Lavallee S, Radermacher K, Rau G (1999). CRIGOS: A compact robot for image guided orthopaedic surgery. IEEE Trans. Inform. Technol. Biomed. 3:252-260

Brisson G (2008). The Precision Freehand Sculptor: A robotic tool for less invasive joint surgery. PhD Thesis, Carnegie Mellon University

Brugioni DJ, Falkel J (2004). Total Knee Replacement and Rehabilitation. Hunter House Inc. publishers, Alameda

Bucholz R, Macneil W, Fewings P, Ravindra A, McDurmont L, Baumann C (2000). Automated rejection of contaminated surface measurements for improved surface registration in image guided neurosurgery. Stud Health Technol Inform 70: 39-45

Buckwalter JA, Hunziker EB, Rosenberg LC (1988). Articular cartilage: Composition and structure in Woo SL, Buckwalter JA (Eds.) "Injury and repair of the Musculoskeletal Soft Tissues". American Academy of Orthopaedic Surgeons, Park Ridge. pp 405-425

Buckwalter JA, Mankin HJ, Grodinzsky AJ (2005). Articular Cartilage and Osteoarthritis. AAOS Instructional Course Lectures. 54:465-480

Carl JD, Olsson LE, Leander P, Ekberg O, Dahlberg L (2003). Delayed Gadolinium-Enhanced MRI of Cartilage (dGEMRIC) in Early Knee Osteoarthritis. Magnetic Resonance in Medicine. 49:488-492

Carrillon Y (2008). Imaging knee osteoarthritis in Bonnin M, Chambat P (Eds.) "Osteoarthritis of the knee". Springer. pp 3-14

Carrillon Y (2012). Imaging of the patellofemoral joint in Bonnin M., Amendola NA, Bellemans J, MacDonald SJ (Eds.) "The knee joint: Surgical Techniques and Strategies". Springer Verlag Berlin Heidelberg. pp 525-531

Castillo RAC, Wahrburg J (2007). Improving robot arm control for safe and robust haptic co-operation in orthopaedic procedures. The International Journal of Medical Robotics and Computer Assisted Surgery. 3:316-322

Chen XN, Xia Q, Zhang SH, Zhou Y (2005). 3D Laser Scanner System for Surveying and Engineering in Proc. of the ISPRS joint conf. of 3rd Int. Symp. Remote Sensing and Data Fusion over Urban Areas and 5th Int. Symp. Remote Sensing of Urban Areas, Tempe, AZ, USA

Cheng T, Zhao S, Peng Z, Zhang X (2012). Does computer-assisted surgery improve postoperative leg alignment and implant positioning following total knee arthroplasty? A meta-analysis of randomized controlled trials? Knee Surg Sports Traumatol Arthrosc. 20:1307–1322

Cheung A, Goh SK, Tang A, Keng TB (2008). Complications of total knee arthroplasty. Current Orthopaedics. 22:274-283

China SouVR Co., Inc. (2008)
http://en.souvr.com/
DOA: 08-07-2011, 15.30

Chiropractic books (2008)
http://www.chiropractic-books.com/Knee-Joint-Distraction.html
DOA: 17-03.2013. 18.10

Cicuttini FM, Wluka AE, Stuckey SL (2001). Tibial and femoral cartilage changes in knee osteoarthritis. Ann Rheum Dis. 60:977-980

Clarke RH, Horsley VA (1906). On a method of investigating the deep ganglia and tracts of the central nervous system (cerebellum). Br Med J. 2: 1799-1800

Cobb J, Pearle A (2013). Unicompartmental Knee Arthroplasty: Robotics in Catani F, Zaffagnini S (Eds.) “Knee Surgery using Computer Assisted Surgery and Robotics”. Springer, London. pp 95-104

Cohen ZA, Mccarthy DM, Kwak SD, Legrand P, Fogarasi F, Ciaccio EJ, Ateshian GA (1999). Knee cartilage topography, thickness, and contact areas from MRI:in-vitro calibration and in vivo measurements. Osteoarthritis and cartilage. 7:95-109

Colizza WA, Insall JN, Scuderi GR (1995). The posterior stabilized total knee prosthesis: assessment of polyethylene damage and osteolysis after a ten-year-minimum follow-up. J Bone Joint Surg Am.77:1713-1720

Coon T, Driscoll M, Conditt MA (2008). Does less medial tibial plateau resection make a difference in UKA? at ‘Proceedings of the 21st annual congress of the international society of technology in arthroplasty’, International Society for Technology in Arthroplasty, Sacramento. SUPP. I 157:274

Cosio FA, Castañeda MAP (2003). Computer Assisted Surgery. Medical Physics: Seventh Mexican Symposium on Medical Physics. AIP Publishing. 682(1):38-45

Creamer P, Hochberg MC(1997). Osteoarthritis. Lancet. 350:503-509

Cruces RAC, Wahrburg J (2007). Improving robot arm control for safe and robust haptic co-operation in orthopaedic procedures. Int. J. Med. Robotics Comput. Assist. Surg. 3: 316-32

Curless B (1999) Overview of active vision techniques. In SIGGRAPH 99 Course on 3D Photography

Dalley G, Flynn P (2002). Pair-wise range image registration: A study in outlier classification. Comput Vis. Image Underst. 87(1-3):104-115

Davies B (2000). A review of robotics in surgery. Proceedings of the Institute of Mechanical Engineers Part H: Journal of Engineering in Medicine. 214(1):129-140

Davies BL, Hibberd RD, Ng WS, Timoney AG, Wickham JEA (1991). A surgeon robot for prostatectomies in Fifth International Conference on Advanced Robotics (ICAR). 871–875

Davies BL, HO SC, Hibberd RD (1994). The use of force control in robot assisted knee surgery at MRCAS, Pittsburgh, PA. 2:258-262

Davies BL, Rodriguez y Baena FM, Barrett AR, Gomes MP, Harris SJ, Jakopec M, Cobb JP (2007). Robotic control in knee joint replacement surgery. Proceedings of the Institution of Mechanical Engineers, H. 221:71–80

Davis J, Ramamoorthi R, Rusinkiewicz S (2003). Spacetime Stereo: A unifying framework for depth from triangulation in Proc. IEEE Computer Society Conference on Computer Vision and Pattern Recognition. 2(II):359-366

De Vaus D (1993). Surveys in Social Research. (3rd Ed.), London, UCL Press.

Demtroder W (2003). Laser Spectroscopy, Basic concepts and instrumentation. (3rd Ed.) Springer-Verlag. Berlin

Dessenne V, Lavallee S, Julliard R, Orti R, Martelli S, Cinquin P (1995). Computer-Assisted Knee Anterior Cruciate Ligament Reconstruction: First Clinical Tests. J. of Image Guided Surgery. 1(1):59-64

Diduch DR, Insall JN, Scott WN, Scuderi GR, Font-Rodriguez D (1997). Total knee replacement in young, active patients: long-term follow-upand functional outcome. J Bone Joint Surg Am. 79:575–582

Dillingham MF, Fanton GS, Thabit G (1995). Laser-Assisted Arthroscopic Meniscal Surgery of The Knee. Operative Techniques in Orthopaedics. 5(1):39-45

Doneusa M, Brieseb C, Feraa M, Janner M, (2008). Archaeological prospection of forested areas using full-waveform airborne laser scanning 35:882-893

Dongming Lu, Yunhe Pan (2010). Digital preservations of heritages. Zheziang University Press, Springer

Dorsch RG, Häusler G, Herrmann JM (1994). Laser triangulation: fundamental uncertainty in distance measurement. Applied Optics. 33(7):1306-1314

Dye SF (2005). Knee Arthroplasty to Maximize the Envelope of Function in Bellemans J, Ries MD, Victor JMK (Eds.) "Total Knee Arthroplasty: A Guide to Get Better Performance". Springer Medizin Verlag, Heidelberg. pp 14-17

Ecker T M, Tannast M, Puls M (2014). Computer-Assisted Orthopaedic Surgery in Jolesz F A (Eds.) "Intraoperative Imaging and Image-Guided Therapy". Springer, New York

Eckstein F, Charles HC, Buck RJ, Kraus VB, Remmers AE, Hudelmaier M, Wirth W, Evelhoch JL (2005). Accuracy and precision of quantitative assessment of cartilage morphology by magnetic resonance imaging at 3.0T. Arthritis Rheum. 52:313-326

Eckstein F, Cicuttini F, Raynauld JP, Waterton JC, Peterfy C (2006). Magnetic resonance imaging (MRI) of articular cartilage in knee osteoarthritis (OA): morphological assessment. Osteoarthritis and Cartilage. 14:46-75

Eckstein F, Hudelmaier M, Wirth W (2011). Quantitative MR Imaging of Cartilage Morphology in Osteoarthritis in Link TM (Ed.) "Cartilage Imaging". Springer, New York. pp 127-141

Eckstein F, Sittek H, Milz S, Schulte E, Kiefer B, Reiser M (1995). The potential of magnetic resonance imaging (MRI) for quantifying articular cartilage thickness-a methodological study. Clin Biomech 10:434-40

Einstein A (1916). The Quantum Theory of Radiation. Physikalische Zeitschrift. 18(121):63-71.

El-Katatny I, Masood SH, Morsi YS (2010). Error analysis of FDM fabricated medical replicas. Rapid Prototyping Journal. 16(1):36-43

Ellis VA, Merrill L, Wingfield JC, O'Loghlen A, Rothstein SI (2012). Changes in immunocompetence and other physiological measures during molt in Brown-headed Cowbirds (Molothrus ater). The Auk. 129(2):231-238

Elsen VD, Pol EJD, Viergever MA (1993). Medical image matching-A review with classification. IEEE Engineering in Medicine and Biology. 12:26-39

FARO (2015)
http://www.faro.com/products/metrology/faro-scanarm/overview.
DOA: 31-01-2015, 18.22

Faxin Yu, Zheming Lu, Hao Luo, Pinghui Wang (2010). Three-Dimensional Model Analysis and Processing. Zheziang University Press and Springer

Felson DT, Lawrence RC, Dieppe PA, Hirsch R, Helmick CG, Jordan JM (2000). Osteoarthritis: new insights. Part 1: the disease and its risk factors. Ann Intern Med 133:635-646

Felson DT, Neogi T (2004). Osteoarthritis: is it a disease of cartilage or of bone? Arthritis Rheum. 50:341-344

Feng HY, Liu Y, Xi F (2001). Analysis of digitizing errors of a laser scanning system. Journal of the International Societies for Precision Engineering and Nanotechnology. 25:185-191

Feng W, Zhang YF, Wu YF, Wang YS (2005). Three dimensional Data Capturing and Processing in Gibson I (Ed.) "Advanced manufacturing technology for medical application Reverse Engineering, Software Conversion and Rapid Prototyping". Wiley. pp 59-77

Fischer MA, Bolles RC (1981). Random sample consensus: a paradigm for model fitting with application to image analysis and automated cartography. Communications of the ACM. 24(6):381-395

Fitzpatrick JM, Hill DLG, Maurer CR Jr. (2000). Image registration in Handbook of medical imaging. SPIE Press. 2:447-513

Fleming PS, Marinho V, Johal A (2011). Orthodontic measurements on digital study models compared with plaster models: a systematic review. Orthodontics & Craniofacial Research. 14(1):1-16

Franca JDJM, Gazziro MA, Ide AN, Saito JH (2005). A 3D scanning system based on laser triangulation and variable field of view in Image Processing, ICIP IEEE International Conference 1:425-428

Garg U, Garg MK, Singh M (2013) Lasers in medicine. Journal of Advance Researches in Biological Sciences. 5(2):177-180

Geomagic (2011)
http://dl.geomagic.com/media/marketing/2012_Brochures/MASTER-12_29_11_QQP_A4_English_eVersion.pdf.
DOA: 10-05-2013, 09.10

Geomagic (2013)
http://support1.geomagic.com/link/portal/5605/5668/Article/2173/Geomagic-Studio-Wrap-Qualify-and-Qualify-Probe-User-Guides.
DOA: 15-02-2013, 16.15

Gomes P (2011). Surgical robotics: Reviewing the past, analysing the present, imagining the future. Robotics and Computer-Integrated Manufacturing 27:261-266

Goodfellow JW, O'Connor JJ, Murray DW (2010). A critique of revision rate as an outcome measure. J Bone Joint Surg. 92(B):1628-1631

Goshtasby A (2012). Image registration: Principles, Tools and Methods. Springer-Verlag London Limited, London

Gotte H (1996). A new less invasive approach to knee surgery using a vision guided manipulator at IARP Workshop on Medical Robotics, Vienna. 99-107

Griffin FM, Math K, Scuderi GR, Insall JN. Poilvache PL (2000). Anatomy of the epicondyles of the distal femur: MRI analysis of normal knees. The Journal of Arthroplasty. 15(3):354-359

Haase A, Frahm J, Matthaei D, Hanicke W, Merboldt KD (1986). FLASH imaging. Rapid NMR imaging using low flip-angle pulses. Journal of Magnetic Resonance. 67:258-266

Hagag B, Abovitz R, Kang H, Schmitz B, Conditt M (2011). RIO: Robotic-Arm Interactive Orthopedic System MAKOplasty®:User Interactive Haptic Orthopedic Robotics in Rosen J, Hannaford B, Satava RM (Eds.) "Surgical Robotics Systems Applications and Visions". Springer, New York. pp 219-246.

Hanssen AD, Stuart MJ, Scott RD, Scuderi GR (2000). Surgical Options for the Middle-Aged Patient with Osteoarthritis of the Knee Joint. The Journal of Bone & Joint Surgery. 82(12):1767-1767

Hariharan P (1996). Optical Holography Principles, techniques and applications. (2nd Ed.) Cambridge University Press, Cambridge

Harmon L, Vayda A, Erlandson E (1994). 3D Laser Scanning for Image-Guided Neurosurgery. AAAI Technical Report. 94(05):106-109

Harwin S (2003). Complications of Unicompartmental Knee Arthroplasty. Seminars in Arthroplasty. 14(4):232-244

Hattori K, Mori K, Habata T, Takakura Y, Ikeuchi K (2003). Measurement of the mechanical condition of articular cartilage with an ultrasonic probe: quantitative evaluation using wavelet transformation. Clin Biomech (Bristol, Avon). 18(6):553-557

Hayashi D, Duryea J, Roemer FW, Guermazi A (2011). Conventional Radiography as an Indirect Measure for Cartilage Pathology in Link TM (Ed.) "Cartilage Imaging". Springer, New York. pp 27-36

Hebert M, Krotkov E (1992). 3-D Measurements From Imaging Laser Radars: How Good Are They? International Journal of Image and Vision Computing. 10(3):170-178

Hecht J (1994). Understanding Lasers (2nd Ed.) IEEE Press, New York

Herbert M, Kortkov E (1992). 3-D Measurements From Imaging Laser Radars: How Good Are They? International Journal of Image and Vision Computing. 10(3): 170-178

Hoffman J, Westendorff C, Leitner C, Bartz D, Reinert S (2005). Validation of 3D-laser surface registration for image-guided Cranio-maxillofacial surgery. Journal of Cranio-Maxillofacial Surgery 33:13–18

Hollinghurst D, Stoney J, Ward T, Gill HS, Newman JH, Murray DW, Beard DJ (2006). No deterioration of kinematics and cruciate function 10 years after medial unicompartmental arthroplasty. Knee. 13:440-444

Howitt D, Cramer D (2005). Introduction to Research Methods in Psychology (2nd Ed.). Pearson Education Limited, Essex

HPA (2014)
http://www.hpa.org.uk/Topics/Radiation/UnderstandingRadiation/UnderstandingRadiationTopics/Lasers/Lasersafetymanagement/
DOA: 05-06-2014, 18.00

Huang YP, Zheng YP (2009). Intravascular Ultrasound (IVUS): A Potential Arthroscopic Tool for Quantitative Assessment of Articular Cartilage. The Open Biomedical Engineering Journal. 3:13-20

Huising EJ, Pereira LM (1998). Errors and accuracy estimates of laser data acquired by various laser scanning systems for topographic applications. ISPRS Journal of Photogrammetry & Remote Sensing. 53:245–261

Imhoff AB (1995). The Use of Lasers In Orthopaedic Surgery. Operative Techniques in Orthopaedics. 5(3):192-203

Isheil A, Gonnet JP, Joannic D, Fontaine JF (2011). Systematic error correction of a 3D laser scanning measurement device. Optics and Lasers in Engineering 49:16-24

Jakopec M, Rodriguez FYB, Harris SJ, Gomes P, Cobb J, Davies BL (2003). The Hands-On Orthopaedic Robot "Acrobot": Early Clinical Trials of Total Knee Replacement Surgery. IEEE Transactions on Robotics and Automation. 19(5):902-911

Jasson T (2006) Feature Based Registration
http://campar.in.tum.de/twiki/pub/Chair/TeachingWs05SegmentationRegistrationHauptseminar/05JanssonFeatureBasedRegistration.pdf
DOA: 08-04-2014, 14.32

Jia-Chong D, Hung-Chao T (2007). 3D laser scanning and GPS technology for landslide earthwork volume estimation. Automation in Construction. 16:657-663

Joern WPM, Klaus USB, Peer E (2010). The Epidemiology, Etiology, Diagnosis, and Treatment of Osteoarthritis of the Knee. Dtsch Arztebl Int. 107(9):152–62

Jones CW, Smolinski D, Kirk T.B, Zheng MH (2005). Confocal laser scanning microscopy in orthopaedic research. Progress in Histochemistry and Cytochemistry. 40(1):1-71

Kao JY, Tarng YS (2006). The registration of CT image to the patient head by using an automated laser surface scanning system- A phantom study. Computer methods and programs in biomedicine. 83:1-11

Karp JS, Kuhn A, Perkins AE, Surti S, Werner ME, Daube-Witherspoon ME, Popescu L, Vandenberghe S, Muehllehner G (2005). Characterization of a time-of-flight PET scanner based on lanthanum bromide in Nuclear Science Symposium Conference Record. 4(5):23-29

Katzir A (1993). Lasers and Optical Fibres in Medicine. Academic Press Inc., California

Kazanzides P, Mittelstadt BD, Musits BL, Bargar WL, Zuharset al JF (1995). An integrated system for cementless hip replacement .IEEE Eng. Med. Biol. Mag. 14:307-313

Keating EM, Meding JB, Faris PM, Ritter MA (2002). Long-term follow-up of nonmodular total knee replacements. Clin Orthop Relat Res. 404:34-39

Kieffer JC, Krol A, Jiang Z, Chamberlain CC, Scalzetti E, Ichalalene Z (2002). Future of laser-based X-ray sources for medical imaging. Appl. Phys. 74(B):75-81

Kluge W (2007). Computer-assisted knee replacement techniques. Mini-Symposium: Computer-Assisted Surgery in Orthopaedics. Current Orthopaedics. 21:200-206

Knutson K, Lindstrand A, Lidgren L (1986). Survival of knee arthroplasties. J Bone Joint Surg 68(B):795-803

Ko SH, Pan H, Grigoropoulos CP, Luscombe CK, Fréchet JMJ, Poulikakos D (2007). All-inkjet-printed flexible electronics fabrication on a polymer substrate by low-temperature high-resolution selective laser sintering of metal nanoparticles. Nanotechnology. 18(34):1-8

Koo S, Giori AJ, Gold GE, Dyrby CO, Andriachhi TP (2009). Accuracy of 3D Cartilage Models Generated From MR Images Is Dependent on Cartilage Thickness: Laser Scanner Based Validation of In Vivo Cartilage. J Biomech Eng.131(12):1-13

Koo S, Gold GE, Andriacchi TP (2005). Considerations in measuring cartilage thickness using MRI: factors influencing reproducibility and accuracy. Osteoarthritis and Cartilage. 13(9):782-789

Kornaat PR, Reeder SB, Koo S, Brittain JH, Yu H, Andriacchi TP, Gold GE (2005). MR imaging of articular cartilage at 1.5 T and 3.0 T: Comparison of SPGR and SSFP sequences. Osteoarthritis and Cartilage. 13:338-344

Koulalis D, O'Loughlina PF, Plaskos C, Kendoff D, Cross MB, Pearle AD (2011). Sequential versus automated cutting guides in computer-assisted total knee arthroplasty. The Knee. 18:436-442

Krebs B, Sieverding P, Korn B (1996). A fuzzy ICP algorithm for 3D free form object recognition in International conference on pattern recognition. 539-543

Krishnan R, Raabe A, Seifer V (2004). Accuracy and applicability of laser surface scanning as new registration technique in image-guided neurosurgery. International Congress Series 1268:678–683

Kuroki H, Nakagawa Y, Mori K, Kobayashi M, Yasura K, Okamoto Y, Suzuki T, Nishitani K, Nakamura T (2006). Ultrasound properties of articular cartilage in the tibio-femoral joint in knee osteoarthritis: relation to clinical assessment (International Cartilage Repair Society grade). Arthritis Research & Therapy. 10:1-13

Kwoh YS, Hou J, Jonckheere EA, Hayati S (1988). A robot with improved absolute positioning accuracy for CT guided stereotactic brain surgery. IEEE Transactions on Biomedical Engineering. 35(2):153-160

Laasanen MS, Toyras J, Korhonen RK,. Rieppo J, Saarakkala S, Nieminen MT, Hirvonen J, Jurvelin JS (2003). Biomechanical properties of knee articular cartilage. Biorheology 40:133-140

Laasanen MS, Toyras J, Vasara A, Saarakkala S, Hyttinen MM, Kiviranta I, Jurvelin JS (2006). Quantitative ultrasound imaging of spontaneous repair of porcine cartilage. OsteoArthritis and Cartilage 14: 258-263

LaBarbera V (2015)
http://quizlet.com/18647852/vml-anatomy-patella-flash-cards/
DOA: 18-03-2014. 14.40

Lang JE, Mannava S, Floyd AJ, Goddard MJ, Smith BP, Mofidi A, Seyler TM, Jinnah RH (2011). Robotic systems in orthopaedic surgery. Journal of Bone Joint Surgery, British edition. 93(B):1296-1299

Laurencin C, Zelicof SB, Scott RD, Ewald FC (1991). Unicompartmental versus total knee arthroplasty in the same patient: a comparative study. Clin Orthop 273:151-156

Lavallee S, Sautot P, Troccaz J, Cinquin P, Merloz, P (1995). Computer-Assisted Spine Surgery: A Technique for Accurate Transpedicular Screw Fixation Using CT Data and a 3-D Optical Localizer. J. Image Guided Surgery. 1(1):65-73

Lavallee S, Szeliski R (1995). Recovering the position and orientation of free-form objects. IEEE Trans. PAMI 17:378-390

Leadshine (2015)
http://www.leadshine.com/UploadFile/Down/M542d.pdf
DOA: 01-12-2012, 10.00

Ledderose GJ, Stelter K, Leunig A, Hagedorn H (2007). Surface laser registration in ENT-surgery: accuracy in the paranasal sinuses – a cadaveric study. Rhinology. 45:281-285

Leon AC, Lori LL, Kraemer HC (2011). The role and interpretation of pilot studies in clinical research. Journal of Psychiatric Research. 45:626-629

Leopold SS (2009). Minimally Invasive Total Knee Arthroplasty for Osteoarthritis. N Engl J Med 360(17):1749-1758

Lester H, Arrige SR (1999). A Survey of hierarchical non-linear medical image registration. Pattern recognition. 32-129-149

Levine III H (2010). Development and societal impact of medical imaging technologies from the discovery of the X-ray – Fluorography, CT, MRI, PET, SPECT. Greenwood Press/ABC-CLIO, Santa Barbara, CA

Link TM (2011). Cartilage as a Biomarker in Link TM (Ed.) "Cartilage Imaging". Springer, New York. pp 205-212

Link TM, Stahl R, Woertler K (2007). Cartilage imaging: motivation, techniques, current and future significance. Eur Radiol. 17:1135-1146

Link TM, Steinbach LS, Ghosh S, Ries M, Lu Y, Lane N, Majumdar S (2003) . Osteoarthritis: MR Imaging Findings in Different Stages of Disease and Correlation with Clinical Findings Radiology; 226:373-381

Loftus GR (1978). On interpretation of interactions. Memory & Cognition. 6 (3):312-319

Lohmander LF, Hoerrner LA, Lark MW (1993). Metalloproteinases, Tissue Inhibitor, and Proteoglycan Fragments in Knee Synovial Fluid in Human Osteoarthritis. Arthritis and Rheumatism. 36(2):181-189

Lombardi AV Jr, Berend KR, Tucker TL (2007). The incidence and prevention of symptomatic thromboembolic disease following Unicompartmental Knee Arthroplasty. Orthopaedics. 30(5):46-48

Lonner JH, Kerr GJ (2012). Robotically Assisted Unicompartmental Knee Arthroplasty. Oper Tech Orthop. 22:182-188

Lonner JH, Smith JR, Picard F, Hamlin B, Rowe PJ, Riches PE (2015). High degree of accuracy of a novel image-free handheld robot for unicondylar knee arthroplasty in a cadaveric study. Clin Orthop Relat Res. 473(1):206-212

Lucas B, Kanade T (1981). An Iterative Image Registration Technique with an Application to Stereo Vision. Proceedings 7th Intl Joint Conf. on Artificial Intelligence (IJCAI), Vancouver, British Columbia: 674-679

Lutzner J, Kasten P, Günther KP, Kirschner S (2009). Surgical options for patients with osteoarthritis of the knee. Nature Reviews Rheumatology. 5:309-316

Lyons MC, MacDonald SJ, Somerville LE, Naudie DD, McCalden RW (2012). Unicompartmental versus Total Knee Arthroplasty Database Analysis. Clin Orthop Relat Res. 470:84–90

Mada SK, Smith ML; Smith LN, Midha P (2002). Overview of passive and active vision techniques for hand-held 3D Data Acquisition in Proc. SPIE 4877, Opto-Ireland: Optical Metrology, Imaging, and Machine Vision

Magne P (2007). Efficient 3D finite element analysis of dental restorative procedures using micro-CT data. Dental materials. 23:539-548

Maintz JBA and Viergever MA (1998). A survey of medical image registration. Medical Image Analysis. 2(1):1-36

MAKO Surgicals (2014)
http://www.makosurgical.com/physicians/products/restoris-mck-multicompartmental-implant-system
DOA: 06-03-2014, 16.48

Mallik A (1999). Lasers in defense. International Symposium on Photonics and Applications. International Society for Optics and Photonics

Mandelbaum BR, Browne JE, Fu F, Micheli L, Mosely JB Jr., Erggelet C, Minas T, Peterson L (1998). Articular Cartilage Lesions of the Knee. THE American Journal of Sports Medicine. 26(6): 853-861

Manninen P, Riihimaki H, Heliovaara M, Suomalainen O (2001). Physical Exercise and Risk of Severe Knee Osteoarthritis Requiring Arthroplasty. Rheumatology. 40:432-437

Marcacci M, Tonet O, Megali G, Dario P, Carrozza MC, Nofrini L, Palombara PF (2000). A Navigation System for Computer Assisted Unicompartmental Arthroplasty: Medical Image Computing and Computer-Assisted Intervention. Lecture Notes in Computer Science. 1935: 1152-1157

Margo BJ, Radney CS, Scuderi GR (2010). Anatomy of the Knee in Scuderi GR and JTria A Jr. (Eds.), "The Knee A Comprehensive Review". World Scientific Publishing Co.Pe.Ltd, Singapore. pp 1-19

Marieb EN, Hoehn K (2007). Human Anatomy and Physiology (7th Ed.), Pearson Education, Inc. New York

Markelj P, Tomaz˘evic D, Likar B, Pernuš F (2010). A review of 3D/2D registration methods for image-guided interventions. Medical Image Analysis. 16(3):642-661

Markelj PZ, Toma˘zevi˘ D, Pernu˘s F, Likar B (2008). Robust Gradient-Based 3-D/2-D Registration of CT and MR to X-Ray Images. IEEE Transactions on Medical Imaging. 27(12):1704-1714

Marmulla R, Hassfeld S, Luth T, Muhling J (2003). Laser-scan-based navigation in Cranio-maxillofacial surgery. Journal of Cranio-Maxillofacial Surgery 31:267-277

Marmulla R, Luth T (2000). Method and device for instruments and bone segment- and tissue-and organ-navigation. PCT/EP2000/012685

Marmulla R, Luth T, Muhling J, Hassfeld J (2004). Automated laser registration in image-guided surgery: evaluation of the correlation between laser scan resolution and navigation accuracy. International Journal of Oral and Maxillofacial Surgery 33: 642-648

Marmulla R, Muhlinga J, Luthb T, Eggersa G, Hassfeld S (2004). Image-to-patient-registration by the natural anatomical surfaces of the auricle, mandible, and maxilla. International Congress Series. 1268:1192–1197

Maroudas A, Bullough P, Swanson SA, Freeman MA (1968). The permeability of articular cartilage. J Bone Joint Surg Br. 50(1):166-177

Marsh AA, Blair RJR (2007). Deficits in facial affect recognition among antisocial populations: A meta-analysis. Neuroscience and Biobehavioral Reviews. 32:454-465

Martin A, Sheinkop MB, Prenn M, Moosmann D, Strempel AV (2009). 2-Year Outcomes of CT Based and CT Free Navigation for Total Knee Arthroplasty. J Bone Joint Surg Br. 91-B :SUPP I 124-125

Materialise MIMICS (2014)
http://biomedical.materialise.com/mimics
DOA: 05-10-2014, 12.30

Maurer CR, Fitzpatrick JM (1993). A review of medical image registration in Maciunas RJ (Ed.) “Interactive Image guided Neurosurgery”. American Association of Neurological Surgeons, Parkridge, IL. pp. 17–44

Medical Multimedia Group (2000).
http://www.methodistorthopedics.com/Articular-Cartilage-Problems-of-the-Knee
DOA: 06-05-2014, 14.00

Medical Multimedia Group (2008).
http://www.methodistorthopedics.com/bodyortho.cfm?id=41847
DOA: 06-05-2014, 13.40

Mezhov V, Ciccutini FM, Hanna FS, Brennan SL, Wang YY, Urquhart DM, Wluka AE (2014). Does obesity affect knee cartilage? A systematic review of magnetic resonance imaging data. Obesity Reviews. 15(2):143-157

Miga M, Sinha TK, Cash DM, Galloway RL, Weil RJ (2003). Cortical Surface Registration for Image-Guided Neurosurgery Using Laser-Range Scanning. IEEE Transactions on Medical Imaging. 22(8):973-985

Mittelstadt B, Kazanzides P, Zuhars, Williamson B, Cain P, Smith F, Bargar W (1996). The evolution of a surgical robot from prototype to human clinical use, in Taylor RH, Lavallee S, Burdea G, Mosges R(Eds.) Computer-Integrated Surgery, Cambridge, MA: MIT Press. pp. 397–407

Moctezuma J, Bernasch J, Lohmann G, Schweikard A, Gosse F (1994). Robotic surgery and planning for corrective femur osteotomy. Intelligent Robots and Systems '94. 'Advanced Robotic Systems and the Real World', IROS '94. Proceedings of the IEEE/RSJ/GI International Conference. 2:870-877

Moss JP, Linney AD, Grindrod SR, Moss CA (1989). A Laser Scanning System for the Measurement of Facial Surface Morphology. Optics and Lasers in Engineering. 10:179-190

Motohashi N, Kurdoa T (1999). A 3D computer-aided design system applied to diagnosis and treatment planning in orthodontics and orthognathic surgery. European Journal of Orthodontics. 21:263-274

Mow VC, Rosenwasser MP (1988). Articular cartilage: Biomechanics in SL Woo, JA Buckwalte (Eds.) “Injury and Repair of the Musculoskeletal Soft Tissue”, AAOS Publ, Rosemont, IL. pp 427-463

Mowles SL, Rundle SD, Cotton PA (2011). Susceptibility to Predation Affects Trait-Mediated Indirect Interactions by Reversing Interspecific Competition. PLoS ONE 6(8): e23068

Mrosek EH, Lahm A, Erggelet C, Uhl M, Kurz H, Eissner B, Schagemann JC (2006). Subchondral bone trauma causes cartilage matrix degeneration: an immunohistochemical analysis in a canine model. Osteoarthritis Cartilage 14(2): 171-178

MTI Instruments (2011)
http://www.mtiinstruments.com/pdf/products/microtrak2.pdf
DOA: 21-03-2011, 11.00

Murray DW, Goodfellow JW, O’Connor JJ (1998). The Oxford medial unicompartmental knee arthroplasty: a ten-year survival study. J Bone Joint Surg Br. 80:983-989

Nagabhushana S, Sathyanarayana N (2010). Lasers and Optical Instrumentation. International Publishing House Pvt. Ltd. New Delhi

Newman I, Newman C (1994). Conceptual Statistics for beginners (2^{nd} Ed.). Lanham, MD, University Press of America

Newman JH, Ackroyd CE, Shah NA (1998). Unicompartmental or total knee replacement? The Journal of Bone and Joint Surgery. 80(B):862-865

Nitz WR (1999). MR imaging: acronyms and clinical applications Eur. Radiol. 9: 979-997

Niu HJ, Wang Q, Wang YX, Li DY, Fan YB, Chen WF (2012). Ultrasonic reflection coefficient and surface roughness index of OA articular cartilage: relation to pathological assessment. BMC Musculoskeletal Disorders. 13:34

Nogler M, Mayr E, Krismer M, Thaler M (2008). Reduced variability in cup positioning: the direct anterior surgical approach using navigation. Acta Orthop. 79(6):789-93

Nouri M, Massudi R, Bagheban AA, Azimi S, Fereidooni (2009). The accuracy of a 3-D laser scanner for crown width measurements. Aust Orthod J. 25(1):41-47

O'Rourke MR, Gardner JJ, Callaghan JJ, Liu SS, Goetz DD Vittetoe DA, Sullivan PM, Johnston RC (2005). The John Insall Award: Unicompartmental knee replacement: a minimum twenty-one year followup, end-result study. Clin Orthop Relat Res. 440:27-37

Orthopilot (2015)
http://www.orthopilot.com/
DOA: 31-03-2015, 18.43

Orthopod (2014)
http://www.eorthopod.com/adult-knee-patient-guides
DOA: 17-03-2014, 16.45

Osgood RM Jr. (1983). Laser Microchemistry and its Application to Electron-Device Fabrication. Annual Review of Physical Chemistry. 34:77-101

Otake Y, Armand M, Armiger RS, Kutzer MD, Basafa E, Kazanzides P, Taylor RH (2012). Intraoperative Image-based Multiview 2D/3D Registration for Image-Guided Orthopaedic Surgery: Incorporation of Fiducial-Based C-Arm Tracking and GPU-Acceleration. IEEE Transactions on Medical Imaging. 31(4):948-962

Panwar AK, Singh A, Kumar A, Kim H (2002). Terahertz Imaging System for Biomedical Applications: Current Status. International Journal of Engineering & Technology 13(2):33-39

Papagelopoulos PJ, Mavrogenis AF, Galanis EC, Wenger DE, Kelekis NL, Sim FH, Soucacos PN (2005). Minimally Invasive Techniques in Orthopaedic Oncology: Radiofrequency and Laser Thermal Ablation. Orthopaedics. 28(6):563-568

Paul HA, Bargar WL, Mittlestadt B, Musits B, Taylor RH, Kazanzides P, Zuhars J, Williamson B, Hanson W (1992). Development of a surgical robot for cementless total hip arthroplasty. Clin Orthop Relat Res. 285:57-66

Pearle AD, Kendoff D, Stueber V, Musahl V, Repicc JA (2009). Perioperative Management of Unicompartmental Knee Arthroplasty Using the MAKO Robotic Arm System (MAKOplasty®). Am J Orthop. 38(2):16-1

Pearle AD, O'Loughlin PF, Kendoff DO (2010). Robot-Assisted Unicompartmental Knee Arthroplasty: The Journal of Arthroplasty 25(2):230-237

Pelizzari CA, Chen GTY, Spelbring DR, Weichselbaum RR, Chen CT (1989). Accurate three-dimensional registration of CT, PET, and/or MR images of the brain. J. Comp. Ass. Tomog. 13 (1):20-26

Peng Q, Juzeniene A, Chen J, Svaasand LO, Warloe T, Giercksky K-E, Moan J (2008). Lasers in Medicine. Rep. Prog. Phys. 71(5):056701

Pétillon JP, Voillaume DH, Trétout H (1998). Applications of Laser Based Ultrasonics for Aerospace Industry. ECNDT '98 – Proceedings, Copenhagen.

Picard F, Moody JE, DiGioia III AM, Jaramaz B, Saragaglia D (2004). History of Computer Assisted Orthopaedic Surgery in DiGioia III AM, Jaramaz B, Picard F, Nolte L-P (Eds.) "Computer and Robotic Assisted Knee and Hip Surgery". Oxford University Press, Oxford. pp 1-22

Plancher KD, Lipnik SL (2010). Meniscal injuries in Scuderi GR, JTria A Jr. (Eds.) The Knee : A Comprehensive Review. World Scientific Pub Co Pte. Singapore. Pp 183-194

Plaskos C, Cinquin P, Lavalle´e S, Hodgson AJ (2005). Praxiteles: a miniature bone-mounted robot for minimal access total knee arthroplasty. Int J Medical Robotics and Computer Assisted Surgery. 1(4):67-79

Popat H, Richmond S, Playle R, Marshall D, Rosin PL, Cosker D (2008). Three-dimensional motion analysis - an exploratory study. Part 1. Assessment of facial movement Orthod Craniofac. 11:216-223

Price AJ, Webb J, Topf H, Dodd CA, Goodfellow JW, Murray DW (2001). Rapid recovery after Oxford unicompartmental arthroplasty through a short incision. J. Arthroplasty. 16:970-976

Raabe A, Krishnan R, Wolff R, Hermann E, Zimmermann M, Seifert V (2002). Laser surface scanning for patient registration in intracranial image-guided surgery. Neurosurgery. 50:797-803

Rangarajan, Flannery BP, Teukolsky SA, Vetterling WT (1997). A robust point-matching algorithm for autoradiograph alignment. Medical Image Analysis 1(4):379=398

Ready JF (1997). Industrial applications of lasers. Academic Press, San Diego

Recht MP, Kramer J, Marcelis S, Pathria MN, Trudell D, Haghighi P, Sartoris DJ, Resnick D (1993). Abnormalities of articular cartilage in the knee: analysis of available MR techniques. Radiology. 187(2):473-478

Rivas M, Sergiyenko O, Aguirre M, Devia L, Tyrsa V, Rendón I (2008). Spatial data acquisition by laser scanning for robot or SHM task in in Proc. IEEE ISIE, Cambridge, U.K. 1458-1463

Roach HI, Tilley S (2008). The Pathogenesis of Osteoarthritis in Bronner F, Farach-Carson MC (Eds.) “Bone and Osteoarthritis”. Springer-Verlag London. pp 1-18

Robotshop,
http://www.robotshop.com/en/geared-bipolar-stepper-motor-3v-555-oz-in.html
DOA: 15-11-2012, 13.00

Roche M, Augustin D, Conditt MA (2008). Accuracy of robotically assisted UKA. In: Proceedings of the 21st annual congress of the international society of technology in arthroplasty, International Society for Technology in Arthroplasty, Sacramento, p. 175

Roche MW, Horowitz S, Conditt MA (2010). Four year outcomes of robotically guided UKA. in 23rd Annual Congress of ISTA. Dubai, UAE

Roemer FW, Crema MD, Trattnig S, Guermazi A (2011). Advances in Imaging of Osteoarthritis and Cartilage. Radiology. 260(2):332-354

Rogers AD, Payne JE, Yu JS (2013). Cartilage Imaging: A Review of Current Concepts and Emerging Technologies. Semin Roentgenol. 48(2):148-57

Rohling R, Munger P Hollerbach J, Peters T (1994). Comparison of Relative Accuracy between a Mechanical and an Optical Position Tracker for Image-Guided Neurosurgery. Proc. MRCAS ’94, Pittsburgh, PA. pp. 277-282

Rui W, Minglu L (2003). An Overview of Medical Image Registration at Proceedings of the Fifth International Conference on Computational Intelligence and Multimedia Applications (ICCIMA’03). 385-390

Saarakkala S, Korhonen RK, Laasanen MS, Toyras J, Rieppo J, Jurvelin JS (2004). Mechano-acoustic determination of Young’s modulus of articular cartilage. Biorheology. 41:167-179

Saarakkala S, Laasanen MS, Jurvelin JS, To¨rro¨nen K, Lammi MJ, Lappalainen R Toyras J (2003). Ultrasound indentation of normal and spontaneously degenerated bovine articular cartilage. OsteoArthritis and Cartilage. 11:697-705

Saggin PR, Dejour D, Meyer X, Tavernier T (2010). Computed Tomography and Arthro-CT Scan in Patellofemoral Disorders in Stefano Zaffagnini, David Dejour, Elizabeth A. Arendt (Eds.) Patellofemoral Pain, Instability, and Arthritis. Springer-Verlag Berlin Heidelberg. pp 73-78

Saied A, Bossy E,. Watrin A, Pellaumail B, Loeuille D, Laugier P, Nette P, Berger G (2000). Quantitative Assessment of Arthritic Cartilage Using High-Frequency Ultrasound. IEEE Ultrasonics Symposium. 2:1375-1378

Salvi S, Matabosch C, Fofi D, Forest J (2007). A review of recent range image registration methods with accuracy evaluation. Image and Vision Computing. 25(5):578-596

Sanz R, Llorens J, Rosell JR, Gregorio E, Palacin J (2011). Characterisation of the LMS200 Laser Beam under the Influence of Blockage Surfaces. Influence on 3D Scanning of Tree Orchards. Sensors. 11-2751-2772

Satava RM (2011). Future Directions in Robotic Surgery in Rosen J, Hannaford B, Satava RM (Eds.) "Surgical Robotics Systems Applications and Visions". Springer, New York. pp 3-12.

Schlaier J, Warnat J, Brawanski A (2002). Registration Accuracy and Practicability of Laser-Directed Surface Matching. Computer Aided Surgery 7:284-290

Schmid GF, Papastergiou GI, Nickla DL, Riva CE, Lin T, Stone RA, Laties AM (1996). Validation of laser Doppler interferometric measurements in vivo of axial eye length and thickness of fundus layers in chicks. 15(6):691-696

Schulz AP, Seide K, Queitsch C, Haugwitz vA, Meiners J, Kienast B, Tarabolsi M, Kammal M, Jürgens C (2007). Results of total hip replacement using the ROBODOC® surgical assistant system: Clinical outcome and evaluation of complications for 97 procedures at International Journal of Medical Robotics and Computer Assisted Surgery. 3(4):301-306

Scott WN, Scuderi G (2006). Surgery of knee, (4th Ed.) Churchil Livingstone Elsevier, Philadelphia

Scuderi G R (2010). Nonoperative Treatment of the Arthritic Knee in Scuderi G R, Tria A F (Eds.) "The Knee: A Comprehensive Review". World Scientific Pub Co Pte, Singapore. pp 323-333

Scuderi GR (2002). The Basic Principles in Scuderi GR, Tria AJ (Eds.) "Surgical Techniques in Total Knee Arthroplasty". Springer Verlag, New York Inc. pp 165-167

Shamir RR, Freiman M, Joskowicz L, Spektor S, Shoshan Y (2009). Surface-based facial scan registration in neuronavigation procedures: a clinical study. J. Neurosurg. 111(6):1201-1206

Sharkey PF, Hozack WJ, Rothman, RH, Shastri S, Jacoby SM (2002). Why Are Total Knee Arthroplasties Failing Today? Clin Orthop Relat Res. 404:7-13

Shcherbakov I (2011). Lasers and Medicine. Scientific Session of the General Meeting of the Russian Academy of Sciences. 81(3):271-275

Shoham M, Burman M, Zehavi E, Joskowicz L, Batkilin E, Kunicher Y (2003). Bone-mounted miniature robot for surgical procedures: concept and clinical applications. IEEE Trans Rob and Autom. 19:893-901

Simon D (1997). What is "Registration" and Why is it so Important in CAOS? Proceedings of the First Joint CVRMed / MRCAS Conference: 57-60

Simon D, O'Toole RV, Blackwell M, Mogan F, Dingoia AM, Kanade T (1995). Accuracy Validation in Image-Guided Orthopaedic Surgery. Proceedings of the Second International Symposium on Medical Robotics and Computer Assisted Surgery: 185-192

Simon DA, Hebert M, Kanade T (1995). Techniques for Fast and Accurate Intra-Surgical Registration. J. Image Guided Surgery. 1(1):17-29

Singh V, Rana RK, Singhal R (2013). Analysis of repeated measurement data in the clinical trials. J Ayurveda Integr Med. 4(2):77-81

Sinha SS, Jain R (1994). Range Image Analysis. Handbook of Pattern Recognition and Image Processing: Computer Vision 2:186-195

Smith JR, Picard F, Rowe PJ, Deakin A, Riches PE (2013). The Accuracy of a Robotically-Controlled Freehand Sculpting Tool for Unicondylar Knee Arthroplasty. Bone Joint J. 95(B) Supp. 28 68

Solomon L, Warwick DJ, Nayagam S (2005). Appley's Concise System of Orthopedics and Fractures, Holder Arnold London

Sonin AH, Pensy RA, Mulligan ME , Hatem S (2002). Grading Articular Cartilage of the Knee Using Fast Spin-Echo Proton Density–Weighted MR Imaging Without Fat Suppression. Am J Roentgenol. 179:1159-1166

Soucy G, Ferrie, FP (1997). Surface recovery from range images using curvature and motion consistency. Comp. Vision and Image Under. 65(1):1-18

Sowers MF, Hayes C, Jamadar D, Capul D, Lachance L, Jannausch M (2003). Magnetic resonance-detected subchondral bone marrow and cartilage defect characteristics associated with pain and X-ray-defined knee osteoarthritis. Osteoarthritis Cartilage. 11:387-393

Spector TD, MacGregor AJ (2004). Risk factors for osteoarthritis: genetics. Osteoarthritis and Cartilage. 12:39-44

Stacy GS, Basu PA (2013). Primary Osteoarthritis Imaging. Review article. http://emedicine.medscape.com/article/392096-overview#a19
DOA: 11-03-2011, 15.06

Stahl R, Krug R, Kelley DAC, Zuo J, Benjamin CM, Majumdar S, Link TM (2009). Assessment of cartilage-dedicated sequences at ultra-high-field MRI: comparison of imaging performance and diagnostic confidence between 3.0 and 7.0 T with respect to osteoarthritis-induced changes at the knee joint. Skeletal Radiol 38:771-783

Steiner H (2003). Interactions of laser radiation with biological tissue in Berlien HP, Muller GJ (Eds.) "Applied Laser Medicine". Springer, Berlin. pp 101-106

Stern SH, Becker MW, Insall JN (1993). Unicompartmental knee arthroplasty: An evaluation of selection criteria. Clin Orthop 286:143-148

Stevens (1999) University of Oregon
http://pages.uoregon.edu/stevensj/interaction.pdf
DOA: 03-01-2015, 13.00

Stryker (2015)
http://www.stryker.com/en-us/products/OREquipmentConnectivity/SurgicalNavigation/index.htm
DOA: 31-03-2.15, 17.10

Sugano N (2003). Computer-assisted orthopaedic surgery. J Orthop Sci. 8(3):442-448

Sugano N (2013). Computer-Assisted Orthopaedic Surgery and Robotic Surgery in Total Hip Arthroplasty. Clinics in Orthopaedic Surgery. 5:1-9

Surti S, Karp JS (2008). Design considerations for a limited-angle, dedicated breast, TOF PET scanner. Phys Med Biol. 53(11):2911-21

Sven M (2011)
https://github.com/landis/arduino/blob/master/Katie/Katie.ino
DOA: 20-01-2012

Tabor OB Jr, Tabor OB. (1998). Unicompartmental arthroplasty: a long term follow-up study. J Arthroplasty. 13:373–379

Tang P, Akinci B, Huber D (2009). Quantification of edge loss of laser scanned data at spatial discontinuities. Automation in Construction 18:1070-1083

Tarwala R, Lawrence D. Dorr (2011). Robotic assisted total hip arthroplasty using the MAKO platform. Current Reviews in Musculoskeletal Medicine. 4(3):151-156

Taylor R, Paul HA, Mittelstadt B, Glassman E, Musits BL, Bargar WL (1989). A robotic system for cementless total hip replacement surgery in dogs. In: Second workshop on medical and healthcare robotics, Newcastle-on-Tyne, September p. 79–89

Taylor RH (2006). A Perspective on Medical Robotics. Proceedings of the IEEE. 94(9):1652-1664

Taylor RH, Paul HA, Kazandzides P, Mittelstadt BD, Hanson W, Zuhars JF, Williamson B, Musits BL, Glassman E, Bargar WA (1994). An image-directed robotic system for precise orthopaedic surgery, IEEE Trans. Robot. Automat. 10(3):261-275.

Taylor RH, Stoianovici D (2003). Medical Robotics in Computer-Integrated Surgery. IEEE Transactions on Robotics and Automation. 19(5):765-781

Tecklenburg K, Dejour D, Hoser C, Fick C (2006). Bone and cartilaginous anatomy of the patellafemoral joint. Knee Surg Sports Traumatol Arthrosc. 14(3):235-240

Teijlingen VE, Hundley V (2002). The importance of pilot studies. Nursing Standard. 16(40):33-36

Teitel AD (2013)
http://www.nlm.nih.gov/medlineplus/ency/presentations/100088_1.htm
DOA: 13-03-2012, 15.50

Thabanel L, Ma J, Chu R, Cheng J, Ismaila A, Rios LP, Robson R, Thabane1 M, Giangregorio L, Goldsmith H (2010). A tutorial on pilot studies: the what, why and how. BMC Medical Research Methodology. 10:1-10

Thiruvenkatachari B, Al-Abdallah M, Akram NC, Sandler J, O'BrienK (2009). Measuring 3-dimensional tooth movement with a 3-dimensional surface laser scanner, American Journal of Orthodontics and Dentofacial Orthopedics. 135(4): 480-485

Tiderius CJ, Olsson LE, Leander P, Ekberg O, Dahlberg L (2003). Delayed gadolinium-enhanced MRI of cartilage (dGEMRIC) in early knee osteoarthritis. Magn Reson Med. 49(3):488-92

Tortora GJ (2005). Principal of Anatomy and Physiology (10^{th} Ed.), John willey and sons, Inc New York

Toyras J, Rieppo J, Nieminen MT, Helminen HJ, Jurvelin JS (1999). Characterization of enzymatically induced degradation of articular cartilage using high frequency ultrasound. Phys. Med. Biol. 44:2723-2733

Trinh NH, Lester J, Fleming BC, Tung G, Kimia BB (2006). Accurate Measurement of Cartilage Morphology Using a 3D Laser Scanner in Beichel RR, Sonka M (Eds.) "Computer Vision Approaches to Medical Image Analysis". Second International ECCV Workshop, CVAMIA, Graz, Austria. pp 37-48

Troccaz J (2009). Computer and Robot-Assisted Medical Intervention in Nof SY (Ed.) "Springer Handbook of Automation," Springer-Verlag Berlin Heidelberg. pp 1451-1466

Tsai RY (1986). An efficient and accurate camera calibration technique for 3D machine vision in IEEE Conf. Computer Vision and Pattern Recognition. 364-374

Umeda K (2010). 3D-2D registration. CRV Tutorial

Usman N, Nuhmani S (2013). Osteoarthritis of Knee-A Review of Current Concepts. Middle East Journal of Age & Ageing. 10(2):38

Valuframe (2013)
http://www.valuframe.co.uk/Series-8-Aluminium-Profiles.html
DOA: 20-02-2013, 10.00

Vision Research (2015)
http://www.visionresearch.com/Products/High-Speed-Cameras/
DOA: 30-03-2015, 14.30

Vorlat P, Putzeys G, Cottenie D, Van Isacker T, Pouliart N, Handelberg F, Casteleyn PP, Gheysen F, Verdonk R. (2006). The Oxford unicompartmental knee prosthesis: an independent 10-year survival analysis. Knee Surg Sports Traumatol Arthrosc. 14:40-45

Voss F, Sheinkop MB, Galante JO, barden RM (1995). Miller-Galante Unicompartmental knee arthroplasty at 2 to 5 year follow-up evaluations. J Arthroplasty 10:764-771

Wan R, Li M (2003). An Overview of Medical Image Registration. Proceedings of the Fifth International Conference on Computational Intelligence and Multimedia Applications (ICCIMA'03): 385-390

Wang L, Tschudi T, Halldorsson T, Petursson PR (1998). Speckle reduction in laser projection systems by diffractive optical elements. Applied Optics. 37(10):1770-1775

Wang Q, Zheng YP, Niu HJ, Mak AF (2007). Extraction of mechanical properties of articular cartilage from osmotic swelling behaviour monitored using high frequency ultrasound. J Biomech Eng. 129(3): 413-422

Webber L, Wallace M (2007). Quality control for dummies. Wiley, NJ

Weidow J, Mars I, Ka¨rrholm J (2005). Medial and lateral osteoarthritis of the knee is related to variations of hip and pelvic anatomy. Osteoarthritis and Cartilage. 13:471-477

Wilson MG, Kelley K, Thornhill TS (1990). Infection as a complication of total knee-replacement arthroplasty. Risk factors and treatment in sixty-seven cases. J Bone Joint Surg Am.72(6):878-883

Winder RJ, Darvannb TA, McKnightc W, Mageed JDM, Ramsay-Baggs P (2008). Technical validation of the Di3D stereophotogrammetry surface imaging system. British Journal of Oral and Maxillofacial Surgery. 46:33-37

Winkelbach S, Molkenstruck S, Wahl FM (2006). Low-cost Laser range scanner and fast surface registration approach in DAGM'06 Proceedings of the 28th conference on Pattern Recognition 718-728

Wobbrock, JO, Findlater L, Gergle D, ,Higgins JJ (2011). The Aligned Rank Transform for nonparametric factorial analyses using only ANOVA procedures in Proc. CHI '11. New York: ACM Press, 143-146

Woessner JF Jr, Gunja-Smith Z (1991). Role of metalloproteinases in human osteoarthritis. The Journal of Rheumatology. Suppl. 27:99-101.

Wolf A, Jaramaz B, Lisien B, DiGioia A M (2005). MBARS: mini bone-attached robotic system for joint arthroplasty. Int. J. Med. Robotics Comput. Assist. Surg. 1: 101-121.

Wyawahare MV, Patil PM, Abhyankar HK (2009). Image Registration Techniques: An overview. International Journal of Signal Processing, Image Processing and Pattern Recognition. 2(3):11-28

Xia YH, Fang YM, Yang XY, Chen J, Zuo XQ (2009). Error Analysis and Calibration of 3D Laser Scanner in Surveying in Finished Stopes at Computer Science and Information Engineering, WRI World Congress. 7:139-143

Yangkeun A, Minwook K, Kwangmo J, Taehyoung K, Jaehoon A, Sukil H (2010). TOF Camera based 3D Fingertip Location Estimation- Reliable and Autonomous Computational Science Autonomic Systems. 397-408

Yen P L, Hsiao H-M, Hung S-S (2010). Design of the Surgical Robots for Orthopaedics Applications at International Conference on System Science and Engineering, Taipei, Taiwan. pp. 559-564,

Yokus H, Baughman W, Balci S, Bolus M, Wilbert D; Kung P, Seongsin MK (2013) Identification of tissue interaction of terahertz radiation toward functional tissue imaging. Proc. SPIE 8585, Terahertz and Ultrashort Electromagnetic Pulses for Biomedical Applications. 85850K

Yoshioka Y, Siu D, Cooke D (1987). The anatomy and functional axes of the femur. J Bone Joint Surg Am 69(6):873-880

Zang S, Block KT, Frahm J (2010). Magnetic Resonance Imaging in Real Time: Advances Using Radial FLASH Zhang. J Magn Reson Imaging 31(1):101-109

Zargochev L, Goshtasby A (2006). A paintbrush laser range scanner. Computer vision and image understanding 101:65-86

Zeibak R, Filin S (2008). Managing uncertainty in the detection of changes from terrestrial laser scanners data at XXIst ISPRS Congress: Commission V, WG 3, Beijing. 501-506

Zhang R, Tsai P-S, Cryer JE, Shah M (1999). Shape from Shading: A Survey in Pattern Analysis and Machine Intelligence, IEEE Transaction. 21(8):690-706

Zhang Z (1994). Iterative point matching for registration of free-form curves and surfaces. Int. J. Comp. Vision 13 (2), 119-152

Zilberman O, Huggare JV, Parikakis KA (2003). Evaluation of the Validity of Tooth Size and Arch Width Measurements Using Conventional and Three-dimensional Virtual Orthodontic Models. The Angle Orthodontist. 73(3):301-306

Zimmer (2014)
http://www.zimmer.com/medical-professionals/our-science/hip/hip-cas.html
DOA: 31-03-2015, 18.00

Zitova B, Flusser J (2003). Image registration methods: a survey. Image and Vision Computing. 21:977-1000

APPENDIX

APPENDIX A

Automated Controller circuit

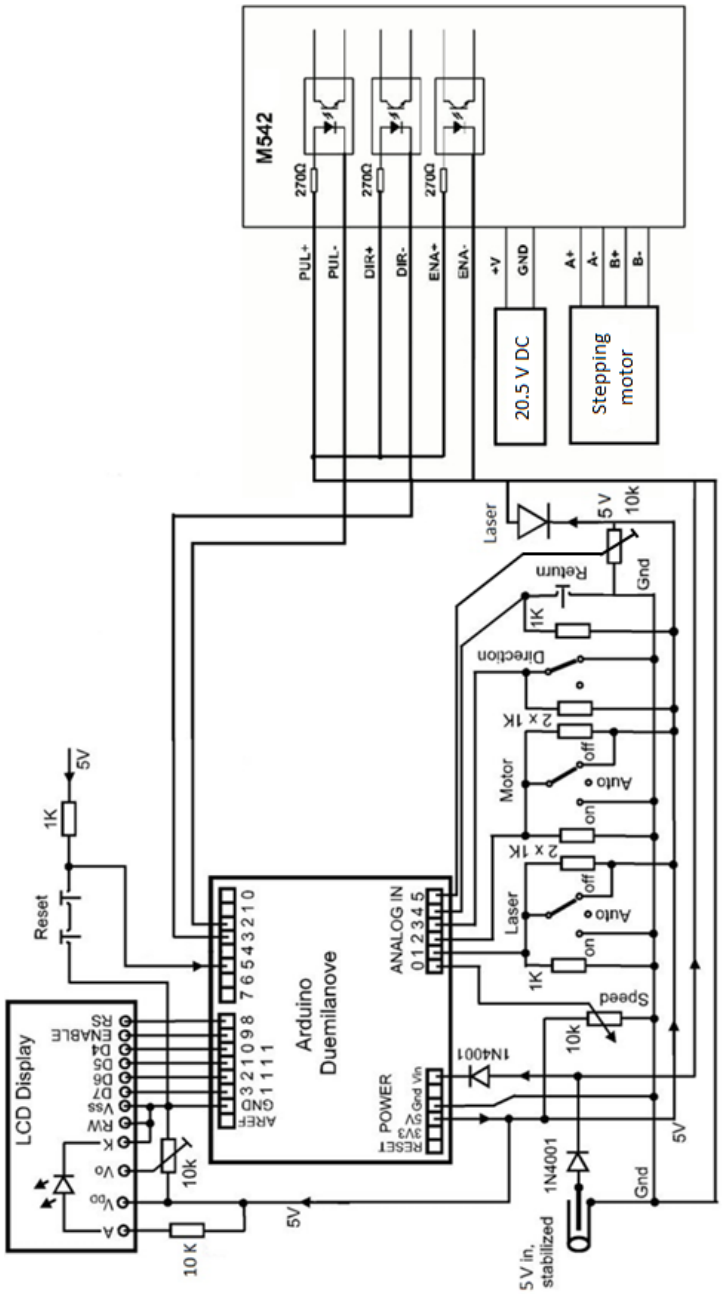

APPENDIX B

Source Code for controller

```
// Welcome meessage:
#include <LiquidCrystal.h>

const char PROGRAM_VERSION[20] = "3D Laser Scanner";


// Global Parameter Definitions:
const bool FORCE_REMOTE_CONTROL = true;

// analog input pins:
const int PIN_IN_SPEED   = A0;
const int PIN_IN_LASER   = A1;
const int PIN_IN_MOTOR   = A2;
const int PIN_IN_DIR     = A3;
const int PIN_IN_GO_ZERO = A4;

// digital output pins:
const int PIN_OUT_CLOCK  = 2;
const int PIN_OUT_DIR    = 3;
const int PIN_OUT_LASER  = 4;
const int PIN_OUT_LCD    = 8;

// digital input pins:
const int PIN_IN_SET_ZERO = 5;

// speed steps and their delays [Âµs]:
const int NUM_SPEED_STEPS=6;
const unsigned long DELAYS[NUM_SPEED_STEPS] =
{50000,20000,10000,5000,2000,1000};  // in Âµs
const unsigned long HOMING_MOTOR_DELAY = 1000;  // defines the speed for
the "return" = "go home" = "go to zero" command [Âµs]

// Gearbox backlash compensation:
const long BACKLASH_STEPS = 500;  // number of steps

const long MIDDLE_POS = 2000;
const long NUM_STEPS_FAST = 100;

// Time interval [ms] for display updates:
const unsigned long DISPLAY_INTERVAL = 200;  // 200ms --> 5 Hz
```

// Global Variable Declarations:

```
long g_motorPos = 0;              //< global motor step counter
int g_speed = 0;                 //< global speed setting in [0,NUM_SPEED_STEPS-1]
bool g_isLaserOn = false;         //< global state of laser (on or off)
int g_lastCOM = ' ';              //< latest COM message
long g_dir = -1;                 //< scan direction (1 or -1)

LiquidCrystal g_lcd(PIN_OUT_LCD, PIN_OUT_LCD+1, PIN_OUT_LCD+2,
PIN_OUT_LCD+3, PIN_OUT_LCD+4, PIN_OUT_LCD+5);  // initialize the library
with the numbers of the interface pins



/// modes for laser and motor
enum eMode
{
  MODE_ON   = 0,
  MODE_AUTO = 1,  // "auto" means remote controlled, e.g. via serial COM port
  MODE_OFF  = 2,
};


long analogToDiscrete(long value, long num, long mod=1024)
{
  return (value*num)/mod;

}

/// Maps an "analog" input value into one of the eModes MODE_OFF,
MODE_AUTO, or MODE_ON. See #analogToDescrete and #eMode.
eMode analogToMode(long value, long mod=1024)
{
  return (eMode)analogToDiscrete(value,3,mod);
}

void delaySinceLastCall(unsigned long delay_us, unsigned long &lastTime)
{
  unsigned long m;

  do
  {
    m=micros();  // get current time stamp
    if (m<lastTime) lastTime=m;  // reset when micros() has flown over (happens
every 2^32 Âµs = 71.6 minutes)
  }
  while (m-lastTime <= delay_us);  // loop until delay_us Âµs have passed
```

```
  lastTime = m;
}


//Setup

// The setup() method runs once, when the sketch starts.
void setup()
{
  // Init LC Display:
  g_lcd.begin(20, 2);

  // Init serial port:
  Serial.begin(9600);

  // Init input pins:
  pinMode(PIN_IN_SPEED,    INPUT);
  pinMode(PIN_IN_LASER,    INPUT);
  pinMode(PIN_IN_MOTOR,    INPUT);
  pinMode(PIN_IN_DIR,      INPUT);
  pinMode(PIN_IN_GO_ZERO,  INPUT);
  pinMode(PIN_IN_SET_ZERO, INPUT);

  // Pull inputs to HIGH by a pull-up resistor, in case they are left "open":
  digitalWrite(PIN_IN_SPEED, HIGH);
  digitalWrite(PIN_IN_LASER, HIGH);
  digitalWrite(PIN_IN_MOTOR, HIGH);
  digitalWrite(PIN_IN_DIR, HIGH);
  digitalWrite(PIN_IN_GO_ZERO, HIGH);
  digitalWrite(PIN_IN_SET_ZERO, HIGH);

  // Init output pins:
  pinMode(PIN_OUT_CLOCK, OUTPUT);
  pinMode(PIN_OUT_DIR,   OUTPUT);
  pinMode(PIN_OUT_LASER, OUTPUT);

  // Show welcome message:
  g_lcd.clear();
  g_lcd.setCursor(0,0);
  g_lcd.print(PROGRAM_VERSION);
  g_lcd.setCursor(0,1);
  g_lcd.print("Strathclyde 3D Scanner");
  delay(3000);
  g_lcd.clear();
}
//Display
void printFormattedFloat(LiquidCrystal &lcd, float value, int width, int precision)
{
```

```
  char string[20];  // temporary string buffer
  dtostrf(value, width, precision, string);  // convert to string using dtostrf
  lcd.print(string);  // print
}


// Shows the current state (step counter, laser on/off, motor speed, COM message) on
LCD.
// Prints only those values to the LCD which have changed.
void showState()
{

  static int  last_isLaserOn = -42;
  static long last_motorPos = -42;  // for step display
  static long last_motorPos2 = -42;  // for speed measurement
  static int  last_speed = -42;
  static int  last_ch = 0;

  static unsigned long lastTime = 0;  // remember last call time stamp


  // First LCD Line:
  // Laser on/off:
  if (g_isLaserOn!=last_isLaserOn)  // if the laser has changed since last time
  {
    g_lcd.setCursor(0,0);
    g_lcd.print("Laser:");
    if (g_isLaserOn) g_lcd.print("1");
    else             g_lcd.print("0");
    last_isLaserOn = g_isLaserOn;  // remember new laser state
  }

  // motor step counter:
  if(last_motorPos!=g_motorPos)  // if the motor position has changed since last time
  {
    g_lcd.setCursor(8,0);
    g_lcd.print("Step        ");
    g_lcd.setCursor(12,0);
    g_lcd.print(":");
    g_lcd.setCursor(13,0);
    g_lcd.print(g_motorPos);
    last_motorPos = g_motorPos;  // remember new motor position
  }

  // Second LCD Line:
  // COM:
  if (last_ch!=g_lastCOM)
  {
```

```
  g_lcd.setCursor(0,1);
  g_lcd.print("COM: ");
  g_lcd.setCursor(4,1);
  g_lcd.print((char)g_lastCOM);
  last_ch = g_lastCOM;
 }
 g_lastCOM = ' ';  // show nothing next time

 // Speed setting:
 if (last_speed!=g_speed)  // if speed has changed
 {
  g_lcd.setCursor(6,1);
  g_lcd.print("Spd:");
  if (g_speed<0) g_lcd.print("R");       // Show "R" for "Returning"
  else           g_lcd.print(g_speed+1);  // speed is [0-5], but show as [1-6]
  last_speed = g_speed;  // remember for next time
 }

 // Measured speed:
 {
  g_lcd.setCursor(13,1);
  long stepsPassed = g_motorPos-last_motorPos2;
  unsigned long now = micros();  // current time stamp
  if (0!=stepsPassed)
  {
   float dt = (float)(now-lastTime)/1E6;  // delta t in s
   float spd = (float)stepsPassed / dt;  // steps per second
   printFormattedFloat(g_lcd, fabs(spd), 5, 1);
   g_lcd.print("Hz");
   lastTime=now;  // remember time stamp for next time
   last_motorPos2=g_motorPos;  // remember new motor position
  }
  else
  {
   g_lcd.print("       ");  // show no speed
  }
 }
}
```

//Motor

```
void moveMotorRel(long steps, unsigned long
motorDelay=HOMING_MOTOR_DELAY)
{
 if (steps>0) digitalWrite(PIN_OUT_DIR, HIGH);  // move forward
 else         digitalWrite(PIN_OUT_DIR, LOW);   // move backward
 delayMicroseconds(50);  // Time for the motor driver to set direction

 static unsigned long lastTime=0;
```

```
  for (long i=0; i<abs(steps); ++i)
  {
    delaySinceLastCall(motorDelay,lastTime);
    digitalWrite(PIN_OUT_CLOCK, HIGH);
    delaySinceLastCall(motorDelay,lastTime);
    digitalWrite(PIN_OUT_CLOCK, LOW);
  }

  g_motorPos += steps;  // update the global step counter
}

/// Moves the motor to a given absolute step position.
void moveMotorAbs(long pos, unsigned long
motorDelay=HOMING_MOTOR_DELAY)
{
  moveMotorRel(pos-g_motorPos, motorDelay);
}

/// Moves the motor to a given absolute step position, and updates display regularly.
void moveMotorAbs_withDisplay(long pos, unsigned long
motorDelay=HOMING_MOTOR_DELAY)
{
  // Go step by step:
  long stepsToGo = abs(pos-g_motorPos);  // how many steps
  long dir = (pos>g_motorPos) ? 1 : -1;  // direction of each step (1 or -1)

  unsigned long lastTime=0;  // time stamp for display update
  for (long i=0; i<stepsToGo; ++i)  // each step separately
  {
    moveMotorRel(dir,motorDelay);  // make one step

    unsigned long time=millis();      // in ms
    if (time-lastTime>DISPLAY_INTERVAL)  // if at least DISPLAY_INTERVAL
ms have passed
    {
      showState();  // update display
      lastTime=time;  // reset time stamp
    }
  }
}

// Moves the motor to the zero position. Always goes BACKLASH_STEPS over 0 to
compensate gearbox backlash.
void moveMotorHome(unsigned long motorDelay=HOMING_MOTOR_DELAY)
{
  // move a little over 0 to compensate backlash:
  moveMotorAbs_withDisplay(-g_dir*BACKLASH_STEPS,  motorDelay);
```

```
  // move to 0:
  moveMotorAbs(0, motorDelay);
}

// Moves the motor to the zero position. Always goes BACKLASH_STEPS over 0 to
compensate gearbox backlash.
// Uses moveMotorAbs_withDisplay which regularly updates the display.
void moveMotorHome_withDisplay(unsigned long
motorDelay=HOMING_MOTOR_DELAY)
{
  int rememberedSpeed = g_speed;
  g_speed = -1;  // for display

  // move a little over 0 to compensate backlash:
  moveMotorAbs_withDisplay(-g_dir*BACKLASH_STEPS,  motorDelay);

  // update display:
  showState();
  delay(200);

  // move to 0:
  moveMotorAbs_withDisplay(0, motorDelay);
  delay(200);

  g_speed = rememberedSpeed;  // re-set speed
}
```

//Laser

```
// setLaser(true) switches the laser on. setLaser(false) switches the laser off.
void setLaser(bool on)
{
  if (on==g_isLaserOn) return;  // nothing to do

  if (on==true)
  {
    // switch the laser on
    digitalWrite(PIN_OUT_LASER, HIGH);
  }
  else
  {
    // switch the laser off
    digitalWrite(PIN_OUT_LASER, LOW);
  }

  g_isLaserOn = on;  // remember the new laser state
}
```

//Main Loop

```
// the loop() method runs over and over again, as long as the Arduino has power
void loop()
{
  // Read input pins:
  // Laser: OFF, AUTO, or ON. See #eMode declaration.
  eMode laserMode = analogToMode(analogRead(PIN_IN_LASER));

  // Motor: OFF, AUTO, or ON. See #eMode declaration.
  eMode motorMode = analogToMode(analogRead(PIN_IN_MOTOR));

  // Direction: -1=down, 1=up
  g_dir = analogToDiscrete(analogRead(PIN_IN_DIR),2) * 2 - 1;

  if (FORCE_REMOTE_CONTROL)
  {
        // Overwrite to AUTO:
        laserMode = MODE_AUTO;
        motorMode = MODE_AUTO;
        g_dir = 1;
  }

  // Speed: 0 to NUM_SPEED_STEPS-1
  g_speed =
analogToDiscrete(analogRead(PIN_IN_SPEED),NUM_SPEED_STEPS);

  // Move to zero
  bool moveHome = 1-analogToDiscrete(analogRead(PIN_IN_GO_ZERO),2);

  // Set counter to zero:
  bool setZero = !digitalRead(PIN_IN_SET_ZERO);

  //--------------------------
  // Act according to inputs:
  //--------------------------
  // Set laser:
  if     (MODE_OFF  ==laserMode) setLaser(false);
  else if (MODE_ON   ==laserMode) setLaser(true);
  else if (MODE_AUTO ==laserMode && MODE_AUTO!=motorMode)
setLaser(MODE_ON==motorMode);

  // Motor:
  if (moveHome) moveMotorHome_withDisplay(HOMING_MOTOR_DELAY);
  if (MODE_ON==motorMode) moveMotorRel(g_dir,DELAYS[g_speed]);  // move
one step in the desired direction
```

```
  // Counter:
  if (setZero) g_motorPos = 0;

  //----------------------------
  // Read serial input into ch:
  //----------------------------
  int ch = 0;
  if (Serial.available() > 0)
  {
    // read the incoming byte:
    ch = Serial.read();
    g_lastCOM = ch;  // remember in g_lastCOM (for display)
  }

  // Act according to ch, if motorMode and laserMode allow:
  if (MODE_AUTO==motorMode)  // allow remote control of motor
  {
    if ('+' == ch)      moveMotorRel(1);                                  // one step forward
    else if ('-' == ch) moveMotorRel(-1);                                  // one step backward
    else if ('>' == ch) moveMotorRel(NUM_STEPS_FAST);    // several steps forward
    else if ('<' == ch) moveMotorRel(-NUM_STEPS_FAS     // several steps backward
    else if ('M' == ch) moveMotorRel(g_dir);                                  // one step forward
    else if ('Q' == ch) moveMotorHome_withDisplay(HOMING_MOTOR_DELAY);
                                                                  // move to zero [deprecated?]
    else if ('#' == ch)  // move laser into camera image:
    {
      if (MODE_AUTO==laserMode) setLaser(true);                           // switch laser
on
      moveMotorAbs_withDisplay(g_dir*MIDDLE_POS,
HOMING_MOTOR_DELAY);         // move to MIDDLE_POS
    }
    else if ('P' == ch)  // Prepare for next scan:
    {
      if (MODE_AUTO==laserMode) setLaser(true);                           // switch laser
on
      moveMotorHome_withDisplay(HOMING_MOTOR_DELAY);    // move to zero
      if (MODE_AUTO==laserMode) setLaser(false);                          // switch laser
off
    }
  }

  if ('m' == ch)    // move motor with given number of steps
  {
    int sign = 1;  // The direction (+1 or -1)
    int numSteps = 0;  // number of steps to move
    for (int i=0; i<6; ++i)  // read up to 6 characters
    {
```

```
    while (Serial.available()<1) {};  // wait for new character
    int ch2 = Serial.read();  // read one new character
    if      ('+'==ch2) sign = 1;  // set positive direction
    else if ('-'==ch2) sign = -1;  // set negative direction
    else if (ch2>='0' && ch2<='9') numSteps = numSteps*10 + (ch2-'0');  // read one
numeric digit into numSteps
    else break;  // invalid character, e.g. semicolon --> stop reading
   }
   numSteps *= sign*g_dir;  // apply direction + or -
   if (MODE_AUTO==motorMode)
   {
    moveMotorRel(numSteps);  // move!
   }
  }

  if (MODE_AUTO==laserMode)  // allow remote control of laser
  {
   if ('S' == ch) setLaser(true);                                  // scan start --> switch laser
on
   else if ('L' == ch) setLaser(true);                              // switch laser on
   else if ('l' == ch) setLaser(false);                             // switch laser off
   else if ('1' == ch) setLaser(false);                             // cam.calib --> switch
laser off
   else if ('3' == ch) setLaser(false);                             // texturing --> switch
laser off
  }

  if ('T' == ch)  // received "Stop"
  {
   if (MODE_AUTO==laserMode) setLaser(false);                              // switch laser
off
   if (MODE_AUTO==motorMode)
moveMotorHome_withDisplay(HOMING_MOTOR_DELAY);  // move to zero
  }

  if ('0' == ch) g_motorPos = 0;                                   // Reset step counter

  // Show the current state on display:
  static unsigned long lastTime=0;  // in ms
  unsigned long time=millis();      // in ms
  if (time-lastTime>DISPLAY_INTERVAL)  // if at least DISPLAY_INTERVAL
ms have passed
  {
   showState();  // update display
   lastTime=time;  // reset timer
  }
}
```

APPENDIX C

Mechanical drawing for stepper motor

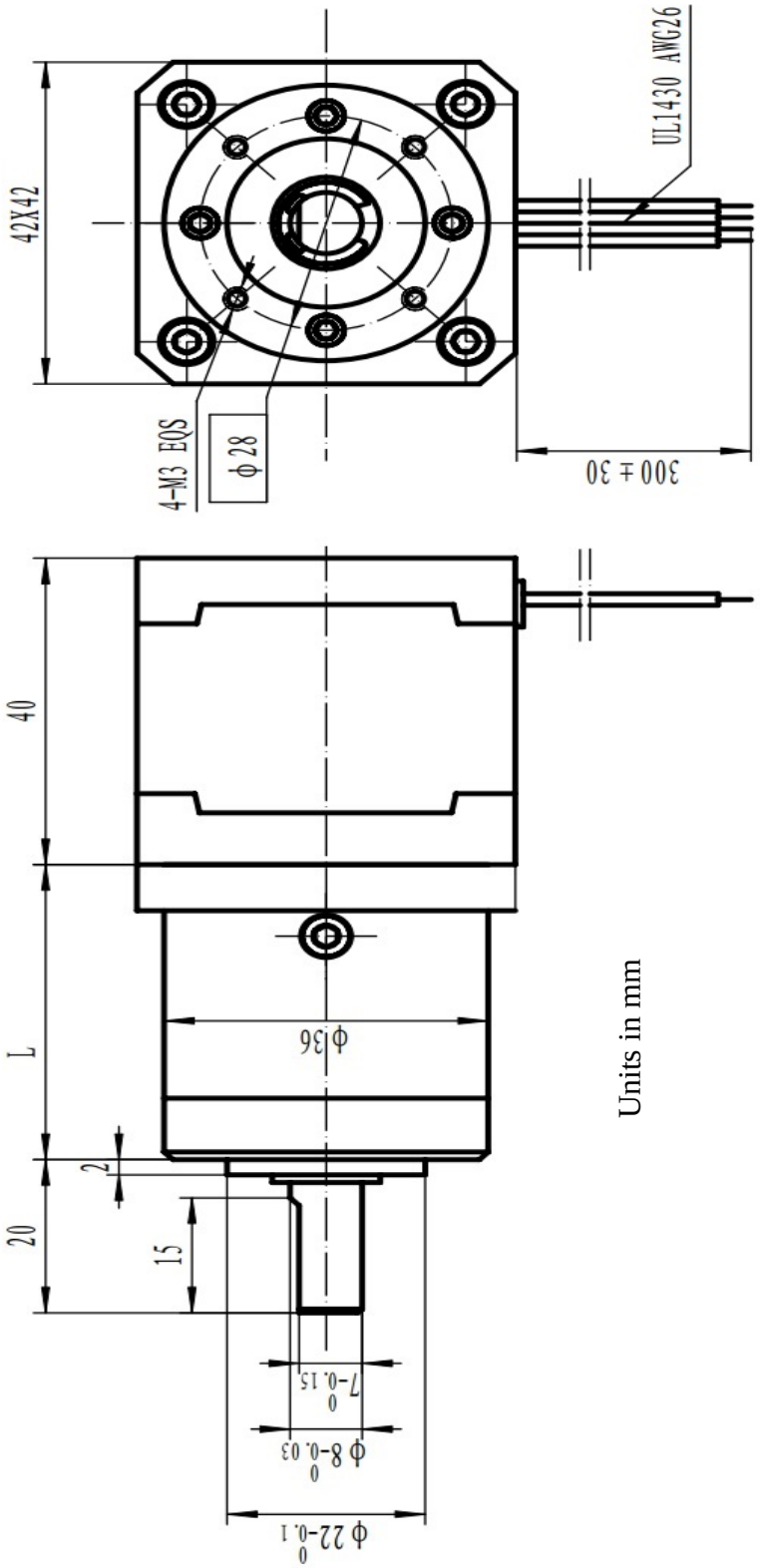

Units in mm